33/5-16-95 JS(2)

# BROOKHAVEN NATIONAL LABORATORY

## Long Baseline Neutrino Oscillation Experiment

### Long Island, New York

### E889 Collaboration

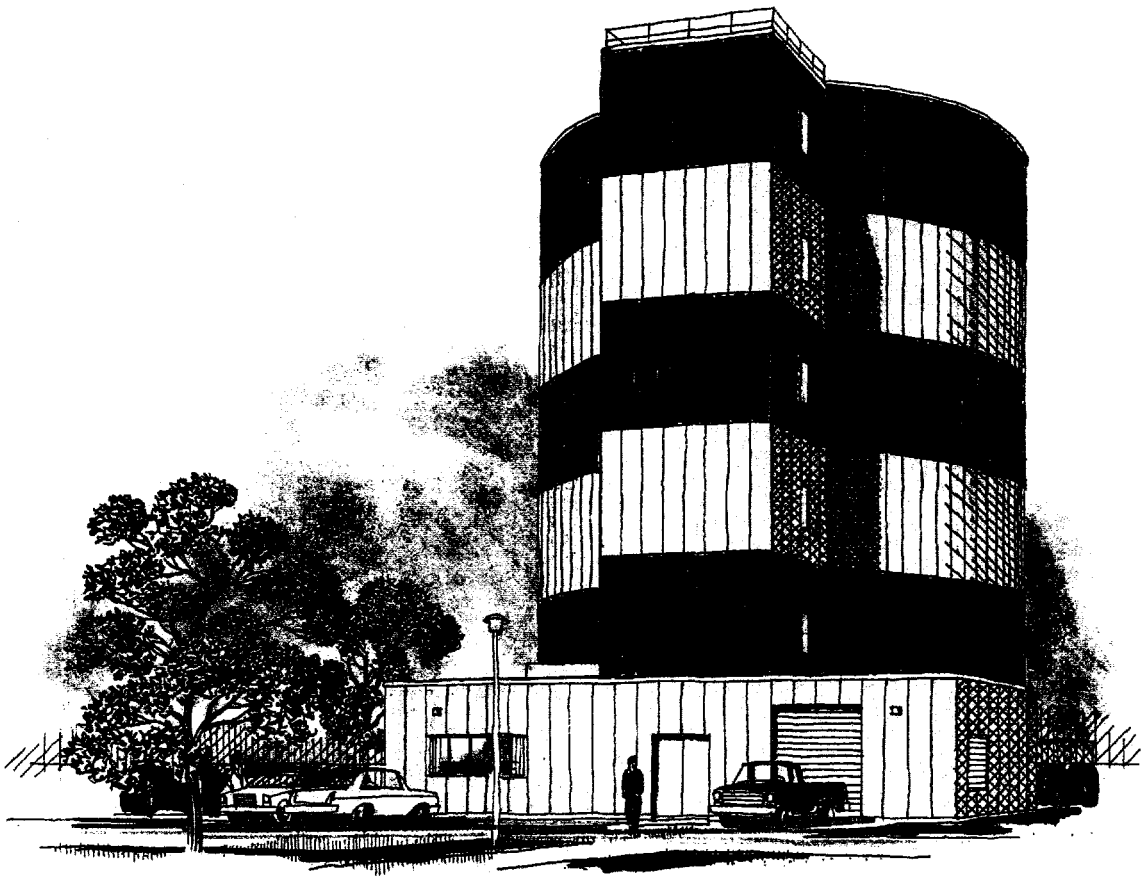

Neutrino Oscillation Experiment
Brookhaven National Laboratory, Long Island, N.Y.

**Physics Design Report**
**BNL No. 52459**
**April 1995**

MASTER

## DISCLAIMER

## DISCLAIMER

Portions of this document may be illegible in electronic image products. Images are produced from the best available original document.

# Long Baseline Neutrino Oscillation Experiment at the AGS
## Approved by the HENPAC as AGS Experiment 889

*D. Beavis, A. Carroll, I. Chiang, M. Diwan* †, *J. Frank, S. Kahn,*
*M. Marx* *, *S. McCorkle, M. Murtagh, J. Sondericker III, H. Takai, P. Yamin*
Brookhaven National Laboratory, Long Island, NY

*D. Bauer, D. Caldwell, A. Lu, S. Yellin*
University of California, Santa Barbara

*R. L. Imlay, W. Metcalf*
Louisiana State University, Baton Rouge, LA

*B. Barakat, C. Athanassopoulos, M. Elaasar, K. Johnston*
Louisiana Tech University, Ruston, LA

*G. Azuelos, P. Depommier, F. Gingras, B. Moffat*
University of Montreal, Montreal, Canada

*B. Dieterle, R. Reeder*
University of New Mexico, Albuquerque, NM

*J. Hill, A. K. Mann* †
University of Pennsylvania, Philadelphia, PA

*A. Fazely*
Southern University and A & M College, Baton Rouge, LA

*C. Fred Moore, S. Mordechai* **
University of Texas at Austin

*M. Barnes, J. Beveridge, P. Gumplinger, R. Helmer* †, *J-M. Poutissou,*
*G. Wait, D. H. Wright*
TRIUMF, Vancouver, B.C., Canada

*D. D. Koetke, R. W. Mainweiler, T. D. S. Stanislaus*
Valparaiso University, Valparaiso, IN

*R. Appel*
Yale University, New Haven, CT

† Co-spokespersons
*Permanent Affiliation: SUNY, Stony Brook
**Permanent Affiliation: Ben Gurion University, Israel

This work was supported by the U.S. Department of Energy under contract
DE-AC02-76CH00016.

Table of Contents

## EXECUTIVE SUMMARY

We present a design for a multi-detector long baseline neutrino oscillation experiment at the BNL AGS. It has been approved by the BNL-HENP-PAC as AGS Experiment 889. The experiment will search for oscillations in the $\nu_\mu$ disappearance channel and the $\nu_\mu \leftrightarrow \nu_e$ appearance channel by means of four identical neutrino detectors located 1, 3, 24, and 68km from the AGS neutrino source. Observed depletion of the $\nu_\mu$ flux (via quasi-elastic muon neutrino events, $\nu_\mu n \rightarrow \mu^- p$) in the far detectors not attended by an observed proportional increase of the $\nu_e$ flux (via quasi-elastic electron neutrino events, $\nu_e n \rightarrow e^- p$) in those detectors will be *prima facie* evidence for the oscillation channel $\nu_\mu \leftrightarrow \nu_\tau$. The experiment is directed toward exploration of the region of the neutrino oscillation parameters $\Delta m^2$ and $\sin^2 2\theta$, suggested by the Kamiokande and IMB deep underground detectors but it will also explore a region more than two orders of magnitude larger than that of previous accelerator experiments.

The experiment is designed to capitalize on the advantages of the AGS: high proton beam intensity (currently the AGS can provide $6 \times 10^{13}$ per pulse every 1.6 sec) yielding a correspondingly high intensity, low energy, pure ( $\nu_e/\nu_\mu$ flux ratio of $10^{-2}$) muon neutrino beam, and the narrow time-structure (20-30 ns wide 8 bunches per pulse) of the fast extracted proton beam to permit the detectors to be located on the earth's surface. We have requested $10^{21}$ protons on target in the fast extraction mode for the entire experiment, but as discussed below some of this running will occur without the full complement of detectors.

The experiment will run in a mode new to BNL. It will receive the fast extracted proton beam on the neutrino target approximately 20 hours per day when the AGS is not filling RHIC.

A key aspect of the experimental design involves placing the detectors 1.5 degrees off the center line of the neutrino beam, which has the important advantage that the central value of the neutrino energy ($\approx$ 1 GeV) and the beam spectral shape are, to a good approximation, the same in all four detectors. Another significant advantage of the 1.5 degree beam is that the low energy ($\approx$ 1 GeV) flux is increased while the higher energy flux is decreased relative to the flux in the zero degree beam. This appreciably diminishes the rate of inelastic neutrino interactions with respect to the dominant quasi-elastic interactions that constitute the signals of the experiment.

The proposed detectors are massive, imaging, water Cherenkov detectors similar in large part to the Kamiokande and IMB detectors. Our design has profited from their decade-long

experience, and from the detector designs of the forthcoming SNO and SuperKamiokande detectors.

An important principle in the design of the experiment has been to provide detailed, precise, and redundant control of possible systematic errors. This accounts for the requirement of four identical detectors, and their relative spacing, which yields data of high statistical quality in the upstream detectors with which to study the neutrino beam properties and the response of the massive, large volume detectors. This ensures proper understanding of the response of the far detectors and correct high precision predictions of the fluxes reaching the far detectors in the absence of oscillations. To this end, the ratio $QE(\mu)/NC(\pi^0) - QE(\mu)$ is the count rate of quasi-elastic muon neutrino events, and $NC(\pi^0)$ is the count rate of neutral current $\pi^0$ events – is also measured in each of the four detectors to provide an essentially independent search for oscillations in the $\nu_\mu$ disappearance channel, as well as in the channel $\nu_\mu \leftrightarrow \nu_{(sterile)}$.

The experiment will evolve in a continuous fashion, dictated by the rates at which construction and funding are likely to proceed. The detectors will be built in the sequence D3, D24, D68, and the fourth detector at D1. this permits operation as soon as each detector is completed, and makes possible the extraction of significant oscillation results from D3 and D24 early in calendar 1999. All four tanks would be in operation one year later.

A cost and schedule document (CDR) has been submitted to the DOE which provides the basis for the total project cost and schedule. This schedule is funding driven and might be advanced by a half year with an improved funding profile.


| | | | |
|---|---|---|---|
| Contacts : | M.V. Diwan | BNL | 516-282-3327; diwan@bnlcl6.bnl.gov |
| | R.L Helmer | TRIUMF | 604-222-1047; sfu@erich.triumf.ca |
| | A.K. Mann | UPENN | 215-898-8155; mann@dept.physics.upenn.edu |

# I. Introduction

## A. Neutrino oscillation results from solar and atmospheric neutrino data.

In the last few years, questions concerning the masses of the light, standard model neutrinos and the degree to which they mix have received increasing attention. The situation is summarized in Fig. 1 in which are plotted both the solar neutrino results and also the most recent atmospheric neutrino results interpreted in the framework of neutrino oscillations.

In one current interpretation the results from solar neutrino detectors [1] suggest that the disappearance of electron type neutrinos ($\nu_e$) may be due to resonant neutrino oscillations in the matter of the Sun, and that the $\nu_e$ and the neutrino type into which it oscillates, possibly $\nu_\mu$, have small, $\leq 10^{-2}$ eV, mass. In addition, recent results on atmospheric neutrinos from the Kamiokande and IMB imaging water Cherenkov detectors suggest that the observed disappearance of muon type neutrinos ($\nu_\mu$) may be due to vacuum neutrino oscillations, and that the mass of the neutrino into which the $\nu_\mu$ oscillates, possibly the $\nu_\tau$, lies in the interval from $10^{-2}$ to $O(1)$ eV [2].

A second scenario explains the solar neutrino deficit via $\nu_e \leftrightarrow \nu_s$, where both the $\nu_e$ and the sterile neutrino $\nu_s$ are much lighter ($\Delta m^2_{es} \sim 10^{-5} eV^2$) than the $\nu_\mu$ and $\nu_\tau$ [3]. The mass difference of $\nu_\mu$ and $\nu_\tau$, as indicated by the atmospheric neutrino results, $5 \times 10^{-3} \lesssim \Delta m^2_{\mu\tau} \lesssim 3 \times 10^{-2} eV^2$, allows both $\nu_\mu$ and $\nu_\tau$ masses to be approximately equal and of the order of a few eV. This scenario is motivated in part by the need for an admixture (20–40%) of hot dark matter—roughly 7 eV worth—relative to the total, which would be consistent with the cosmic background radiation fluctuations, galaxy position and cluster correlations and large scale velocity flows.

We emphasize that the experiment discussed here, AGS E889, is important in either scenario, as will be discussed in detail in what follows.

Confirmation or repudiation of the solar neutrino results will be forthcoming in the next few years as the new solar neutrino detectors now under construction come into operation [4]. The experimental prospects for exploitation of the atmospheric neutrino results is, however, less clear. The present data sample is based on approximately 15 kiloton-years and more data continue to be acquired. A larger statistical sample will be of value, but the inherent limitation in the interpretation of the data is in the normalization which rests largely on a calculation of the expected atmospheric neutrino flux ratio $\nu_\mu/\nu_e$ and the interactions of the $\nu_\mu$ and $\nu_e$ in the detectors. In certain salient respects the calculation is less suspect than usual, e.g., the absolute magnitude and constitution of the primary cosmic ray flux cancel

out of the $\nu_\mu/\nu_e$ ratio, and all extant calculations yield the same value for the ratio within 5% uncertainty as seen in Table I. Furthermore, the model used to describe the interactions of $\nu_\mu$ ($\bar{\nu}_\mu$) and $\nu_e(\bar{\nu}_e)$ with $^{16}O$ is unlikely either to be seriously incorrect or to require corrections that might explain the effect, as shown in Table II and described in reference [5].

Fig. 2 shows a comparison of the $\cos\theta_Z$ distributions of the sub-GeV and multi-GeV atmospheric neutrino data [6], which indicates for the first time an energy dependence consistent with a neutrino oscillation interpretation of the totality of the data; the parameter regions allowed for the channels $\nu_\mu \leftrightarrow \nu_e$ and $\nu_\mu \leftrightarrow \nu_\tau$ are shown in Fig. 3. This result will be extended and exploited with high statistics in the data forthcoming from Superkamiokande. In short, while scepticism remains, no source of error in the atmospheric neutrino data or its interpretation has been uncovered. Nevertheless, the normalization of the data, i.e., the predicted ratio of muon to electron events necessary for comparison with the observed ratio, remains a semi-empirical calculation, and prevents a definitive conclusion on neutrino mass and mixing from being reached.

Attempts in other, smaller detectors, i.e., the Fréjus and Soudan [7] iron plate-chamber detectors of approximately 1 kiloton total mass, to reproduce the results from the imaging water Cherenkov detectors have been statistically inconclusive, in part because of small mass and relatively short exposures. Fréjus claims no discrepancy similar to that in Table II within approximately $2\sigma$ while the central value of the $\mu/e$ ratio from Soudan is consistent with the average value in Table II but at present only $2\sigma$ away from unity.

The range of $\Delta m^2$ and $\sin^2 2\theta$ obtained from the atmospheric neutrino data does, however, suggest that a properly designed, long baseline neutrino oscillation experiment carried out with relatively low energy $\nu_\mu$ from an accelerator over a reasonable distance would definitively answer the questions relating to the observed $\nu_\mu$ disappearance in the atmospheric neutrino data. Such an experiment would eliminate the normalization problem in the atmospheric neutrino observations and conclusively confirm or deny the occurrence of neutrino oscillations in a $\Delta m^2 - \sin^2 2\theta$ region which would include all of the region indicated by the atmospheric neutrino data in Fig. 3 and some beyond. Of equal importance, a single long baseline accelerator experiment with several detectors would provide sufficient control of possible systematic errors to ensure a convincing result and to allow a quite small region of the $\Delta m^2 - \sin^2 2\theta$ space to be specified as the result of the experiment.

At present, there are two data-taking accelerator experiments in the world, Karmen and LSND, directed toward a small part of the $\Delta m^2 - \sin^2 2\theta$ region indicated by the atmospheric neutrinos [8]. These experiments, which look for $\nu_\mu \rightarrow \nu_e(\bar{\nu}_\mu \rightarrow \bar{\nu}_e)$ oscillations expect to

cover the interval $\Delta m^2 \gtrsim 0.1eV^2$ and $\sin^2 2\theta \geq 10^{-2}$, i.e., a part of the allowed interval delineated by the atmospheric neutrino data (see below).

For completeness, we note that two neutrino oscillation experiments, Chorus and Nomad, directed primarily toward the oscillation channel $\nu_\mu \leftrightarrow \nu_\tau$ have been operating at CERN [9]. These are similar in concept and in plan to an earlier experiment at Fermilab [10] in that they seek to observe $\tau$ leptons produced by $\nu_\tau$ from oscillations. The region in the $\Delta m^2 - \sin^2 2\theta$ space of vacuum oscillations that the past and future Fermilab and present CERN experiments will explore is shown in Fig. 4, which indicates, first, that they have no overlap with the region specified by the atmospheric neutrino result in Fig. 3, and consequently none with the experiment proposed here; and, second, that these experiments and the AGS experiment described here will together explore practically the entire region of the neutrino oscillation space in which a tau neutrino mass might be of such magnitude as to be influential as dark matter in the universe.

Before concluding this introductory section, we note that there is additional information in Fig. 1 from the atmospheric neutrino observations beside that from the data described earlier and shown in Table II. The cross hatched area marked "KAM allowed" showing the implications of the atmospheric neutrino data for neutrino oscillations is the result of studies of atmospheric $\nu_\mu$– and $\nu_e$–induced events in the Kamiokande and IMB detectors that are completely or partially contained, which ensures that the momentum of each produced $\mu$ and $e$ is measured or approximated along with particle identification, and gives high probability that no other particles with velocities above the Cherenkov radiation threshold are present. The virtue of this method is that the observed ratio of muon single (Cherenkov) ring events to electron single ring events can be directly compared to the corresponding calculated ratio based on estimates of the atmospheric flux ratio $\phi(\nu_\mu)/\phi(\nu_e)$, as stated above. In calculating the flux ratio $\phi(\nu_\mu)/\phi(\nu_e)$, absolute knowledge of certain factors that enter the calculation is unnecessary, e.g., the absolute value of the primary components of the cosmic rays that impinge on the earth's atmosphere cancels out of the ratio $\phi(\nu_\mu)/\phi(\nu_e)$. As a consequence, the ratio $\phi(\nu_\mu)/\phi(\nu_e)$ is thought to be known within an uncertainty of less than 5% (Table I), while the absolute values of $\phi(\nu_\mu)$ and $\phi(\nu_e)$ are not estimated to better than about 30%. The uncertainty in the predicted ratio of atmospheric $\nu_\mu$–induced events to atmospheric $\nu_e$–induced events includes the 5% uncertainty in the incident flux ratio as well as other possible systematic uncertainties (Table II and reference [5]), the total of which amount to a systematic error of the order of 10%. References [2], and [5], give a more complete explanation of the contained event data.

The additional information from atmospheric neutrino studies comes from observations of upward-going muons produced in the rock or salt surrounding the Kamiokande and IMB detectors by the atmospheric $\nu_\mu$ flux. There is little background from cosmic ray muons in the upward-going sample. Most of the upward-going muons, which are the products of neutrinos of average energy roughly 100 GeV, pass through the detectors, but about 20% of the upward-going muons are produced in reactions of neutrinos of average energy about 10 GeV and stop in the detectors. To use the through-going upward muon intensity alone as a means to search for neutrino oscillations requires that the neutrino flux in the interval 10 to 1000 GeV be calculated absolutely and that absolute neutrino cross sections with matter in that energy region be estimated accurately. These introduce uncertainties in the upward through-going muon flux calculations of about 20% and lead to corresponding uncertainties in the neutrino oscillation parameters $\Delta m^2 - \sin^2 2\theta$ [11]. The ratio of upward stopping muons to upward through-going muons is, however, less ambiguous, principally because uncertainties in absolute scale approximately cancel [10]. That ratio provides the excluded region in Fig. 1 marked "IMB atmos. upward muons (stopping/thru)" [12].

## References


1. L. Wolfenstein, Phys. Rev. D17, 2369 (1978); 20, 2634 (1979); S.P. Mikheyev and A.Yu. Smirnov, Yad. Fiz. 42, 1441 (1985) [ Sov. J. Nucl. Phys. 42, 913 (1985)]; Nuovo Cimento 9C, 17 (1986).

2. K.S. Hirata et al., Phys. Lett B205, 416 (1988); B280, 146 (1992); R.M. Bionta et al., Phys. Rev. D38, 768 (1988); R. Becker-Szendy et al., Phys. Rev. D46, 3720 (1992); E. W. Beier et al. Phys. Lett. B283, 446 (1992). See also P.F. Harrison, D.H. Perkins, and W.G. Scott, Preprint RAL-94-125 (Dec. 1994).

3. D. O. Caldwell and R.N. Mohapatra, Phys. Rev. D48, 3259 (1993).

4. See, for example, R. Davis, Jr., in *Frontiers of Neutrino Astrophysics*, ed. by Y. Suzuki and K. Nakamura (Universal Academy Press, Tokyo, 1993), p. 47.

5. A.K. Mann, Phys. Rev. D48, 422 (1993); J. Engel et al, Phys. Rev. D48, 3048 (1993).

6. Y. Fukuda et al., Phys. Lett. B335, 237 (1994).

7. Ch. Berger et al. (Fréjus Collab.), Phys. Lett. **B227** (1989) and **B245**, 305 (1990); P. Litchfield et al. (Soudan 2 Collab.), Proc. of Int'l Workshop on $\nu_\mu/\nu_e$ Problem in Atmospheric Neutrinos, Laboratori Nazionali del Gran Sasso, Italy, March 1993, P. 114; M.C. Goodman et al. (Soudan 2 Collab), Proc. 23rd Int'l Cosmic Ray Conference, Calgary, Canada, July 1993.

8. G. Drexlin (Karmen Collab), Prog. Part. Nucl. Phys., 32, 375 (1994); M. Albert et al., (LSND Collab), Phys. Rev. C 51, R1065 (1995).

9. CERN experiments CHORUS and NOMAD, talk to HEPAP Subpanel by G. Feldman, March 1995.

10. N. Ushida et al. (Fermilab Collaboration) Phys. Rev. Lett. 57 2897 (1986); See also M. Gruwe et al., Phys. Lett. B309, 463 (1993).

11. W. Frati, T. Gaisser, A.K. Mann, T. Stanev, Phys. Rev. D48, 1140 (1993).

12. R. Becker-Szendy et al., Phys. Rev. Lett. 69, 1010 (1992).

Table I.. The calculated ratio $R_\nu \equiv \phi(\nu_e + \bar{\nu}_e)/\phi(\nu_\mu + \bar{\nu}_\mu)$ obtained from the neutrino flux calculations in the cited references for the interval $0.1 \lesssim E_\nu \lesssim 1.5$ GeV. There is a small energy dependence of $R_\nu$ above the energy interval specified. From T.K. Gaisser in Proc. Conf. on Long Baseline Neutrino Oscillations (Fermilab, Nov 17-21, 1991) (ed. M. Goodman) p.111.

| Reference | Method | Interaction model | $R_\nu$ |
|---|---|---|---|
| G. Barr, Gaisser & Stanev | M.C. | Parametrized data | 0.48 |
| Lee & Koh | M.C. | " | 0.48 |
| Honda, Kasahara *et al.* | M.C. | NUCRIN + LUND | 0.46 |
| Kawasaki & Mizuta | analytic | Analytic parametrization | 0.49 |

Table II. Ratios of muon and electron events from the IMB and Kamiokande detectors for different momentum thresholds and different neutrino flux calculations. The upper limit of momentum interval in all entries is 900 MeV/c. $R_{meas}(\mu/e)$, $R_{calc}(\mu/e)$, and $R^{meas}_{calc}(\mu/e)$ are, respectively, the measured, calculated, and measured over calculated ratios. For assignments of systematic errors, see the original papers. From reference [5].

| Detector | $R(\mu/e)_{meas}$ | $R(\mu/e)_{calc}$ | $R(\mu/e)^{meas}_{calc}$ | Thresholds (MeV/c) | |
|---|---|---|---|---|---|
| | | | | $P_e$ | $P_\mu$ |
| IMB (LEE FLUX) | 0.531 ± 0.0535 | 0.987 | 0.54 ± 0.054 | 100 | 300 |
| | 0.849 ± 0.0936 | 1.884 | 0.45 ± 0.050 | 300 | 300 |
| | 0.829 ± 0.108 | 1.871 | 0.44 ± 0.058 | 400 | 400 |
| | 0.764 ± 0.123 | 1.798 | 0.43 ± 0.068 | 500 | 500 |
| KAM (LEE FLUX) | 0.671 ± 0.0895 | 1.051 | 0.64 ± 0.085 | 100 | 300 |
| | 1.093 ± 0.163 | 1.836 | 0.60 ± 0.089 | 300 | 300 |
| (Gaisser flux) | 0.671 ± 0.0895 | 1.067 | 0.63 ± 0.084 | 100 | 300 |
| | 1.093 ± o.163 | 1.860 | 0.59 ± 0.088 | 300 | 300 |

# Figure Captions

Figure 1a. Summary of all available data for the neutrino oscillation channels $\nu_\mu \rightarrow \nu_x$ and $\nu_e \rightarrow \nu_x$ bearing on the $\Delta m^2 - \sin^2 2\theta$ region shown. The shaded areas are allowed for neutrino oscillations. The solar neutrino data which yield the allowed region below $\Delta m^2 \approx 10^{-4} eV^2$ are described in reference [1], the reference to E531 is [7]. The data in the upper half of the plot including the atmospheric neutrino data are from [2] and references therein. (b). Another representation of the totality of neutrino oscillation data, from the last citation in reference 2, also includes all data and is based on the assumption that 3-fold neutrino oscillations are taking place.

Figure 2. Plots of $\cos\theta_Z$ from the sub-GeV and multi-GeV data of Kamiokande, from Phys. Lett. B335, 237 (1994).

Figure 3. Plots of $\Delta m^2$ vs $\sin^2 2\theta$ for $\nu_\mu \leftrightarrow \nu_e$ and $\nu_\mu \leftrightarrow \nu_\tau$, showing allowed regions cross hatched, from Phys. Lett. B 335, 237 (1994).

Figure 4. The cross hatched region shows $\Delta m^2 - \sin^2 2\theta$ for $\nu_\mu \leftrightarrow \nu_\tau$ accessible to two approved CERN experiments [9] and a proposed Fermilab experiment [10].

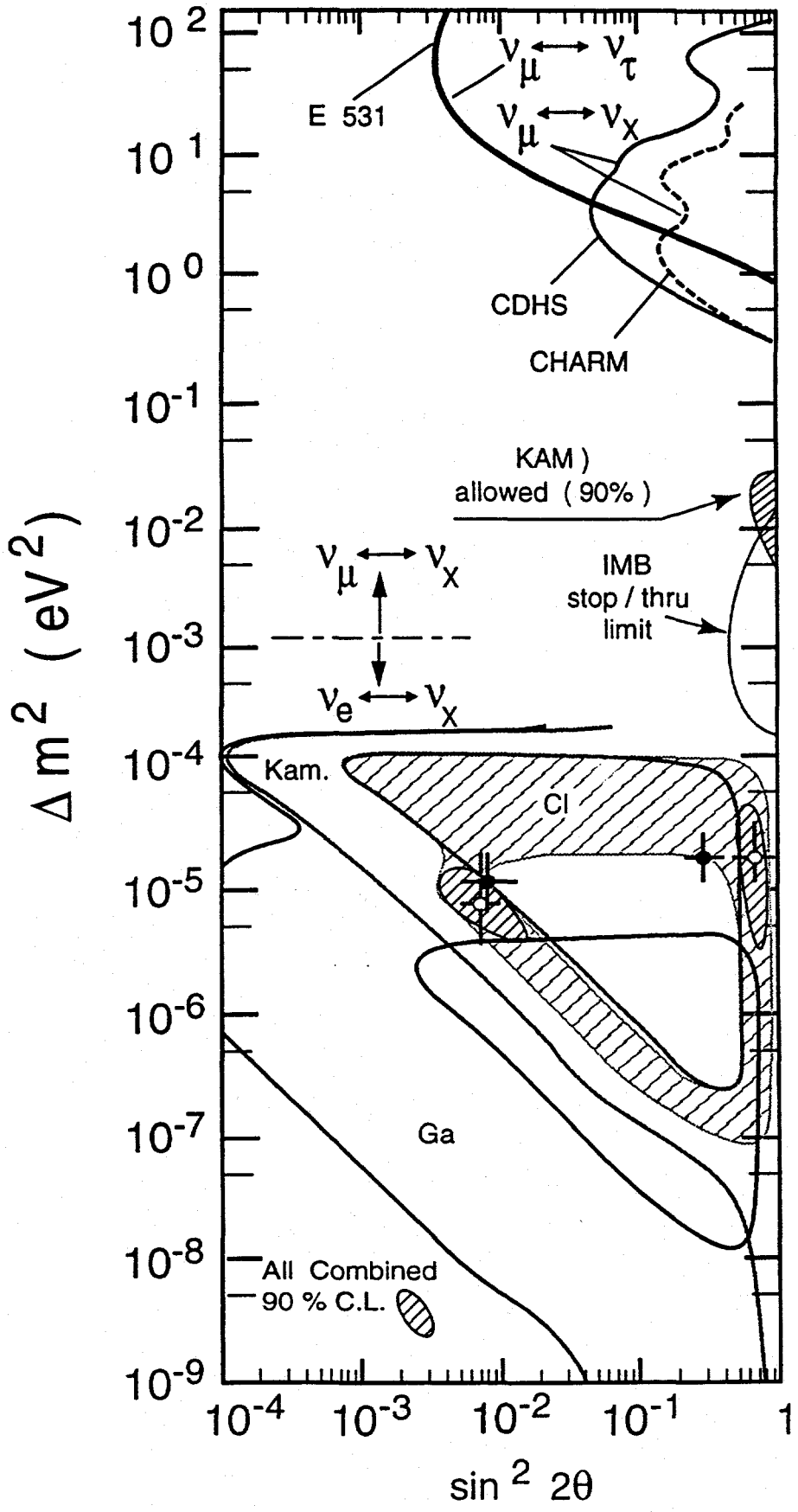
$10^{2}$
$10^{1}$
$10^{0}$
$10^{-1}$
$10^{-2}$
$10^{-3}$
$10^{-4}$
$10^{-5}$
$10^{-6}$
$10^{-7}$
$10^{-8}$
$10^{-9}$
$\Delta m^2$ ($eV^2$)
$10^{-4}$ $10^{-3}$ $10^{-2}$ $10^{-1}$ 1
$\sin^2 2\theta$
$\nu_\mu \leftrightarrow \nu_\tau$
$\nu_\mu \leftrightarrow \nu_x$
E 531
CDHS
CHARM
KAM )
allowed ( 90% )
IMB
stop / thru
limit
$\nu_\mu \leftrightarrow \nu_x$
$\nu_e \leftrightarrow \nu_x$
Kam.
Cl
Ga
All Combined
90 % C.L.

Fig. 1a

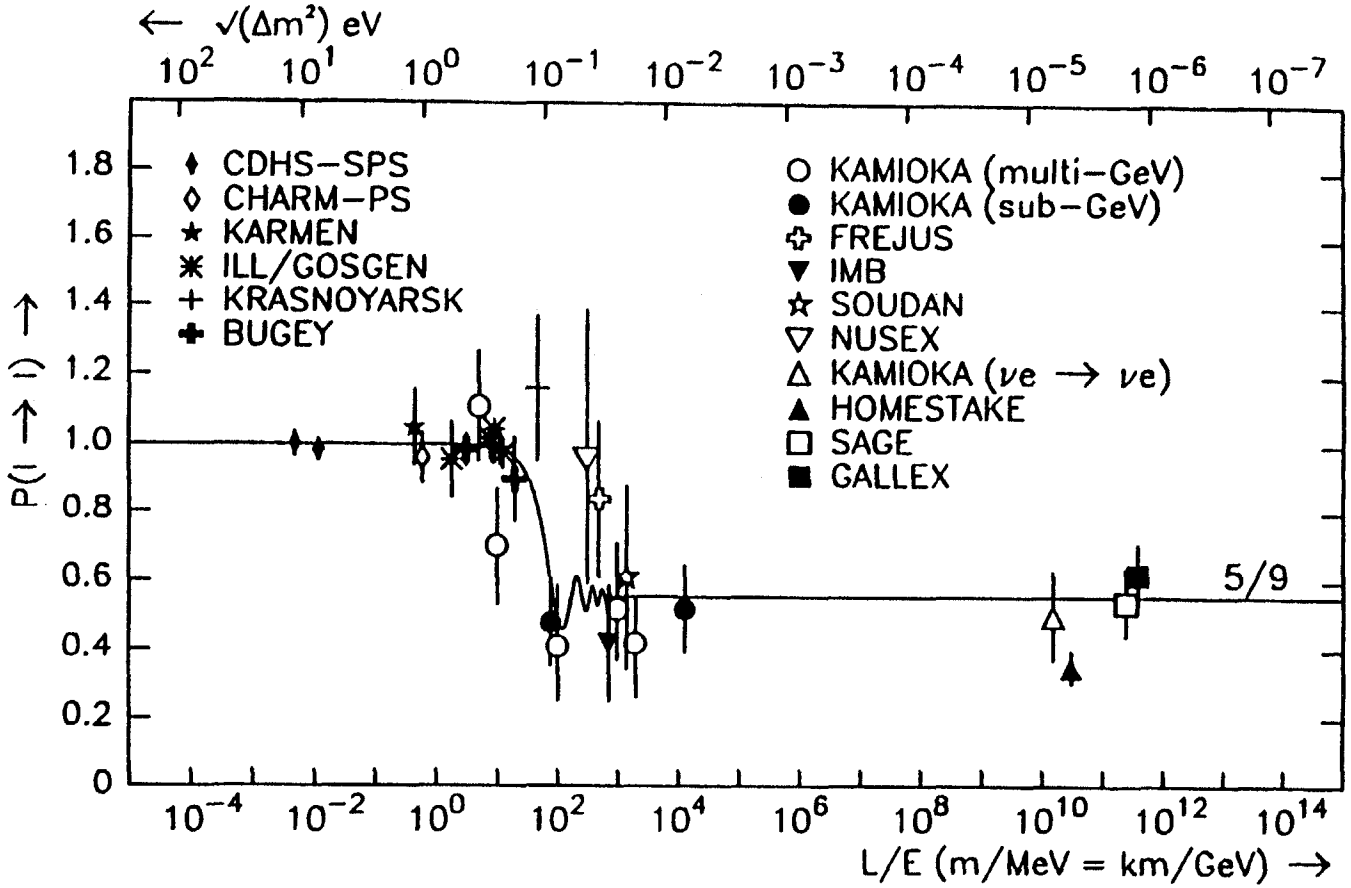


From P.F. Harrison et al.
RAL-94-125 ( '94 )

**Fig. 1b**

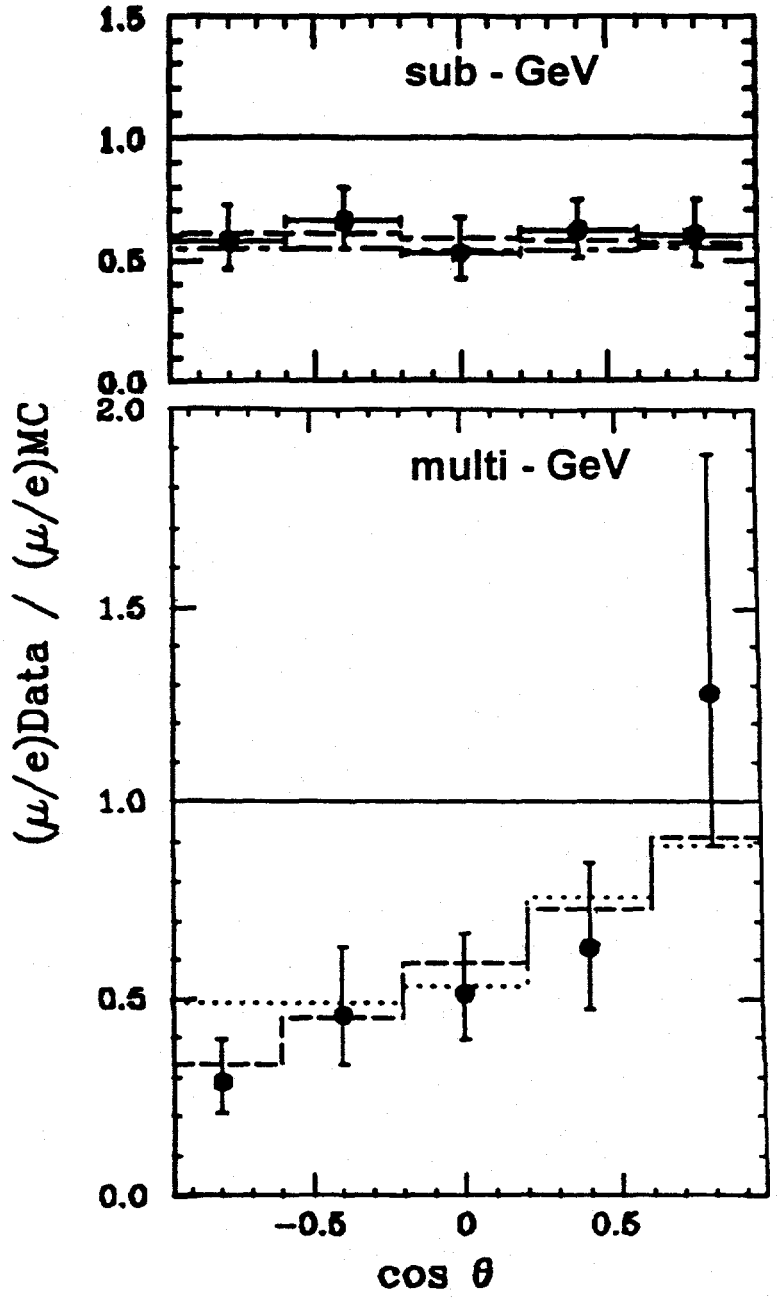
sub - GeV
multi - GeV
(μ/e)Data / (μ/e)MC
cos θ
1.5
1.0
0.5
0.0
2.0
1.5
1.0
0.5
0.0
−0.5
0
0.5

Fig. 2

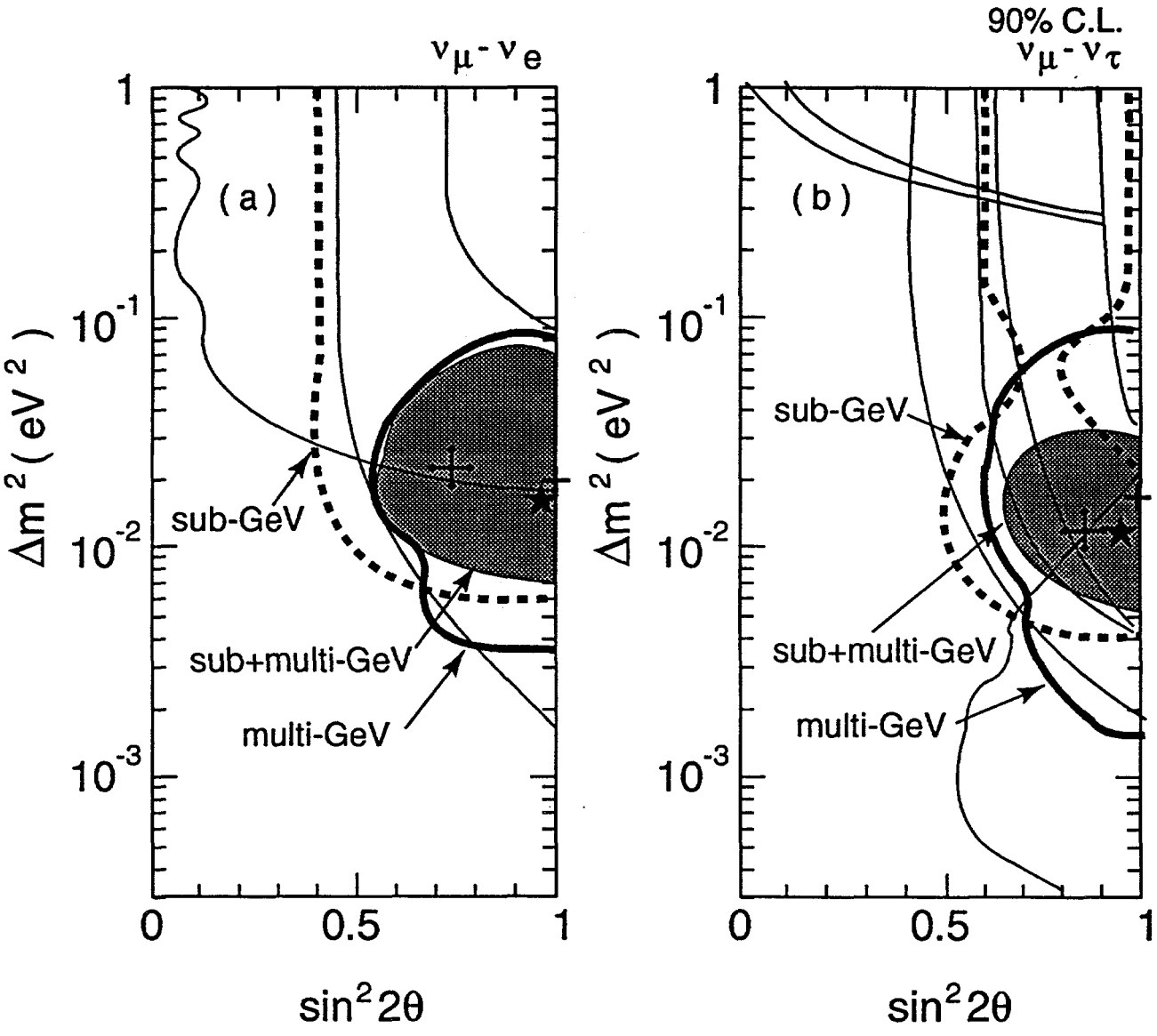


**KAM collab., Phys. Lett. B335, 237 ( 1994 )**

Fig. 3



95-0084j2

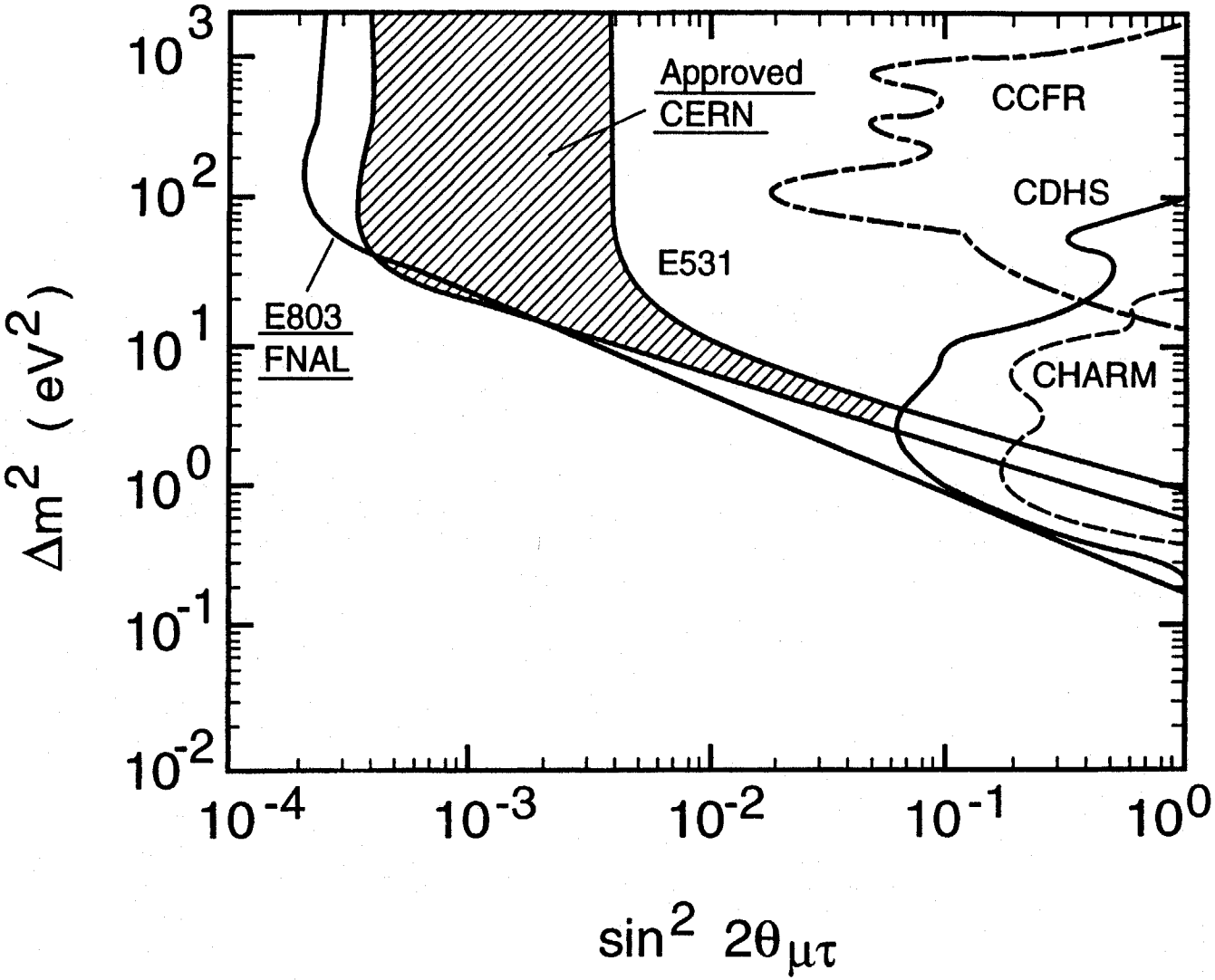


Fig. 4



92-0104a

# II. Overview of the Long Baseline Experiment

## A. Prefatory Remark

The experiment is aimed at producing a conclusive result—positive or negative—concerning the neutrino oscillation signal suggested by the atmospheric neutrino results shown in Fig. I.3. We have designed it to be capable of reaching well below the lowest allowed values of $\Delta m^2$ and $\sin^2 2\theta$ in Fig. I.3 with high statistical precision and tight control of possible systematic errors. But we have also considered the dispersed distribution of the detectors in our design as a means to explore the relatively large allowed regions in Fig. I.3 in continuous steps of increasing sensitivity. These steps coincide well with reasonable expectations of the rates at which detectors can be built and funds are likely to flow to a long baseline neutrino oscillation experiment.

This experiment was proposed in 1992 and approved by the BNL-HENPAC as AGS Experiment 889 in 1993. In Fall 1994 the design was reviewed and validated by an external committee chaired by S. Aronson.

## B. General nature of the experiment

The experiment makes use of the BNL AGS, which has the advantages of high proton intensity, fast, fine-time structured extraction of the external proton beam, and relatively low neutrino energy. All of these properties are vital for a successful neutrino oscillation experiment. High intensity allows a baseline as long as 68 km to be used effectively. Fast, time structured extraction of the proton beam allows the massive far detectors to be operated on the earth's surface by means of timing and live veto suppression of cosmic rays traversing the detectors. Low neutrino energy not only makes possible values of the quantity $L/E_\nu$ competitive with those at any proton accelerator in the world, but also limits the fraction of deep inelastically produced background events in the detector relative to the dominant quasielastic signal events.

An AGS based search for $\nu_\mu$ oscillations can easily cover all of the region of $\Delta m^2 - \sin^2 2\theta$ indicated by the atmospheric neutrino data in Fig. I.3. These data specify the distance $L$ at which the far detector should be located for a given average AGS produced neutrino energy, according to the oscillation probability equation, $P(\nu_\mu \leftrightarrow \nu_x) = \sin^2 2\theta_{\mu x} \sin^2(1.27\Delta m^2_{\mu x} L/E_\nu)$, where $\sin^2 2\theta_{\mu x}$ is the strength of mixing between $\nu_\mu$ and $\nu_x$, $\Delta m^2_{\mu x} \cong |m(\nu_\mu)^2 - m(\nu_x)^2|$ in $eV^2$, $L$ is the neutrino source to detector distance in km, and $E_\nu$ is the neutrino energy in

GeV. A ratio $L/ < E_\nu > \cong 100$ is feasible in an AGS based experiment. It has the advantage over atmospheric neutrino experiments that the $\nu_e$ content in the produced $\nu_\mu$ beam at the AGS is approximately $10^{-2}$, which allows a sensitive search in the oscillation channel $\nu_\mu \leftrightarrow \nu_e$ to be made in addition to a high sensitivity search in the $\nu_\mu$ disappearance mode. Although the $\nu$ beam energy of the AGS is below the effective threshold energy for $\tau$ production, depletion of the $\nu_\mu$ in the beam at the far detector not attended by a corresponding large fractional change in the number of $\nu_e$-induced events in that detector would provide *prima facie* evidence for oscillations in the channel $\nu_\mu \leftrightarrow \nu_\tau$. Furthermore, neutrino-induced single $\pi^0$ production through the flavor independent weak neutral current in each of the detectors of the AGS experiment provides direct normalization of the observed weak charged current event rates internal to each detector. This also makes possible a search for oscillations in the channel $\nu_\mu \rightarrow \nu_{(sterile)}$, and independent confirmation of any positive signal.

The apparatus will ultimately consist of four linearly aligned, widely separated, identical, massive imaging Cherenkov detectors 18 m in diameter $\times$ 18 m high at distances of approximately 1, 3, 24 and 68km from the neutrino source. The two closest detectors would be on the BNL site. The arrangement is shown schematically in Fig. 1. The count rates from the quasielastic reaction $\nu_\mu n \rightarrow \mu^- p$ in the upstream detectors, D1 and D3 —the dominant reaction in all four detectors—serve to disentangle the neutrino beam shape and intensity from the detector response, and to predict precisely and redundantly the count rates in the detectors D24 and D68. With the two far detector sites, the oscillation parameters, $\Delta m^2$ and $\sin^2 2\theta$, are overdetermined. If neutrino oscillations occur and result in a decrease of $\nu_\mu$-induced events in the detector, D24, by as little as a few percent, and proportionally more in the far detector, D68, $\Delta m^2$ and $\sin^2 2\theta$, will be specified with $1\sigma$ errors less than 15%, as shown in Fig. 34 in Chapter V.

Furthermore, as mentioned above, there is an independent method of normalization internal to each of the detectors. With the neutrino beam discussed below, approximately 20% of all $\nu_\mu$-induced events involve the weak neutral current (WNC) reactions $\nu n \rightarrow \nu n \pi^0$ and $\nu p \rightarrow \nu p \pi^0$, which occur with equal probability for all flavors of neutrinos. Consequently, the ratio of $\nu_\mu n \rightarrow \mu^- p$ events to the WNC ($\pi^0$) events in each detector will serve as an additional means of normalization and redundant identification of a positive neutrino oscillation signal. A detailed discussion of the measurement of WNC ($\pi^0$) is given below, along with WCC and WNC backgrounds and their effects.

Moreover, if $\nu_\mu$ oscillates to $\nu_e$ and/or $\nu_\tau$, or even to a "sterile" neutrino, $\nu_s$, (one with appreciably weaker interactions than the known neutrinos), comparison of the event rates

in each detector of $\nu_\mu$–, $\nu_e$– and WNC($\pi^0$)–induced reactions will permit the assignment of an observed decrease in the $\nu_\mu$ event rate to a specific oscillation channel (or channels), and sharply delineate the values of $\Delta m^2$ and $\sin^2 2\theta$ in that channel. We repeat that the ratio of neutrino fluxes $\phi(\nu_e)/\phi(\nu_\mu)$ in a magnetic horn focused $\nu_\mu$ beam at the AGS is approximately $10^{-2}$, which will result in an appreciable increase in the $\nu_e n \rightarrow e^- p$ event rate if even a few percent of $\nu_\mu$ oscillate to $\nu_e$. And, observation of $\nu_\mu$ disappearance without a proportional increase in the number of $\nu_e$-induced events will be unambiguous evidence for oscillations in the $\nu_\mu \leftrightarrow \nu_\tau$ channel.

Taken together, these properties of the experimental arrangement provide tight control of possible systematic errors in the experiment—one of the foremost considerations in the design of the experiment—by monitoring the $\nu_\mu$ and $\nu_e$ content of the beam at several locations along the beam path.

### C. Far Detector Locations

The previous North Area neutrino beam at the AGS has been largely dismantled, and consequently a new beam must be designed and constructed. The direction of the beam is taken to be on a somewhat easterly line toward the north shore of Long Island. A detailed layout of a possible beam is shown in Fig. 2 in which the proton beam line is an extension of the present Fast Extracted Beam Line bent sufficiently to avoid RHIC and to direct it to the D24 and D68 detectors. Locations of the off-site detectors at Northville, L.I. (24 km) and on Plum Island (68 km) are shown in Fig. 3. At Northville, there is an extensive storage facility for gas and oil, consisting of tanks similar to those in this proposal. Space to locate the D24 detector is available to us and a provisional agreement has been authorized. There is a U.S. government facility on Plum Island, maintained by the Department of Agriculture and a provisional agreement to locate D68 there is in process. There is adequate water, electrical power, and security at these sites. It is fortunate that these sites are naturally located along the same line from the neutrino source, as described explicitly in Chapter V.

### D. Detector Evolution

We expect the experiment to evolve in a continuous fashion, dictated by the rates at which construction and funding are likely to proceed. Our current plan involves the use of four identical detectors which permits operation as soon as each tank is completed, and facilitates the extraction of early physics results. We anticipate that the detectors will be built in the

sequence—D3, D24, D68, and the fourth detector most probably at D1. D3 and D24 could be complete by end of calendar 1998, and the additional tanks will be built in the succeeding year so that all 4 tanks would be in operation about one year later.

The first detector, located at D3, will permit early studies of the beam as soon as it is available, and detailed exploration of the detector performance. With the second detector (D24), significant searches for oscillations can begin. In one AGS run of 4 months, quasielastic event samples with statistical errors of approximately 0.3% and 2% (in D3 and D24, respectively) would be accumulated. As shown in Figure 4, most of the region allowed by the Kamiokande data could be excluded in this first run, or conversely, if the Kamiokande best fit value is correct, an effect of over 4 sigma in $\nu_\mu$ disappearance would be observed. During this initial run we can also exclude the entire allowed region in Fig. I.3a for the appearance channel $\nu_\mu \rightarrow \nu_e$, as shown in Fig. 5; if the best fit value in that figure is correct, this initial run will yield a $10\sigma$ effect. The 4 month run the following year ( run II) would include the tank at D68, and would either dramatically confirm the positive signal seen previously, then more than $5\sigma$ at D24, and $10\sigma$ at D68 in $\nu_\mu$ disappearance at best fit, or extend the reach of the the experiment well below the allowed region in Fig. I.3b, as shown also in Fig. 4. In either case, the detector at D1 would provide high precision tests for possible systematic errors in our understanding of the detector performance, the neutrino beam behavior, and detector alignment. Finally, the ultimate reach of the experiment is shown in Fig. 4, which would be obtained from all 4 tanks and 16 months of running. The complete experiment would unequivocally solidify any result found earlier, and would extend the reach of the experiment below $3 \times 10^{-3} eV^2$ at $\sin^2\theta \simeq 1$, well below the lowest allowed value of $\Delta m^2$ in Figure I.3b. If an oscillation signal is found, the complete experiment will measure the oscillation parameters with an accuracy of 10 to 15% at the best fit point.

We continue this chapter with general descriptions of the neutrino beam and the detectors. In later sections we discuss the beam and detectors more fully, and event rates and backgrounds in the oscillation searches in detail.

## E. Neutrino Beam

A useful figure of physics merit for an oscillation experiment is $\phi_\nu(E)\sigma_\nu(E)/E^2$, where $\phi_\nu(E)$ is the flux at a given detector, $\sigma_\nu(E)$ is the cross section for the dominant detected reaction, and $1/E^2$ arises in the oscillation probability for $\Delta m^2$ small. With $\phi_\nu(E)$ expressed as a flux $(\mathrm{GeV} - m^2 - \mathrm{POT})^{-1}$, $L$ cancels out of the figure of merit. To optimize this product in a long

baseline experiment appears at first sight to be infeasible because the core of the neutrino beam produced by magnetic horn focusing of the secondary mesons (necessary for sufficient neutrino intensity) comprises higher energy neutrinos than are present at larger radii; and it is the core of the beam which is usually planned to be seen by distant detectors. It is, nevertheless, possible to reach an approximate optimization in a long baseline experiment such as E889, as will be demonstrated below. First, however, it is useful to show that detailed measurements of a neutrino beam at the AGS with incident proton energy of 28 GeV agreed well with earlier calculations of the properties of that beam, indicating the approximate 10% level of confidence that may be placed in neutrino beam calculations.

Shown in Fig. 6 are the measured and calculated $\nu_\mu$ fluxes produced by 28 GeV protons at the AGS [1], with magnetic horn focusing of the secondary mesons. This beam, which was measured at a distance of 100 m from its source (proton target), has been studied in detail, as have the neutrino interactions induced by it. Note the agreement between the calculated and measured spectra, and also that between the calculated and measured ratios $\phi(\bar{\nu}_\mu)/\phi(\nu_\mu)$ and $\phi(\nu_e)/\phi(\nu_\mu)$, specifying the opposite helicity and $\nu_e$ contaminations in the $\nu_\mu$ beam, which are shown in Figs. 7 and 8, respectively. The calculated and measured radial dependence are shown in Fig. 9.

It is particularly interesting to note the properties of the quasielastic reaction which are determined from those beams, and are shown in Fig. 10. The plot of proton energy deposited in the vertex cell (Fig. 10b) is well reproduced by calculation, and conveys the dominance of low $Q^2$ transitions in quasielastic scattering. Here $Q^2 \approx 2M_pT_p$ where $T_p$ is the proton kinetic energy.

The E-889 collaboration has produced a $\nu$–beam simulation based on the programs GEANT 3.21 + FLUKA (hadronic package) in which proton secondary interactions within the proton target are calculated and there is no modification of particle production cross sections. A test of this work, done at TRIUMF, is shown in Fig. 11 which compares the result of the TRIUMF Monte Carlo calculation with data shown earlier in Fig. 6. We have utilized this beam simulation package in the experimental design described in what follows.

The neutrino fluxes at various distances from the proton target have been calculated for $E_p = 28$ GeV with the program above. Fig. 12 compares the flux at a short distance shown in Fig. 6 with that expected at 1 km and 3 km, all on the center line of the beam. The appreciable increase in average energy of the beam at 1 km relative to that at the shorter distance is clearly evident, and is an issue of first importance in the design of a long baseline neutrino oscillation experiment. By 1 km, however, the flux dependence on increasing distance

is approximately $1/r^2$, and further energy hardening of the beam irradiating an 18 m diameter $\times$ 18 m high detector is small, approximately 1–2% in average energy, as shown by the flux at 3 km.

In the experimental design for E889, the radial dependence of the energy of the neutrinos in the beam, indicated in Fig. 9, provides the means of circumventing the energy hardening of the beam at the long baseline distances. We simply offset the detectors from the central line of the beam by a fixed angle, which is possible because the longitudinal distances involved are relatively so large. We show in Fig. 13 the neutrino fluxes at D1, D3, D24, and D68 as they would be if the detectors were to be located on the beam center line or at an angle of 1.5 degrees with respect to that line. It is clear that the beam shape at 1.5 degrees is to a good approximation identical in all four detectors, unlike the differing shapes in the detectors on the center line of the beam. Furthermore, the off-center line flux is increased in absolute value at low energy and depleted at higher energies relative to the zero degree flux, two additional significant advantages. Finally, the variation in beam intensity with respect to the midline of D1 is 33% across the entire diameter of D1. For D3, the variation is less than 10% relative to the midline, and negligible for D24 and D68. See Fig. III A.9. This variation does not cause any systematic difficulties as shown in Chapter V because the variation is to a good approximation linear across the detectors. Furthermore, the total variation in intensity over the small central region of D1 through which pass the neutrinos reaching D24 and D68 is less than 4%, which will be determined with precision by measurement over the entire fiducial volume of D1, still another advantage and not, as commonly conjectured, a disadvantage. This technique of off-setting the detectors allows the experiment to be run at a high incident proton energy and correspondingly high neutrino intensity, while keeping the average neutrino energy low. It is discussed in detail in Section III A.

## F. The Detectors

The Cherenkov technique is well understood and well tested over long time periods. A detector—Kamiokande II—similar in essentials to those proposed here is shown in Fig. 13 to help fix ideas. The proposed E889 detector is shown in Fig. 1 of III B. The imaging Cherenkov counter has the property of providing good angular and energy resolution as well as particle identification of $\nu_\mu$– and $\nu_e$–produced muons and electrons which are contained within the detector. To illustrate this feature, we show in Figs. 15 and 16 the actual event data [2] for a muon and an electron, respectively, and Monte Carlo simulations of those events

for comparison. Note the sharpness of the outer edge of the Cherenkov ring of the muon as compared to that of the electron, and the increased amount of large angle radiation produced by the electron. These characteristics among others are the bases for algorithms used by the Kamiokande and IMB collaborations to identify successfully muons and electrons and separate them one from the other. WNC ($\pi^0$) events are efficiently ($\sim$ 75%) identified (see Chap. IV. below), which in most instances can be shown to be consistent with the $\pi^0$ mass.

In this connection, it is of interest to note the results of tests made by the Kamiokande group with a 1 kiloton imaging water Cherenkov detector at KEK. Muons and electrons of several known different momenta were injected at several different positions into the 10 m high $\times$ 10 m diameter detector. The resulting rings were analyzed using the same algorithms employed in identification of the atmospheric neutrino events. The data from the 1 kiloton test detector confirm the high efficiency of particle identification claimed in the analysis of the atmospheric neutrino events. See Chapter IV.

The choice of the Cherenkov technique is dictated by the requirements of a large mass to serve as combined target-detector for the neutrino interactions, unrestricted visibility within the detector, and relatively low cost for such large mass. Provision of a $4\pi$ solid angle, highly efficient veto counter within the detector tank is straightforwardly accomplished. The same technique will be employed in the future detectors for the Sudbury Neutrino Observatory and Superkamiokande, whose extensive design studies and cost estimates have contributed significantly to the design of the experiment proposed here.

Each detector tank is 18m in diameter filled with water to a depth of 18m. Above the water level a catwalk for access and support is provided (see Fig 13 of Sec III B). Each tank will be equipped with an array of about 2550 photomultipliers (PMT), each 20cm in diameter. 2200 of these PMT are placed on the inner surface of a 15m high by 15m diameter cylinder, while the remainder view the outer annular volume 1.5m thick which functions as a veto to discriminate against cosmic rays and to tag tracks leaving the fiducial volume. The inner PMT array must be able to locate the trajectory of single particles accurately in time and space, to measure the total energy deposited, and to identify neutrino events having single muons, electrons, pizeros, or multiparticle final states. The PMT array covers 6.5% of the area of the inner cylinder, and this is enhanced by Winston cones to over 10.4%. More details of the detector and its implementation are given in Sec III B.

Much of the system design has been replicated from similar detectors under construction in Japan and Canada. The electronics chain from SNO is well suited to the needs of this experiment. The major differences in application arise from the operation of the detectors

on the earth's surface which necessitates dealing with the 80KHz rate of cosmic rays, and the need to synchronize timing data at widely separated sites with the neutrino beam from the AGS. The former poses no additional problems since the SNO electronics has been designed to handle bursts from supernovae that are in excess of the combined beam and cosmic rates for the closest detector. The latter requires development of a sophisticated timing system that is described in detail in Sec III C.

There are several reasons why the four detectors in E889 are identical. These have to do with the control of systematic errors which are likely to constitute the limiting factor in any long baseline neutrino oscillation experiment, and indeed may be the cause of a spurious result.

(i) Neutrino beams are different from other particle beams in that they are especially dependent at the 10-20% level of uncertainty on the detailed behavior of the focusing system. Consequently, precise knowledge of a given neutrino beam cannot be obtained from Monte Carlo simulations, but requires measurement in an adequate neutrino detector. A comparable uncertainty is present in the simulation of the detector response, which compounds the difficulty. If it is required that there be minimal or no dependence of the experimental result on Monte Carlo simulation of the beam properties or detector response, it is necessary to have two identical detectors, separated in space by a moderate distance and aligned, to measure both the beam properties and the detector response separately and precisely. This is particularly important in achieving a sufficiently precise quantitative understanding of the beam for the offset detectors in E889, and for detectors of such large dimensions as in E889.

(ii) Once having determined the detector properties with high statistics in the two upstream detectors, D1 and D3, it is vital to have detectors of identical mass and construction, i.e., identical response, at the far sites to be able to utilize directly the knowledge of the event selection criteria, the fiducial volume constraints, the event containment criteria, and possible detector limitations from the upstream detectors. No Monte Carlo based predictions of event rates or event or detector properties are necessary for identical detectors in contrast to the simulations required in making extrapolations from smaller upstream to larger downstream detectors or from detectors of one type to detectors of another type. With the arrangement of the four detectors along the same line (see Chapter V), this experiment with identical detectors becomes essentially a simple counting experiment.

(iii) The raw cosmic ray event rates in the four detectors are high since the detectors are at ground level. It is straightforward to minimize the effect of those rates on the experiment by a $4\pi$ solid angle anticounter surrounding each inner detector, which provides both active

and passive shielding, and by making use of the time structure of the fast extracted proton beam of the AGS. These are discussed in detail in Chapter V. Another advantage of making all the detectors identical is that the effort to eliminate background and dead time due to the cosmic ray flux is the same for all the detectors and no individual detector corrections which might limit sensitivity to oscillations are necessary.

(iv). As far as cost saving is concerned, it is easy to show that no significant saving is achieved by a modest reduction in size of D1 and D3, while an appreciable reduction in size would defeat the purpose outlined in (i) and (ii) above. Alternatively, an increase in size of D24 and D68 quickly runs up their cost disproportionately beyond the cost of increased beam time to achieve the same statistical precision in those detectors. At a cost of approximately \$1.5M per kiloton for the completed detectors of E889, they are a bargain when their capabilities are considered.

## G. Event Rates

There are three event types that constitute the signals of E889: WCC types $\nu_\mu n \to \mu^- p$ and $\nu_e n \to e^- p$, and the WNC type $\nu N \to \nu N' \pi^0$. All others comprise the backgrounds. At the low neutrino energies involved, $\nu_\tau$ interact only in the WNC mode. The complete analysis of signals and backgrounds is in Chapter V. We summarize some of the results here.

The cross section $\sigma(\nu_\mu n \to \mu^- p)$ has been measured [3] as a function of $E_\nu$ as has $d\sigma(\nu_\mu n \to \mu^- p)/dQ^2$ [1]. The single pion production neutrino cross sections have been calculated with reasonable accuracy, and also studied experimentally in both bubble chambers and electronic detectors. Extensive references to both theory and experiment are given in [4]. We use this cross section material as input to our Monte Carlo calculation which includes the detailed neutrino beam and detector properties to obtain the results given here.

In calculating the event rates we assume a fiducial volume of 1725 cm$^3$ per tank (6.5 m radius and 13 m height), and a total of $8.8 \times 10^{20}$ POT or 16 months of running at $4 \times 10^{13}$ POT per AGS pulse with 20 hr days. We note that these assumption are quite conservative. The actual volume of the detector tank including the veto volume will be a factor of 2.65 larger, and the AGS has exceeded $6 \times 10^{13}$ POT per pulse.

$\underline{\nu_\mu n \to \mu^- p}$

The integral $\int \sigma(E)\phi(E)dE$ over the interval $0 < E_\nu < 5$ GeV is $1.66 \times 10^{-47}$ at D1 when the measured quasielastic cross section including the effects of Pauli suppression in

| | D1 | D3 | D24 | D68 |
|---|---|---|---|---|
| Contained $QE(\mu)$ | $5.21 \times 10^6$ | $5.80 \times 10^5$ | 9102 | 1136 |
| Deficit with $\Delta m^2 = 0.01$ eV$^2$ | | | | |
| $\sin^2(2\theta) = 1.0$ | – | – | 1214 | 694 |
| Reconstructed $NC(\pi^0)$ | $10.2 \times 10^5$ | $11.3 \times 10^4$ | 1773 | 221 |
| $QE(e)$ Beam and $\pi^0$ bkgd. | $1.63 \times 10^5$ | $1.81 \times 10^4$ | 284 | 35 |
| Excess with $\Delta m^2 = 0.01$ eV$^2$ | | | | |
| $\sin^2(2\theta) = 1.0$ | – | – | 1008 | 706 |

Table 1: *Expected reconstructed $QE(\mu)$, $QE(e)$, and $NC(\pi^0)$ events in the detectors of E889 after $8.8 \times 10^{20}$ POT or 16 months of running. The expected deficit of muons and excess of electrons in the far detectors with $\Delta m^2 = 0.01$ eV$^2$ and full mixing is also shown.*

light nuclei is used. There are $2.68 \times 10^{23}$ neutrons per gm of water. Therefore the number of events in D1 will be $4.43 \times 10^{-15}$/kTon/POT. From simulations using the neutrino spectrum, 0.77 of the $\mu^-$ from $\nu_\mu n \rightarrow \mu^- p$ produced in the fiducial volume will be contained, i.e., stop in the visible volume of a detector tank (15 m diameter by 15 m height) and yield a clear Cherenkov ring. The product of all these factors gives the number of contained quasielastic events in D1. The rates in D3, D24, and D68 to can be calculated to good accuracy by using $1/r^2$ scaling. The actual nature of this scaling and the systematic error are discussed in Chapter V. These quasielastic event rates are shown in Table 1. The expected deficit in case of oscillations with the Kamioka best fit parameters is also shown. There will be additional background reduction cuts on the momentum and the direction of the muon that will be analysis specific; these will not impact the rates shown in Table 1 significantly.

Since the quasielastic events account for about 0.60 of the total cross section at these energies, there will be more than 300 events per month of all types in D68, more than 2400 per month in D24 and much more in the near detectors, so that adequate evaluation of the progress of the experiment will be available.

$\underline{\nu n \rightarrow \nu n \pi^0 \text{ and } \nu p \rightarrow \nu p \pi^0}$

The weak neutral current reactions with a single final state $\pi^0$ (WNC ($\pi^0$)) are known to be produced at approximately 20% of the total quasielastic rate [4] in the neutrino beam of

Fig. 17. Momentum distributions of the final state $\pi^0$ from each of the WNC ($\pi^0$) reactions are shown in Fig. 18. The mean momentum of the $\pi^0$s ($\sim$ 300 MeV/c) is such that for most pions the two decay photons are well separated in angle and thereby produce two clear showering Cherenkov rings. By several independent eyescans we have determined that the $\pi^0$s can be identified with an efficiency of 54% (see Chapter IV) if we require two complete rings and 75% if we require 1 complete ring and extra energy [5]. Accordingly, the WNC ($\pi^0$) rates in the four E889 detectors are approximately $(0.2 \times 0.75)$ times the total $QE(\mu^-)$ rates. These are shown in Table 1.

The detection of WNC ($\pi^0$) events at the above rates allows for normalization of the quasielastic $\mu^-$ rate in each detector by means of the ratio WCC (QE $\mu^-$)/ WNC ($\pi^0$), since the WNC ($\pi^0$) reactions are independent of the flavor of the incident neutrino. In the absence of neutrino oscillations, that ratio should be constant in all four detectors. For completeness, we note that in the unlikely case of oscillations to a sterile neutrino, $\nu_\mu \leftrightarrow \nu_s$ a decrease in the WNC ($\pi^0$) rate will accompany a decrease in the QE ($\mu^-$) rate by the same fractional change.

$\underline{\nu_e n \rightarrow e^- p}$

At neutrino energies above 200 MeV, the cross sections for the quasielastic reactions induced by $\nu_\mu$ and $\nu_e$ are approximately equal. We have calculated that the $\nu_e$ contamination in our magnetic horn focused $\nu_\mu$ beam at 1.5 degrees will be $10^{-2}$. The $e^-$ in the $e^- p$ final state have a lower threshold momentum than $\mu^-$ for Cherenkov radiation, and the $e^-$ containment is essentially unity. The electrons will be recognized as single ring events with a characteristic showering ring pattern without a clean edge. The methods for recognizing showering rings are well understood and we expect to have essentially no background from muon to electron misidentification above 400 MeV. The most significant background to electron rings will be from neutral current produced $\pi^0$s with one of the decay photons missing or the two rings from the two photons overlapping. We have performed a detailed calculation of this background in Chapter V. Including the $\pi^0$ background, in the absence of neutrino oscillations, $(\nu_\mu \rightarrow \nu_e)$ showering single ring events will appear in each detector at a rate of about 4% relative to the total $\mu^-$ from $\nu_\mu n \rightarrow \mu^- p$. Table 1 shows the number of single ring showering events above a cut of 500 photoelectrons along with the expected excess in the case of oscillations. If neutrino oscillations occur in the channel $\nu_\mu \rightarrow \nu_e$ at the level of even a few percent, the fractional increase in the observed number of $e^-$ from $\nu_e n \rightarrow e^- p$ will be very large and

clearly identify that oscillation channel.

In summary, the three signal event types in E889 occur with rates that allow for consistency checks and normalization internal to each detector as well as by comparison of rates among the detectors. This statistically significant control of the systematic errors is, in our opinion, the *sine qua non* of any neutrino oscillation experiment that seeks to measure with precision a real effect as opposed to setting another limit. Finally, the three signal event types will unambiguously determine the neutrino oscillation channel in most of the explored parameter space.

## H. Conclusions of Section II

In this chapter, the assumptions behind the design and the general nature of the proposed experiment have been discussed. Emphasis has been given to the strategy of carrying out the experiment in evolutionary fashion which will yield results at the earliest time, consistent with expected rates of funding and detector construction. Brief descriptions of the experimental arrangement and the promise of each step were given, and also of the neutrino-induced event types and their rates from which redundant signals of neutrino oscillations may be extracted. In a period as short as 4 months beginning early in 1999, we expect to acquire 2275 contained quasielastic muon events and 71 quasielastic electron events in D24, to search for $\nu_\mu$-disappearance and $\nu_e$ appearance at the levels indicated by the contours in Figs. 4 and 5. In later data-taking with three or all four detectors in place, we will reach the boundaries shown in Figs. 4 and 5. Finally, by measurements of muons, electrons, and neutral pions, we expect to specify the oscillation channel, $\nu_\mu \rightarrow \nu_e$, $\nu_\mu \leftrightarrow \nu_\tau$, or both, unambiguously.

## References


1. L.A. Ahrens, Phys. Rev. D34, 75 (1986); ibid 35, 785 (1987).

2. E.D. Frank, Ph.D. Thesis, University of Pennsylvania, 1992 (unpublished).

3. S.J. Barish et al., Phys. Rev. D16, 3103 (1977).

4. M. Nakahata et al., Jour. Phys. Soc. Japan 55, 3786 (1986).

5. For Kamioka this efficiency factor has been studied by T. Kajita. T. Kajita, in Workshop on Atmospheric Neutrinos, Louisiana State University, Baton Rouge, LA, May, 1993 (unpublished).

# Figure Captions

Figure 1. Schematic representation of the long baseline neutrino oscillation experiment proposed here.

Figure 2. Tentative schematic layout of the proposed neutrino facility.

Figure 3. (a) Direction of the proposed neutrino beam and location of the Northville and Plum Island sites. (b) Detail of the Northville site. (c) Detail of the Plum Island site.

Figure 4. Exclusion plot of $\Delta m^2$ vs $\sin^2 2\theta$ for $\nu_\mu \rightarrow \nu_x$ to be reached in 4, 8 and 16 months of data-taking with two, three, and four detectors as described in the text.

Figure 5. Exclusion plot of $\Delta m^2\theta$ vs $\sin^2 2\theta$ for $\nu_\mu \rightarrow \nu_e$ to be reached in 4, 8, and 16 months of data-taking with two, three, and the full complement of 4 detectors.

Figure 6. The $\nu_\mu$ flux calculated and measured at the AGS ($E_p = 28.3$ GeV). The flux from 28.3 GeV protons obtained in a scintillator-wire chamber experiment (E734) at the AGS [13] with magnetic horn focusing, a decay length of 57 m, a 20 m long shield, and another 23 m to the detector is $1.3 \times 10^{-3}\nu_\mu$ per ($m^2$ - GeV - POT) at the peak of the curve.

Figure 7. Measured and calculated ratio $\phi(\bar{\nu})/\phi(\nu_\mu)$ corresponding to the flux in Fig. 6.

Figure 8. Measured and calculated ratio of $\phi(\nu_e)/\phi(\nu_\mu)$ corresponding to the flux in Fig. 6.

Figure 9. Measured and calculated radial dependence of the $\nu_\mu$ flux in Fig. 6 in different intervals of $E_\nu$.

Figure 10. Measured and calculated properties of $\nu_\mu n \rightarrow \mu^- p$; (a) $\theta_\mu$-distribution, and (b) energy deposited in vertex cell vs $E$, both from [2].

Figure 11. Monte Carlo simulation of the $\nu_\mu$ flux in Fig. 6 by the beam program described in the text. This program is used in all beam calculations below.

Figure 12. Comparison of calculated $\nu_\mu$ fluxes at 1 km and 3 km with that measured at 100 m from the target. All on beam axis.

Figure 13. Comparison of spectra for D1, D3, D24, and D68 located on axis ($0^0$) and $1.5^0$ off axis.

Figure 14. Kamiokande detector.

Figure 15. Observed Cherenkov ring from a muon in the Kamiokande II detector. The lower displays are simulated for an electron (left) and muon (right) with the same vertex position, direction, and momentum as the observed event. Solid curves are rings reconstructed from timing and pulse height measurement in each PMT.

Figure 16. Same as Fig. 15 but for an observed electron event. Simulations correspond to the observed event.

Figure 17. Comparison of the neutrino beam shape produced by 12.4 GeV protons (ANL, ZGS) and the beam shape at $1.5^0$ off axis produced by 28.3 GeV protons at 1 km from the source.

Figure 18. (a) Momentum spectra of $\pi^0$ from $\nu_\mu n \rightarrow \mu^- p\pi^0$ and WNC final states $\nu n\pi^0$ and $\nu p\pi^0$ (b) Spectra of $\nu_\mu$ producing $\pi^0$ in (a).

Figure 19. Comparison of atmospheric $\nu_\mu$ spectrum with AGS 28.3 GeV produced spectrum at $1.5^0$ off axis.

# BROOKHAVEN NATIONAL LABORATORY
# AGS Expt 889

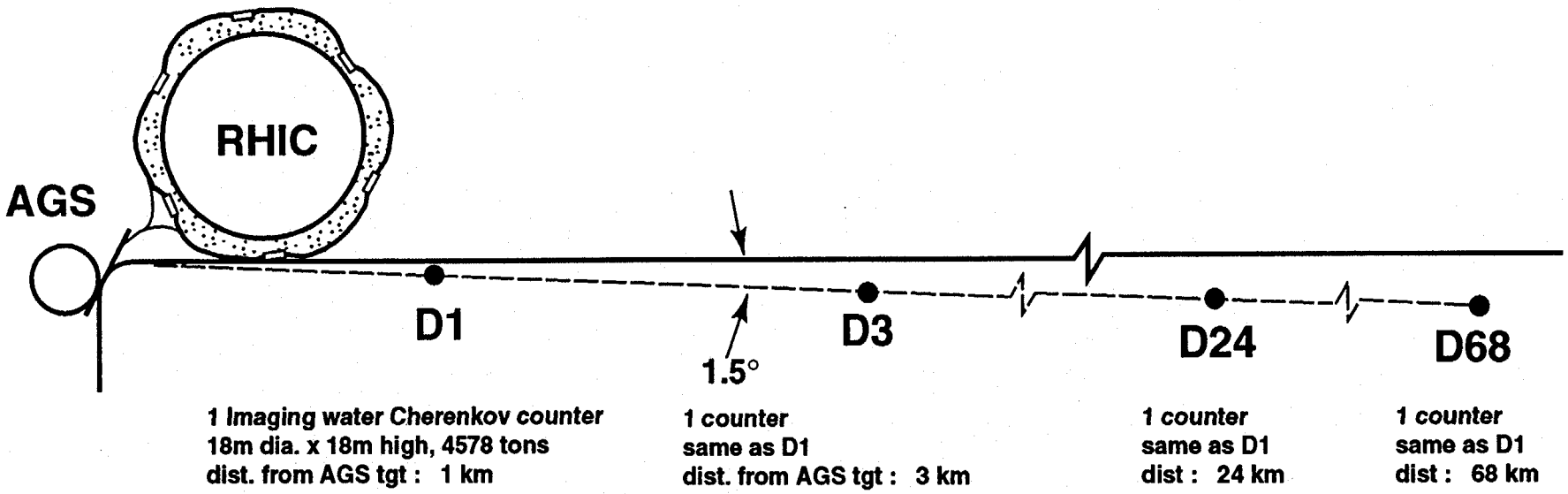


Fig. 1



95-0084u

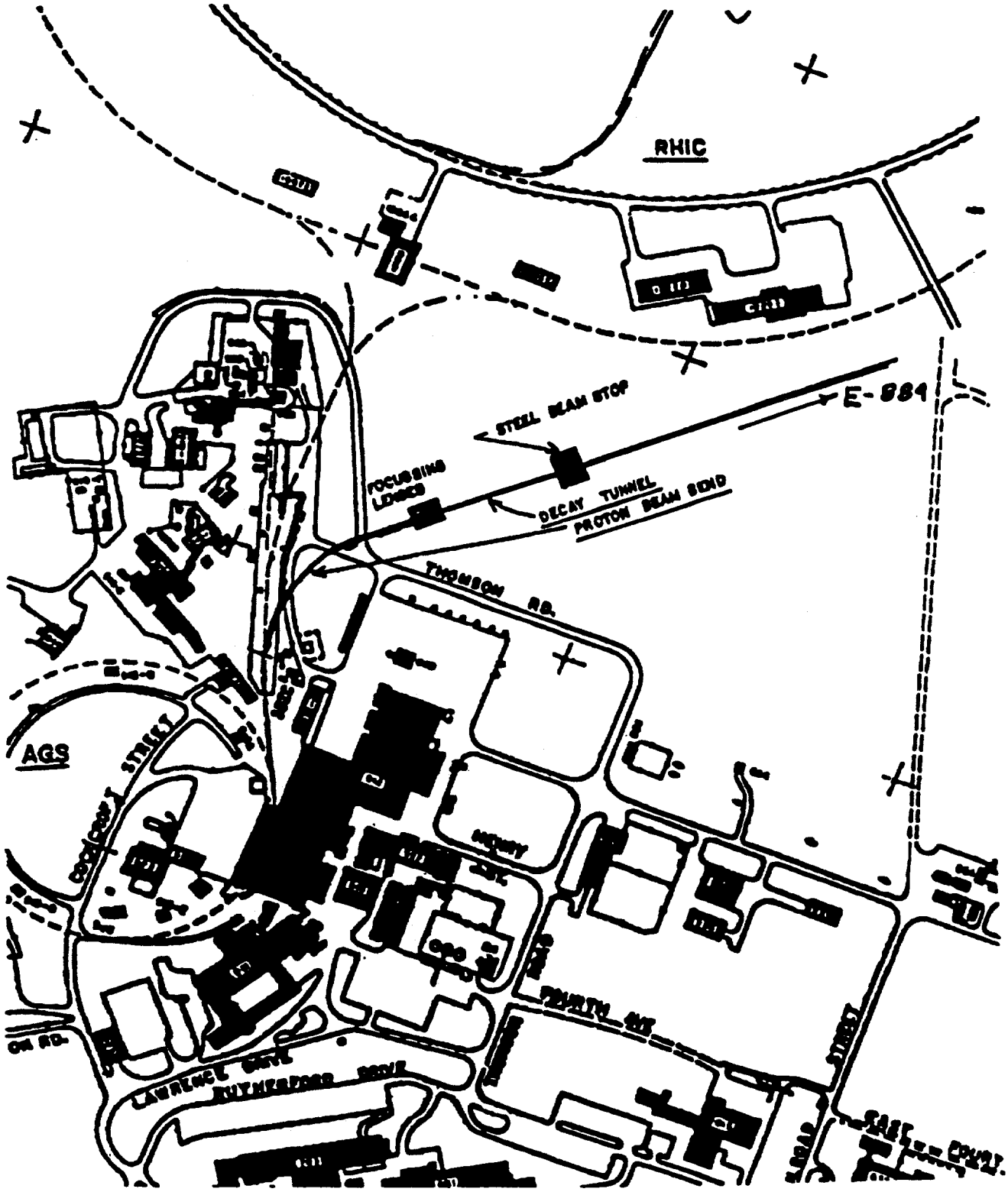


Fig. 2

95-0071b

# *E889 Detector Locations*

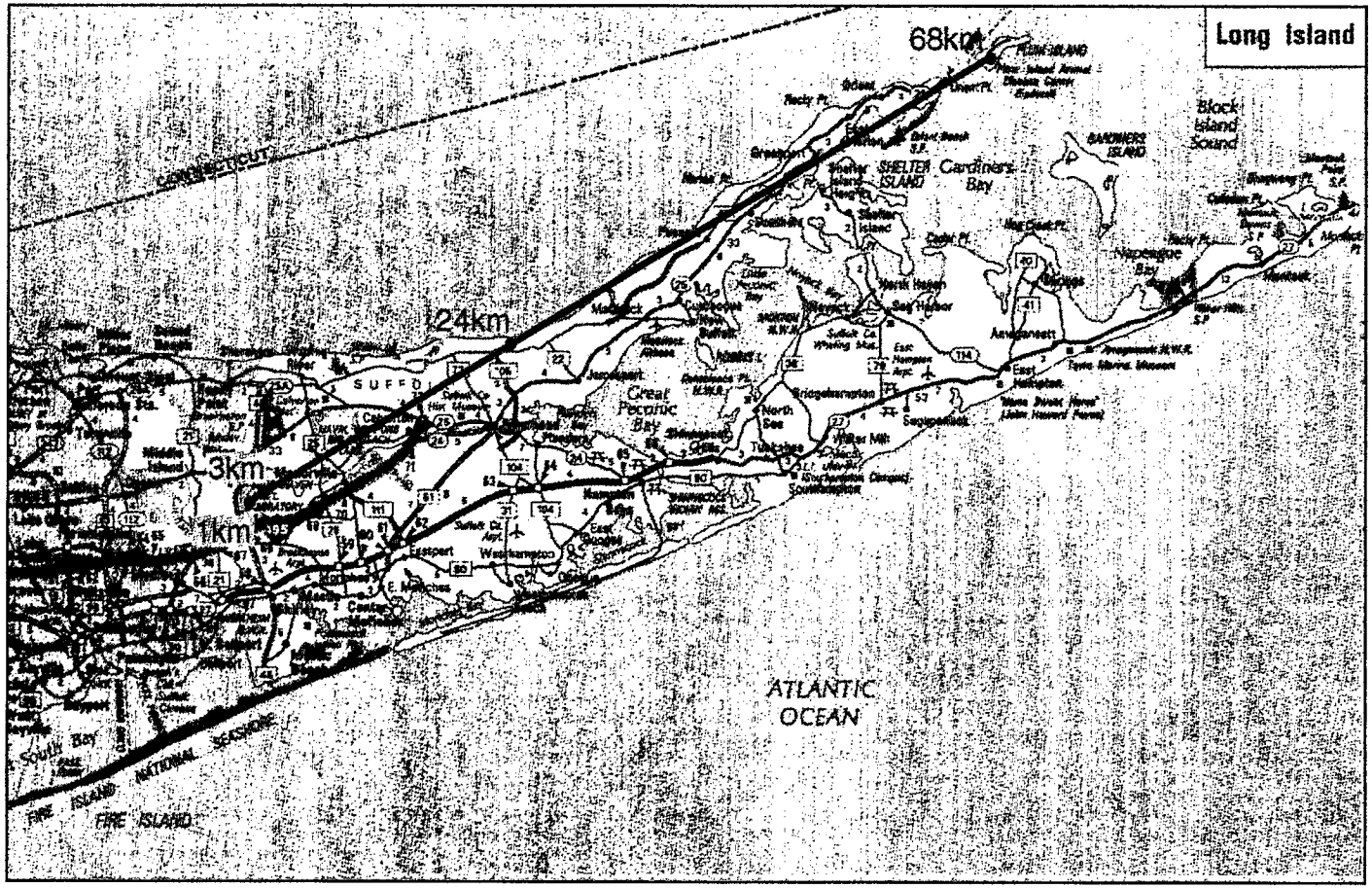


Figure 3a

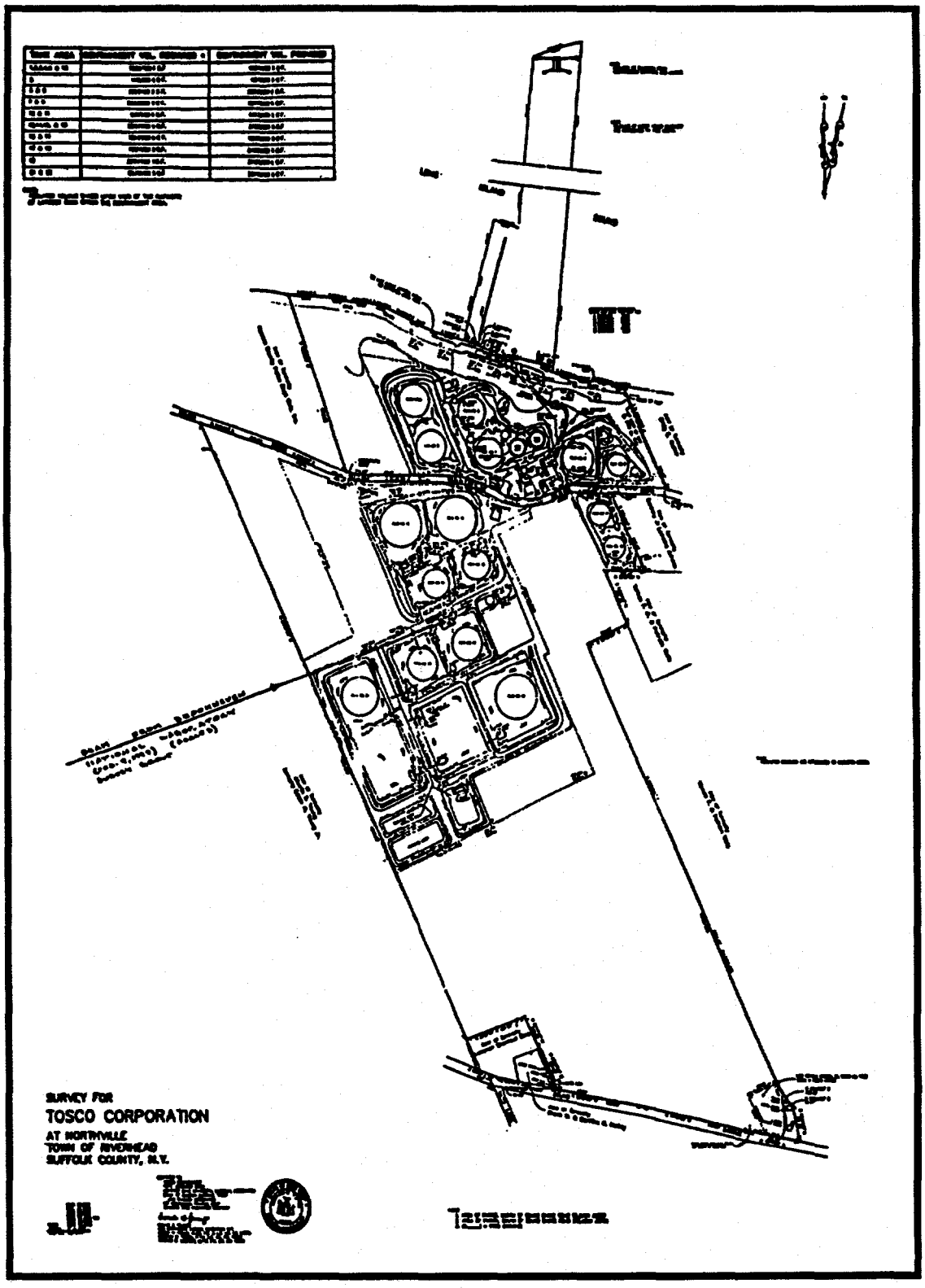
SURVEY FOR
TOSCO CORPORATION
AT NORTHVILLE
TOWN OF RIVERHEAD
SUFFOLK COUNTY, N.Y.

Fig. 3b

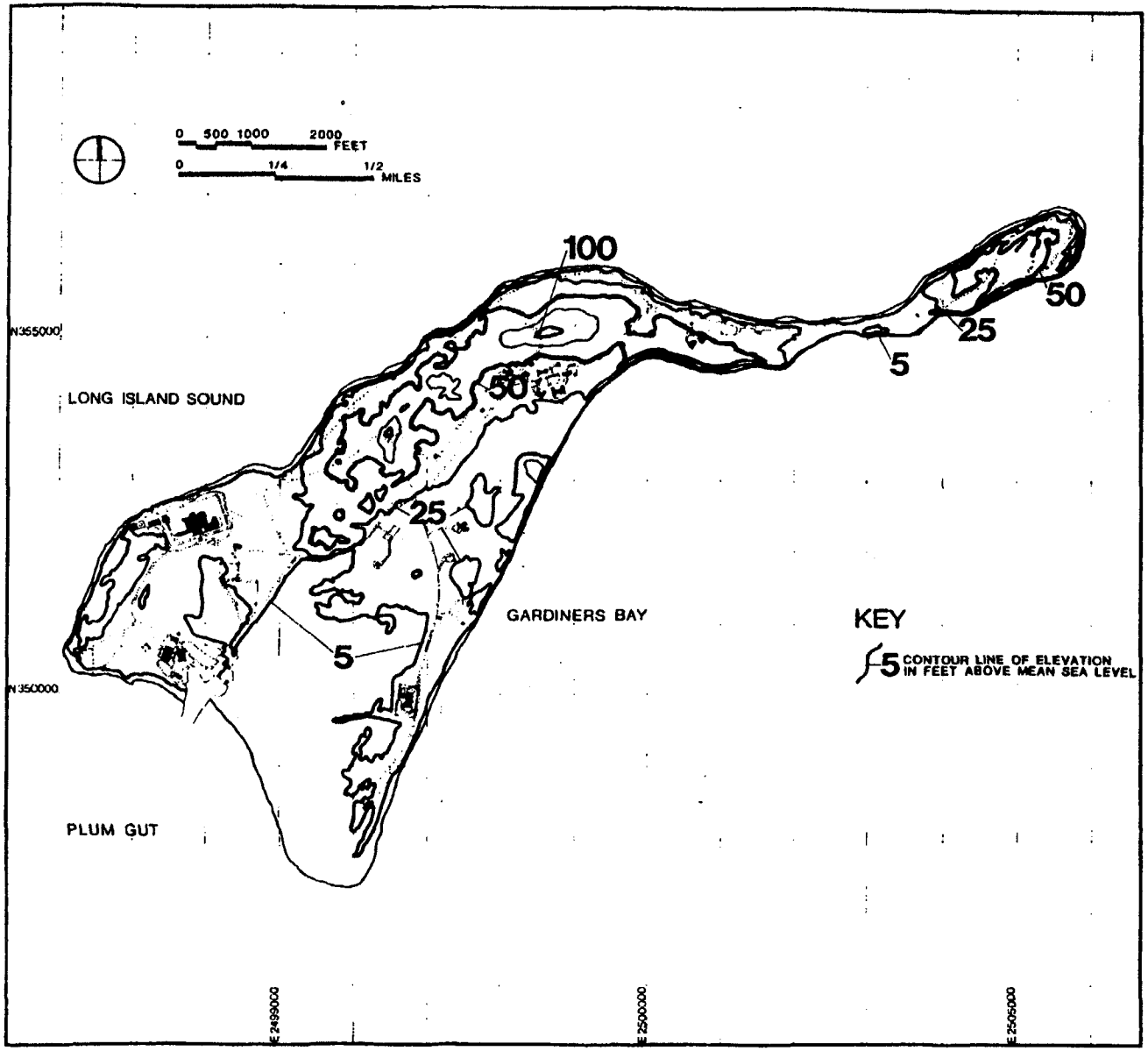


# PLUM ISLAND ANIMAL DISEASE CENTER

GREENPORT, L.I., N.Y.

# MASTER PLAN

January 24, 1977

## Topography

Perkins & Will Architects

Perkins & Will/Architects
445 Hamilton Avenue, White Plains, N.Y.

Dubin-Bloome/Consulting Engineers
42 West 39th Street, New York, N.Y.

B3

Fig. 3c



95-0071c

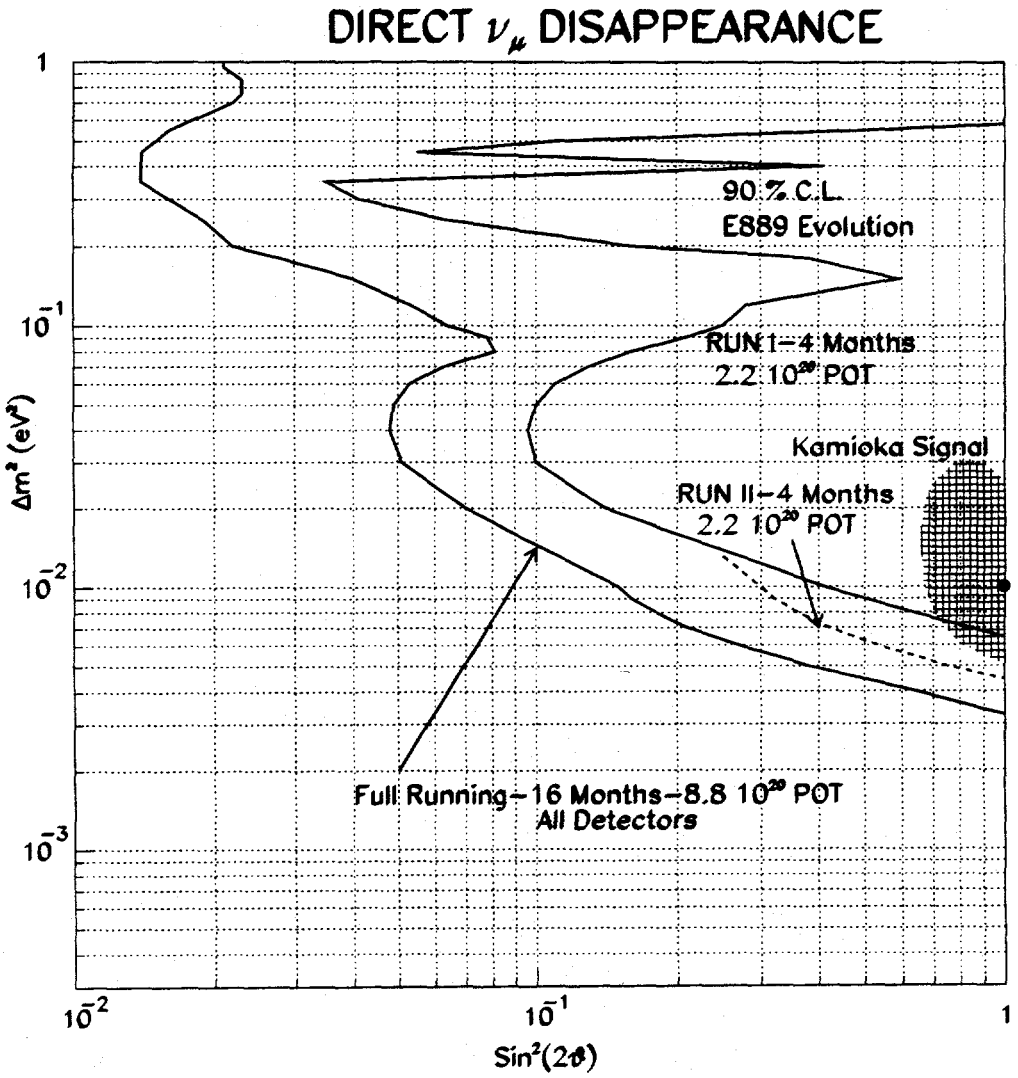


Fig. 4

95-0084r

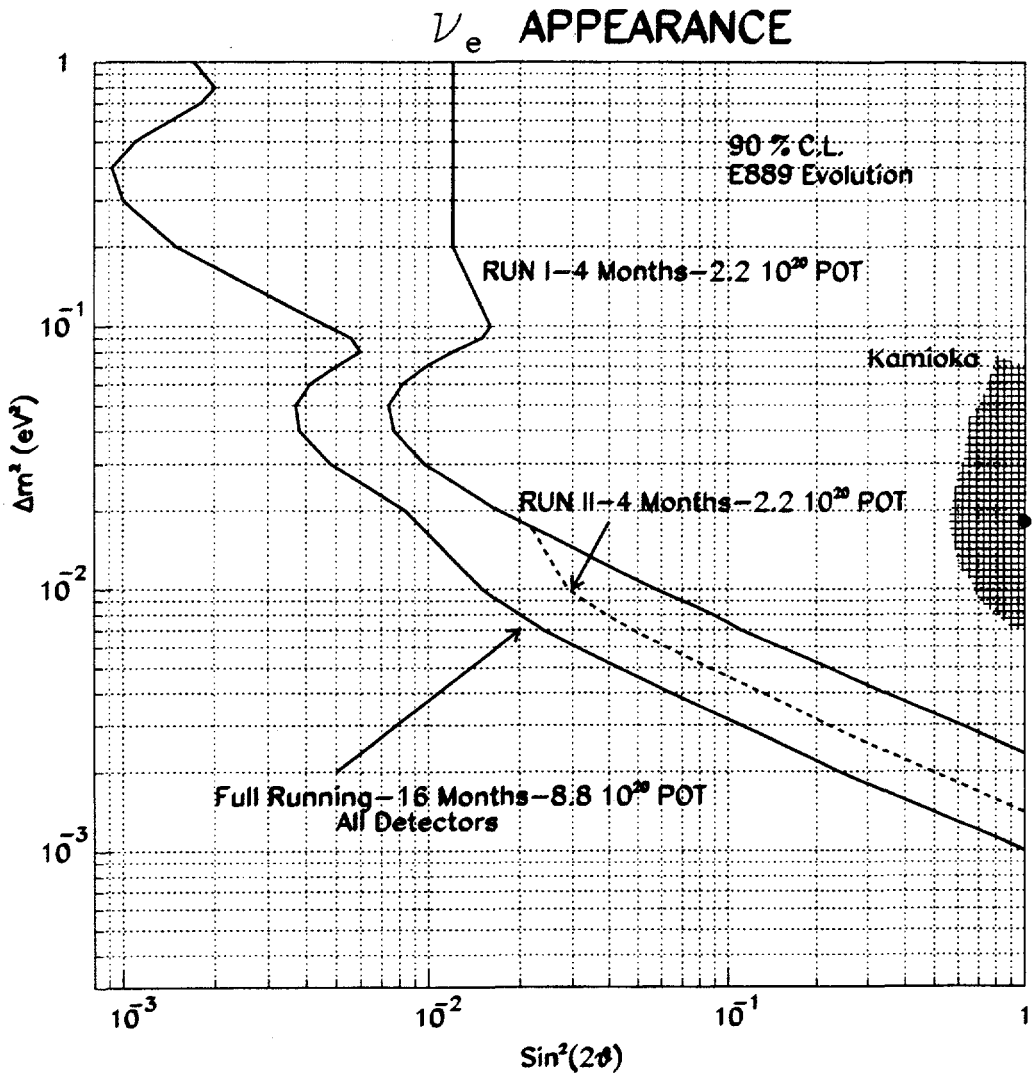


Fig. 5

95-0084s

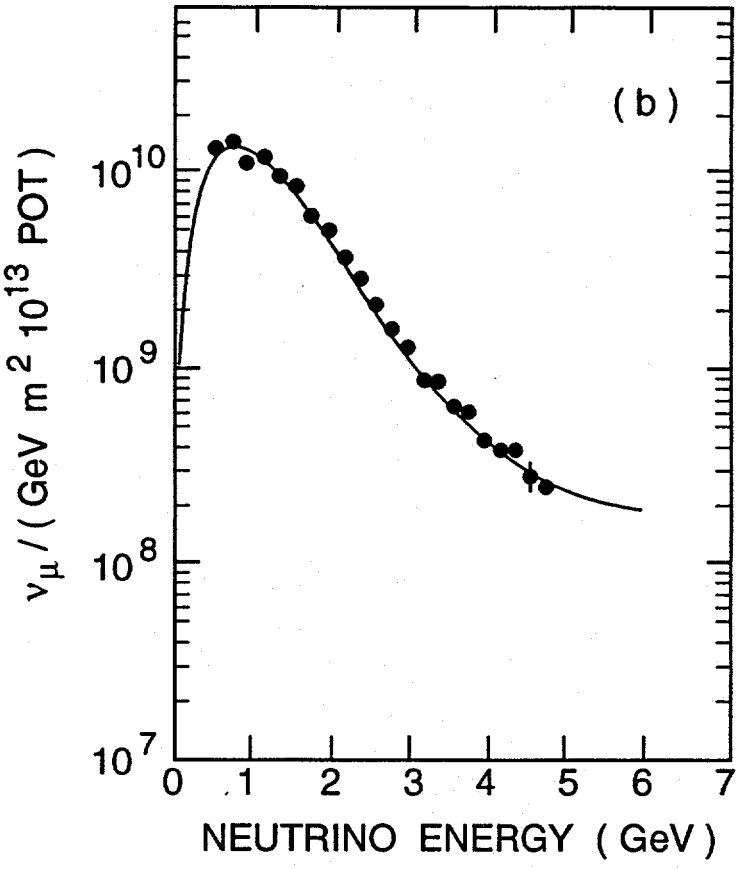
(b)
$10^{10}$
$10^{9}$
$10^{8}$
$10^{7}$
$\nu_\mu$ / (GeV m$^2$ $10^{13}$ POT)
0
1
2
3
4
5
6
7
NEUTRINO ENERGY (GeV)

Fig. 6

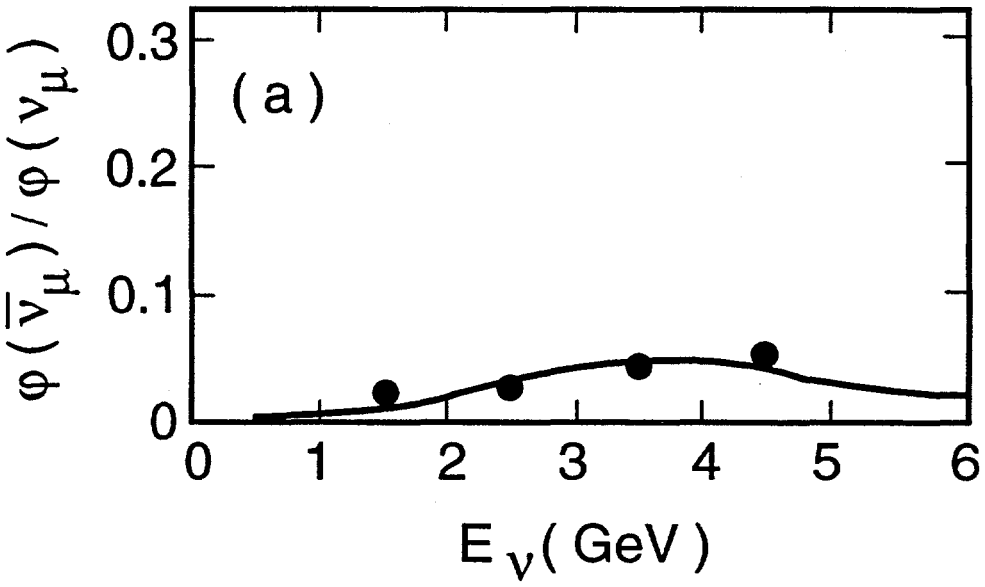


Fig. 7

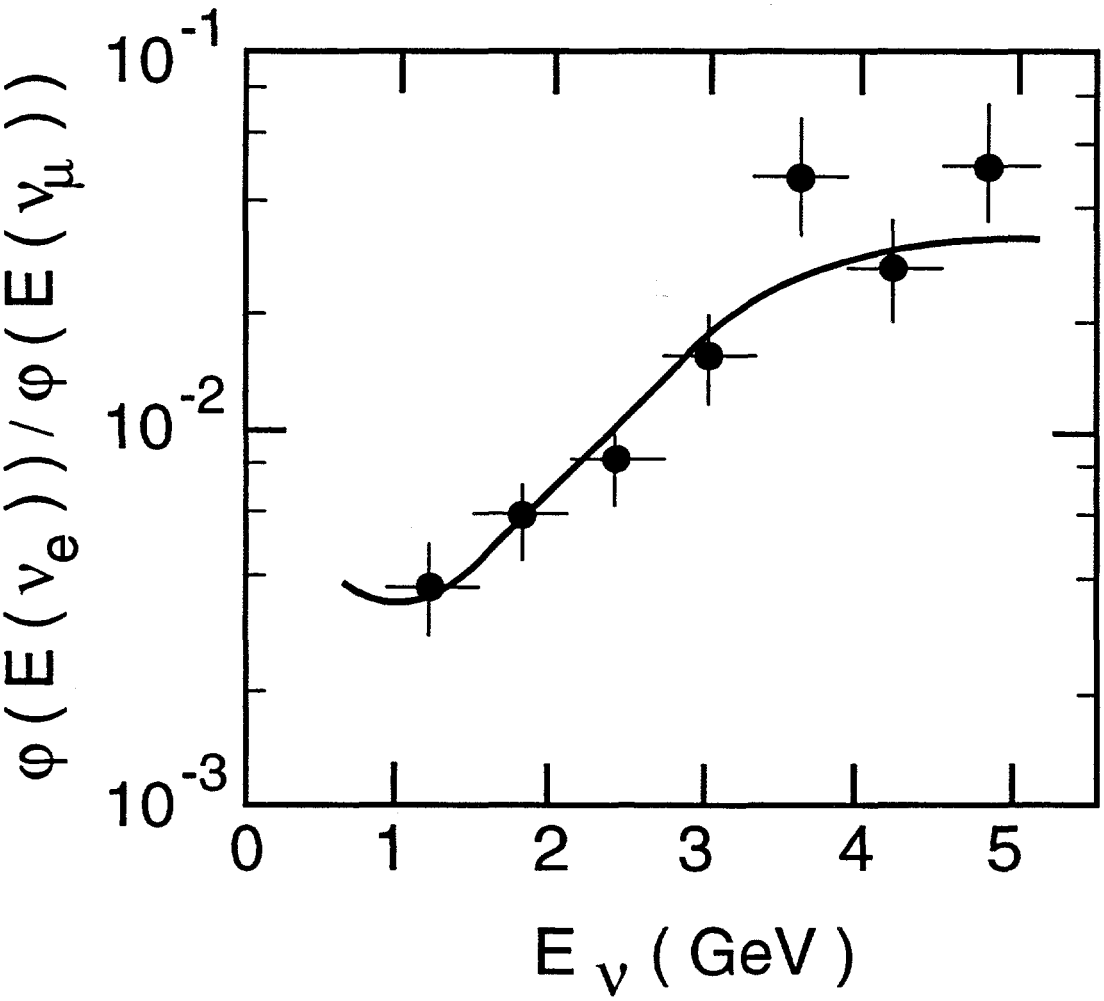


Fig. 8



94-0001b

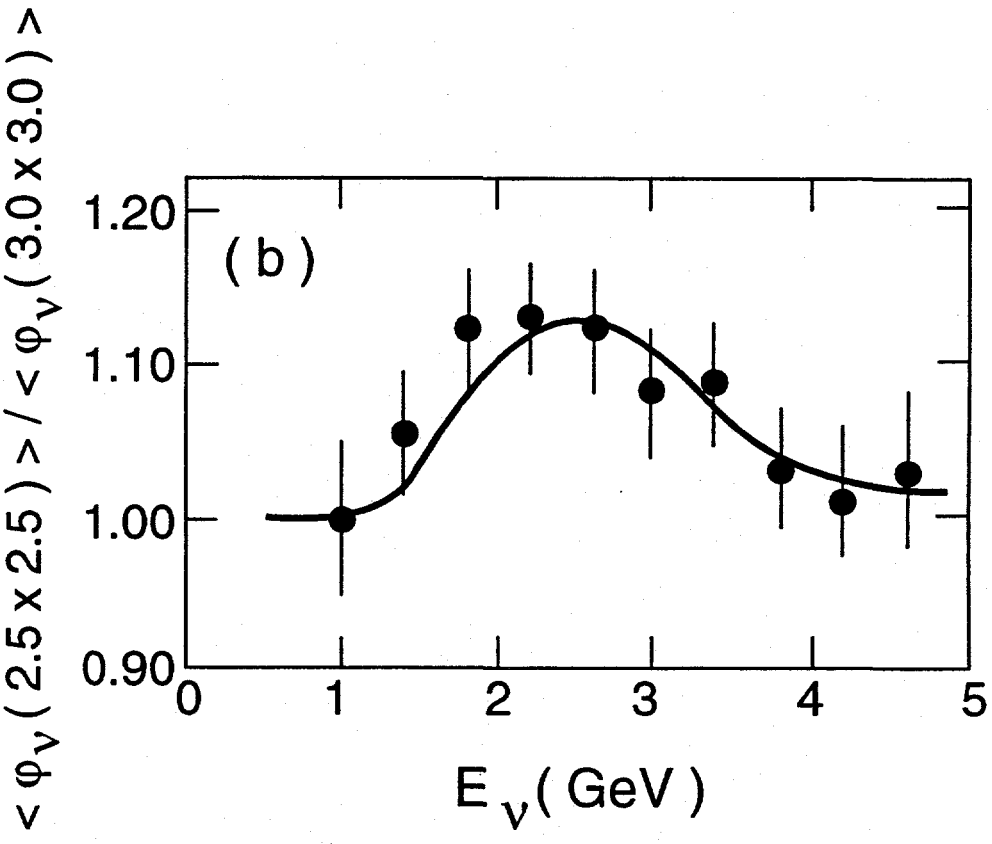
( b )
1.20
1.10
1.00
0.90
0
1
2
3
4
5
$E_\nu$( GeV )
$< \varphi_\nu (2.5 \times 2.5) > / < \varphi_\nu (3.0 \times 3.0) >$

Fig. 9

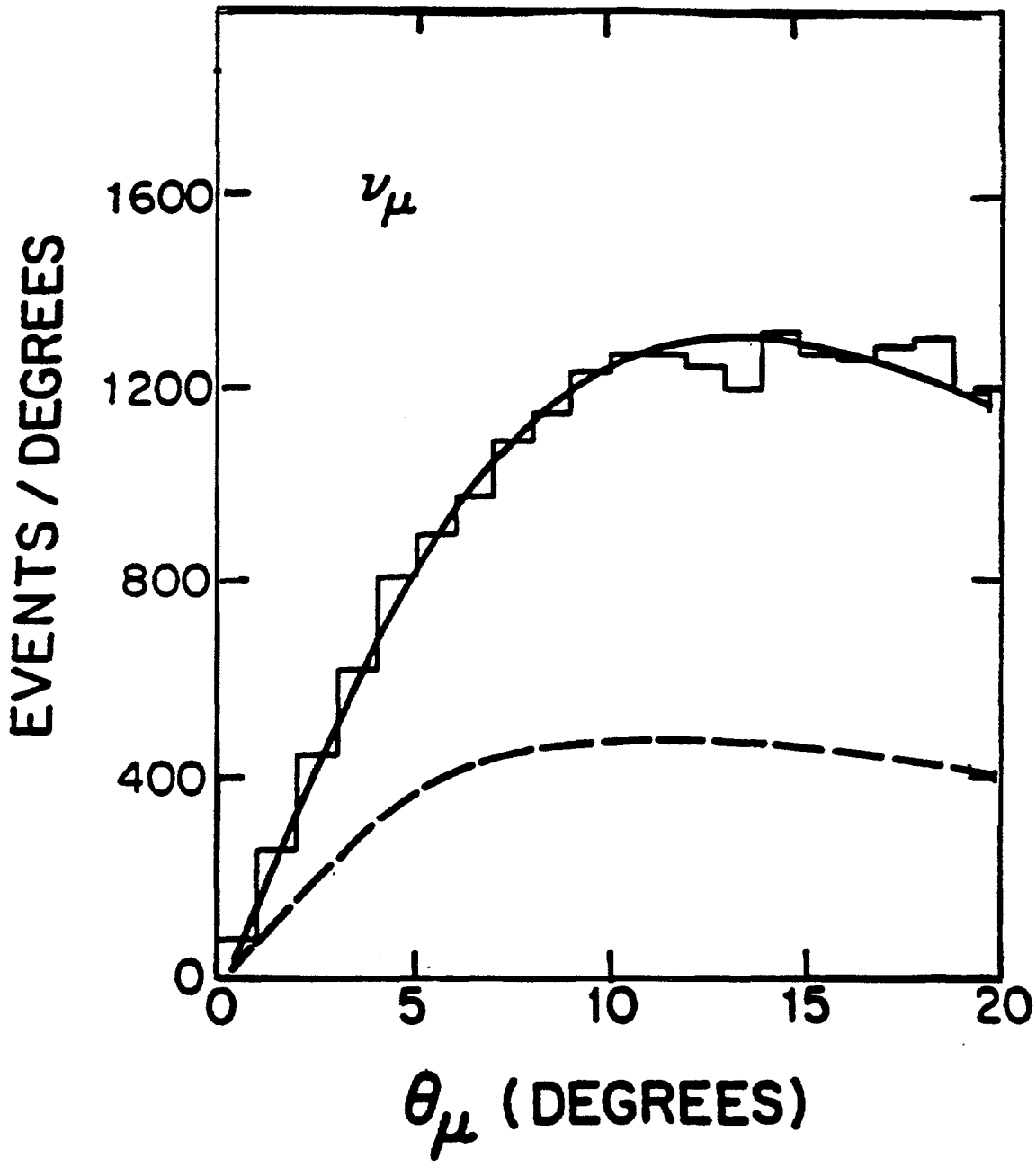


Fig. 10a

95-0094b

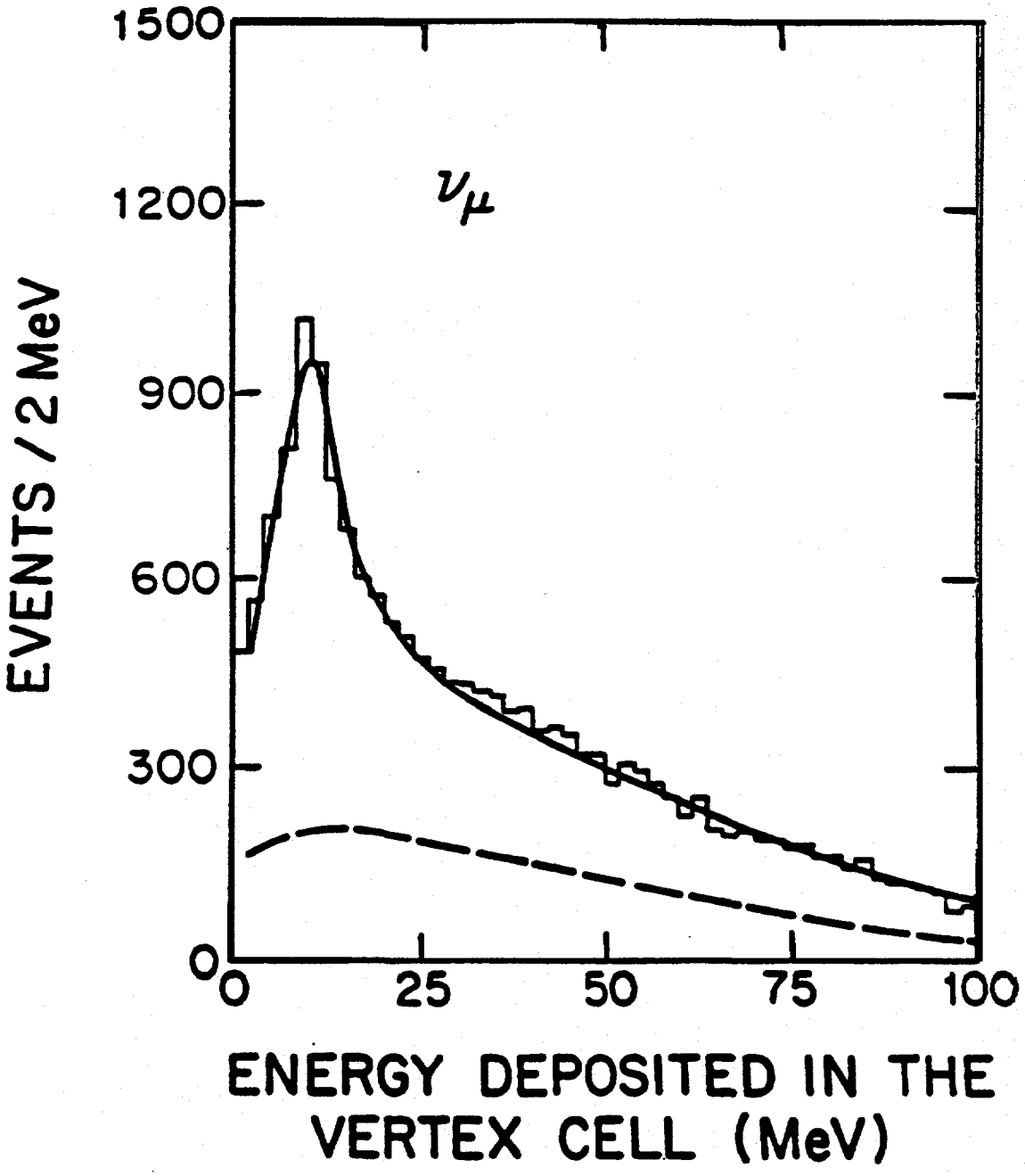
1500
1200
900
600
300
0
$\nu_\mu$
EVENTS / 2 MeV
0
25
50
75
100
ENERGY DEPOSITED IN THE VERTEX CELL (MeV)

Fig. 10b

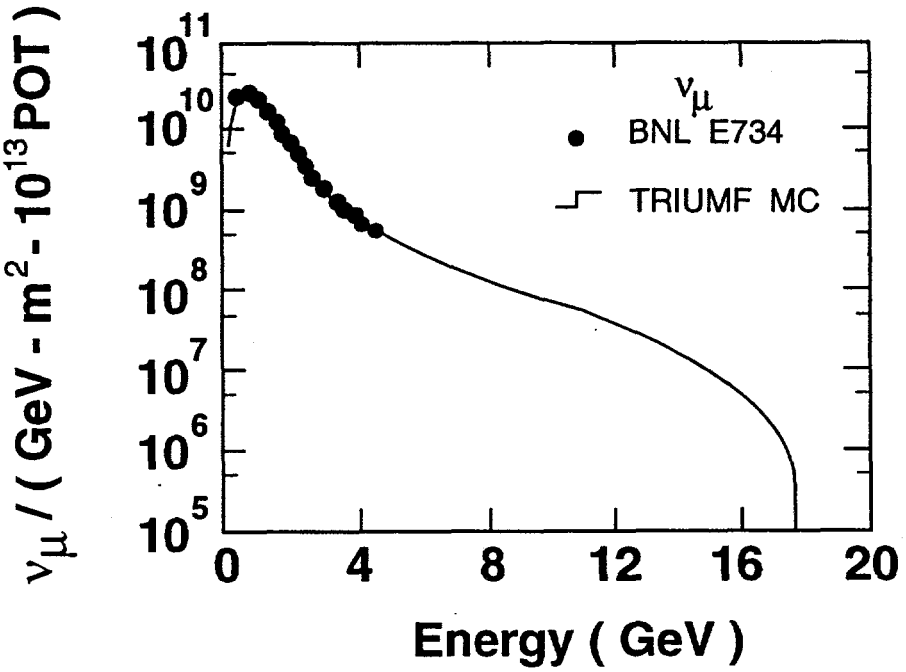
$\nu_\mu$ / ( GeV - m$^2$ - 10$^{13}$ POT )
$10^{11}$
$10^{10}$
$10^9$
$10^8$
$10^7$
$10^6$
$10^5$
0
4
8
12
16
20
Energy ( GeV )
$\nu_\mu$
BNL E734
TRIUMF MC

Fig. 11

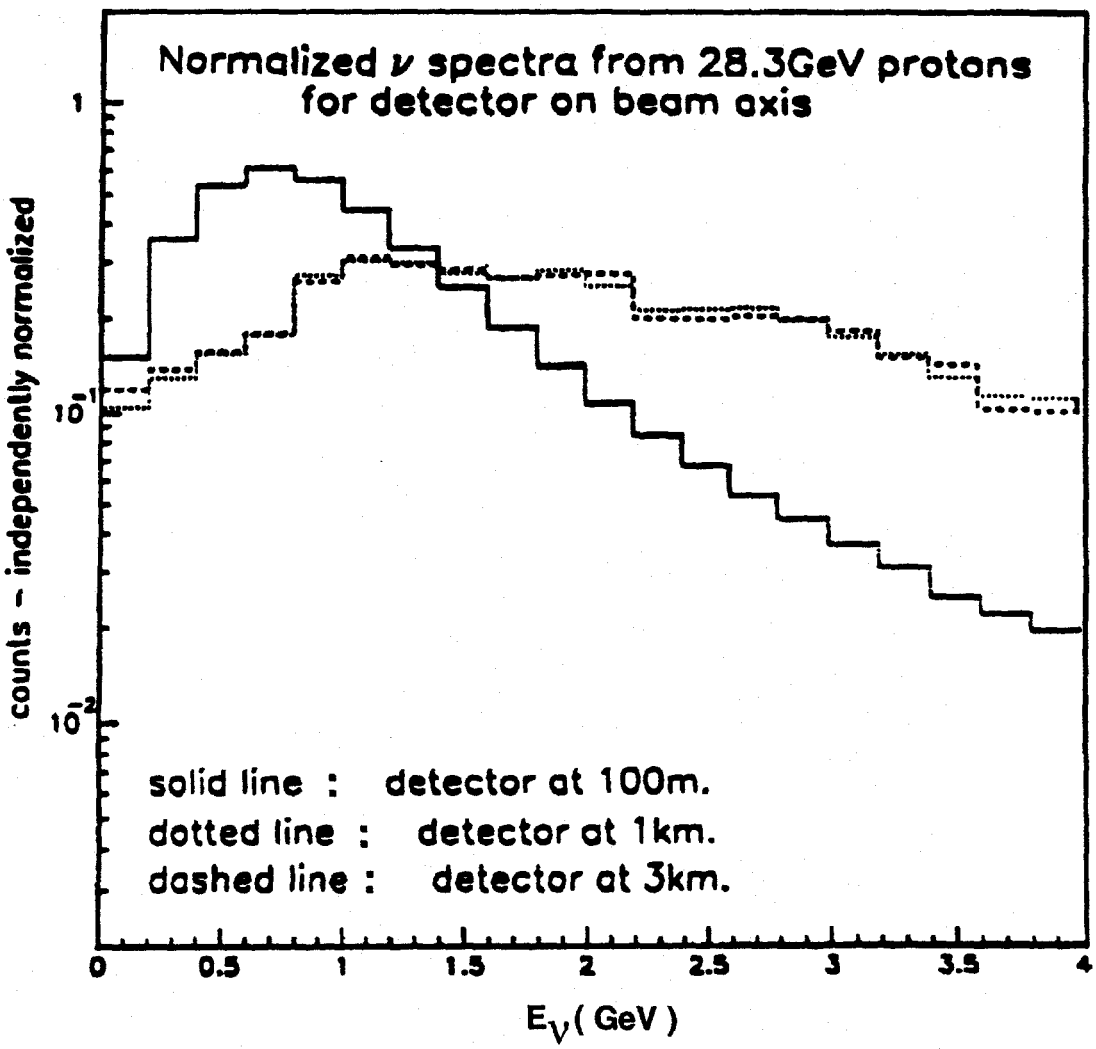
Normalized ν spectra from 28.3GeV protons
for detector on beam axis
counts - independently normalized
1
$10^{-1}$
$10^{-2}$
solid line : detector at 100m.
dotted line : detector at 1km.
dashed line : detector at 3km.
0
0.5
1
1.5
2
2.5
3
3.5
4
$E_\nu$ ( GeV )

Fig. 12

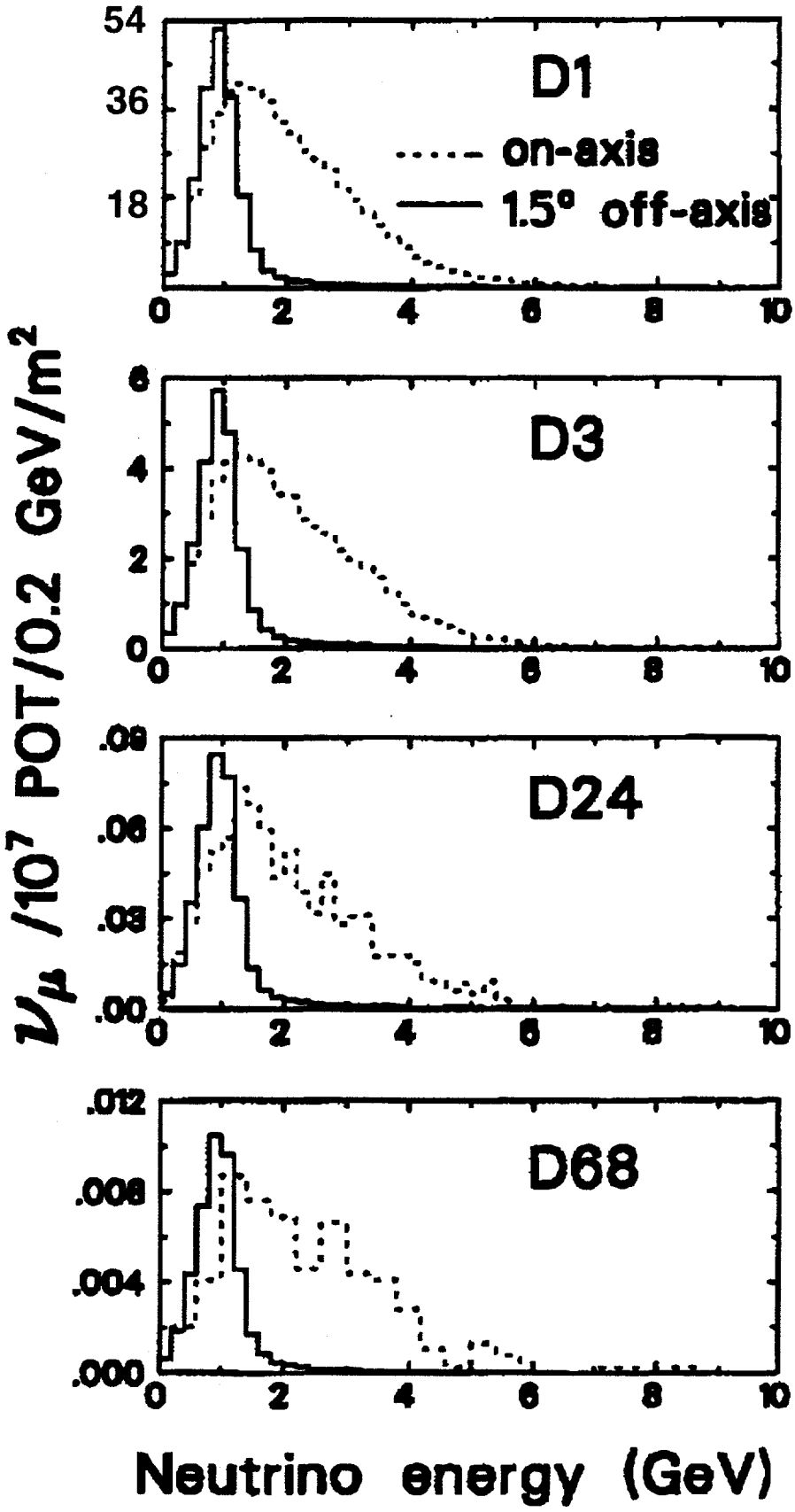


Fig. 13

95-0099a

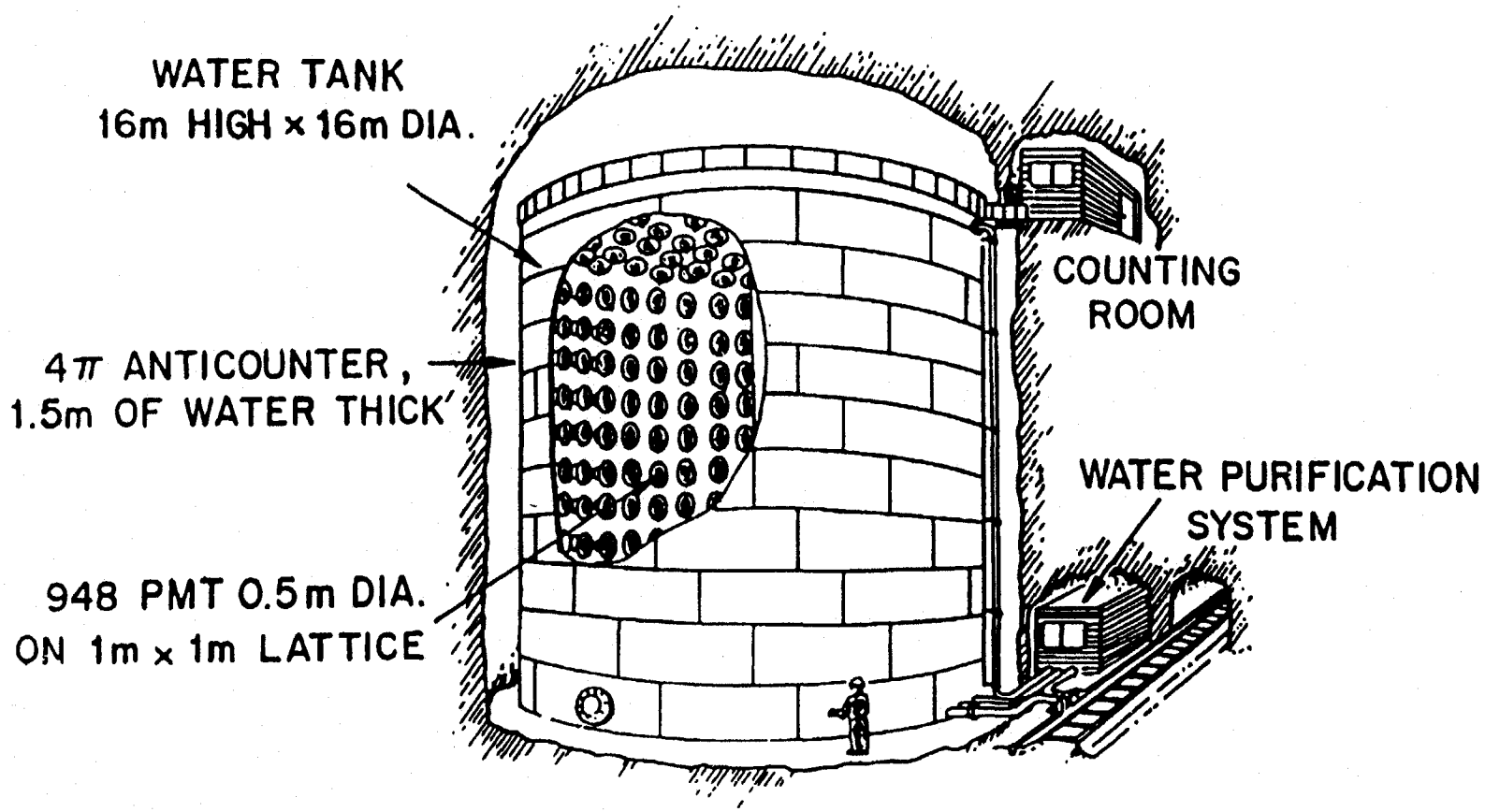


Fig. 14



95-0005c1

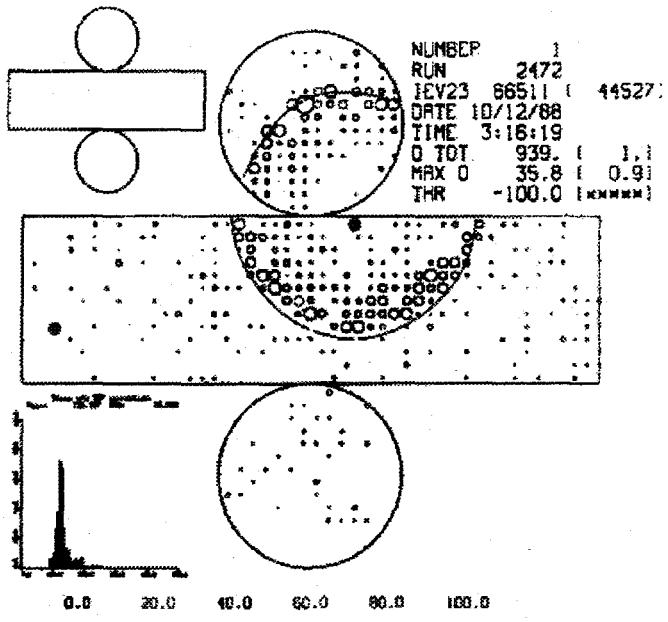


(a) Observed Event, PID=Muon, P=0.548 GeV/c

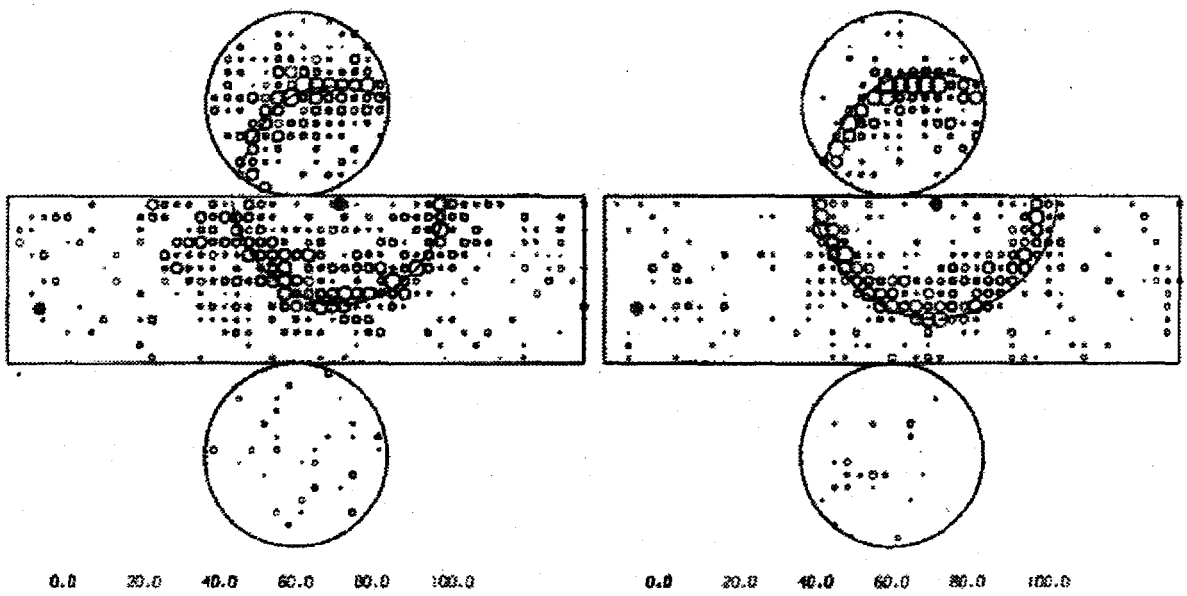


(b) MC Electron

(c) MC Muon

Fig. 15

95-0092x
95-0092x

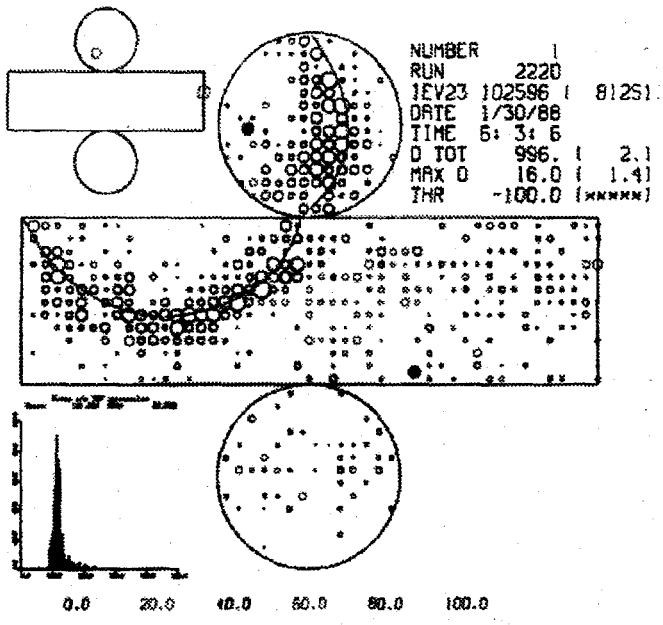


(a) Observed Event, PID=Electron, P=0.332 GeV/c

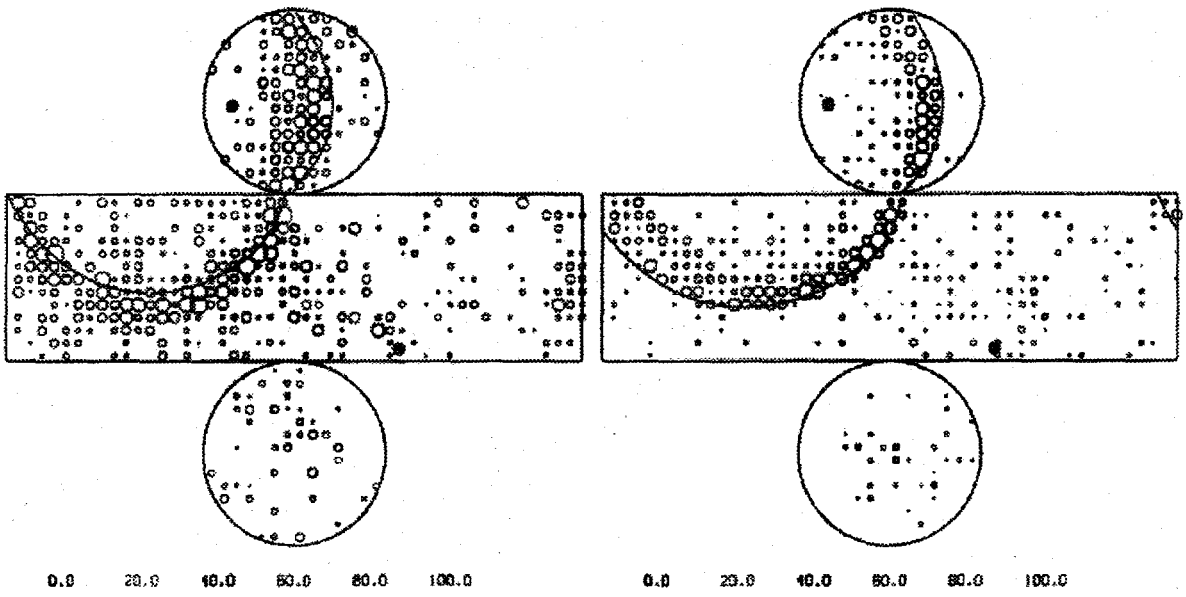


(b) MC Electron

(c) MC Muon

Fig. 16

95-0092w
95-0092w

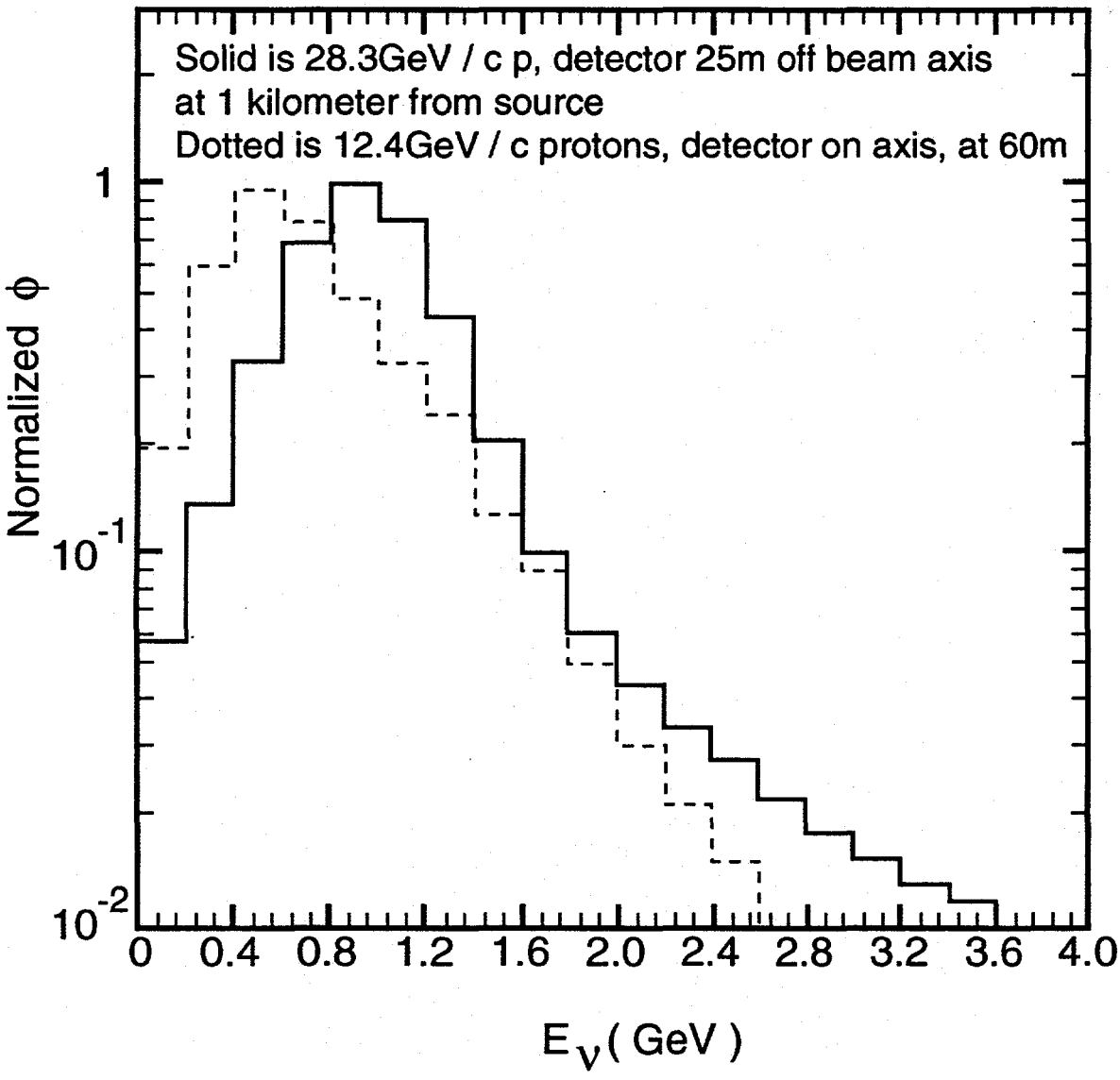


Fig. 17

95-0071h

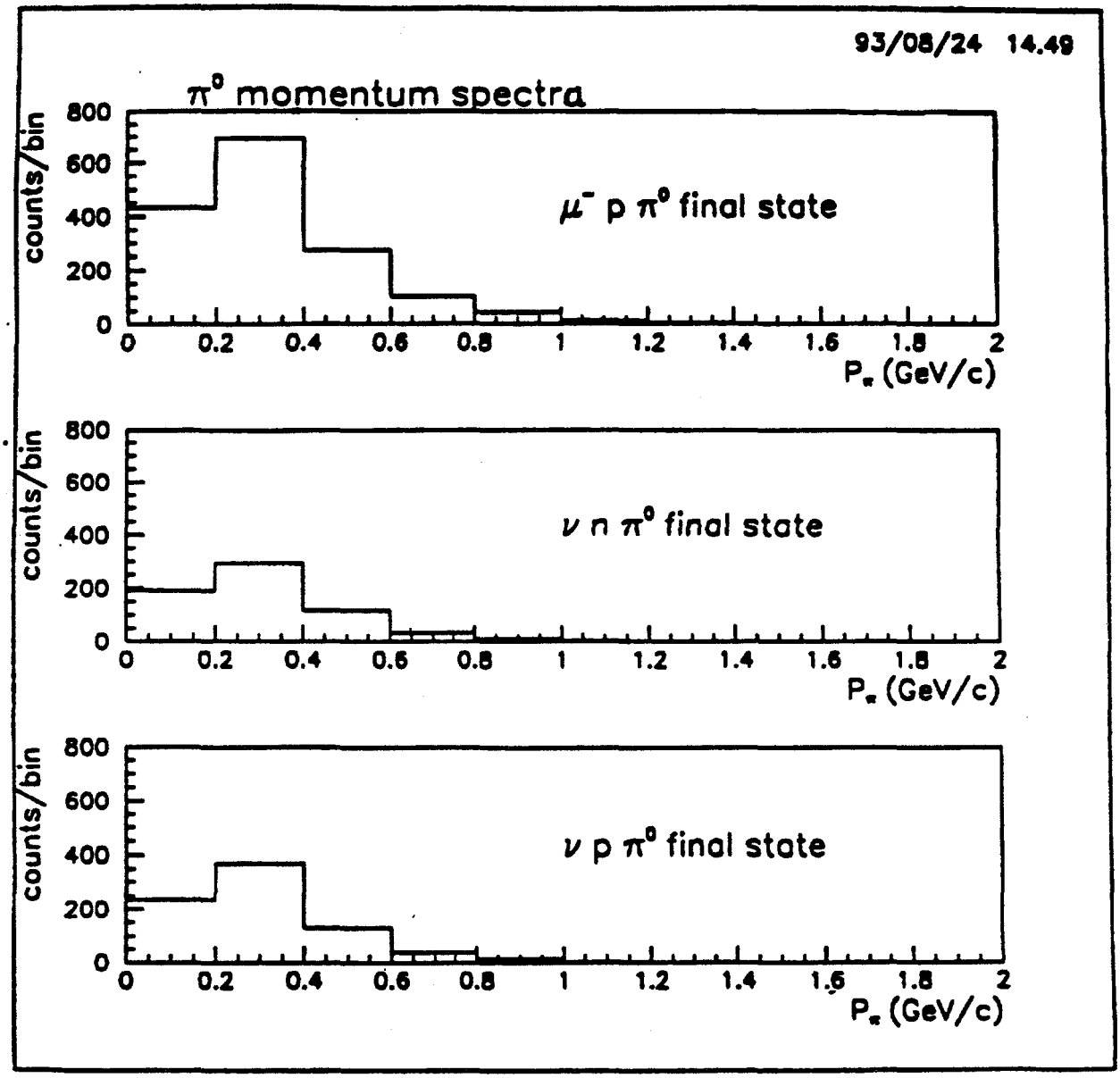


Fig. 18a

95-0071d

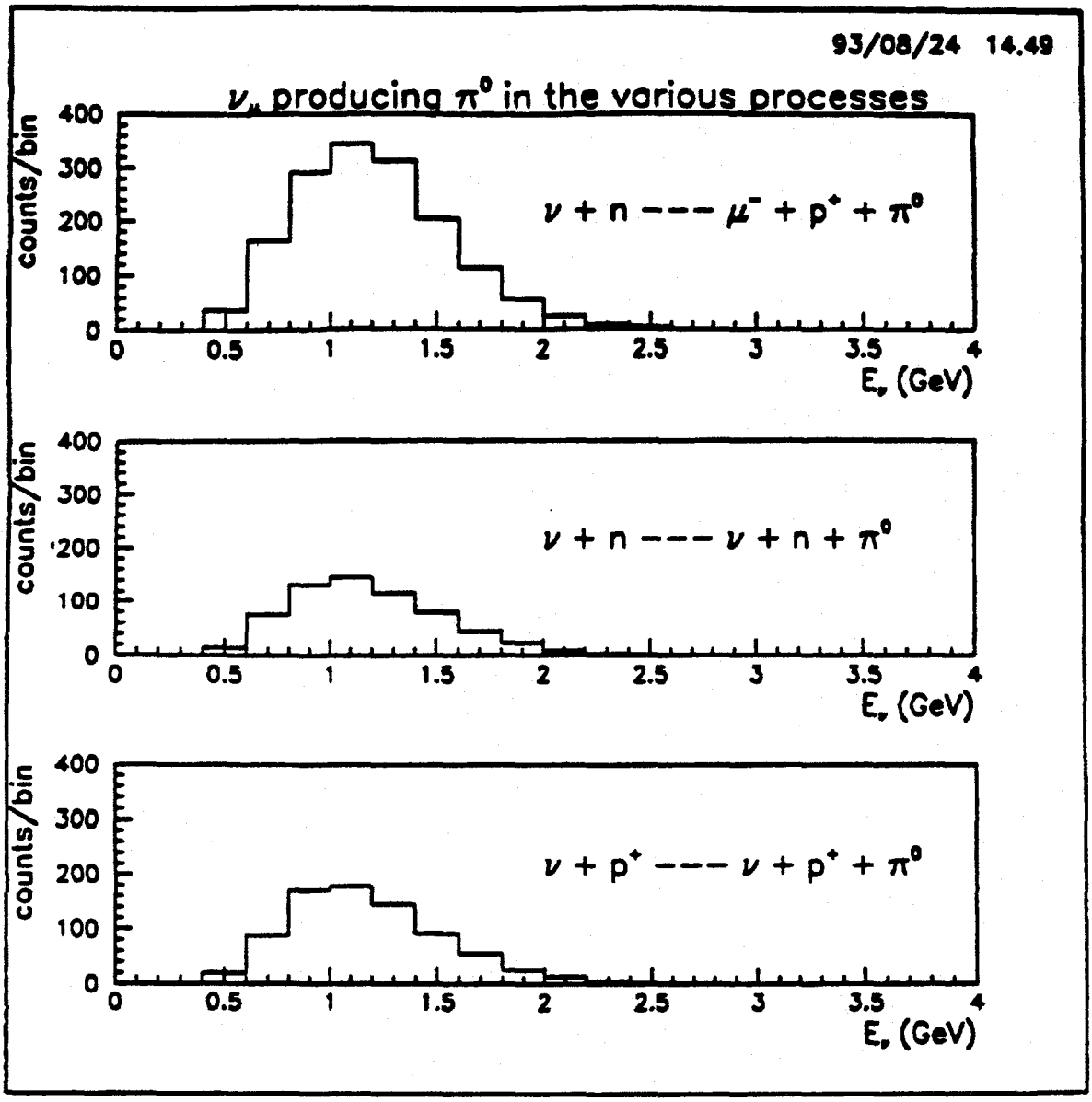


Fig. 18b

95-0071e

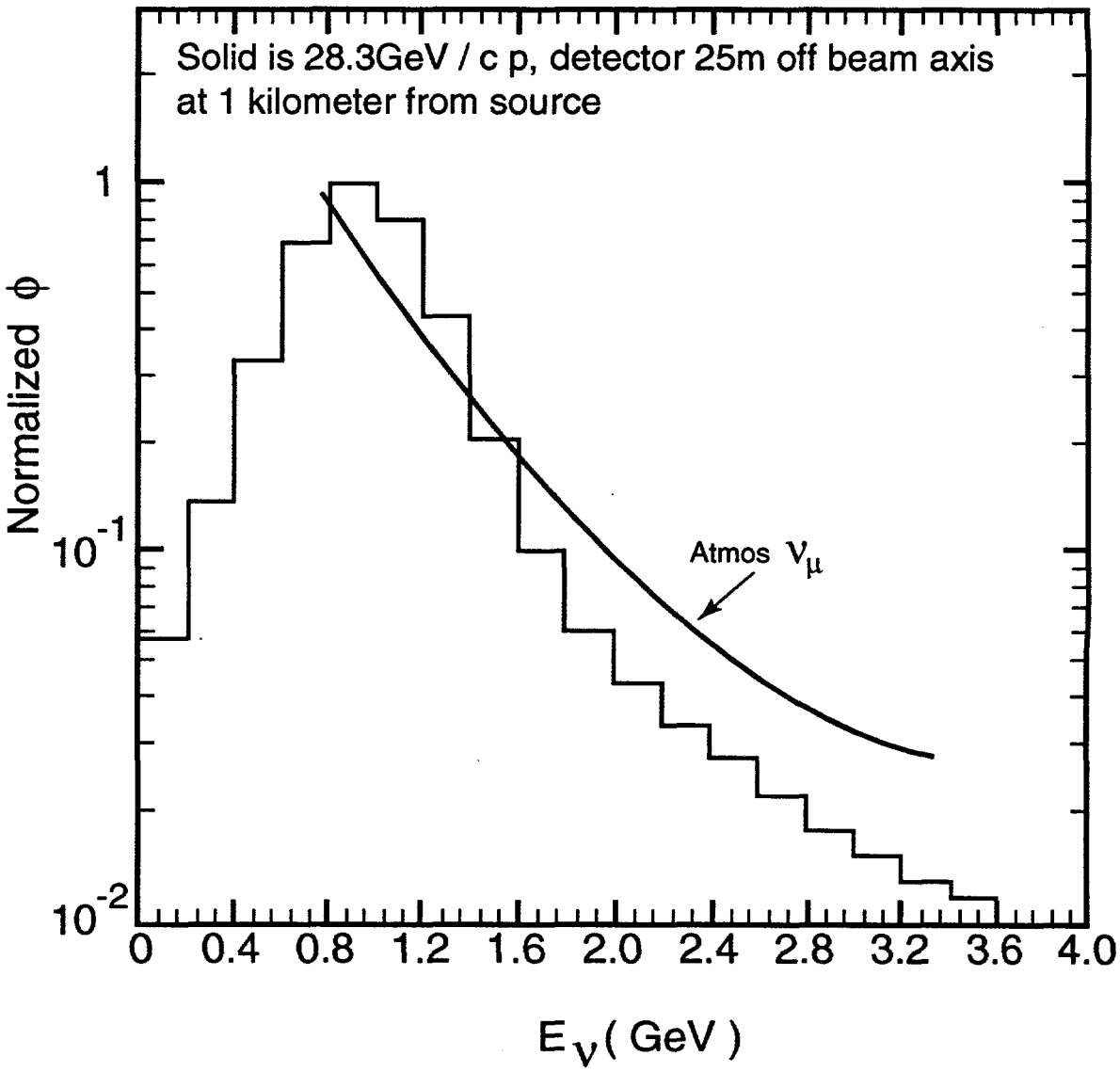
Solid is 28.3GeV / c p, detector 25m off beam axis
at 1 kilometer from source
Normalized ϕ
1
10^-1
10^-2
Atmos ν_μ
0
0.4
0.8
1.2
1.6
2.0
2.4
2.8
3.2
3.6
4.0
E_ν ( GeV )

Fig. 19

# III A. Neutrino Beam Design and Construction

It is desirable to tune the energy spectrum of the neutrino beam to maximize the likelihood of observing an oscillation signal. This amounts to using neutrinos whose energy spectrum is largely confined between 0.5 and 1.5 GeV. The technique we plan to use to produce such a beam [1] is discussed in detail in this chapter (section III.1.1).

At the same time, because the experiment has a long baseline, it is essential that steps be taken to maximize the neutrino flux. To accomplish this goal, the AGS proton intensity needs to be high, the targeting efficient, pion focusing optimized, and the pion decay space long. Since it is necessary to rebuild the entire neutrino beam line, it is possible to influence all these aspects of beam production; they are also discussed in detail here. Finally, the civil construction relating to the beam systems is described.

## III.1 Neutrino energy spectrum

The means by which the energy spectrum can be adjusted is illustrated with the density plot shown in Fig. 1. In this plot it can be seen how the spectrum is softened by increasing the distance of the detector from the axis defined by the center line of the decay tunnel. This is explicitly illustrated in Fig. 2 in which detector width slices of Fig. 1 are shown in one degree steps. The arrows along the abscissae mark the positions of the peaks, and show that the peak energies shift from about 1.3 GeV for the on-axis spectrum to 0.5 GeV for the spectrum 3 degrees off-axis. A further, dramatic illustration of the way in which moving off axis can shape the energy spectrum is shown in Fig. 3, in which the zero degree spectra are overlaid with the 1.5 degree off-axis spectra for detectors located 1, 3, 24, and 68 km from the source. The peaks are clearly shifted to lower energies in the off-axis cases, and in addition there is more flux at these important lower energies. Furthermore, the suppression of the high energy regions of the spectra is also desirable; there will then be lower probability for a high energy event to appear at lower energy. In any case, only those events whose initial energy is less than 4 GeV can be fully contained in the detector.

The reason why the neutrino spectra behave this way can be understood simply from the conservation of momentum and energy. For a pion decaying along a direction defined by the axis of the tunnel, the conservation laws lead to the neutrino energy given by

$$E_\nu = \frac{m_\pi^2 - m_\mu^2}{2(E_\pi - p_\pi cos\theta_\nu)} \qquad (1)$$

where $m_\pi$ and $m_\mu$ are the pion and muon rest masses,

$E_\pi$ is the pion energy,

$p_\pi$ is the pion momentum,

and $\theta_\nu$ is the angle at which the neutrino is emitted.

Differentiating this expression shows that for a given neutrino emission angle, there is a maximum neutrino energy given by

$$(E_\nu)_{max} = \frac{m_\pi^2 - m_\mu^2}{2E_\pi^m sin^2\theta_\nu} \tag{2}$$

For pion energies both greater and less than $E_\pi^m$, $E_\nu$ is less than $(E_\nu)_{max}$. A plot of Equation 1 for neutrino detection angles of 0.0, 1.5 and 3.0 degrees is shown in Fig. 4 to illustrate this point. The curves show that at zero degrees, the neutrino energy is proportional to the pion energy, but in an off-axis direction, there is a maximum in the neutrino energy.

This behavior can be qualitatively understood by considering the transformation from the isotropic decay of a pion in the center of mass to the Lorenz enhanced decay distribution for a pion moving in the laboratory. This is illustrated in Fig. 5 which shows a sequence of momentum distributions of neutrinos emitted from successively faster moving pions. Because there is a maximum neutrino momentum (29.8 MeV/c) perpendicular to the pion's momentum, there is a maximum neutrino momentum at any given angle from the pion direction. Further, this maximum momentum is lowered as the observation angle is increased, as evident from Fig. 5 and shown explicitly in Fig. 2.

From Fig. 4 for the 1.5 degree off-axis case, pions with energies between about 2 and 7 GeV yield a neutrino energy near 1.0 GeV. Typical trajectories of pions that pass through and are focussed by the magnetic horns are plotted in Fig. 6. For pions between 2 and 7 GeV the focusing is essentially point-to-parallel, and it can be expected that the neutrino energy spectrum will peak near 1.0 GeV, as in Fig. 3. The fact that a wide range of pion energies map essentially to a single neutrino energy also explains the increase in flux at this lower energy relative to the on-axis beam.

Further illustration of neutrino beam behavior can be found from projections of the various energy bins of Fig. 1 onto the direction transverse to the central beam axis (the ordinate of Fig. 1). Several of these plots are shown in Fig. 7. Note that as the energy increases, the neutrinos go forward into progressively narrower cones. This behavior is predicted by Equation 2; neutrinos of energy larger than $(E_\nu)_{max}$ must lie in a forward cone defined by an angle smaller than $\theta_\nu$. This observation helps to clarify why a detector located on the central axis has such a large high energy tail. It is apparent that by shifting the position of the detector, the flux of neutrinos in any given energy interval can be maximized, thus

determining the optimum off-axis position at which to place the detectors.

The calculated transverse spreads of the neutrino beam at the distances of the various detectors are shown in Fig. 8. The fall-off with off-axis location shows there will be variation in intensity across the face of each detector. This point is illustrated in Fig. 9. For D1, the intensity varies linearly by ± 25 % relative to the midlife, and for the two far detectors the distributions are essentially flat across the detectors. Fig. 10 shows how the neutrino spectrum shape changes for a 14m by 14m fiducial size located at several distances from the neutrino source. The scale for each plot has been corrected by the $1/r^2$ behavior expected for a point source. The spectrum change from D1 to the far detectors is clearly not significant; furthermore, a simple linear fall in intensity across the face of the detectors does not change the $1/r^2$ dependence of the count rates in the detectors. Consequently, off-axis placement of the detectors will not cause significant systematic errors in the estimates of the fluxes expected in the far detectors. See Chapter V for details.

The way in which the neutrino energy spectrum can be tuned to match the goals of the experiment is clear. The detectors will be placed 1.5 degrees off-axis; it can be seen in Fig. 2 that although the peak energy is lower at 3 degrees, the flux is beginning to decrease significantly. Again, this can be understood by reference to Fig. 4 which shows that while the maximum neutrino energy is lower at 3 degrees, a smaller range of pion energies map to this maximum energy.

A more explicit way to determine the optimum angle is through the figure of merit (FOM) referred to in Chapter II.

$$FOM = \sum_{E_\nu} \phi(E_\nu)\sigma(E_\nu)/E_\nu^2 \tag{3}$$

where $\phi(E_\nu)$ is the flux as a function of neutrino energy $E_\nu$,

and $\sigma(E_\nu)$ is the cross section.

This figure of merit is plotted in Fig. 11, which shows less than 10% variation from about 0.75 degrees to 2 degrees. Consequently, other factors, such as ease of placement, can be considered when choosing the exact location of the detectors.

Other methods of shaping the neutrino spectrum have also been investigated. The most straightforward is to use momentum selection devices in the horn, but it is already known from previous experience at the AGS [2] that there would be an accompanying unacceptable reduction in intensity.

It might naively be expected that lowering the proton beam energy would reduce the high energy tail. A plot of the spectra expected in D24 for both the on-axis and 1.5° off-axis cases, for proton energies of 12 GeV and 28 GeV, is shown in Fig. 12. The on-axis spectrum at 12 GeV indeed has a somewhat lower high energy tail than the 28 GeV spectrum, but the effect is not nearly as dramatic as is the effect of moving off the axis. The main result of lowering the proton energy is simply to reduce the overall flux of neutrinos, at low energies as well as high energies.

The simulation spectra above have all been generated assuming a proton beam that strikes the target on center and parallel to the target axis. Furthermore, the integrity of the target has been assumed, which will be discussed in section III.3.3. Simulation studies have been made to investigate the effects expected if these conditions are not met. An example of a case in which the detectors are at the same offset angle but 180° apart in azimuth is shown in Fig. 13. The proton beam has been mis-steered so as to strike the target 1.6mm (half the target radius) off-center. There would be a significant spectrum difference between the left and right detectors in this case, so that the prediction of the neutrino flux at a detector on one side of the beam axis from observations in a detector on the other side of the axis would be uncertain without calculated corrections. It will be seen in Chapter V that the actual separation of the far detectors, D24 and D68, is $10^0$ in azimuth, so the effect in Fig. 13 is unimportant. A second example is shown in Fig. 14 in which the proton beam is directed onto the target at a small angle (7mrad), chosen so that the beam remains within the endcap of the decay tunnel. Again a small spectrum shift is evident. The AGS proton beam is routinely kept and monitored within 1 mrad.

## III.2 Neutrino beam intensity

There are a variety of ways by which the intensity can be increased over that of the previous beam at the AGS. A straightforward improvement, nearly independent of neutrino production considerations, has already been achieved with the recent addition of the Booster ring. The proton beam intensity has been raised to over $5 \times 10^{13}$ protons per pulse, and the goal of $6 \times 10^{13}$ is within reach, to be compared with the previous maximum of $2 \times 10^{13}$. However, this higher current might introduce new problems not encountered in the earlier AGS experiments. These are dealt with in section III.3.3.

Other straightforward ways to increase the intensity are to lengthen and/or widen the decay tunnel. The previous tunnel was 52m long; Fig. 15 indicates that lengthening it to

240m would result in about a factor of three increase in flux. The old tunnel was 1.84m in radius, but from Fig. 16 there is not much gain (about 13%) if it were widened to 3m radius. It is also seen from Fig. 16 that for a tunnel 3m in radius half the flux comes from the innermost 60cm. It is too expensive to consider a tunnel more than 2m in radius; again, 90% of the flux for a 2m radius tunnel originates in the innermost 1.5m. We have used a radius of 1.5m and a length of 180m for our simulations; the actual design of the tunnel in Section III.3.4 calls for a tunnel with a aperture that varies with distance.

The use of a horn as the first element in the pion focusing system has also been scrutinized. Possible alternatives, such as a large aperture Li lens of the type used extensively at the CERN and Fermilab antiproton production sources, or a plasma lens such as the one under development at Erlangen [3], might be a superior option. Shown in Fig. 17 is a comparison of simulation studies of a system using a z-pinch plasma lens as the first element with one using a horn [4]. The parameters used in this calculation were precisely those of the former Brookhaven neutrino line [5]. At most, 75% of the horn focused flux can be obtained with this lens. Another problem, common to both plasma and lithium lenses, is that it is difficult to build such devices with an aperture large enough for an intense neutrino beam. In the case of antiproton production the source is very bright and tightly focussed, but this is not the situation here. Therefore, our beam design has been based upon a double horn system. An important consideration, besides the difficulties with other devices mentioned above, is that horns are a well-known and well-tested technology.

## III.3 Detailed description of the neutrino beam

The fast extraction of the proton beam for E889 from the AGS is basically the same as for RHIC and the g-2(E821) experiment. It is done with the same kicker magnet at the same location. However, the duration of the kicker pulse for E889 will be sufficient to extract all of the beam in the AGS ring. The micro-structure will consist of 8 rf buckets. The extracted protons are transported to the 'U' line where the new proton transport for E889 branches off. The facilities for production of the new neutrino beam can be functionally separated into five regions as shown in Fig. 18.

- A conjunction area where the proton transport for E889 splits off from the present 'U' line proton transport in a bend of 12°, and is optically matched into the large bend to the neutrino target.

- The proton transport section where the protons are bent further to a total of 60.5° to aim the neutrino beam in the desired direction. Also included are the final focusing and correcting trims.

- The horn/target area in which pions are produced by the interactions of the proton beam with a target inside the first focusing horn. The second horn creates a parallel beam of pions directed toward the end of the decay tunnel. This area is the maximum radiological concern since the entire AGS beam is striking the target and creating a high level of activation and possible radiation damage.

- The decay tunnel is a simple shielded tunnel, probably filled with helium for most of its length. The length (180m) and diameter (3m) are sufficient to allow most of the pions to decay.

- At the end of the decay tunnel is a massive block of steel shielding to absorb the protons and undecayed pions to avoid activating the soil. In this absorbing block there are a series of slots which allow the muon distribution to be sampled.

Details of the beam production components in these regions are discussed in the following subsections. Civil construction is discussed in section III.4.

### III.3.1 Conjunction area

In terms of beam components, the conjunction area is relatively simple. There are 5 dipoles and 4 quadrupoles to bend the beam by 12° and match the beam size into the large bend. Since this section is connected to the existing RHIC transport line, there are a number of constraints in space and time which must be met. Discussions have been held with the RHIC accelerator staff which indicate that these constraints can be met. No RHIC beam line elements need to be repositioned, and there are a number of possible time windows which will allow the necessary civil construction of this conjunction tunnel to be carried out. A conceptual design for radiation safety for all the affected lines has been considered.

### III.3.2 Proton transport section

The large bend in this portion of the transport is accomplished with the use of RHIC injection line (room temperature) gradient dipoles of the 'C' type with a 3.8cm vertical gap. Existing designs and tooling make the construction of these 20 dipoles relatively quick and

straightforward. Calculations show that the vertical aperture in these dipoles is nearly twice that required for the $100\pi$ mm mrad emittance of the fast extracted proton beam from the AGS. Trim magnets are included between each dipole to keep the beam well centered in the gradient dipoles.

In the final section a set of 4 quadrupoles focuses the beam on the pion production target in the horn. Vertical and horizontal trim magnets provide for steering the beam onto the target.

To keep the proton beam accurately centered on target, a number of instruments are provided along the proton transport. In the dipole arc there are loss monitors, plunging scintillation flags and EPM's (residual gas profile monitors). Just before the target there is a current transformer to measure the intensity, and a series of SWICs to measure the beam position. Beam position monitors developed at TRIUMF for KAON might be preferable to the SWICs in that they are nonintercepting and do not disturb the beam. In either case, it will be possible to maintain the beam position on the target to within 0.1mm of center and the angle of incidence to within 0.5mrad.

The interacting flux is measured with ionization chambers at 90° to the target. Beam timing will be determined by lucite Cherenkov counters.

### III.3.3 Horn/target area

The present pion focusing system is based on two horn focusing elements as shown in Fig. 19. The large magnetic fields (up to 5T) created by the high currents (up to 250 kA) in the first coaxial horn provide strong focusing on the produced particles contained in the narrow neck of the first horn. For a broad range of momenta above and below 3 GeV/c, there is an intermediate focus between the two lenses. The second horn takes the beam from point to parallel down the decay tunnel. Water cooling is necessary in the first horn since there is heating from both the current on the inner conductor and heat deposition in the target. Calculations are being done to check whether the previously used cooling capacity [6] will be adequate in view of the increased proton current.

As noted in section III.2 there may be some new technical difficulties encountered because of the increased proton beam current. These include an increase in the average beam power deposited in the production target and focusing devices, a larger density of energy deposition in the target, increased air activation and ionization in the target region, and the necessity for remote handling of the target and focusing elements. All have been dealt with at other

laboratories and should not present a serious challenge or require new technology to solve.

Too high an energy deposition in the target could cause melting in the central region [7], which would result in a loss of density of the target material. An example of this effect is shown in Fig. 20. The calculation was done for a copper target 50cm long and 7mm in diameter, and the beam was contained in a 3mm ($4\sigma$) diameter spot. There were $10^{13}$ protons per pulse, fewer than anticipated in this experiment, and the pulses were 1.5s apart in time. The plot shows the variation in target density along the rod for the first few pulses, and it is seen that at the downstream end of the rod the density is barely 60% of the initial density after only five pulses.

A serious problem can arise if the energy deposited by the beam is restricted to too small an area of the target[7]. In this case, shock wave propagation can result in destruction of the target. These problems have been solved for antiproton production targets at a number of laboratories. It has been found that a combination of adequate cooling, target containment, and sufficiently spread out proton beam result in a target that lasts for long periods of time [8]. Doubling the diameter of the beam will result in the same energy density deposition in the target as in the previous AGS beam. The diameter of the target would then have to be doubled to accommodate the larger beam. This would result in a 10% reduction in the neutrino flux, as shown in Fig. 21. Detailed calculations are underway for a target design that will withstand all these effects.

Increased proton current will introduce new difficulties in the horn system. The water cooling arrangement for the target and horn system inherently requires that these systems be operated in air (or some other atmospheric environment). AGS safety personnel indicate that activation of the air should not pose a serious problem provided the target area and decay tunnel are sealed and the enclosed atmosphere controlled and monitored. The effects of ionization of the air in the vicinity of the high voltage pulsed focusing devices were not a problem at $2 \times 10^{13}$ protons per pulse, but need to be investigated for the higher intensities anticipated here. However, since the area must be sealed and the atmosphere controlled, such problems could be solved by a suitable choice of gas mixture or improved insulator design, and these options are being investigated.

Remote handling of the target and horn systems may possibly be required and with the increased current may need to be more elaborate than before. TRIUMF, LAMPF, PSI and the antiproton production sources at CERN and Fermilab provide adequate examples of how to resolve the anticipated remote handling problems. It is planned to hang the horns in narrow shielded caves as shown in Fig 14. This is a technique used at the AGS as well as

other laboratories. This problem can be resolved through attention to design details. It may be necessary to provide a rudimentary hot cell and manipulator facility close to the target area.

It will be necessary to build a new supply to power the horns. The high current required, approximately 250 kA, is produced by the discharge of capacitor banks through the horn inductances. The switch in the supply used previously was a series of ignitrons. A pulser using SCRs as the switch has recently been designed at TRIUMF. It is based on the proposed CERN LHC abort kicker system. The SCR design is a new technology for pulsers of this type, but would have several advantages over the ignitron design, such as reduced jitter and improved lifetime. On the other hand, ignitrons have the advantage that they have been operated successfully and are a well known technology at BNL. It is planned to prototype both types of system, and choose between them largely on the basis of reliability.

It might prove advantageous to power each horn with a separate supply; the pulse duration can then be shorter and the ohmic heating effects would be reduced. Calculations are underway to determine whether the modest extra expense would be justified. The supply will be capable of delivering 250kA to the horns but it will run routinely at 200kA, because the undesirable heating and mechanical shock effects vary quadratically with voltage and current. It is shown in Fig. 22 that, although the neutrino yield peaks near 250kA, there is only a 5% loss in running at the lower current.

### III.3.4 Decay tunnel

The decay tunnel consists simply of round pipe sections, and will be 180m long as noted in section III.3. The upstream half will be 2.4m in diameter and the downstream portion will be expanded to 3m. It is planned to fill the tunnel with helium since this reduces the 20% interaction probability by a factor of 5. Since this space is unoccupied by persons or equipment, no facilities are required in the decay tunnel.

### III.3.5 Beam stop

The beam stop will be a cube of steel, about 6m on a side. This probably will be assembled from blocks made out of recycled steel from Oak Ridge. The stop serves two purposes. First it is long enough to attenuate all the strongly interacting particles in the beam to a level where soil activation is no longer an issue. Second, by placing slots at various depths in the steel, the angular distribution of muons for various energies can be measured with arrays of

small ion chambers, as was done during E734 [5]. Since the muons result from the same pion decays which produce the neutrinos, the muons are a good monitor of neutrino beam and a measure of their energy spectrum.

## III.4 Civil construction

In this section the civil construction for the proton transport, target/horn building, and decay tunnel is discussed.

A plan view of the new facilities for producing the neutrinos for E889 is shown in Fig. 23. Represented in this figure are the proton transport tunnel, pion decay tunnel, beam dump, target/horn building, the earthen shield, and the existing structures near the fast extracted beamline.

Several existing utilities require modification for the construction of the new beamline. Catch basins and storm drains used for surface drainage will require relocation. An existing water pipe will be replaced to withstand the increased pressure caused by the earthen shield. Some small storage sheds in the area need to be relocated or demolished. One of the more expensive modifications will be the re-routing of Thomson Road around the beam dump. The schedule of these modifications will be carefully coordinated with the beamline construction.

Three buildings will be built for the beamline. Early completion of the horn/target building is essential for construction and testing the new horn system. The building will be of similar construction to the slow beam experimental halls. The building has been sized (5000 $ft^2$) to house the proton target and pion focusing horns, the horn power supply systems, power supplies for magnets in the later portion of the proton transport, and the closed loop water cooling system for the horns. A 25 ton crane will be used for shielding and horn rigging operations. A shielded storage area will house an activated horn should it require removal after operations. The shielding around the target area will occupy a large portion of the building. Besides the usual building utilities, substantial electrical power will be distributed to specified locations for the horn and magnet power supplies. The target/horn building construction and utilities will be completed within six months after the start of construction.

The remaining two structures can be completed at a later time in the construction schedule. A 900 $ft^2$ power supply building will be located near the beginning of the proton transport. It will house the power supplies for the initial portion of the new proton beamline. A small roofed structure will be built over a portion of the beam dump which has muon detectors. This structure will serve as a weather shield for the detectors which will be placed

into slots inside the iron dump.

The construction of the conjunction area where the proton transport is joined to the existing U-line will be coordinated with AGS operations. During the 3 months required for the construction of the conjunction area, there can be no beam extracted from the AGS into the U-line. The area will be excavated and a portion of the existing tunnel will be enlarged to accommodate the first bending dipoles. Shielding will be placed along the existing tunnel. This should enable a portion of the proton transport tunnel to be occupied in the future while beam is delivered to the g-2 target station or RHIC. Finally, the front portion of the proton transport tunnel will be installed and sufficient earthen shielding replaced before it will be permitted to extract any beam into the U-line.

The proton transport and decay tunnels are similar to previous tunnels built for the AGS Booster and RHIC transfer line. A plan view of the tunnels is shown in Fig. 18. The proton transport tunnel will be built of 11 foot diameter corrugated pipe sections. A concrete slab will be poured for a tunnel floor. There will be an emergency escape hatch near the beginning of the tunnel. The main entrance has been sized for installation of the magnets and is located near the target building. The completed tunnel will have lighting, ventilation, fire detection/protection, emergency lighting, and power distribution. The earthen shielding on top of the tunnel will be 20 feet thick and considerably thicker on the sides. This thickness is required to reduce potential radiation levels outside the tunnel both from normal beam losses and from fault conditions. The decay tunnel will have a similar earthen shield.

### Summary of Section III A.

The design and characteristics of the proposed new AGS neutrino beam are described. We have discussed at length the neutrino beam energy spectrum and spatial shape, and the evidence that offsetting the E889 detectors with respect to the proton beam center line has several important advantages for a long baseline neutrino oscillation search, and essentially no serious disadvantage. The variation of flux across the cross section of the detectors was shown; its explicit effect on the search for oscillations is treated in Chapter V. The detailed description of the several elements of the proton, meson, and neutrino beam was given, and the civil construction required for these elements specified.

## References


[1] R. L. Helmer, in *Proc. of the $9^{th}$ Lake Louise Winter Institute*, Lake Louise, Canada, 1994, to be published, and TRIUMF preprint TRI-PP-94-34, June, 1994.

[2] A. Carroll et al., IEEE Transaction in Nuclear Science, **NS-32** (1985) 3054.

[3] J. Christiansen et al., in *Proc. of the European Particle Accelerator Conference* (EPAC90), Nice (1990), CERN/PS 90-30 (AR), p. 343 (1990).

[4] R. Weib et al., Universität Münster, Institut Für Kernphysik, Annual Report, (1992/93) p. 45.

[5] L. A. Ahrens et al., Phys. Rev. **D34** (1986) 75.

[6] W. Leonhardt et al., in *Proc. of the Particle Accelerator Conference*, Washington, D.C., (1987) vol. 3, p. 1740.

[7] T. A. Vsevolozhskaya, Preprint 84-88, Novosibirsk, 1984, unpublished. G. Silvestrov, in *Proc. of the XIII Int. Conf. on High Energy Accelerators*, Novosibirsk, 1986.

[8] T. Eaton, TRIUMF Design Note TRI-DN-89-K41, (1989), unpublished.

## Figure Captions

Fig. 1. Density plot showing the variation in neutrino spectrum shape over a $\pm 3°$ angular range 1.5km from the production target.

Fig. 2. Variation of neutrino spectrum shape for D1 located at several angles from the central axis. The arrows mark the positions of the peaks.

Fig. 3. Comparison of spectra for D1, D3, D24 and D68 located on axis (0°) and 1.5° off axis.

Fig. 4. Variation of neutrino energy with pion energy when the neutrino is observed in the direction of the pion decay (0°), and at angles of 1.5° and 3.0° from this direction. The upper part outlines the kinematics.

Fig. 5. Neutrino momentum ellipses for various pion momenta directed along the abscissa. The number labeling each ellipse is the pion momentum in GeV/c. Note the expanded ordinate scale. For a given pion momentum, the neutrino momentum in any direction is the length of the vector from the origin to the boundary of the ellipse in that direction.

Fig. 6. Typical pion trajectories through the horns. Each pion originated at the front of the target and was emitted at an angle of 0.1 radian. The number labeling each trajectory is the pion energy in GeV.

Fig. 7. Changes of neutrino flux at D1 in several energy bins as the distance off-axis is varied.

Fig. 8. Transverse spread of the neutrino beam at the distances of the various detectors.

Fig. 9. Distribution of neutrinos incident on a flat square offset by $1.5^0$ from the beam axis. The fall of neutrino intensity is well fit by a function $A_0 + A_1 x + A_2 x^2$ where $x$ is the distance transverse to the beam axis from the center of the tank. The neutrino spectra for the inner 1/3 (-7.5 m to -2.5 m), the middle 1/3 ($\pm 2.5$ m), and the outer 1/3 (2.5 m to 7.5 m) are shown at the bottom. The approximately 10% shift in the average energy from one side of the fiducial volume to the other is not a problem when the spectrum is folded with

the path-length and the cross section as shown in Chapter V.

Fig. 10. Variation in spectrum shape at several distances from the source. The fiducial size at each distance was taken to be 14m by 14m, and the center of each detector was 1.5° off-axis. The spectra were normalized to one another by correcting for the $1/r^2$ fall-off expected for a point source.

Fig. 11. The figure of merit (FOM) for D24 located at various angles from the central axis.

Fig. 12. The neutrino beam shape produced by 12.4 GeV protons (ANL, ZGS), 60m from the neutrino source and on the beam center line compared with the beam shape at $1.5^0$ off axis produced by 28.3 GeV protons at 1 km from the source.

Fig. 13. Comparison of spectra in D1 located on either side of the central axis when the incident proton beam is displaced by 1.6mm to the left of the target center.

Fig. 14. Comparison of spectra in D1 located on either side of the central axis when the incident proton beam strikes the center of the target at an angle of 7mrad.

Fig. 15. Running sum of the percentage of neutrinos detected in D24 that originate in each 20m long section of the decay tunnel. The total tunnel length was 240m and the radius was 3m.

Fig. 16. Running sum of the percentage of neutrinos detected in D24 that originate in each 20cm thick cylinder of the decay tunnel. The total tunnel radius was 3m, and the length was 240m.

Fig. 17. Comparison of the neutrino flux obtainable with various focusing element combinations (from [4]).

Fig. 18. The facilities required for the production of the new neutrino beam.

Fig. 19. The pion focusing horns.

Fig. 20. Reduction in density along the central 1mm diameter core of the target as it is bombarded by five successive pulses of the proton beam. There were $10^{13}$ protons in each 2.5$\mu$s long pulse, 1.5s between pulses, and the beam width ($4\sigma$) was 3.2mm. The target was a copper rod 50cm long and 7mm in diameter, and it was in vacuum and not cooled. The numbers label the successive pulses.

Fig. 21. Comparison of neutrino spectra predicted for D24 with the previous proton beam ($4\sigma$ = 3.2mm) and production target (diameter=6.4mm) (solid line) and with these two parameters doubled. The statistical errors on the sums are about 1%.

Fig. 22. Variation of neutrino yield with horn current, as observed at D3. The spectra were integrated from 0 to 6 GeV.

Fig. 23. Details of the new beam production area.

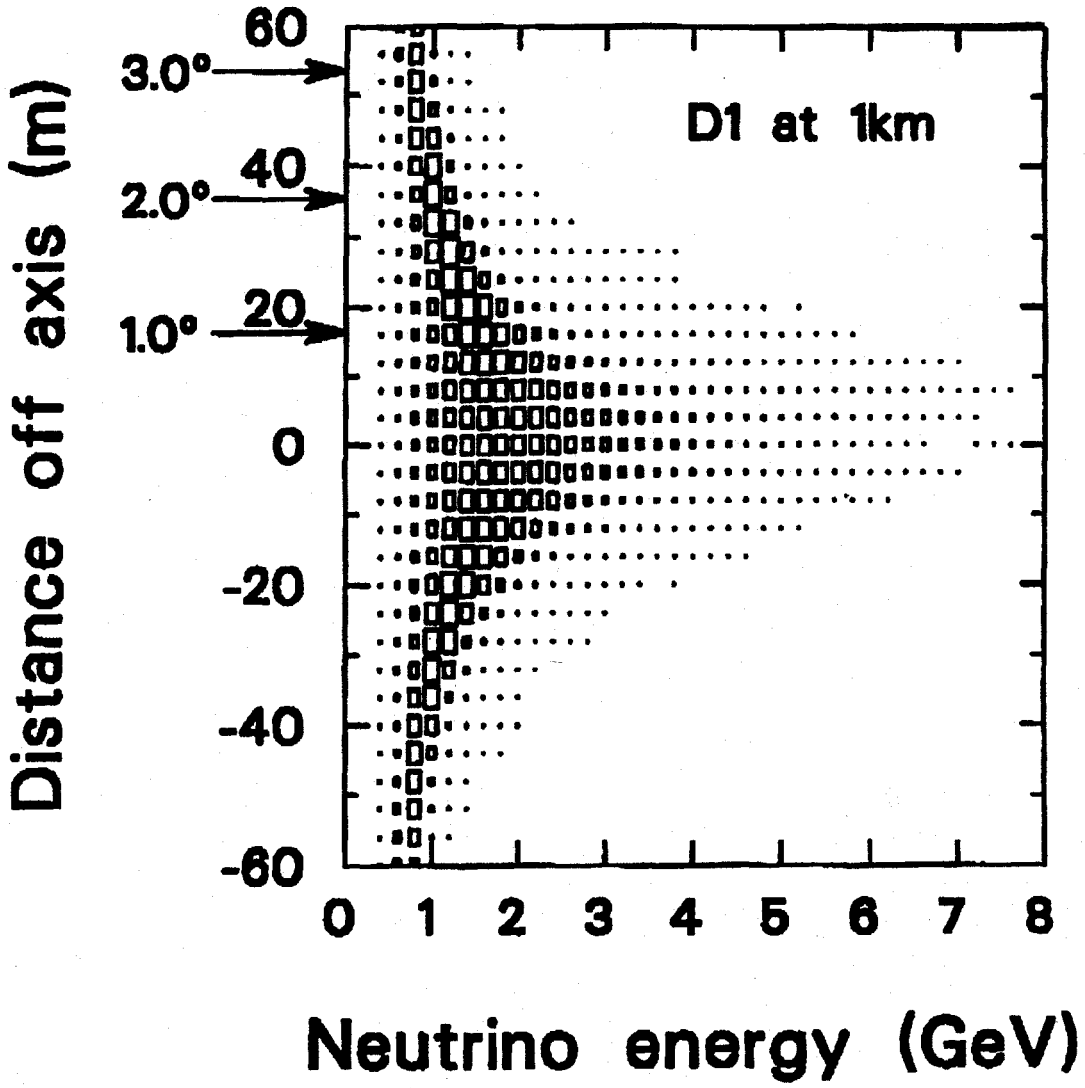
D1 at 1km
Distance off axis (m)
60
40
20
0
-20
-40
-60
3.0°
2.0°
1.0°
0 1 2 3 4 5 6 7 8
Neutrino energy (GeV)

Fig. 1

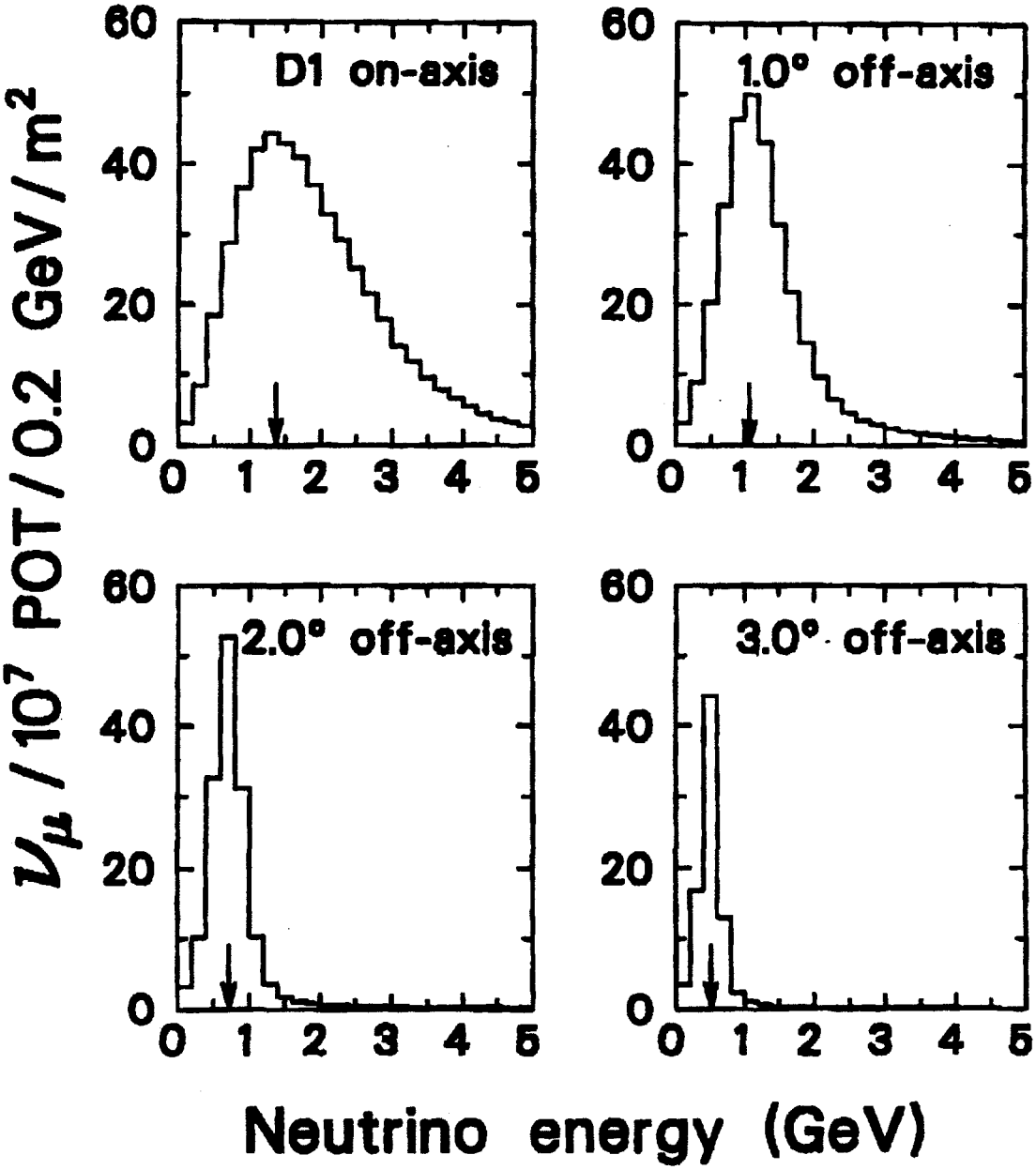
D1 on-axis
1.0° off-axis
2.0° off-axis
3.0° off-axis
60
40
20
0
0 1 2 3 4 5
$\nu_\mu$ / $10^7$ POT / 0.2 GeV / $m^2$
Neutrino energy (GeV)

Fig. 2

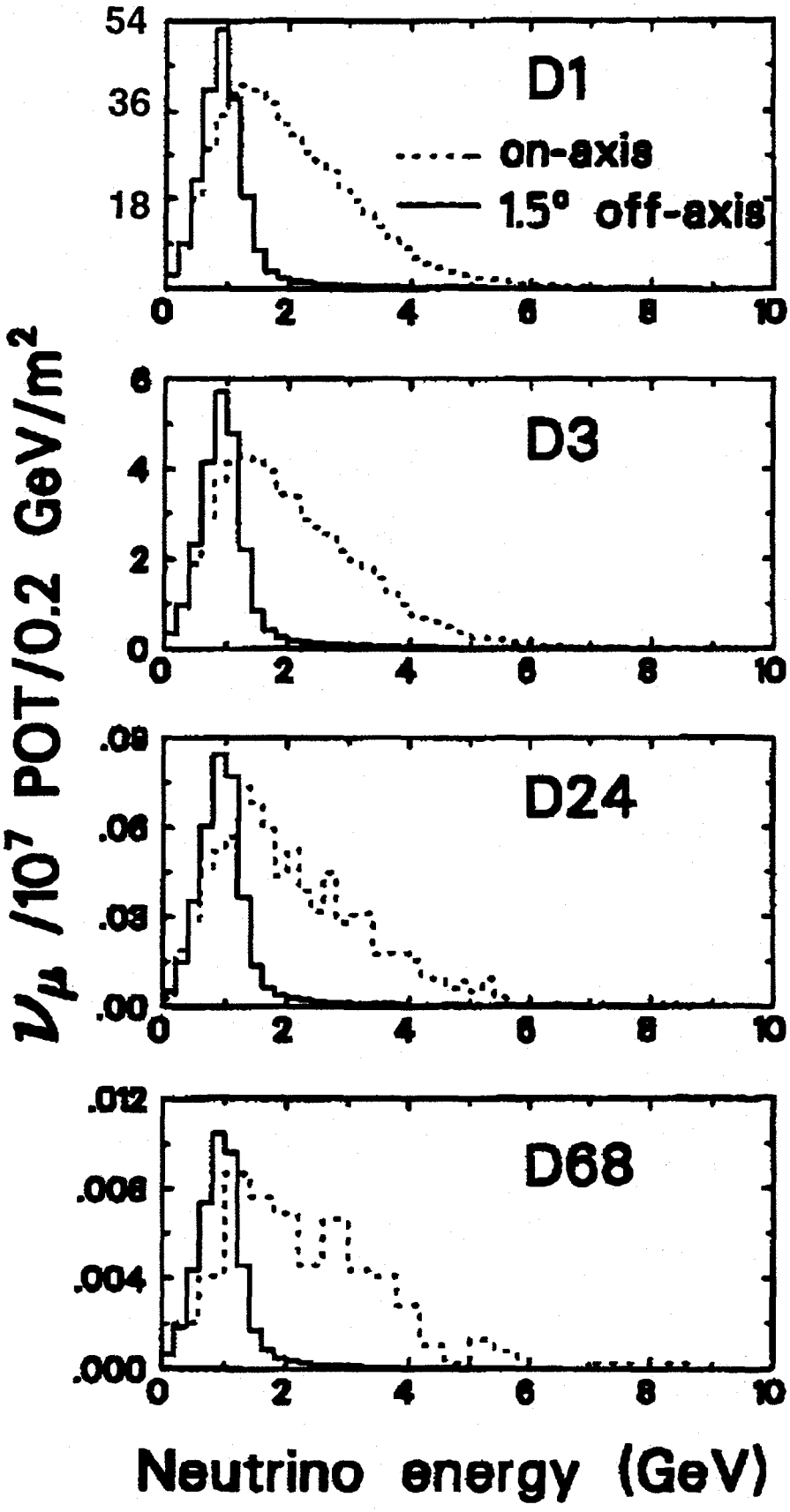


Fig. 3

95-0099a

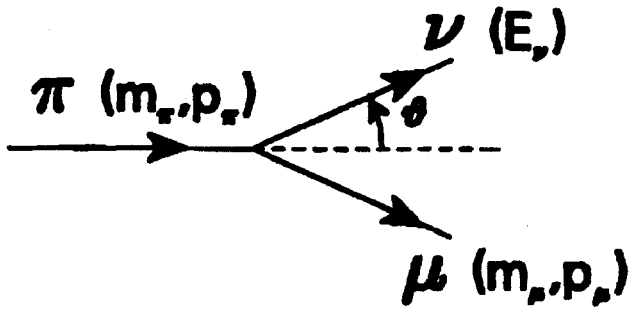


**From energy, momentum conservation**

$$E_\nu = \frac{m_\pi^2 - m_\mu^2}{2(E_\pi - p_\pi \cos\theta)}$$

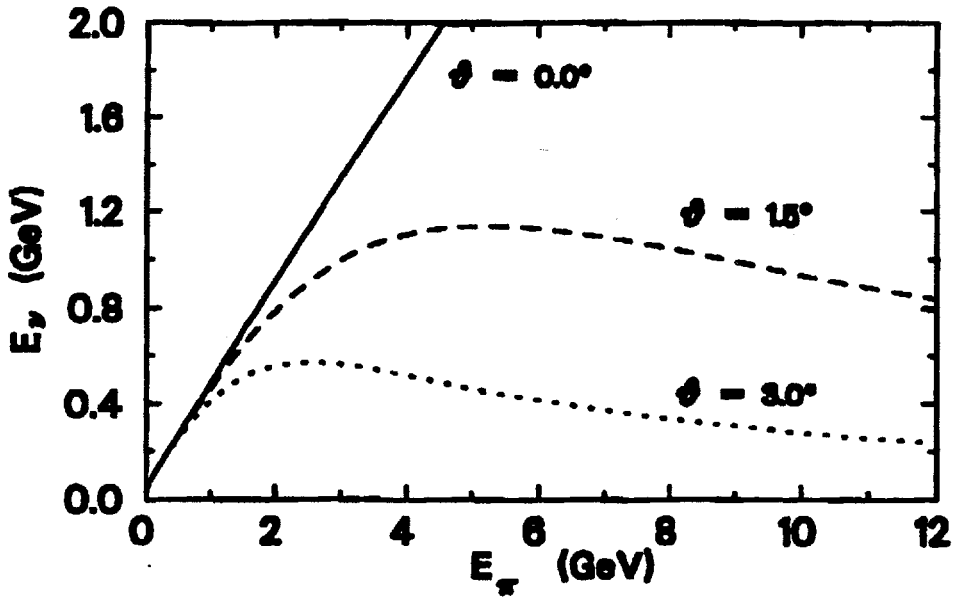


Fig. 4

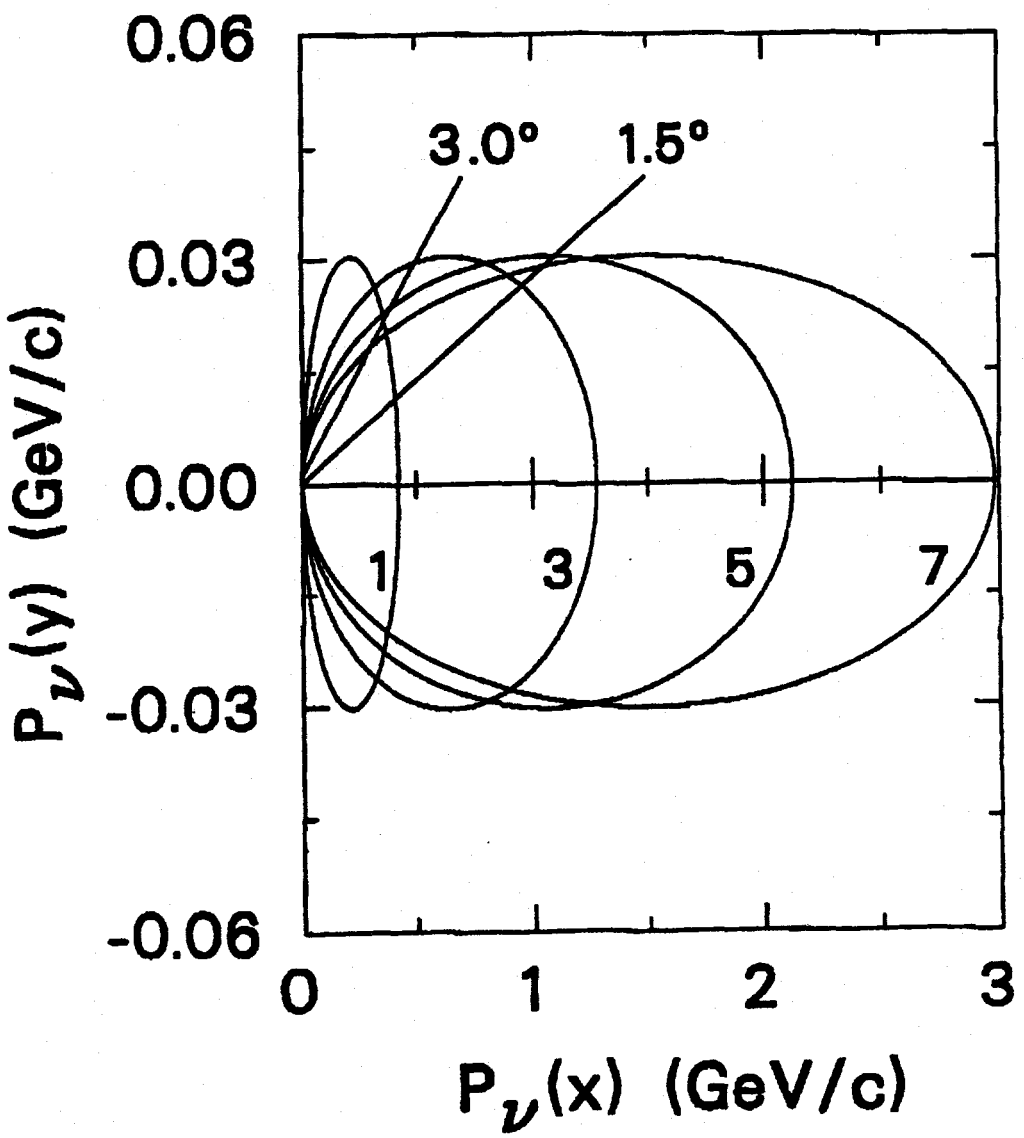


Fig. 5

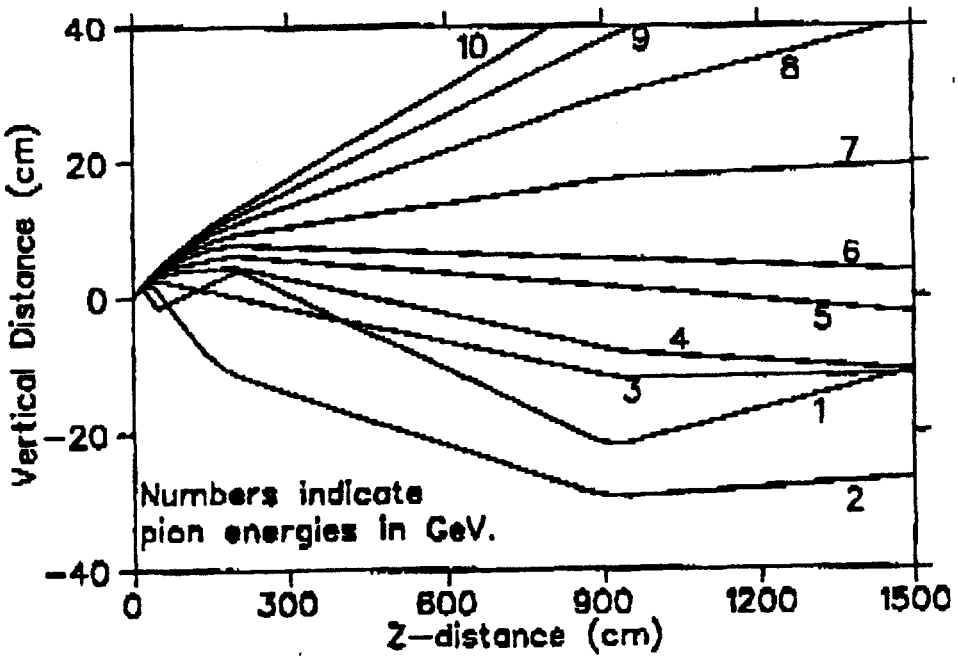
40
20
0
−20
−40
Vertical Distance (cm)
10
9
8
7
6
5
4
3
2
1
Numbers indicate
pion energies in GeV.
0
300
600
900
1200
1500
Z−distance (cm)

Fig. 6

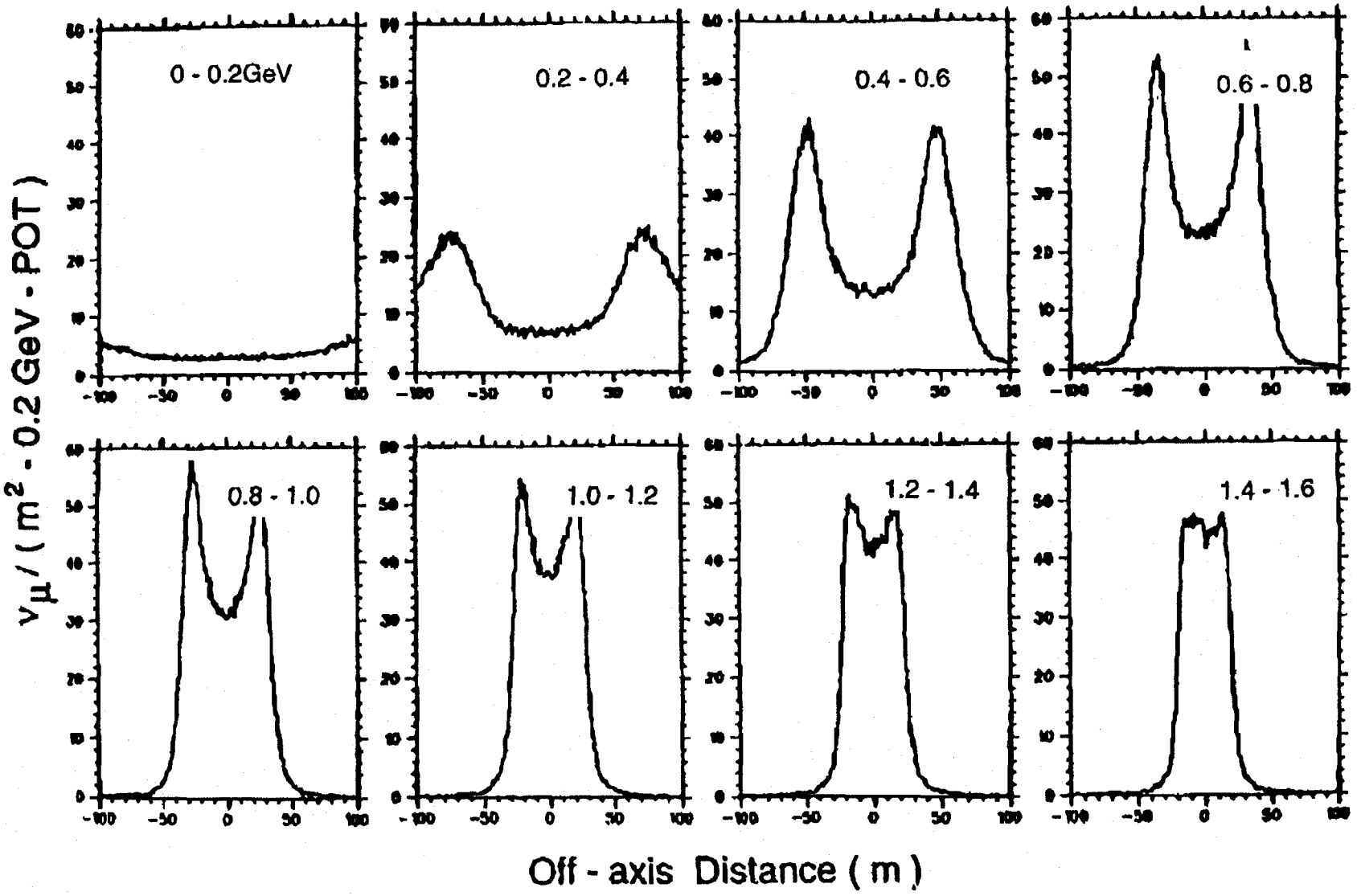


Fig. 7



95-0099d

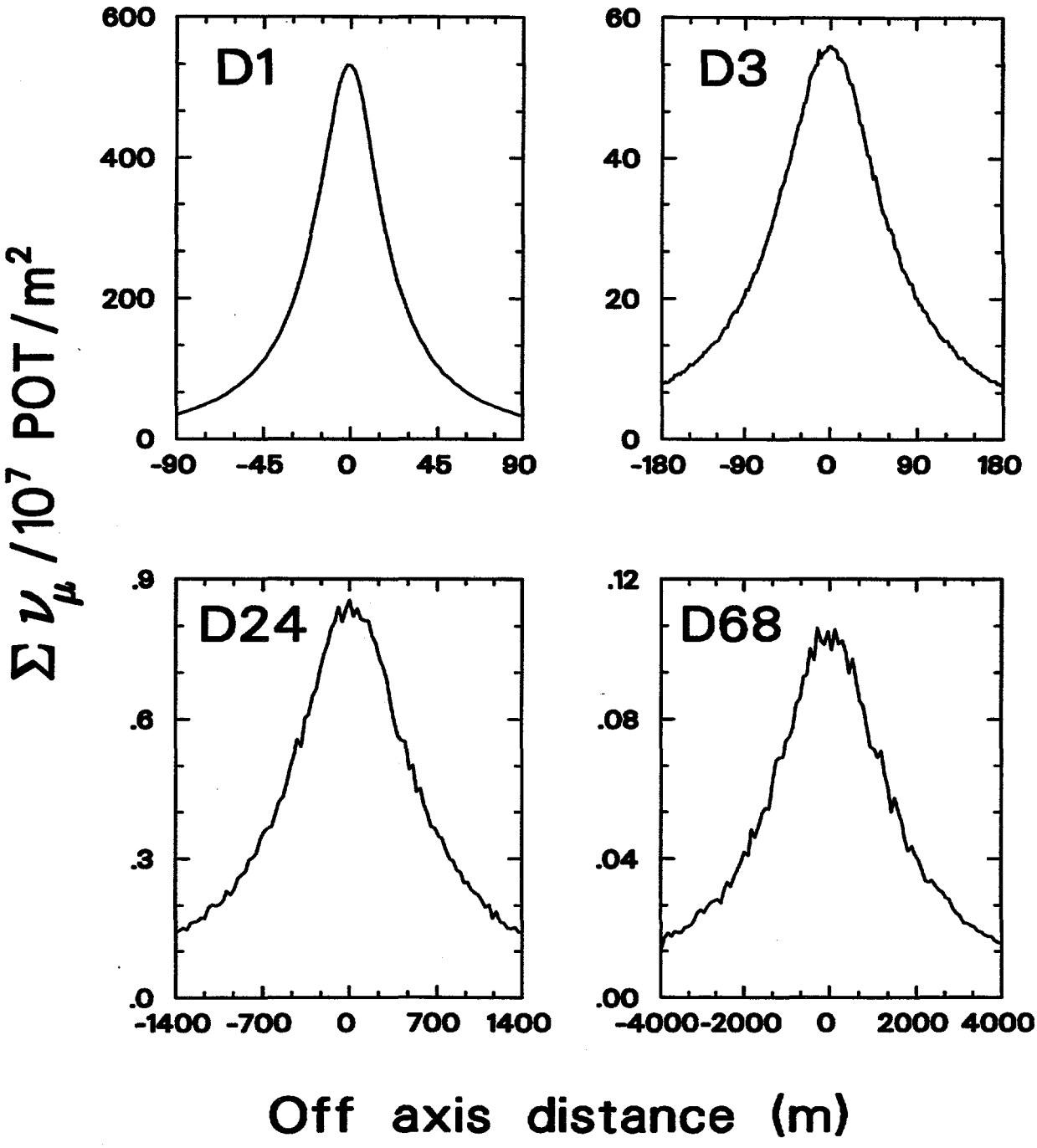
D1
D3
D24
D68
600
400
200
0
60
40
20
0
.9
.6
.3
.0
.12
.08
.04
.00
-90 -45 0 45 90
-180 -90 0 90 180
-1400 -700 0 700 1400
-4000 -2000 0 2000 4000
$\Sigma \nu_\mu / 10^7$ POT / m$^2$
Off axis distance (m)

Figure 8

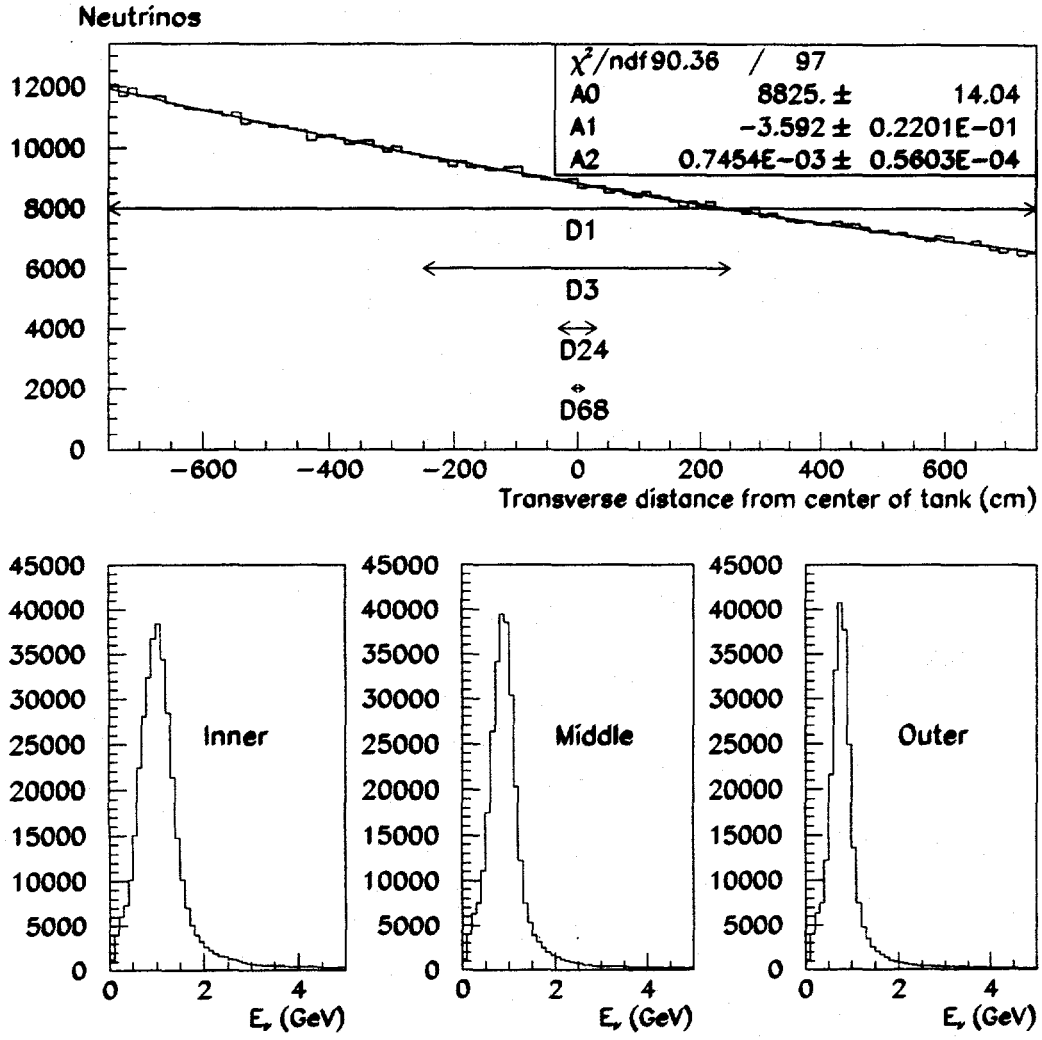
Neutrinos
χ²/ndf 90.36 / 97
A0 8825. ± 14.04
A1 −3.592 ± 0.2201E−01
A2 0.7454E−03 ± 0.5603E−04
D1
D3
D24
D68
Transverse distance from center of tank (cm)
Inner
Middle
Outer
E_ν (GeV)

Fig. 9

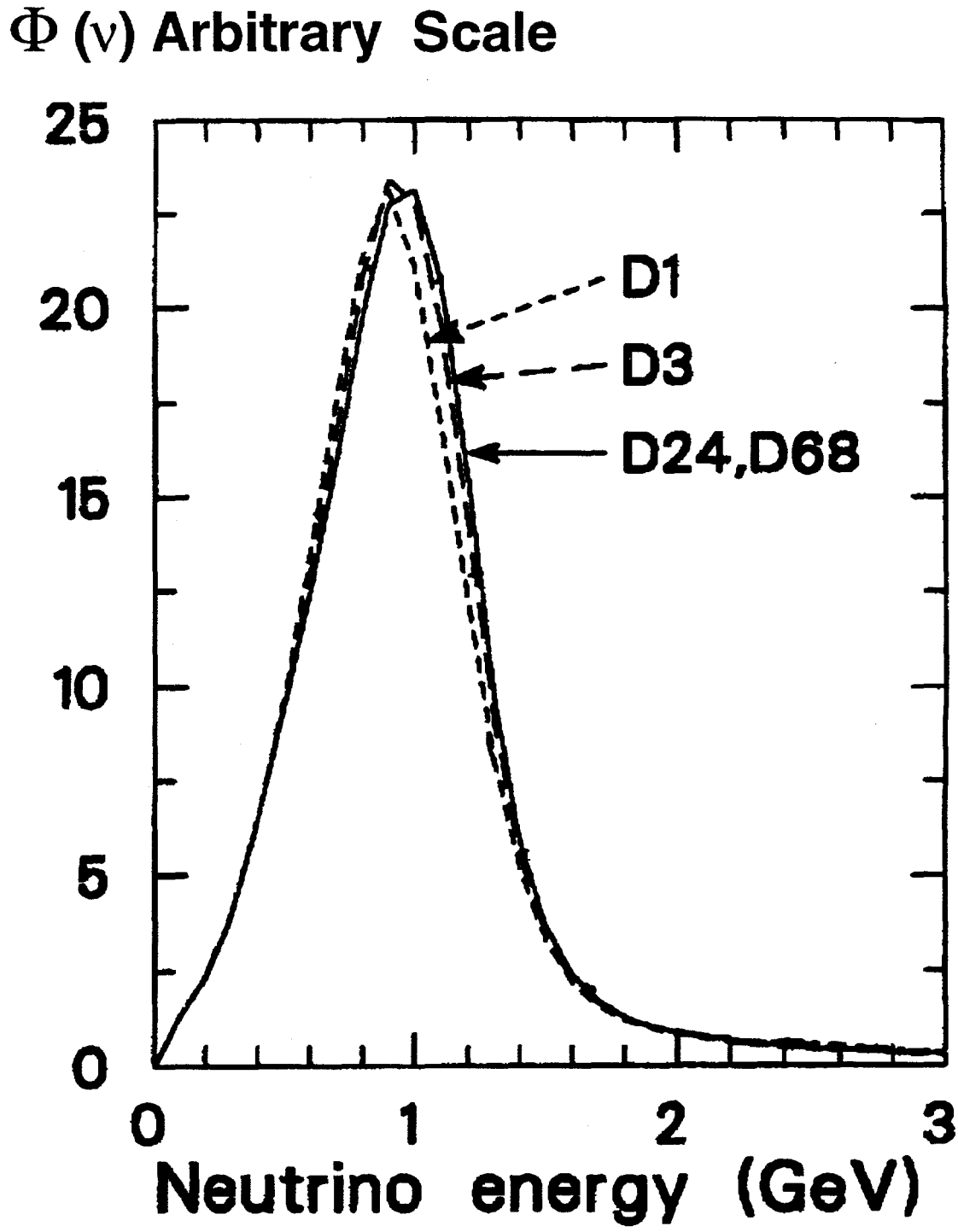


Fig. 10

95-0099c

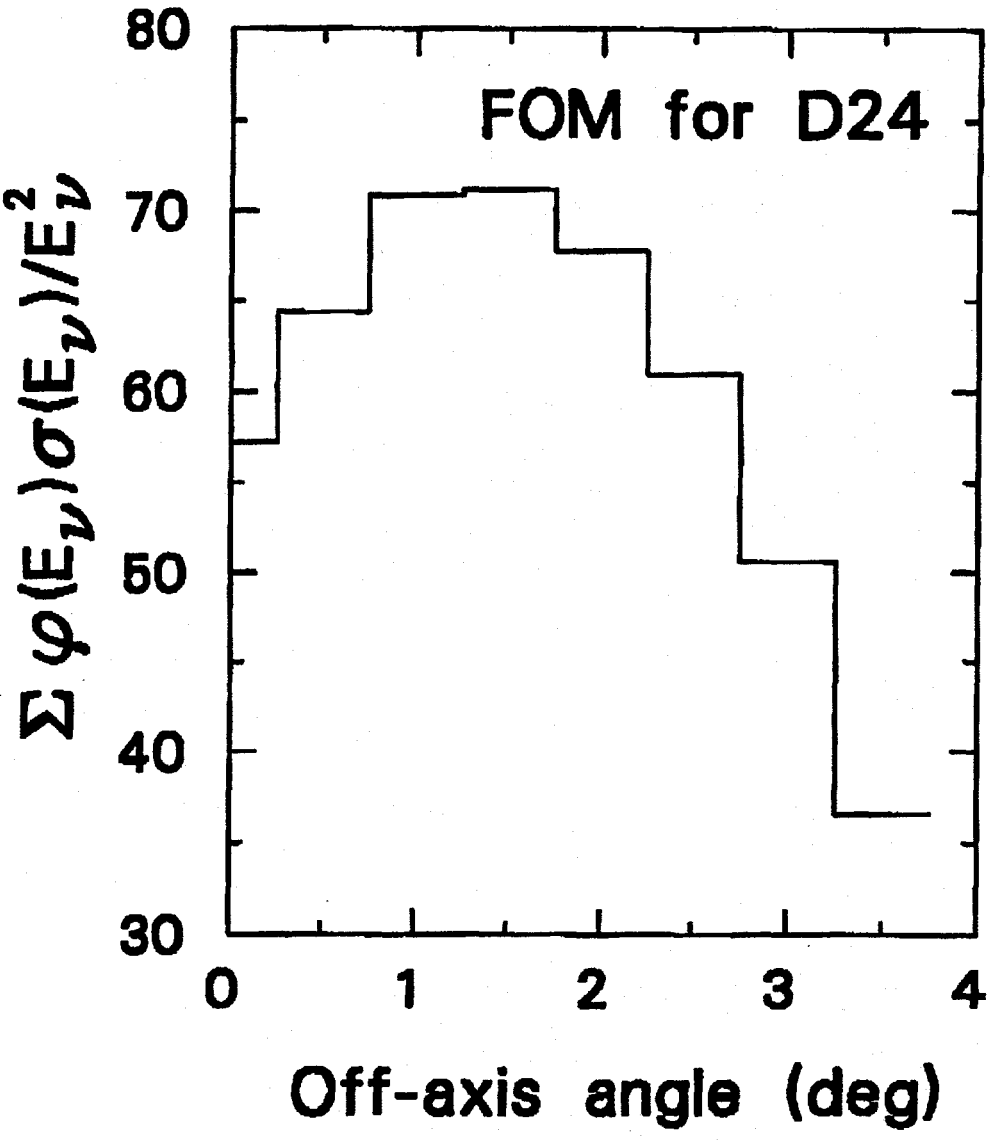
FOM for D24
80
70
60
50
40
30
0
1
2
3
4
$\Sigma \varphi(E_\nu)\sigma(E_\nu)/E_\nu^2$
Off-axis angle (deg)

Fig. 11

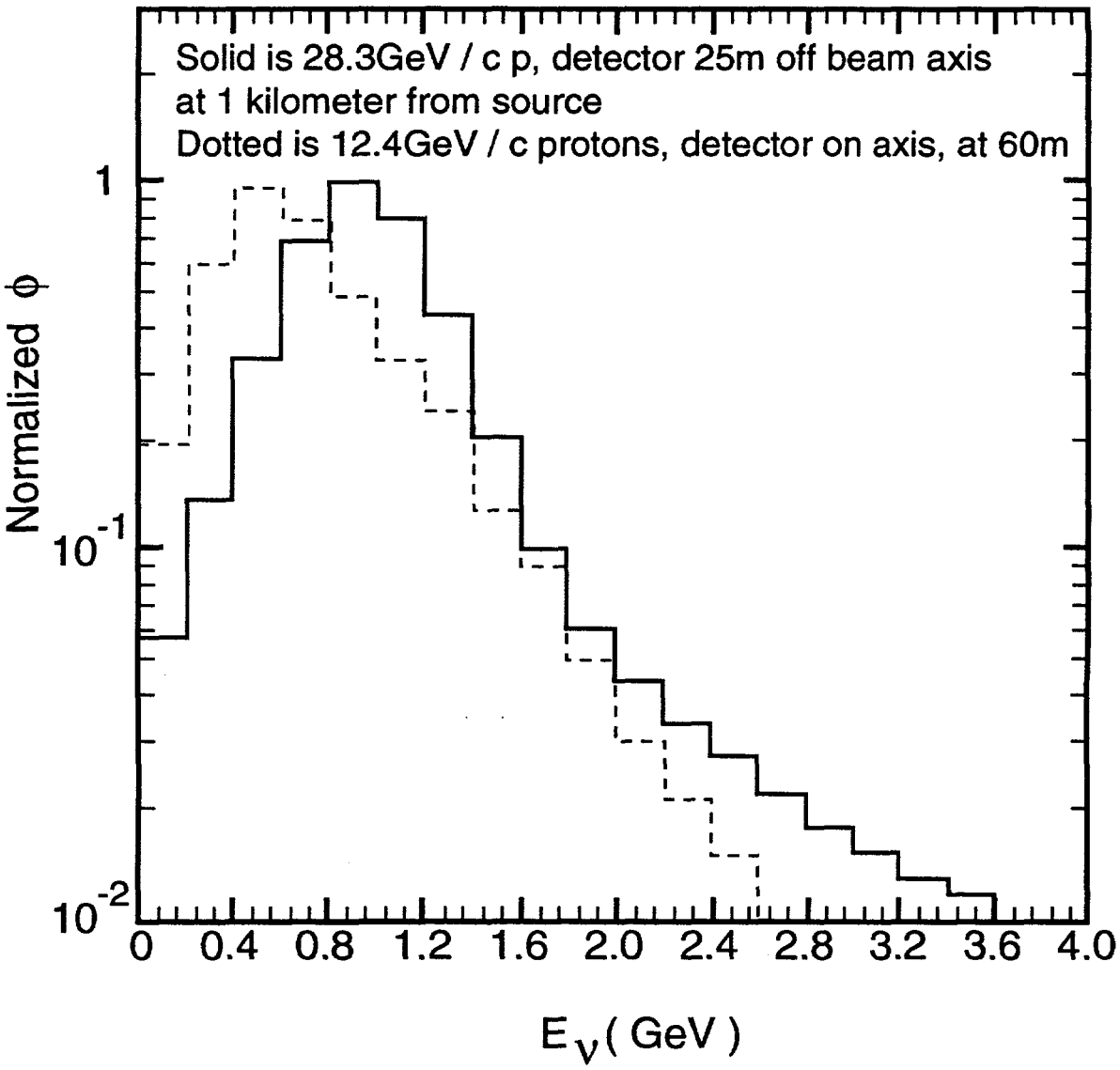
Solid is 28.3GeV / c p, detector 25m off beam axis
at 1 kilometer from source
Dotted is 12.4GeV / c protons, detector on axis, at 60m
Normalized ϕ
1
10^-1
10^-2
0
0.4
0.8
1.2
1.6
2.0
2.4
2.8
3.2
3.6
4.0
E_ν ( GeV )

Fig. 12

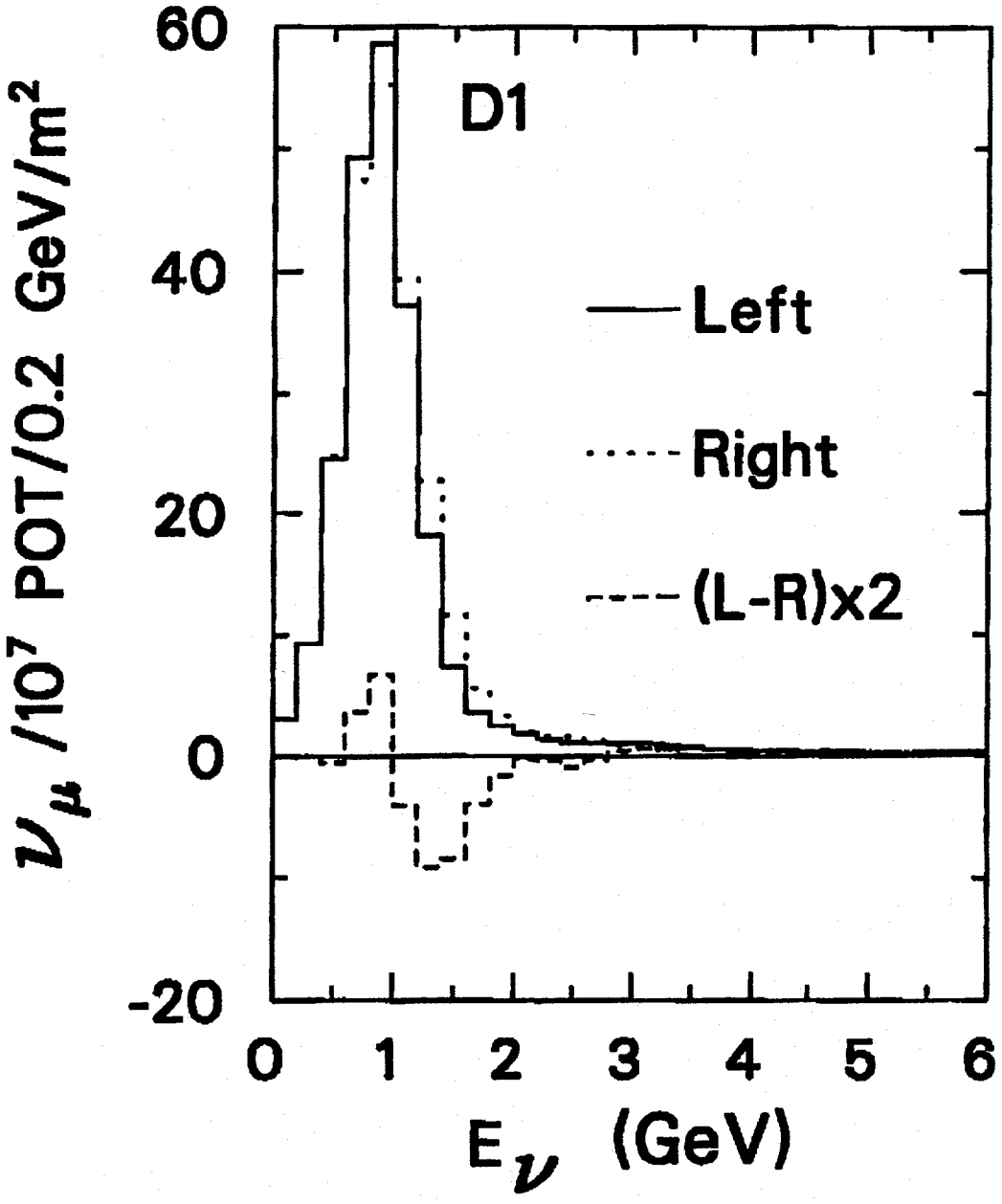
60
40
20
0
-20
D1
Left
Right
(L-R)x2
$\nu_\mu$ /10$^7$ POT/0.2 GeV/m$^2$
0 1 2 3 4 5 6
$E_\nu$ (GeV)

Fig. 13

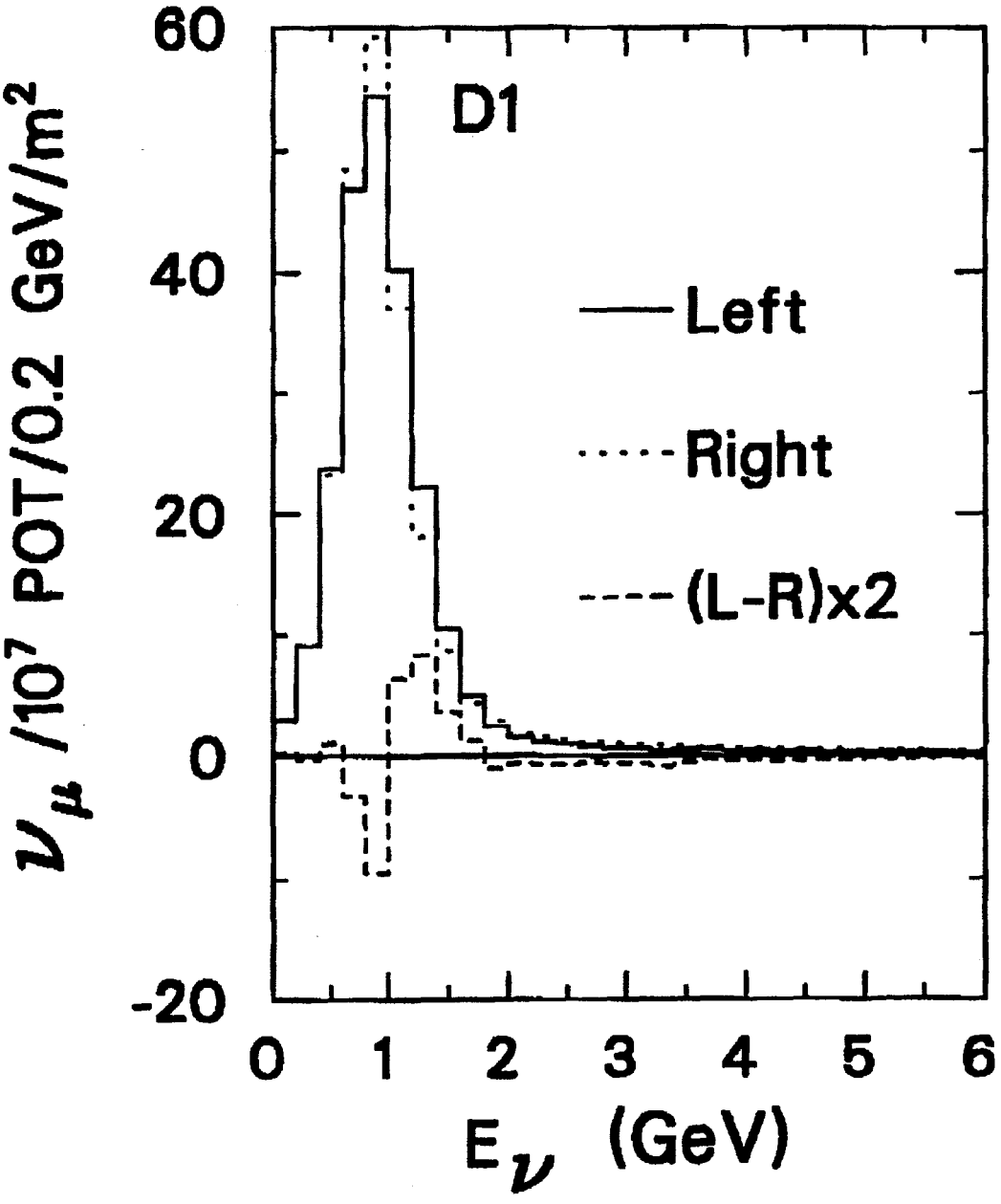
60
40
20
0
-20
D1
Left
Right
(L-R)x2
$\nu_\mu$ /$10^7$ POT/0.2 GeV/$m^2$
0 1 2 3 4 5 6
$E_\nu$ (GeV)

Fig. 14

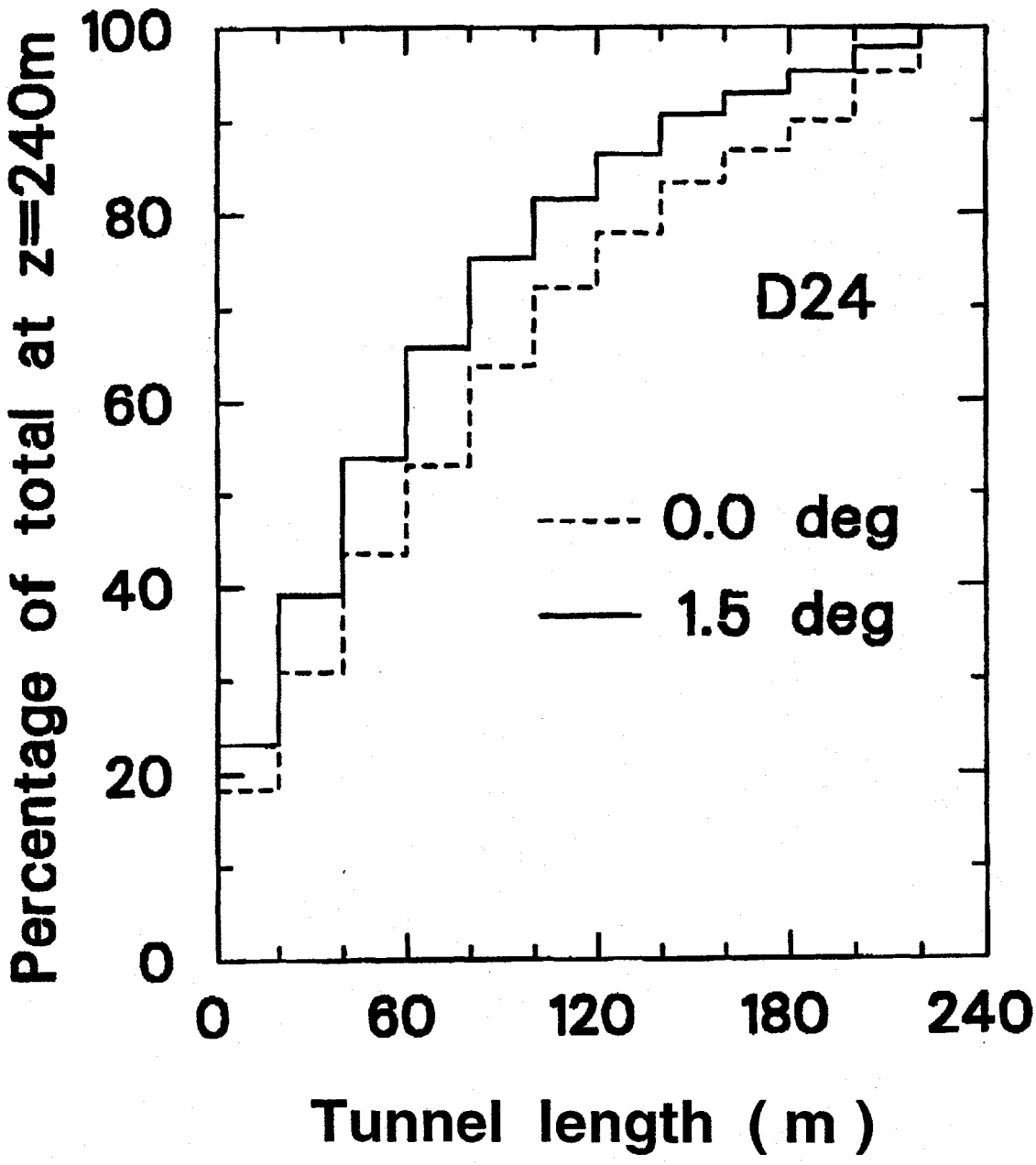
Percentage of total at z=240m
100
80
60
40
20
0
0
60
120
180
240
Tunnel length ( m )
D24
0.0 deg
1.5 deg

Fig. 15

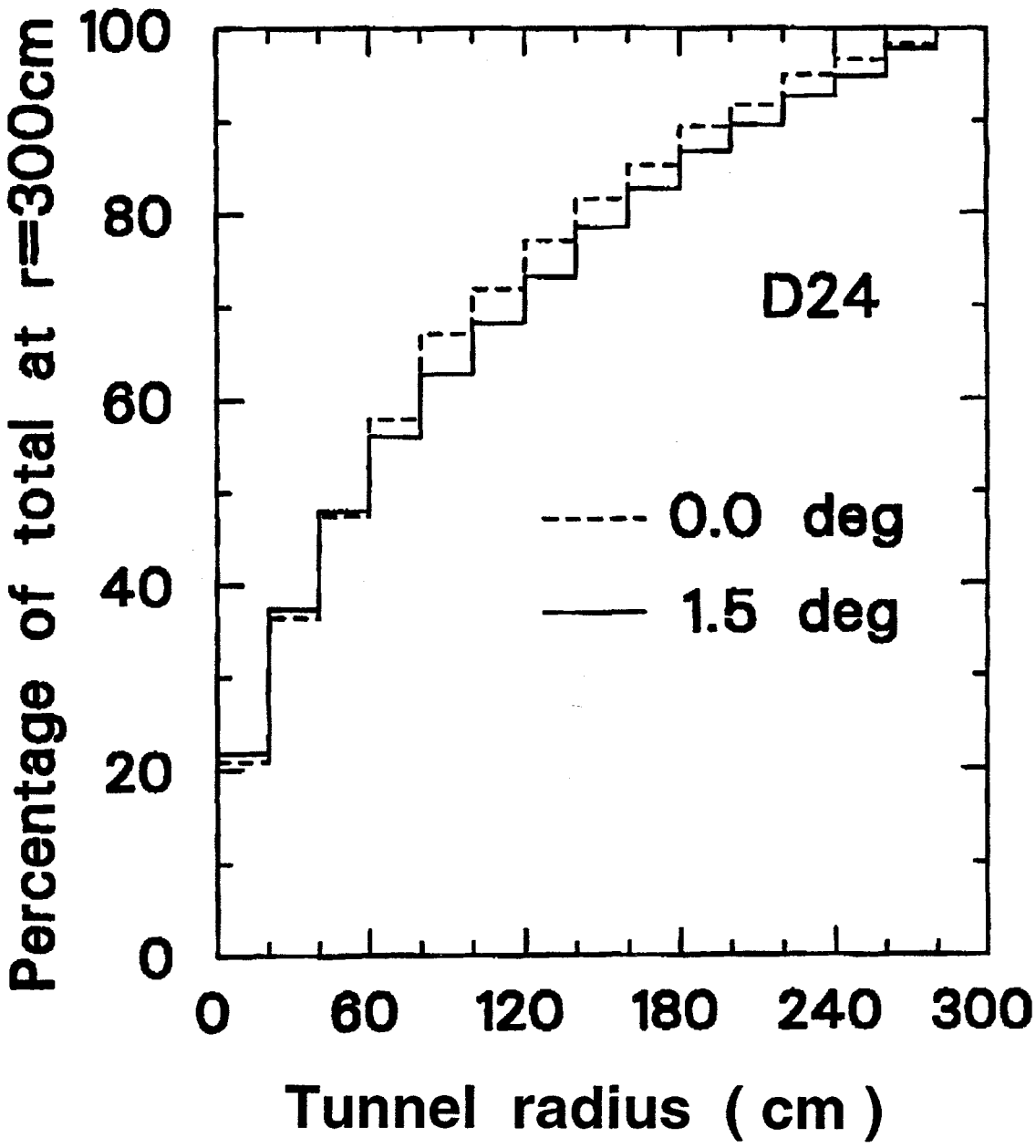
Percentage of total at r=300cm
100
80
60
40
20
0
D24
0.0 deg
1.5 deg
0
60
120
180
240
300
Tunnel radius ( cm )

Fig. 16

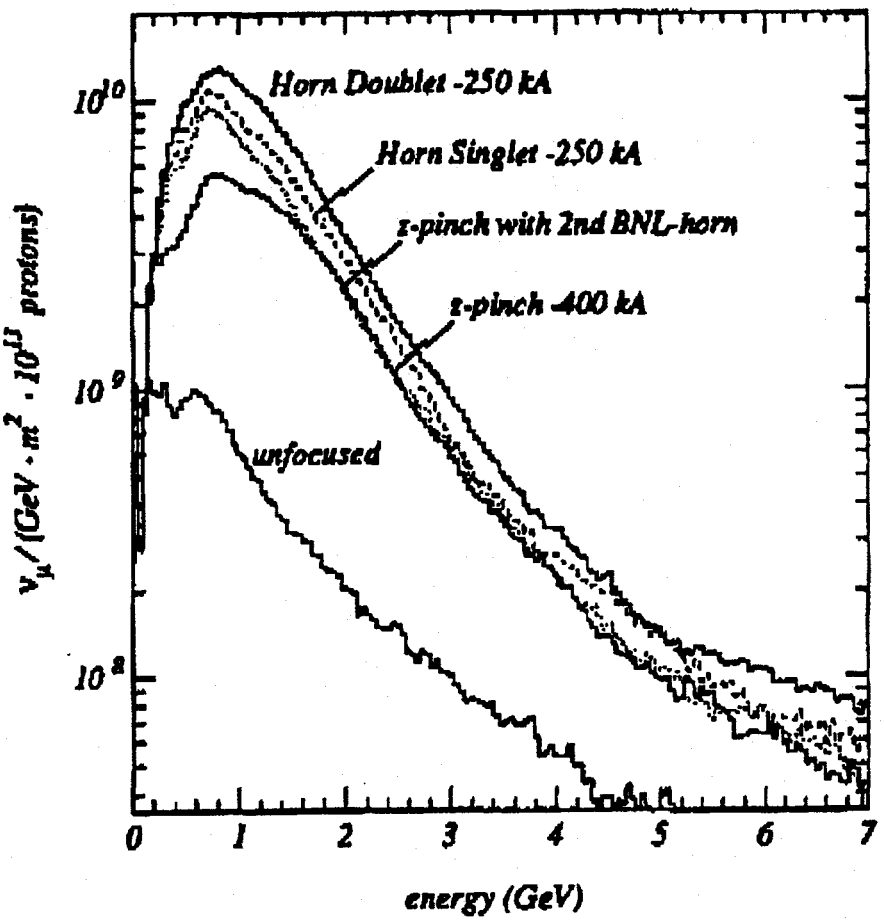
Horn Doublet -250 kA
Horn Singlet -250 kA
z-pinch with 2nd BNL-horn
z-pinch -400 kA
unfocused
$10^{10}$
$10^{9}$
$10^{8}$
$\nu_\mu$/(GeV · m$^2$ · $10^{13}$ protons)
0
1
2
3
4
5
6
7
energy (GeV)

Fig. 17

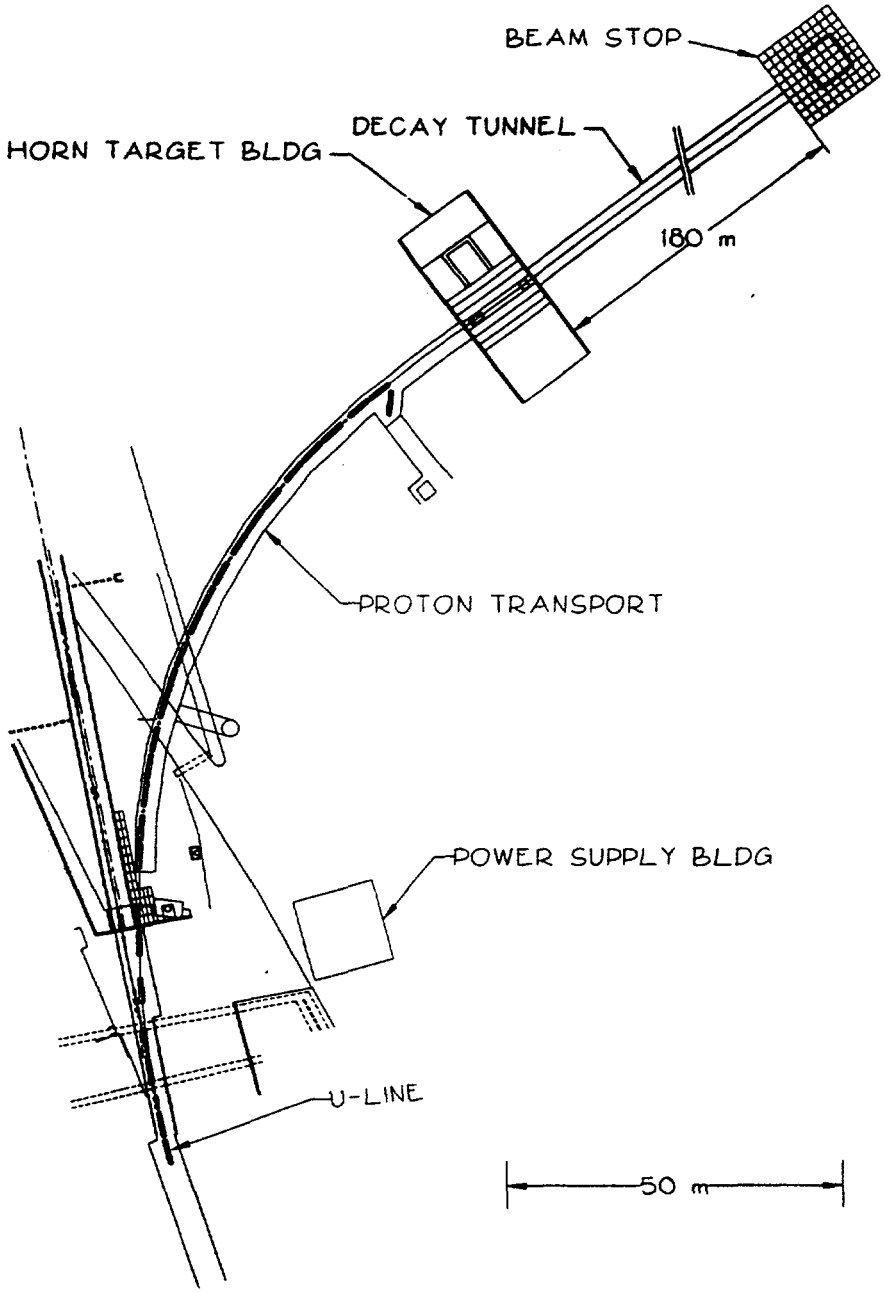
BEAM STOP
DECAY TUNNEL
HORN TARGET BLDG
180 m
PROTON TRANSPORT
POWER SUPPLY BLDG
U-LINE
50 m

Fig. 18

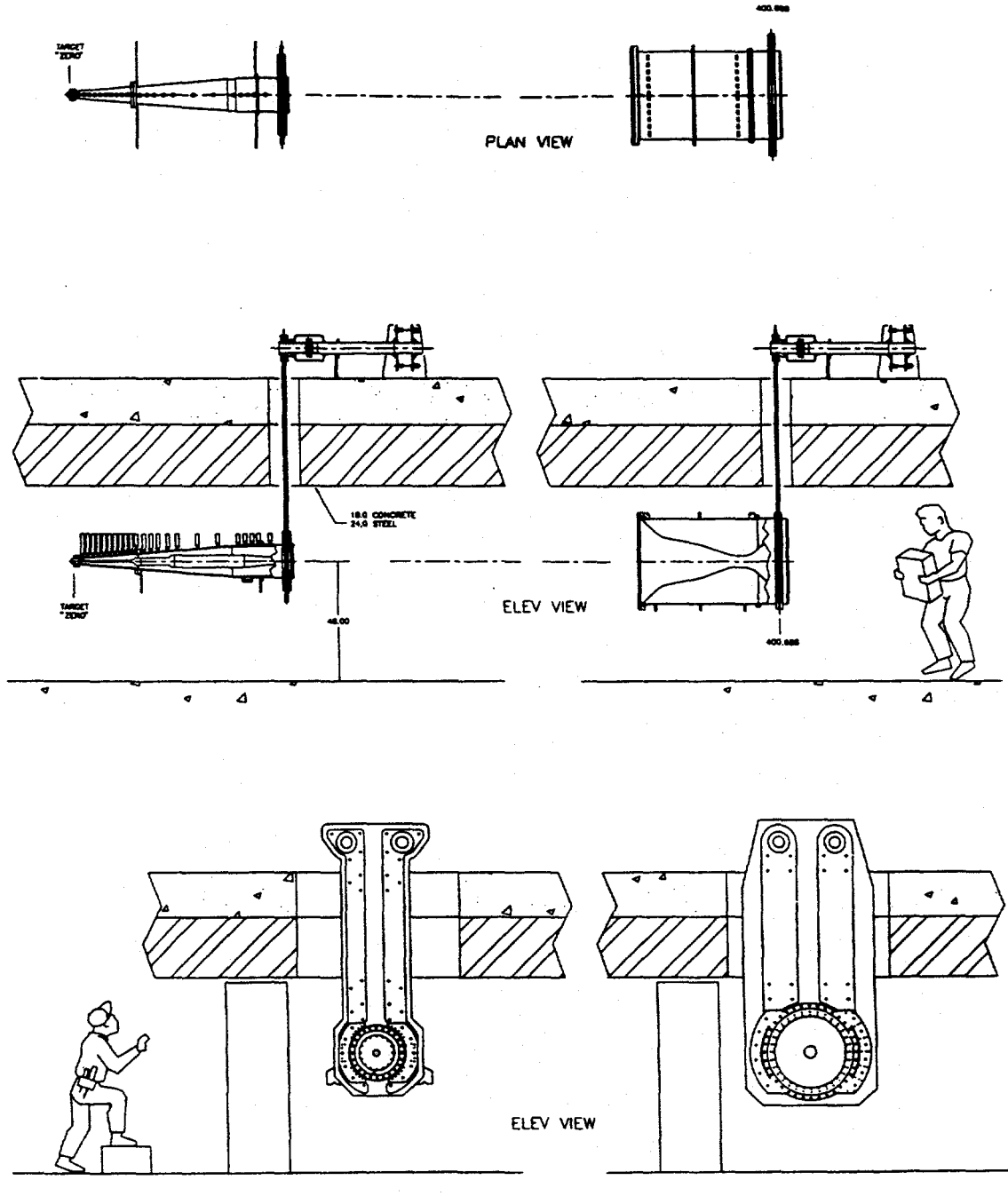


Fig. 19

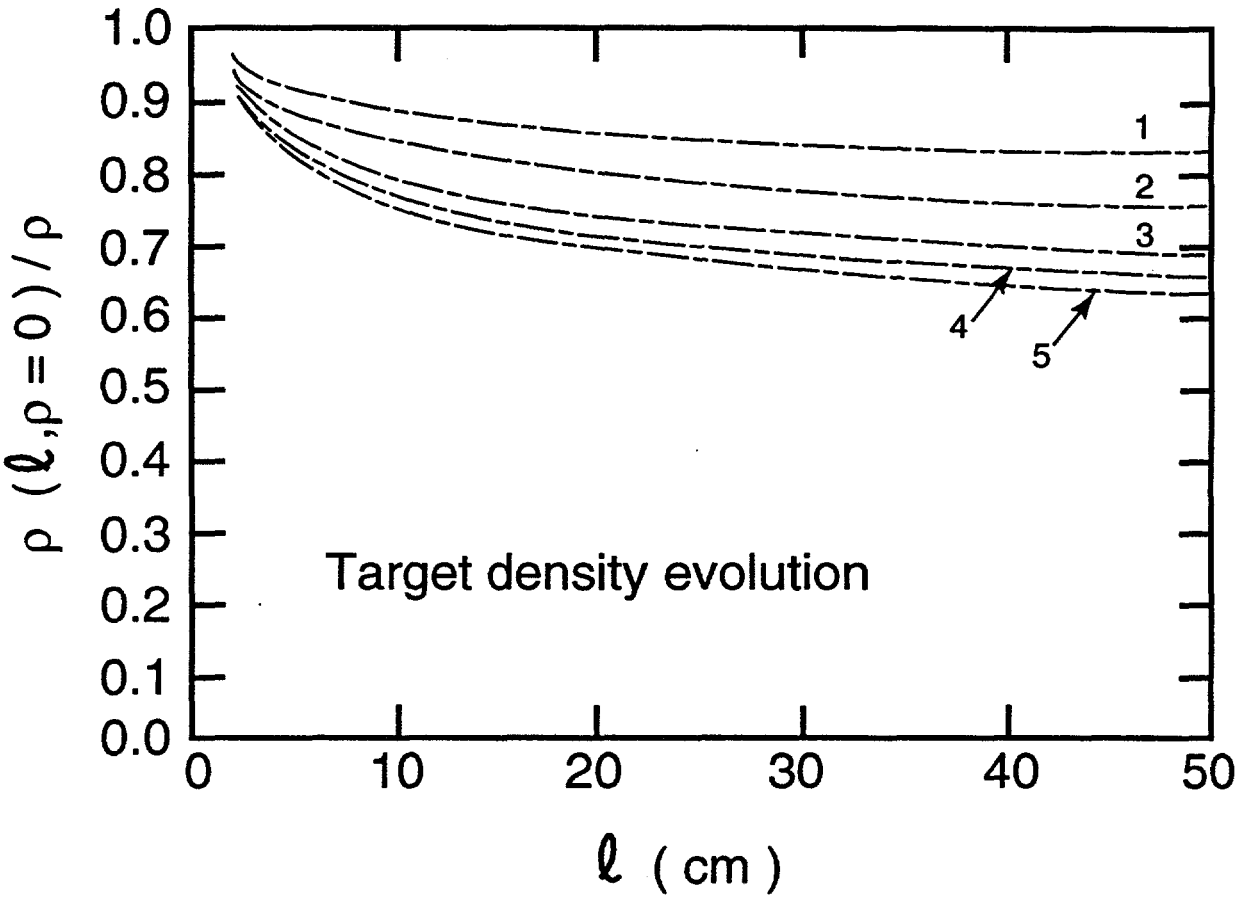
1.0
0.9
0.8
0.7
0.6
0.5
0.4
0.3
0.2
0.1
0.0
ρ (ℓ,ρ = 0) / ρ
0
10
20
30
40
50
ℓ ( cm )
1
2
3
4
5
Target density evolution

Fig. 20

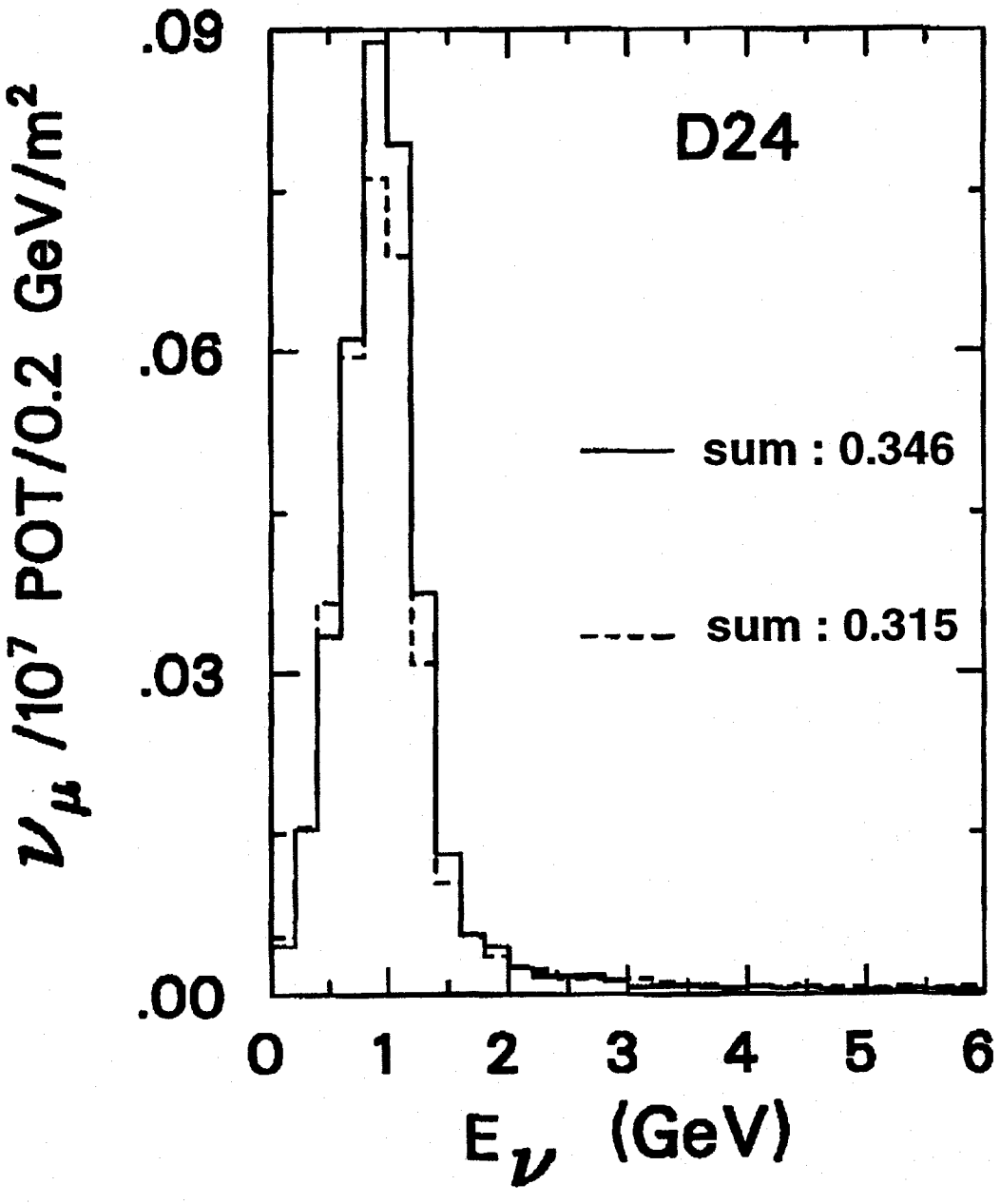
.09
.06
.03
.00
D24
sum : 0.346
sum : 0.315
0
1
2
3
4
5
6
$\nu_\mu$ /10$^7$ POT/0.2 GeV/m$^2$
$E_\nu$ (GeV)

Fig. 21

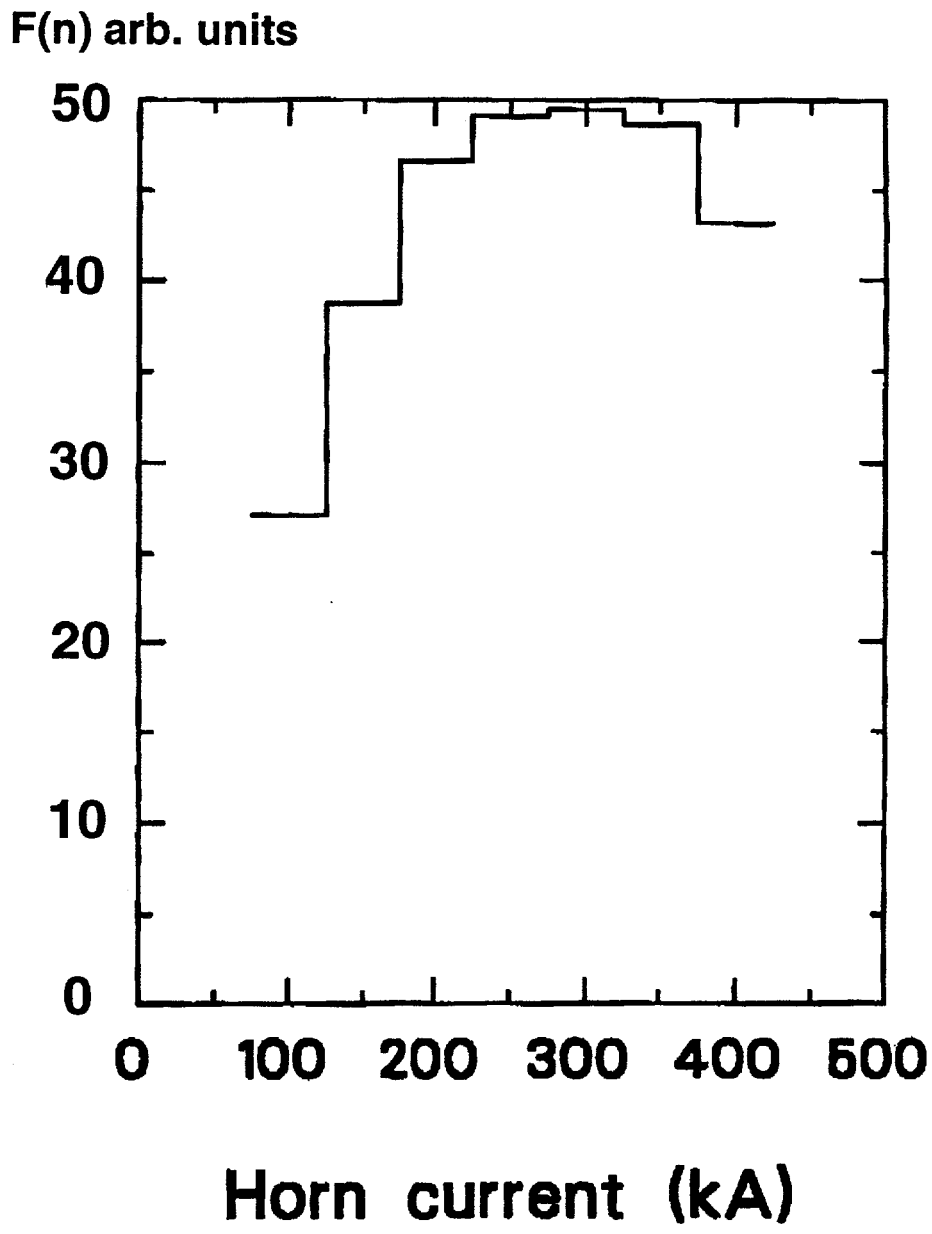


Fig. 22

95-0092u

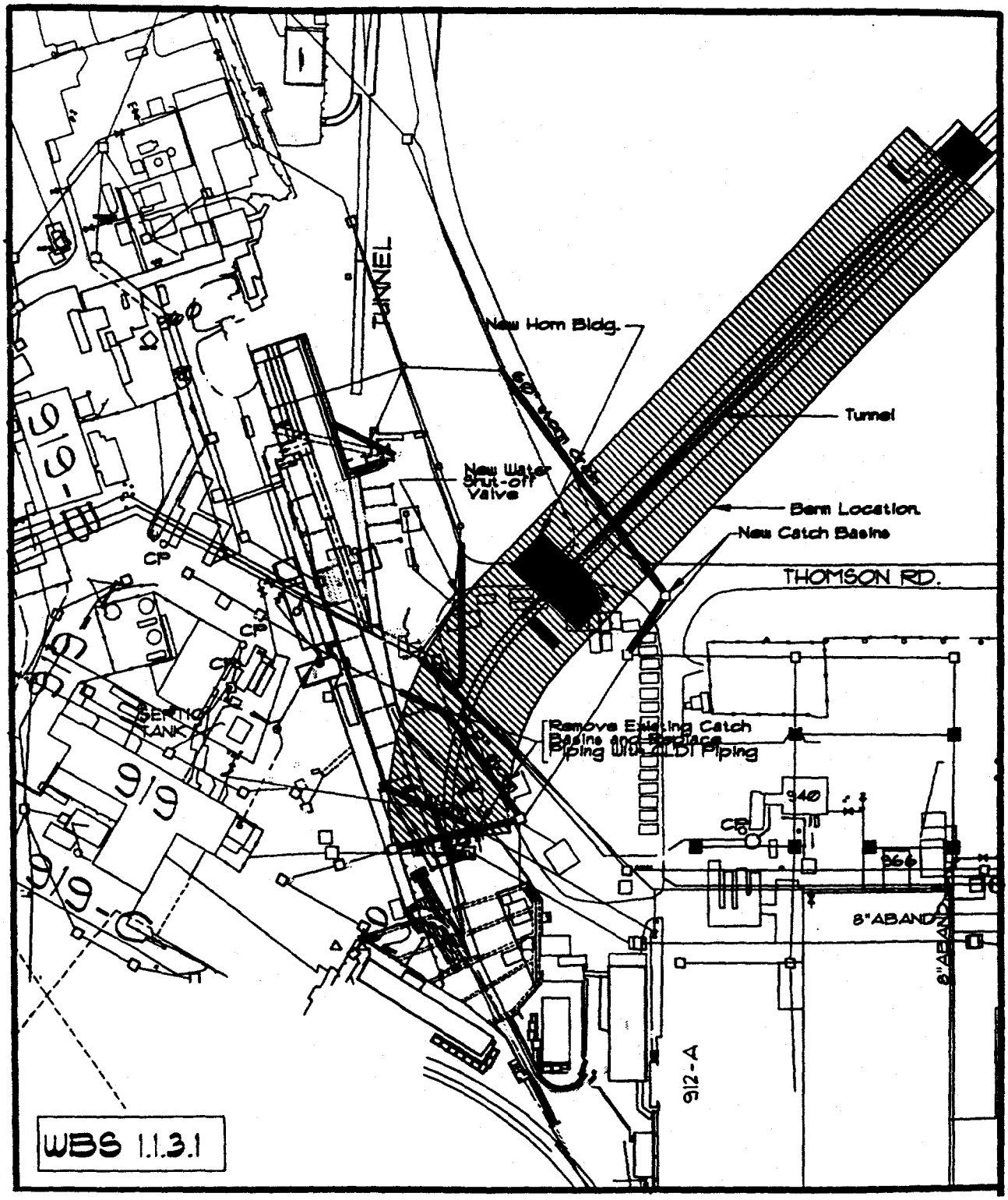
TUNNEL
New Horn Bldg.
Tunnel
New Water Shut-off Valve
Berm Location
New Catch Basins
THOMSON RD.
SEPTIC TANK
Remove Existing Catch Basins and Replace Piping with DIP Piping
940
8"ABAND.
8"ABAND.
912-A
WBS 1.1.3.1

Fig. 23

# Chapter III B. Detector Design and Construction

The experiment will utilize techniques that have been developed for deep underground water Cherenkov detectors during the past decade. There will be four large water tanks located on independent sites ranging from 1 to 68 km from the neutrino source. Each tank will be equipped with a large array of photomultiplier tubes (PMTs) to detect the Cherenkov radiation produced by relativistic particles traversing the water. At each site the signals from the PMTs will be collected, analyzed and time marked for synchronization with the beam and the other detectors. In the first two subsections below the physical layout and installation procedures for the PMTs are described. An outline of the tank construction is given in the next subsection, the water purification system follows, and finally the physical plant at each site is discussed.

## PMT Array

The PMT array must be able to locate the trajectory of single particles accurately in time and space and to identify each particle as a muon, electron or pizero, or to label an event as being due to a multiparticle interaction, and to measure particle momentum. A decade of experience with similar detectors has shown that a dense, regular array of PMTs covering the inner surface of a volume inside the tank can accomplish this purpose [1, 2]. The other critical function is to identify tracks entering or leaving the inner volume, including tracks from the large flux of cosmic rays impinging on the detector. This function is accomplished by a secondary array of PMTs which view an annular volume surrounding the inner volume. Each tank is therefore divided into an inner and outer (veto) volume, with approximately 90% of the PMTs looking inward, and the remainder looking outward, see Fig. 1. The inner volume is 15m in diameter and 15m high. The simulation of the detector response to various neutrino interactions and the reconstruction resolutions are discussed in Chapters IV and V.

To make the coverage as dense as possible in the most cost effective way, it has been decided to use 20cm diameter tubes mounted on a 70cm $\times$ 70cm grid looking inwards, and on an approximately 3m $\times$ 3m grid looking out, see Fig. 2. The effective collection area of each tube is augmented by a hybrid Winston cone mounted on the photocathode. With 2200 tubes facing the inner detector, this combination will provide about 6.5% area coverage from the photocathodes alone, enhanced to 10.4% by the Winston cones.

A number of tubes meet the requirements for the experiment; of particular interest are the R4558 and the R5912, manufactured by Hamamatsu. Both have 20cm diameter hemispherical

photocathodes. The R4558 is identical to the tube used in the SNO detector, except that it is not constructed of low radioactivity glass. A sketch with its dimensions is shown in Fig. 3; the dimensions of the R5912 are similar. The Winston cones will be essentially identical to those used in SNO. A sketch with the cone dimensions is shown in Fig. 4.

The physical layout of the tube bases will also be a copy of the SNO design. However, there will be much larger light levels in the Brookhaven experiment, and timing information is more important than in SNO. Therefore the dynode voltage distribution will be configured in such a way as to provide the best possible timing information. This could help improve track vertex reconstruction for which the accuracy is determined by the spacing of the tubes on the grid and by the timing precision of each tube.

In this regard, the 10 stage box and line dynode structure of the R5912 provides better timing information than the 9 stage venetian blind chain of the R4558. The anode pulse rise time for the R5912 is 3ns and the transit time spread is 2.5ns, compared with 5ns and 3.5ns, respectively, for the R4558. Simulations studies are in progress to answer the question of how critical this timing is. A disadvantage of the R5912 is that its timing and energy response are sensitive to magnetic fields to a large enough extent that it would be necessary to shield these tubes against the earth's magnetic field. The R4558 also shows some sensitivity to magnetic fields, but it is not clear whether shielding would be necessary. A final decision on the choice of tube will be made after further simulation studies, and after a variety of test measurements have been made on each type.

The cable used to transmit the signal, as well as supply the PMT high voltage, is a modified version of 75 ohm RG59 developed for a similar use in the SNO detector. It is a special waterproof variant, designed for long term immersion in water. It has a high density polyethylene outer jacket, and a tinned copper braided shield that is flooded with a polyethylene wax to prevent water wicking along the braid. The braid is wrapped with an aluminum/polypropylene/aluminum laminate which acts as a vapor barrier to withstand long term immersion. The cable is shown in Fig. 5. To facilitate timing of the PMT signals, all cables will be the same length, approximately 60m. In order to bring the cables out of the tank, a feedthrough, complete with O-rings and other fixtures, will be epoxy bonded to each cable as shown in Fig. 6. The cables will be soldered directly, without connectors, to the PMT bases.

Because the tubes will be installed in water at depths up to 18m, it will be necessary to ensure tight waterproofing around the attachment points of the base and cable. This problem has been solved by both SuperKamiokande and SNO. A polyethylene frame is fitted snugly

over the end of the glass bulb of the photomultiplier tube, and a second polyethylene frame then fits snugly over the first, and the combination completely contains the phototube base. The cable is brought out through a port on the second frame. The volume inside the frames is then filled with a suitable insulating epoxy (such as Sanyu Resin SZ-722) to prevent any water from leaking in. The entire assembly is also wrapped with heat shrink polyethylene tubing, mainly for aesthetic purposes. A view of the Kamiokande waterproofing structure, taken from [3], is shown in Fig. 7. E889 will use the SNO variant, which is quite similar.

After the tubes are installed in the tanks, there may be very long periods during which it will be impossible to access them for servicing. Therefore it will be necessary to test each tube for waterproofing, consistency of signal and absence of light leaks, before installation. An automated testing procedure has been developed by SNO, and the cost estimates for E889 include duplicating this system.

## PMT installation

Each phototube will be fitted with a support cradle, shown in Fig. 8, which allows the PMT to be handled, supported and restrained. When the 0.7kg PMT is submerged there is a buoyant force of approximately 3kg that must be counteracted. The basic assembly element is shown in Fig. 9. The PMT and cradle are attached to a square, semirigid sheet of plastic 70cm on a side and 5mm thick. The side facing inwards is absorptive black, and that facing outwards is reflective. One eighth of these units have two PMTs mounted on them, one facing in and the other out. Note that the full unit consists of PMT, plastic sheet, and 60m of cable; the latter is strain relieved directly on the sheet.

Several schemes for installing the array of PMTs have been investigated. Since this is an above ground installation, we are convinced that the appropriate time to do the installation is before the tank is filled with water. This procedure will require access to the bottom of the tank, and limited access inside the tank above the level of the full array (16.5m above the bottom). To accomplish the latter we have provided for a cat walk above this level, accessible from outside the tank.

There are still two distinct support structures which can accomplish our needs. These are a rigid structure supported from the bottom and stabilized from the sides of the tank, or a flexible cable array hung from the tank roof or catwalk. Each of these schemes offers advantages and disadvantages, and the final decision will require both prototyping and careful value engineering to evaluate cost and schedule issues. In either case the top and bottom

arrays are the same. A light framework, suspended from above, allows the PMT/sheet/cable units to be attached working from the floor of the tank. When the top array is complete, it is raised and suspended well above its final position, allowing work on the side arrays to proceed. When the sides are finished, the top array is moved into its final position and secured. At this time the bottom array is mounted on a similar framework already positioned in its final location, just 1.5m from the tank floor.

The side arrays are mounted either to a rigid, but lightweight, stainless steel framework, or to an array of stainless steel cables suspended from the tank roof or catwalk. A mobile boom is used to attach the PMT units to the structure. This unit has a cradle which can support two people. PMT units are independently delivered to the boom to obviate the need for large motions. They are attached starting at the top of the array and working downwards, to avoid working above (and possibly damaging) installed units, as shown in Fig. 10. The tanks are in fact large enough to permit two booms to work in parallel. An attractive variant of the cable support scheme would allow the PMT units to be attached to a pair of cables at ground level. The cables would then be raised either from hoists located on the catwalk, or from ground level hoists working through pulleys on the catwalk, as shown in Fig. 11. While this scheme has many attractive features, it does require more work at the catwalk level to secure completed PMT rows, and to position the hoist system.

As the PMT units are installed, the cables are immediately routed and secured. The cables are brought to an area at the bottom of the tank close to the electronics location outside the tanks, and the feedthroughs already on the cable are passed through special panels, the cables are secured for strain relief, and the feedthrough assembly is completed and leak checked.

When the sides and bottom array are complete, the installation equipment can be removed. At this point the installation process is complete and the tank can be cleaned, secured and filled.

## Detector Sites and Construction

The site preparation and detector construction is similar at all sites. Minor differences are typically associated with the availability of existing utilities and roads. A brief description of the site preparation, tank construction, and support buildings will be given below ignoring the minor differences. An artists conception of a detector site is shown in Fig. 12.

Land improvements are necessary before the contractor can begin the water tank con-

struction. Engineering tests on the soil will be conducted to determine its load bearing capability, needed for final engineering of the tank ring wall. Approximately an acre of land will be cleared around each tank location to provide a substantial area for construction. The entire area will be cleared of trees, grubbed, and graded. An access road will be built to allow all weather access to the detector site by car. These improvements are expected to be completed during the six months required for the tank contractor to obtain the steel.

An elevation view of a detector tank is shown in Fig. 13. The tank will be of conventional construction consisting of welded steel plates. It has been designed to allow for access and PMT installation at both the top and bottom of the tank; when the installation scheme is finalized any unnecessary options will be eliminated to reduce costs. Each tank will be 18m in diameter and 18m high with a domed steel roof and cat walk at the top. Two bolted doors are located at the bottom of the tank. A 6ft $\times$ 8ft door is provided for equipment access. The opening size has been matched to the requirement of using a telescoping boom inside the tank for PMT installation. A 3ft $\times$ 3ft port has been added for additional personnel access/egress. Above the water level of 18m is a large access door with a platform. This door will be accessible from the utility tower, discussed later. The door provides access to the interior, 1.5m wide, catwalk. The tank structure is designed to support a load of 15 tons evenly distributed on the inner edge of the catwalk. A ventilation and lighting system are provided for access into the top of the tank. A second smaller port with a caged staircase is provided as an alternate means of emergency egress from the catwalk. The interior surface of the tank will have a durable epoxy coating suitable for potable water systems. The roof and walls of the tanks will be insulated to a R-10 value to reduce heat transfer from the water to the air. It is expected that the contractor will need approximately three months at a detector location to complete the water tank.

The utility tower and support building will be built after the water tank is complete. A plan view of the water tank, utility tower, and support building is shown in Fig. 14. The utility tower is the central portion of the building structure and is more evident in the elevation view shown in Fig. 15. It provides access to the interior tank catwalk by a set of platform stairs. An option for a small elevator is included but will be eliminated if all tubes are installed from the bottom of the tank. A utility area will house water pipes and control cables which are routed from the mechanical equipment room to the top of the tank. In addition, this area can be used to route signal cables from the PMTs at the top surface of the detector to the electronics room. All cables from the PMTs to the electronics are the same length but follow routes of different length. The excess cable will be stored in cable trays

within the tower. The functions of the utility tower can be achieved with other designs, and is unnecessary if the installation scheme does not require access to the top of the tank. The utility tower was conceived as a convenient centralized solution to tank access, cable routing, and plumbing needs.

The electronics room and office space are on the right hand side of the tower as depicted in Fig. 14. Once the experiment is operational, it is expected that preliminary data analysis and monitoring will occur primarily from the Brookhaven Physics Department. Therefore, only a modest office area for terminals or work stations is provided at the detector site. The electronics area has been sized to accommodate the expected electronics layout with some allowance for expansion. The electronics room and office area will have climate controls. The electronics will be protected from cooling failures with a temperature activated power shutoff. Appropriate alarms for smoke, fire and burglary are included in the building design. In addition, the electronics room will have a fire suppression system.

## Water Filtration

Each tank will be filled with approximately 5 kilotons of water, which must be pure to achieve a long mean free path for Cherenkov light. Contaminants such as ions, organics and bacteria must be excluded as much as possible, and this purity must be maintained on a continuous basis. A filtration system has been designed to meet these criteria. It will be located in the mechanical equipment room on the left hand side of the utility tower.

The filtration system has fast and slow circulation components. A simplified schematic of the system is shown in Fig. 16. The fast circulation system will operate at 83 GPM, requiring 10 days to filter the volume. This system will use an ultraviolet lamp to kill bacteria and a final filter stage of 0.2 microns to remove bacterial fragments. The slow circulation system will have a flow capacity of 33 GPM. A prefilter stage will consist of activated carbon and mixed resin beds for deionization. This is followed by 5 micron and 1 micron filters. The water is further purified by filters with an absolute pore size of 0.5 microns. These absolute rated filters are guaranteed to remove bacteria and therefore an UV system is not employed in this part of the system. A final filter stage containing 0.2 micron filters will remove any potential debris generated by the previous stage and also provide redundancy. Monitors and controls are included in the system.

A reverse osmosis system was considered but rejected due to the large waste water stream generated (10%).

A heat exchanger, chiller, and oil fired heater have been added to the basic filtration system to maintain the water temperature at 10°C with a 5°C tolerance. This temperature was chosen to suppress bacterial growth in the water and decrease phototube noise. The capacity of the system has been matched to the R-10 insulation of the water tank and the expected weather extremes. Area heaters are placed about the equipment room to protect the plumbing from freezing. An emergency generator will supply sufficient power to maintain water circulation, and to run the oil burner and other critical systems, in the event of a power failure.

## Tank Construction Schedule

The installation of utilities at the detector site will be closely coordinated with the site construction. The water supply system will be sufficiently complete so as to provide a source of water for testing the tank for leaks. The flow capacity is sufficient to fill the tank in a reasonable time period, although the initial filling using purified water will require at least one month since the slow circulation system will be used. Completion of the water supply system will be coordinated with the support building construction. AC line power is not required for tank construction, but is needed at the site immediately before construction of the support building. An isolation transformer will provide "clean" power for the experiment's electronics and computers preventing unwanted noise from the mechanical equipment.

The experiment will be given a phased beneficial occupancy of the detector site. Upon completion of the water tank, the experiment will have access to the interior to begin installation of the PMT supporting structure. The utility tower and support building will require approximately six months to complete. However, the utility tower and cable trays will be readied at the earliest possible date to allow the experiment to begin installation of the PMTs onto the support structure, including routing cables into the utility tower. This phased occupancy will be carefully coordinated with the contractor enabling the experiment to begin installation without interfering with a timely completion of site construction.

## References


[1] K. S. Hirata et al., Phys. Lett. **B205** (1988) 416 and Phys. Lett. **B280** (1992) 146.

[2] R. Becker-Szendy et al., Phys. Rev. Lett. **69** (1992) 1010.

[3] A. Suzuki et al., Nucl. Inst. Meth. **A329** (1993) 299.

## Figure captions

Fig. 1. Detector station cross section.

Fig. 2. Arrangement of photomultiplier tubes within the tank.

Fig. 3. Physical dimensions of Hamamatsu R4558 PMT.

Fig. 4. Physical dimensions of the Winston cones.

Fig. 5. Cross section of Belden YR29304 cable.

Fig. 6. Cable feedthrough details.

Fig. 7. Details of the Super-Kamiokande PMT housing assembly (from [3]).

Fig. 8. Support structure for PMT and cable.

Fig. 9. Basic unit for PMT mounting.

Fig. 10. View of the installation procedure, including the mobile crane.

Fig. 11. Two methods for lifting the PMTs into position.

Fig. 12. Conceptual view of a detector site.

Fig. 13. Elevation view of a detector tank, including some details.

Fig. 14. Ground floor plan view of a detector site.

Fig. 15. Cross sectional view of a detector station, including the utility tower.

Fig. 16. The water purification system.

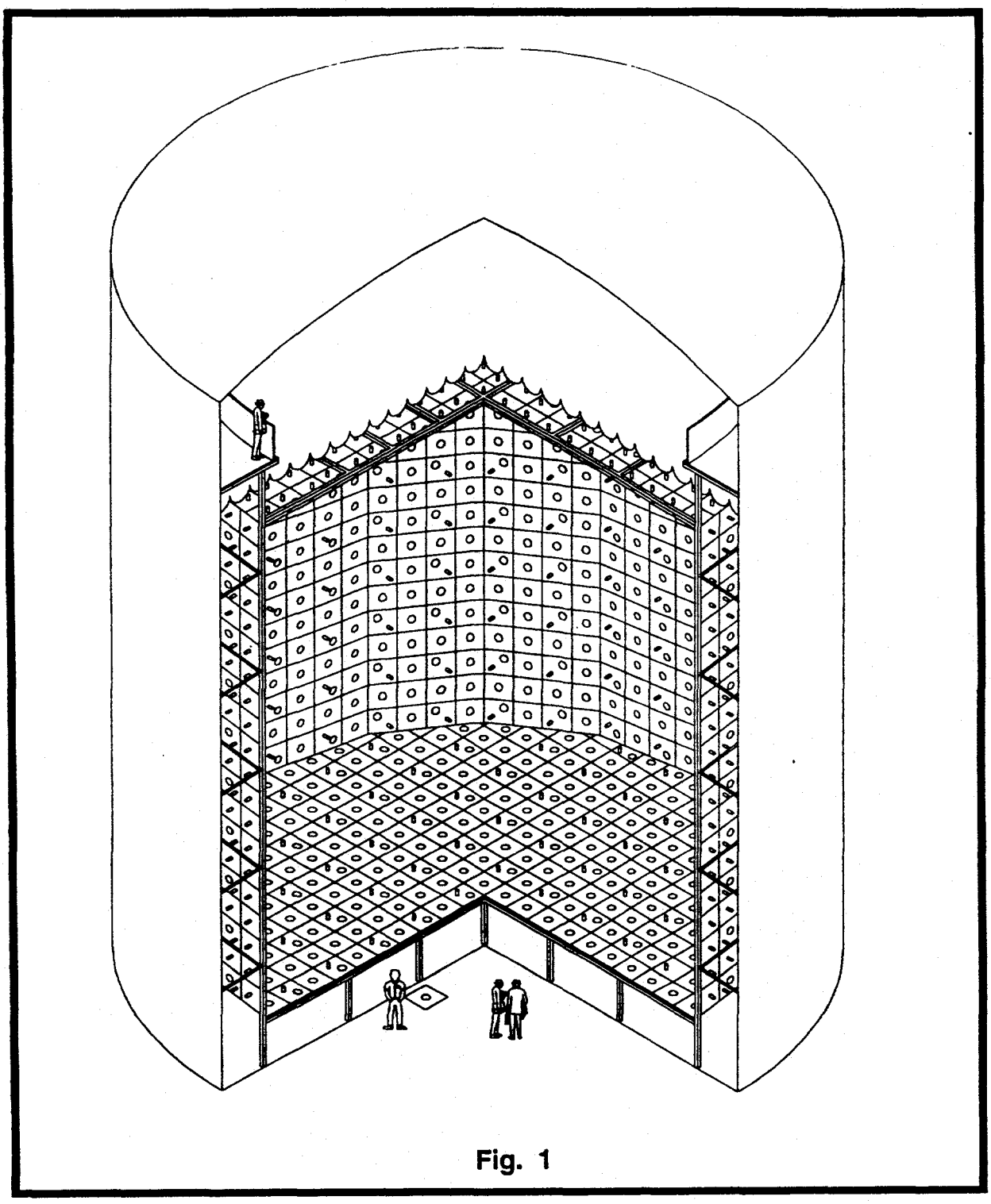

Fig. 1

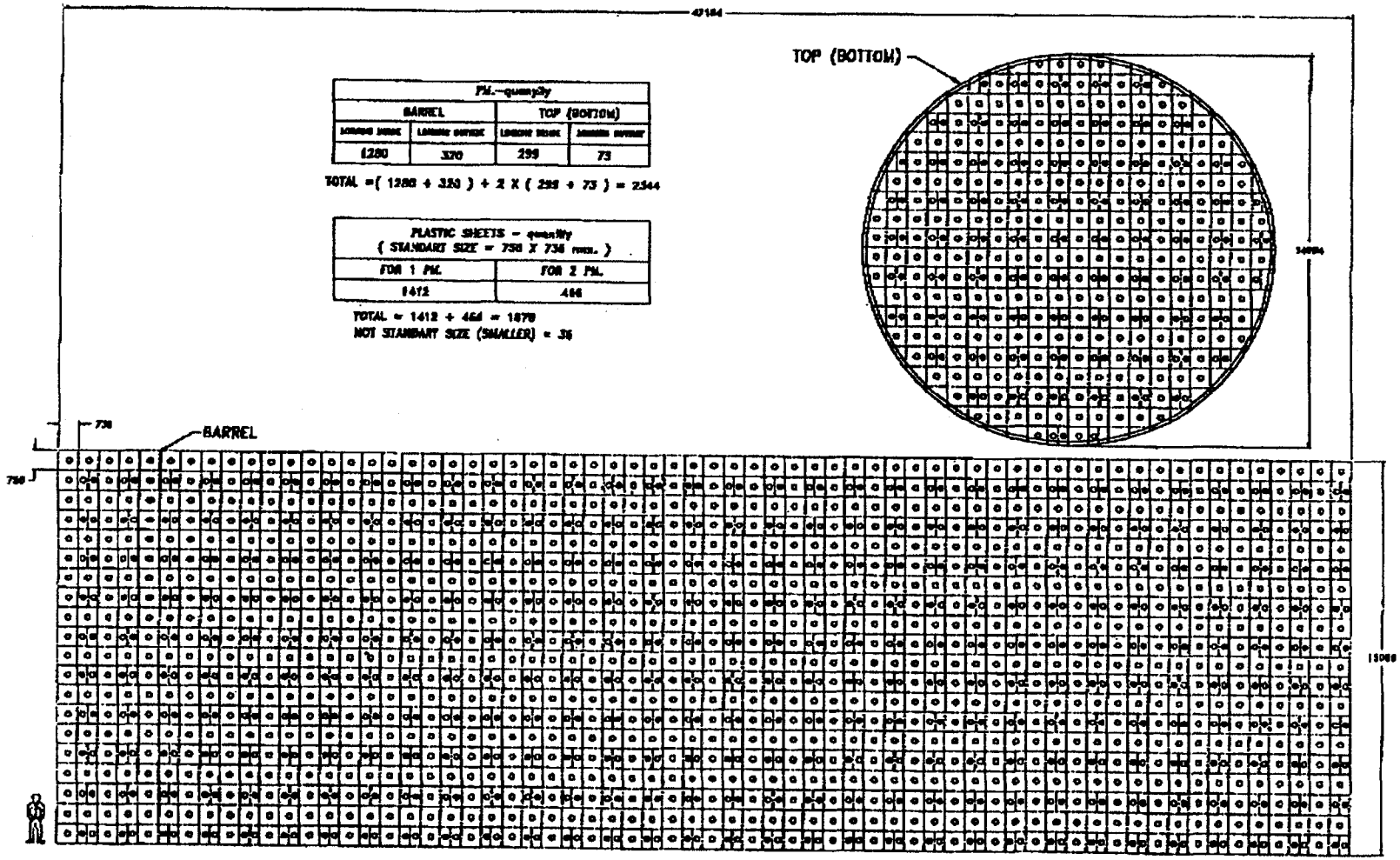


| PM.—quantity | | | |
|---|---|---|---|
| BARREL | | TOP (BOTTOM) | |
| [illegible] | [illegible] | [illegible] | [illegible] |
| 1280 | 320 | 296 | 73 |

TOTAL =( 1280 + 320 ) + 2 X ( 296 + 73 ) = 2544

| PLASTIC SHEETS - quantity ( STANDART SIZE = 750 X 736 mm. ) | |
|---|---|
| FOR 1 PM. | FOR 2 PM. |
| 1412 | 466 |

TOTAL = 1412 + 466 = 1878
NOT STANDART SIZE (SMALLER) = 36

Fig. 2

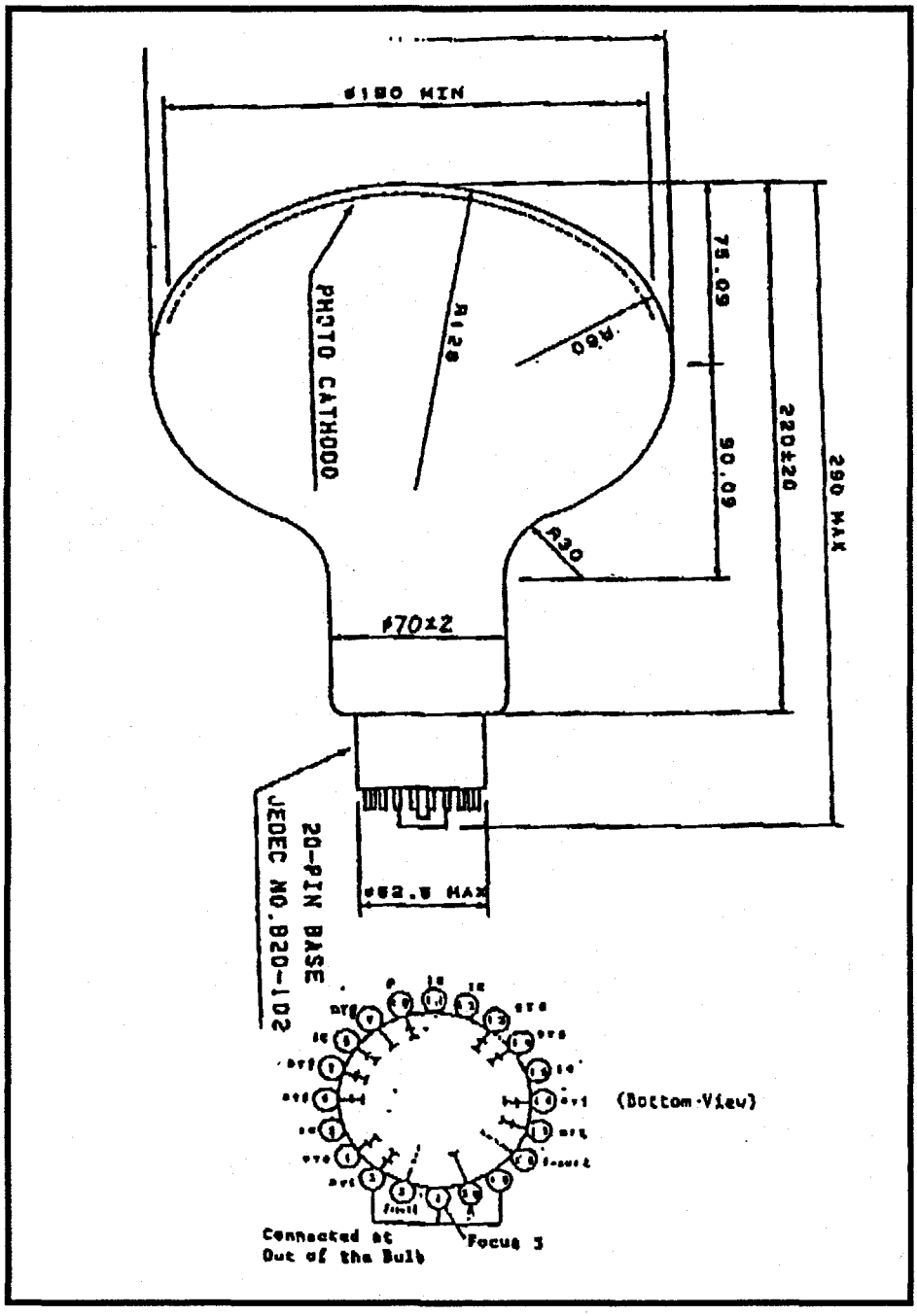
ø180 MIN
PHOTO CATHODE
R128
R60
75.09
90.09
220±20
290 MAX
R30
ø70±2
JEDEC NO.820-102
20-PIN BASE
ø62.5 MAX
(Bottom View)
Connected at
Out of the Bulb
Focus 3

Fig. 3

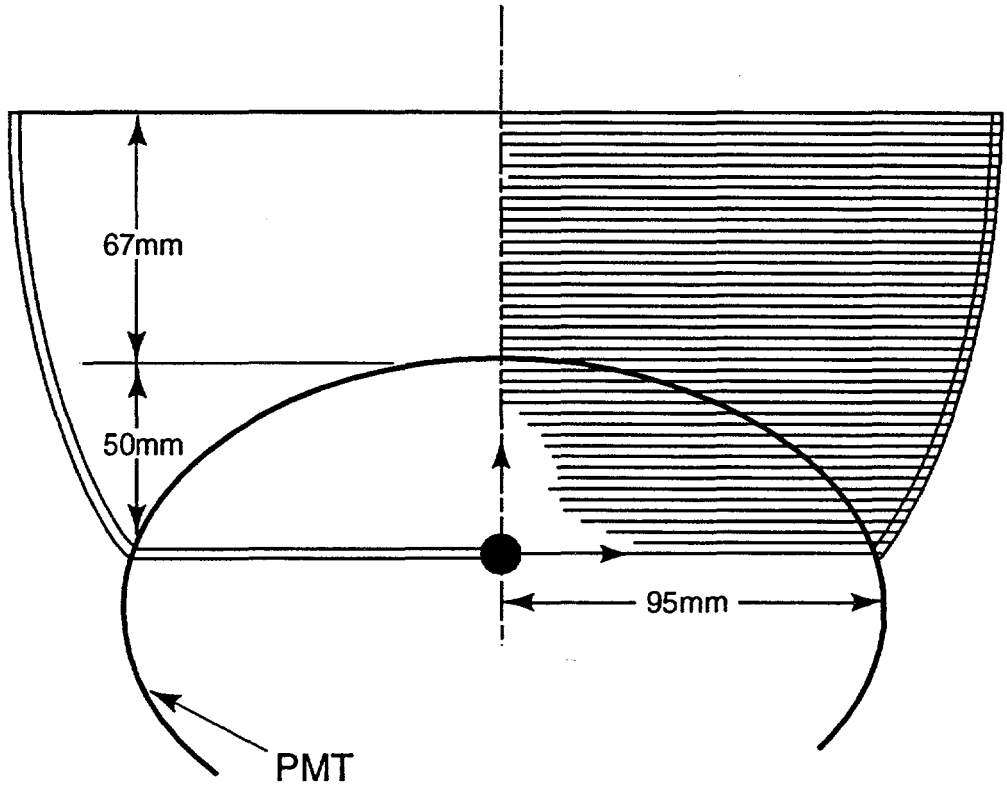


Fig. 4

The cable is electrically similar to RG59, but has a high density polyethylene outer jacket, has the tinned copper braid flooded with a polyethylene wax to prevent water wicking along the braid, and the braid is wrapped with an aluminum/polypropylene/aluminum laminate as a vapor barrier in order to withstand long term immersion in water. Furthermore, to keep the water *clean* and to reduce the water vapor transmission through the outer jacket, the chemical additives in the jacket are reduced to a minimum. Thus no fire retardant is used and the black colorant is reduced to a bare minimum. Because the HDPE jacket makes this cable noticeably stiffer than ordinary PVC jacketed RG59 and because the flooding compound and laminated vapor barrier are somewhat unusual, the cable may require non-standard handling during the bundle assembly process.

Belden YR29304.

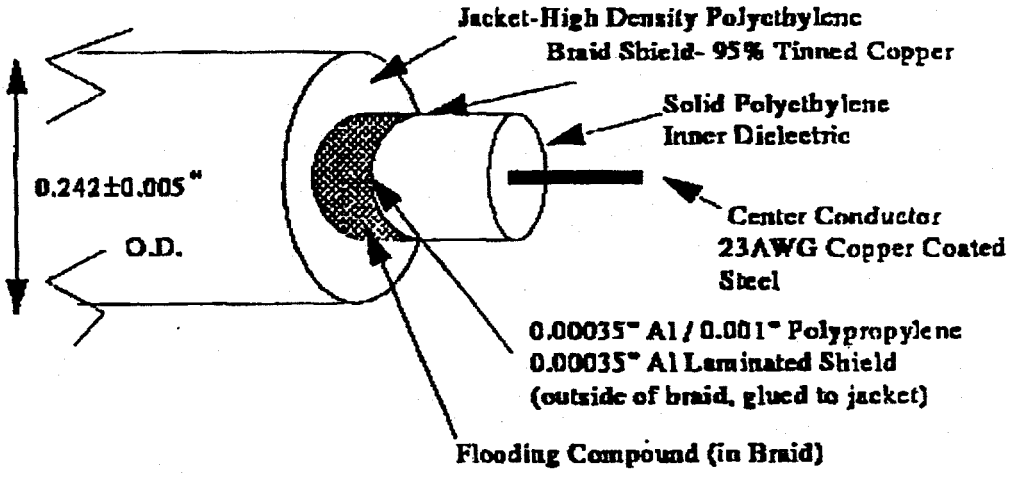


Some of the specifications of the YR29304 cable are listed below.The Belden technical description of the cable is included in the appendix to this document.

1. 23 AWG copper covered steel wire central conductor.
2. Solid polyethylene dielectric insulation (0.146 ± 0.004 " OD).
3. 95% coverage tinned copper braid shield.

Fig. 5

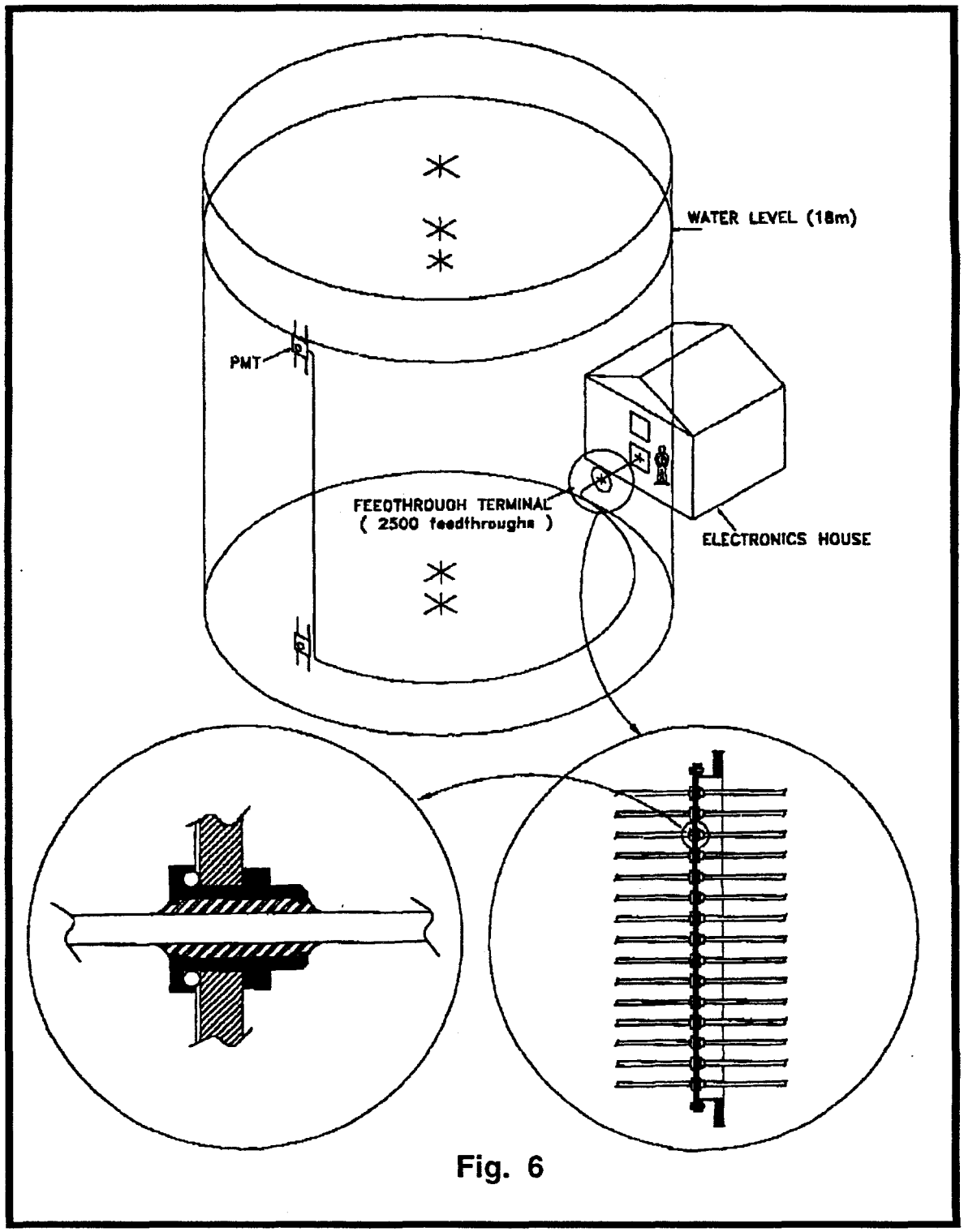
WATER LEVEL (18m)
PMT
FEEDTHROUGH TERMINAL
( 2500 feedthroughs )
ELECTRONICS HOUSE

Fig. 6

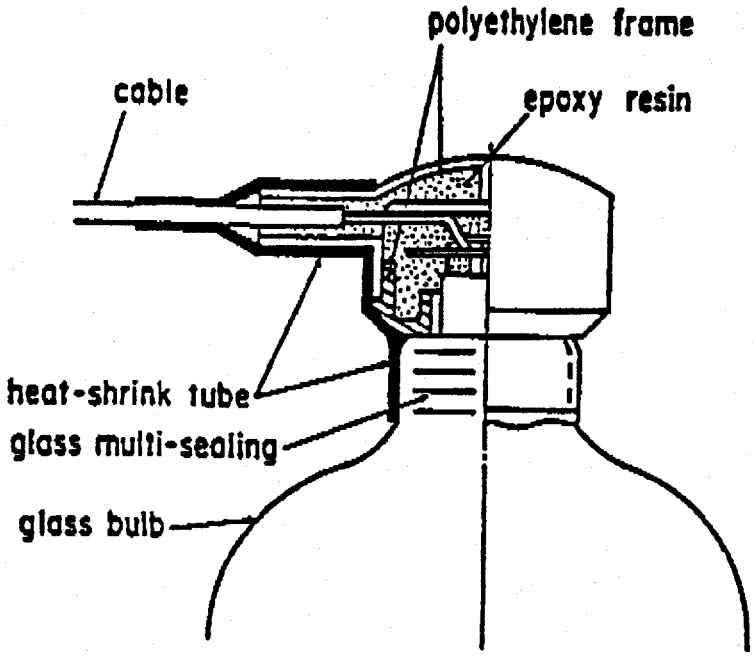
polyethylene frame
cable
epoxy resin
heat-shrink tube
glass multi-sealing
glass bulb

Fig. 7

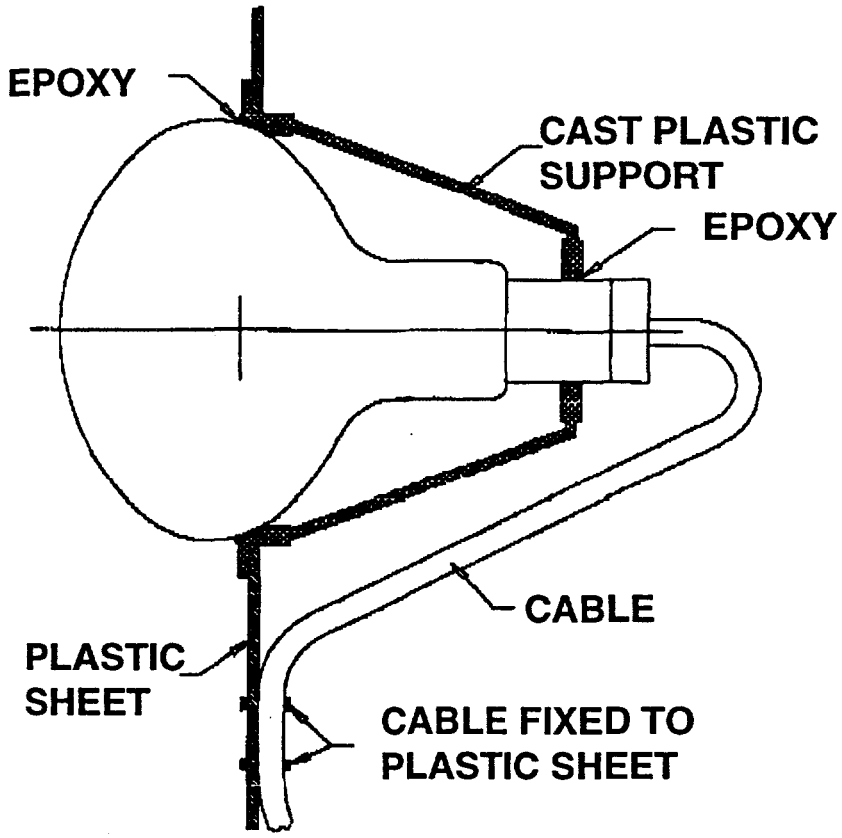
EPOXY
CAST PLASTIC SUPPORT
EPOXY
CABLE
PLASTIC SHEET
CABLE FIXED TO PLASTIC SHEET

Fig. 8

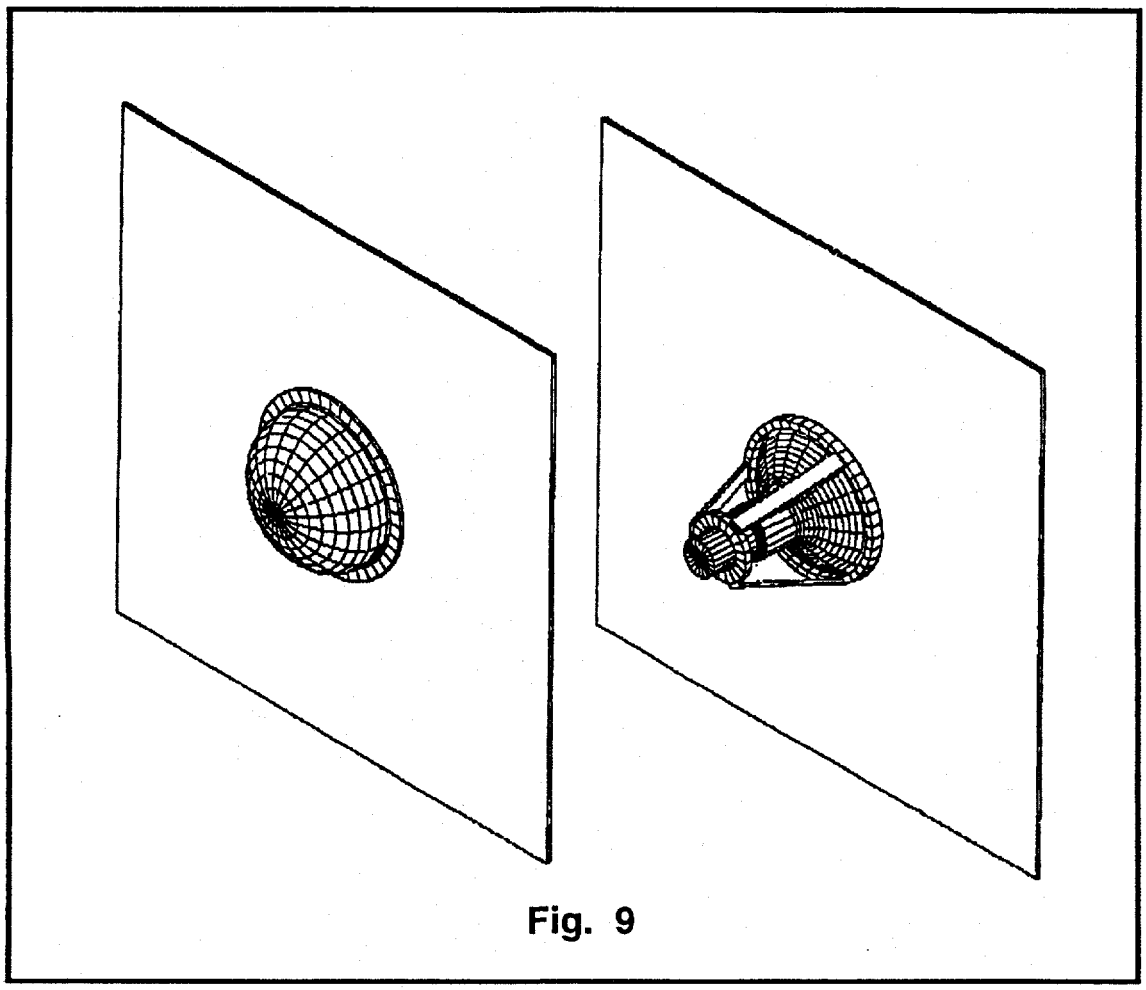

Fig. 9

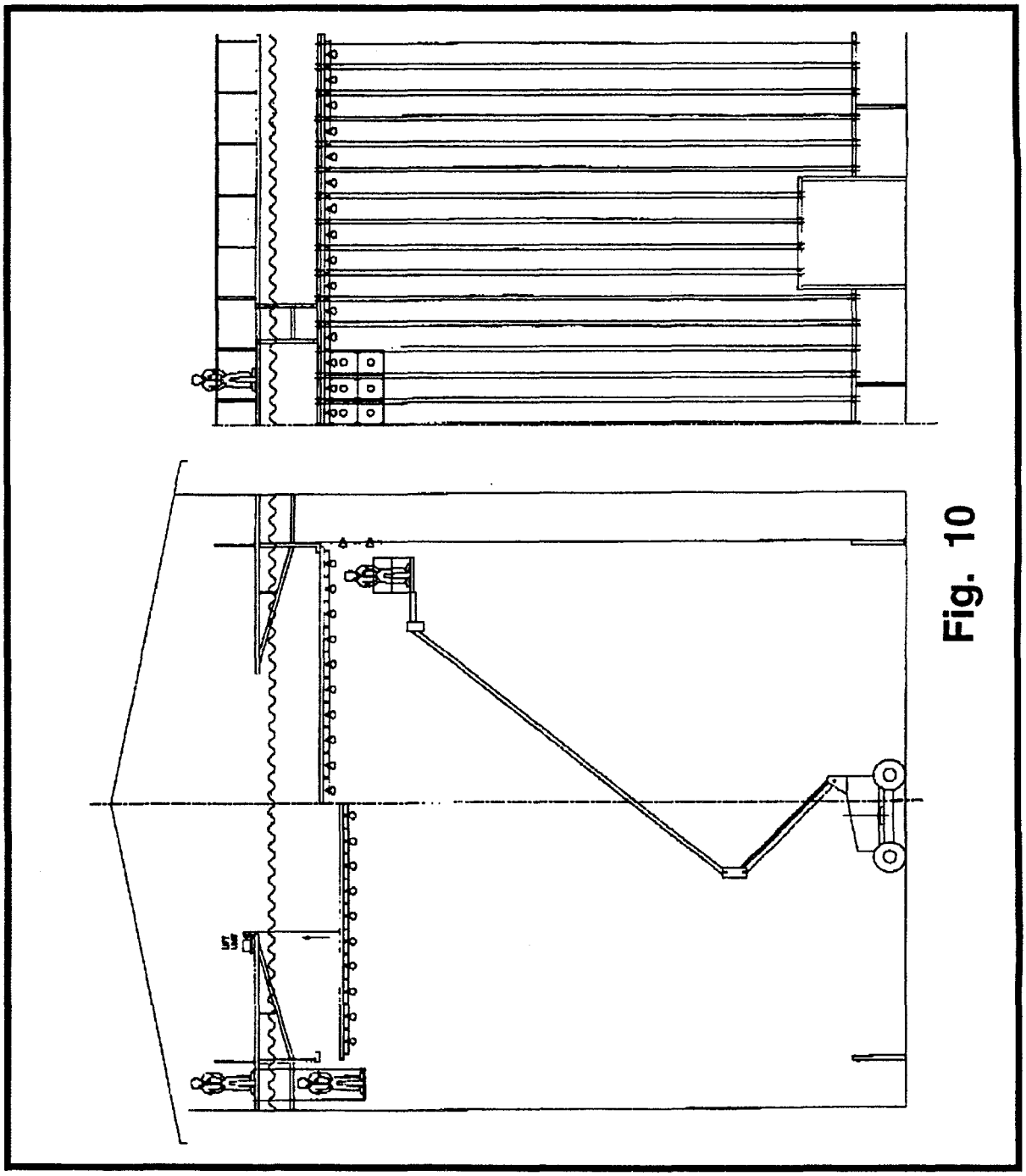

Fig. 10

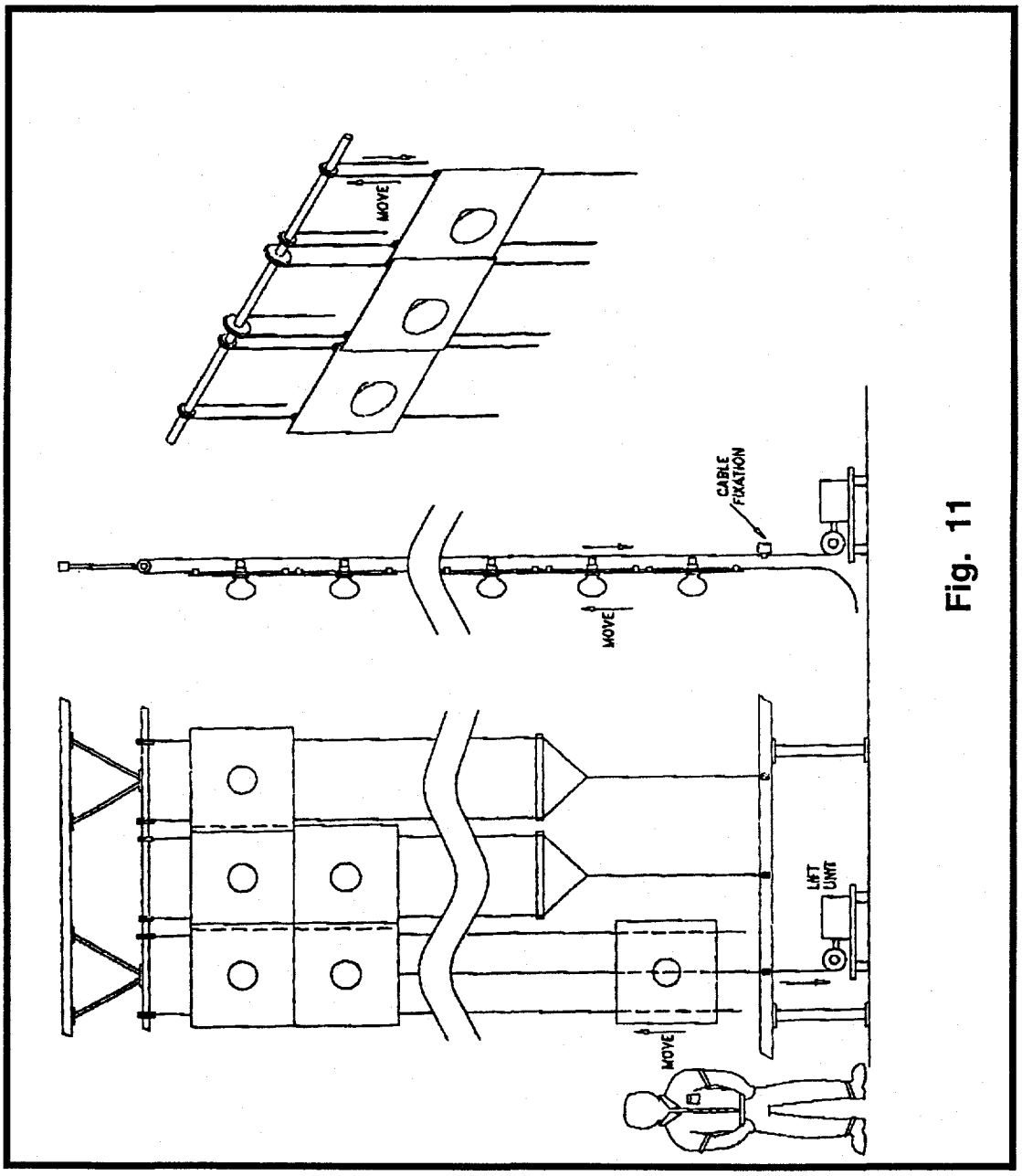


Fig. 11

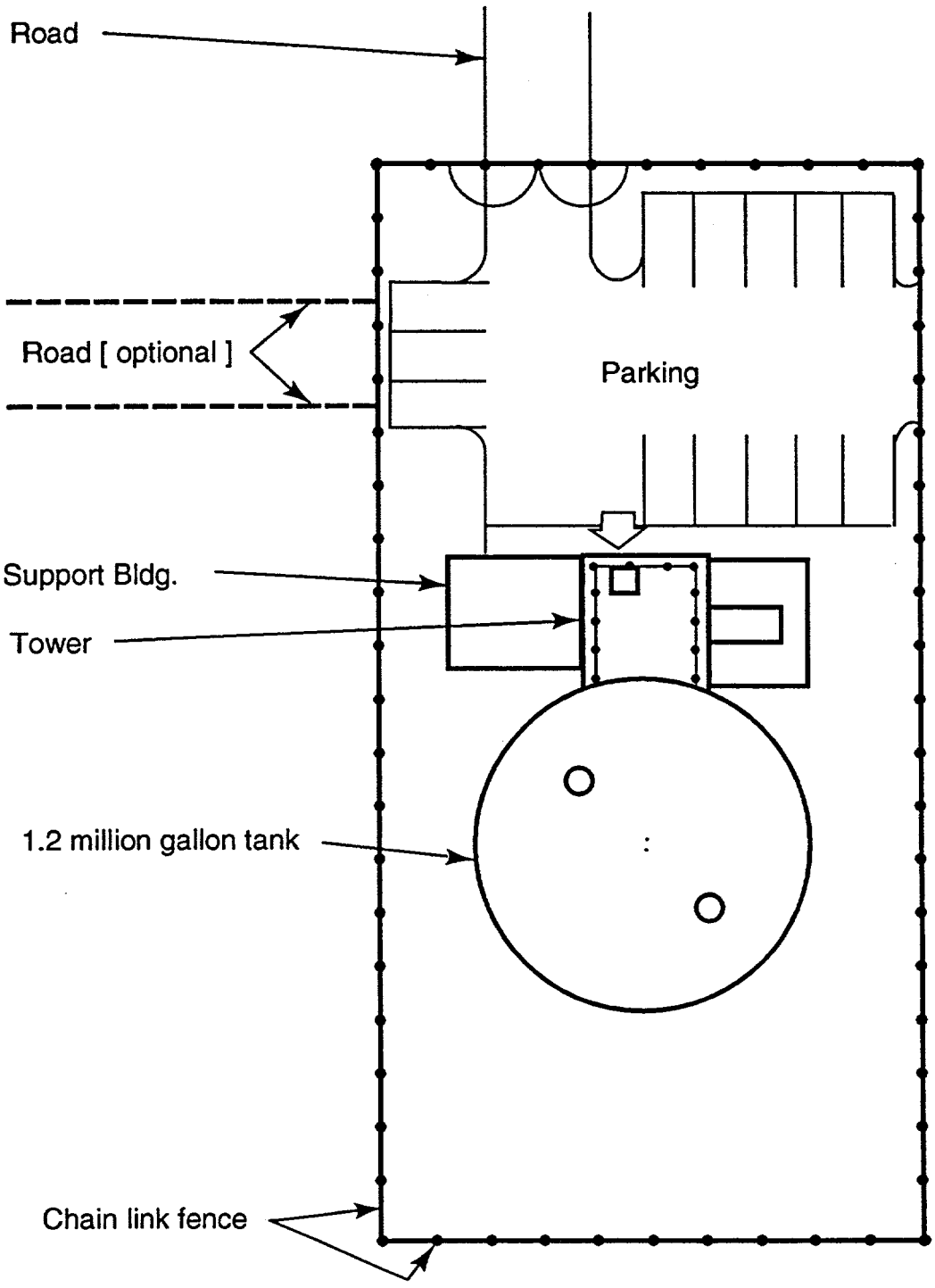
Road
Road [ optional ]
Parking
Support Bldg.
Tower
1.2 million gallon tank
Chain link fence

Fig. 12

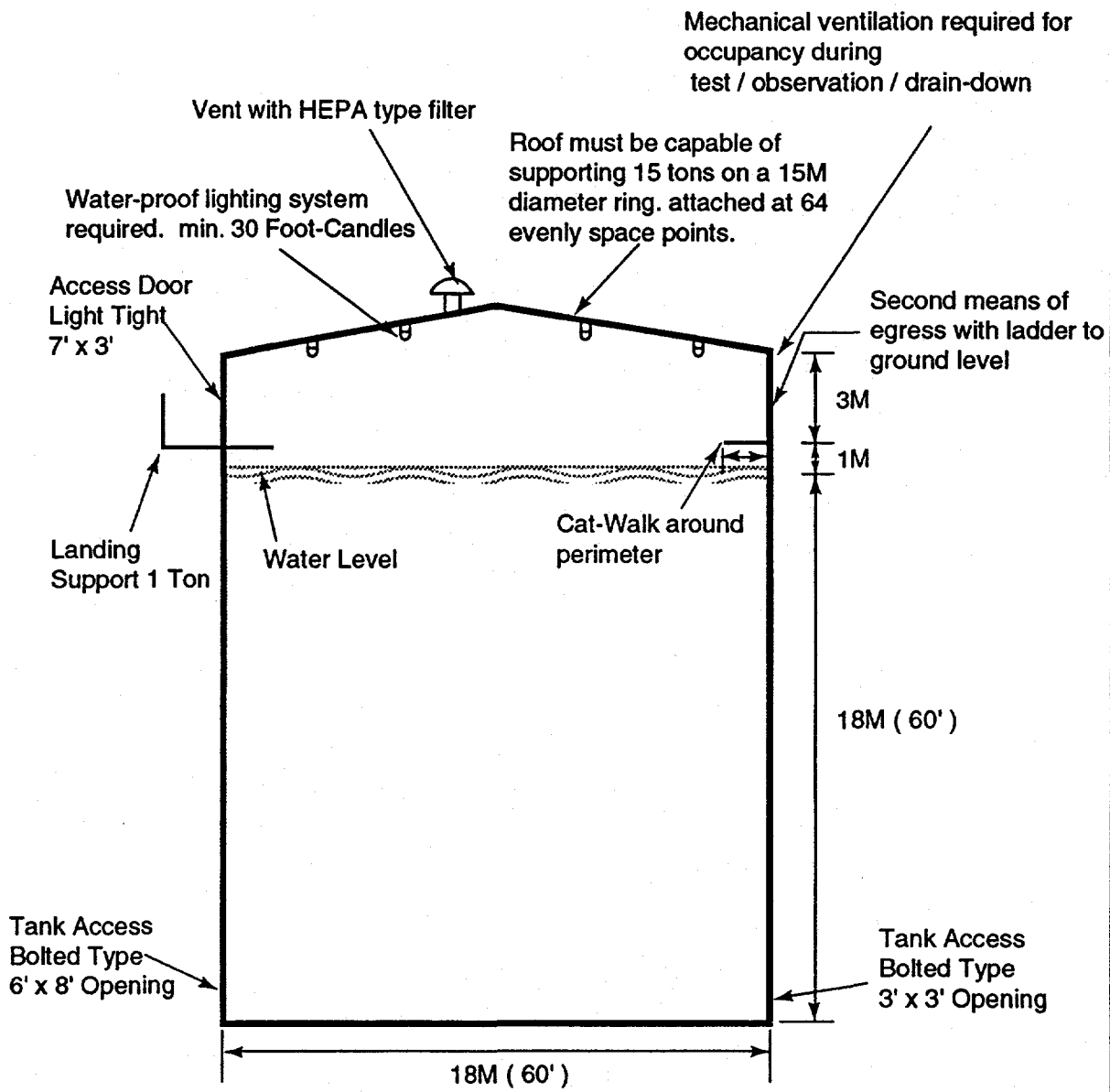


## General Specification :

- Allsteel tank construction : to API-650
- Wall / Side Insulation : R-10
- Siding : Ribbed Aluminum / Steel Jacket
- Coatings - Interior : Epoxy type to Potable Water Quality

Fig. 13

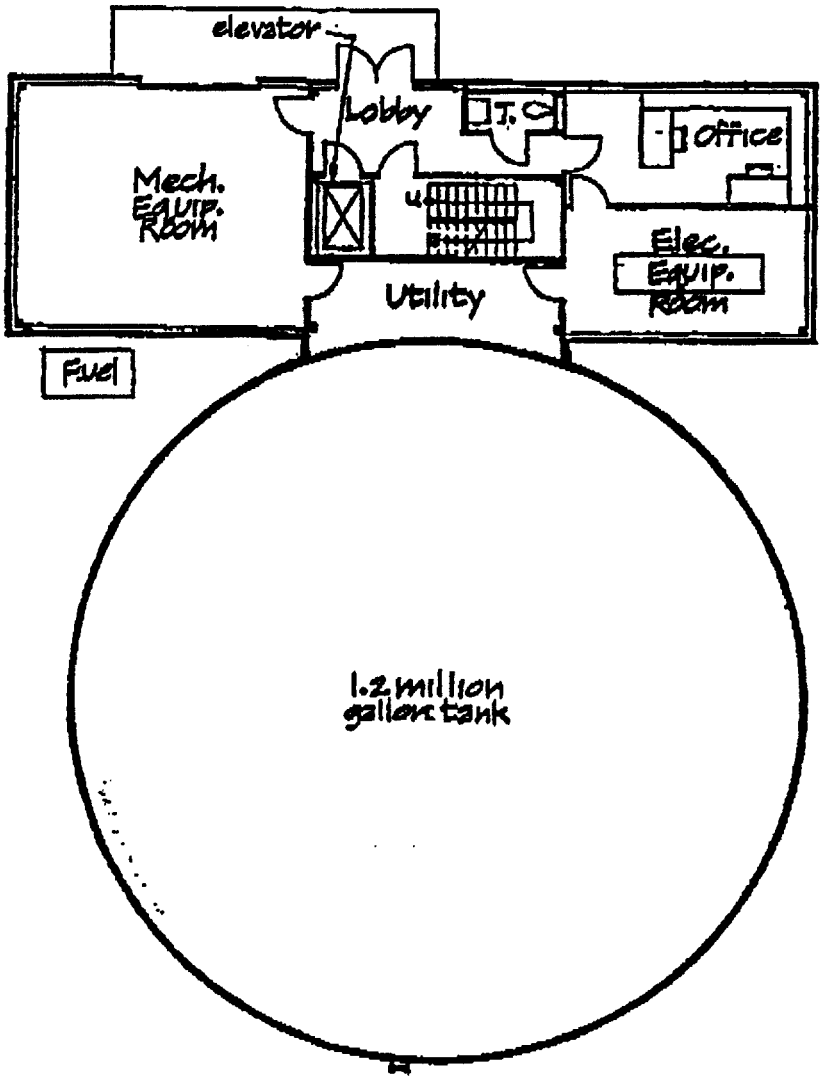
elevator
Lobby
J. C.
Office
Mech. Equip. Room
Elec. Equip. Room
Utility
Fuel
1.2 million gallon tank

Fig. 14

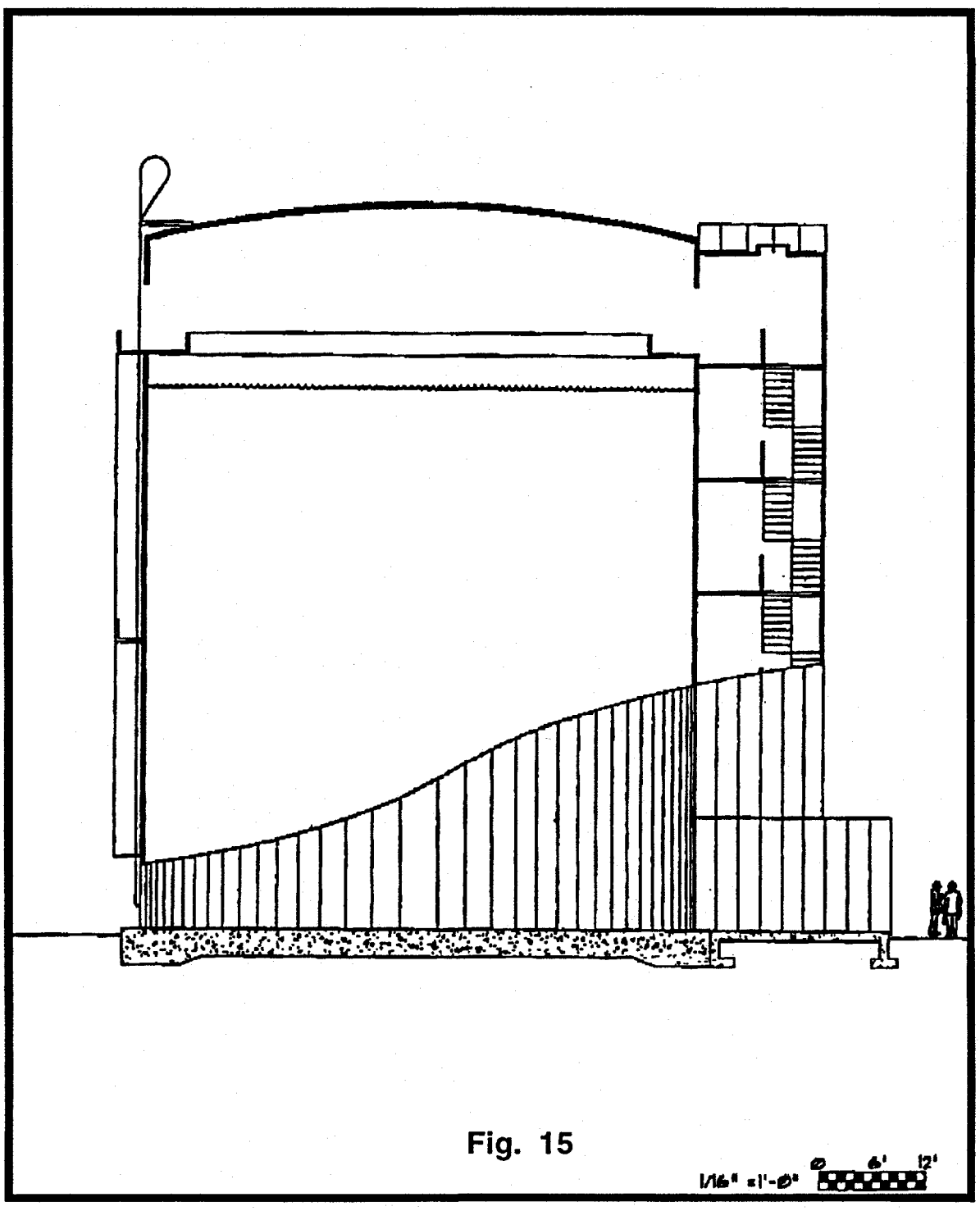


Fig. 15

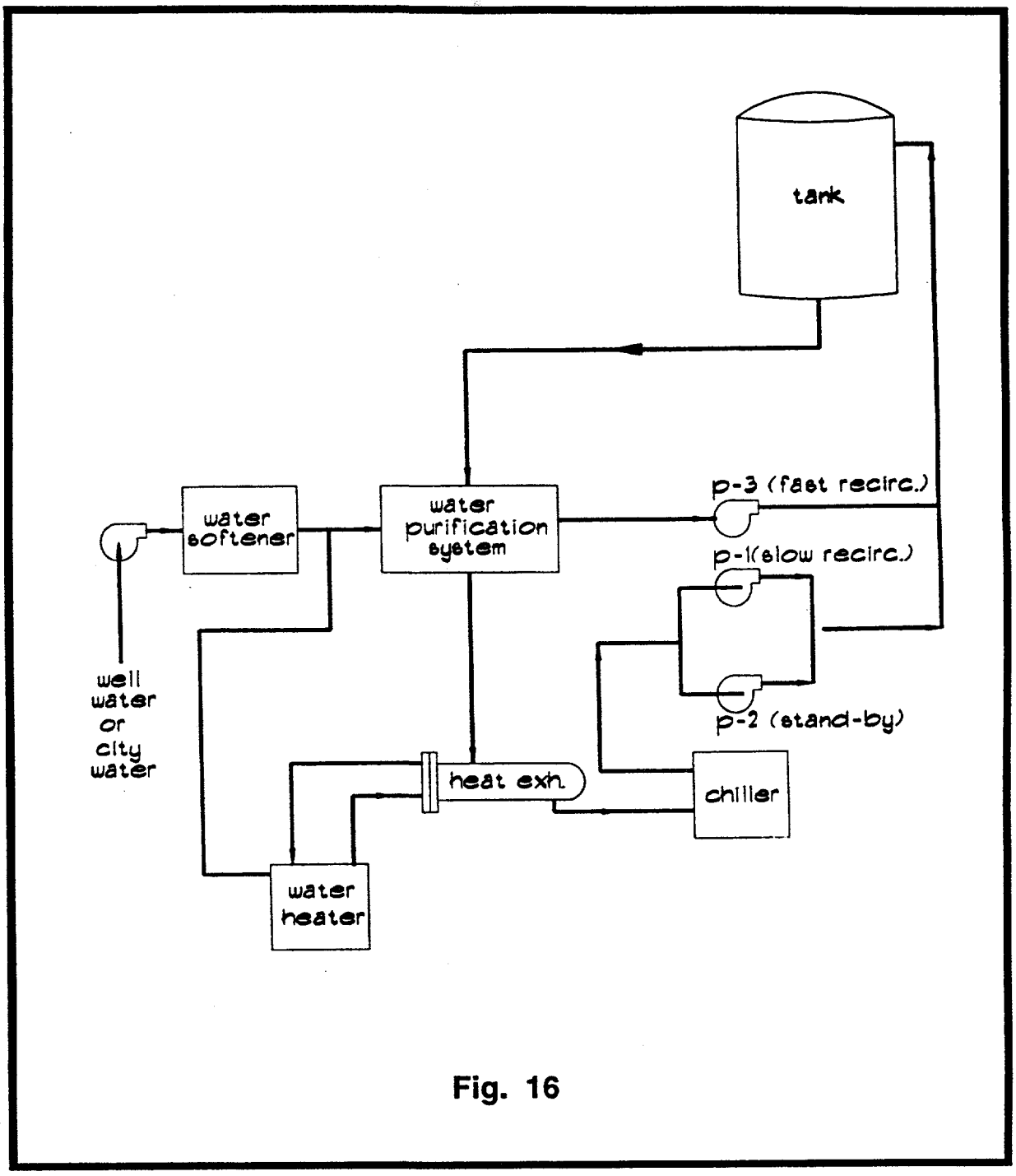
tank
water softener
water purification system
p-3 (fast recirc.)
p-1(slow recirc.)
p-2 (stand-by)
well water or city water
heat exh.
chiller
water heater

Fig. 16

# III C. Detector Electronics, DAQ, and Relative Timing

## Introduction

The physics goals of Experiment 889 impose several requirements for the electronics, such as dynamic range, timing resolution, and event rates. The expected range of signals in a single PMT from neutrino induced events will vary from 0.1 photo electron (p.e.) to 1,000 p.e. An effective dynamic range of 14 bits with a least count of 0.1 p.e. should be adequate for the experiment. Simulations indicate a need for a resolution of $\sigma_t \approx 1$ ns for good vertex resolution. Finally the electronics should handle an instantaneous rate of 100 kHz for brief periods during the AGS spill.

Two other important factors drive the design of the system. First, the system will be widely distributed; two tanks are on site at BNL, 1 km and 3 km from the neutrino production site, while the other two are 24 km and 68 km away. For these last two sites, normal methods of propagating timing signals, such as over coaxial cable or optical fiber, are not practical. Second, the cosmic rate is large compared to the neutrino signal at the far sites. The most effective method for reducing cosmics from the data uses the very narrow time structure of the neutrino beam. Every 1.6 seconds, the AGS will produce a spill of 8 buckets of protons regularly spaced with a period of 335 ns[1] (Figure 1). Each bucket will last 20–30 ns; knowledge of precise event and bucket times at the detectors will allow rejection of all events outside bucket intervals.

An additional consideration is the reliability and remote monitoring of the experiment, since the far and probably the near sites will be mostly unmanned during normal operation.

## System Overview

We plan a widely distributed data collection system that consists of these elements:

- A system at the AGS accelerator which generates a *BEAM-ENABLE* gate that is broadcast to the other locations prior to extraction.
- An electronics/DAQ system at *each* detector (tank) which is responsible for reading the tank PMTs during the *BEAM-ENABLE* gate.
- A system at the neutrino production site which yields accurate times of beam buckets.

[1]The spill length is therefore 2.7 $\mu$sec.

- A base station at BNL which collects and collates data from all sites.

The sites local to BNL will be connected by optical fiber links for logic signals and computer networks, but the remote sites (24 and 68 km) will be linked to BNL with microwave communications transceivers that have multiple analog and digital[2] channels. In addition, the neutrino production and all detector sites will be equipped with identical, accurate, GPS-synchronized timing systems. (see Figure 2).

The *BEAM-ENABLE* signal, about 10 $\mu$sec in duration, will bracket each spill, preceding the first bucket by 2–3 $\mu$sec. It will be transmitted to the detector sites via an analog channel of the microwave communications link. This signal synchronizes data collection with the AGS beam; no events outside this interval will be accepted, so it causes a first-order cosmic-ray rejection based on beam time.

Since the leading edge of the *BEAM-ENABLE* signal indicates that neutrinos are about to arrive, the systems at each tank will start recording all PMT signals above a given threshold for a 10 $\mu$sec interval upon receipt of this signal. At these tanks, precise event times will also be recorded using accurate, Global Positioning System-synchronized (GPS) timing systems. Event records will be stored on a local tape drive for backup, and transmitted via a digital link to the base station. At the neutrino production site, the precise bucket times will be recorded using a timing system identical to that at the tanks. These beam times will also be sent to the base station to be collated with events from the detectors.

## Generation of *BEAM-ENABLE*

The AGS extraction control mechanism (as illustrated in Figure 3) will be used to generate the *BEAM-ENABLE* signal. In the acceleration cycle, at a preset magnetic field, a signal $t_{AGS}$ is generated. After a predetermined number of orbits, $n_{orb}$, the beam is extracted. Since each AGS orbit has a fixed period, $\tau_{orb} = 2.6\mu s$, $n_{orb}$ can be adjusted according to the needed delay time.

[2]EtherNet ready; T1 bandwidth

Table I. Propagation Delays to Sites

| Detector | Distance | Light Travel Time |
|---|---|---|
| D1 | 1 km | 3.3 $\mu s$ |
| D3 | 3 km | 10 $\mu s$ |
| D24 | 24 km | 80 $\mu s$ |
| D68 | 68 km | 227 $\mu s$ |

The *BEAM-ENABLE* signal needs to be derived before the actual extraction time $t_{ext}$, and sent to the microwave transmitter. While the travel times to the detectors are quite large (see table I), we only need to be concerned with delays in cables, transmitters, and receivers when broadcasting to the remote detectors, since both the signal and the neutrinos travel at the same velocity. Although the spill duration is 2.7 $\mu$sec, a window of 10 $\mu$sec will allow detection of $\mu$ decays of stopped muons in the tank from either cosmic rays or neutrino events. A jitter of up to 1 $\mu$sec is tolerable provided the leading edge sufficiently precedes the actual arrival time of the first bucket.

## Detector Systems

The detector systems are composed of five distinct subsystems (Figure 4):

1. **Front end electronics.** The electronics will process the signals from the photomultipliers, measure the signal arrival time at the PMT with respect to the trigger time, digitize all the information and store it in a local memory.

2. **Trigger system.** The trigger system, based on the multiplicity of photomultipliers with signal above a preset level, and coincidence with *BEAM-ENABLE*, will determine if a given event will be readout by the DAQ. It will also allow calibration triggers with pulsers or cosmic rays.

3. **Timing system.** This GPS-synchronized system will allow accurate determination of event time for comparison with bucket times recorded by the AGS Beam History system at the neutrino production site.

4. **Data acquisition system.** For the reading, recording, and transmission to base of all digitizing electronics.

5. **Housekeeping.** This sub-system will keep track of slowly varying detector parameters. It will be used, for example, to monitor the high voltage power supplies.

We discuss these detector subsystems in detail.

## Front End Electronics

At each detector there are 2550 20 cm diameter PMTs of which 2200 face inward for the main detector and 350 face outward for the veto shield. It is the task of the front end electronics to digitize amplitude and timing data from the PMTs. The system must also interface with high voltages, since signals arrive on the same cable carrying high voltage to each PMT.

### The Choice for the Front End

The electronics chosen for the experiment should be able to handle pulses from the photomultipliers in the range of 0.1 p.e. to 1,000 p.e. This implies a system with a dynamic range of 14 bits. Since digitizers with this many bits are very costly, the feasible option will be to have a system with dual gain, and therefore effectively achieve the needed dynamic range.

The timing constraints, on the other hand, are dependent on the position resolution to determine the location of the neutrino interaction. Monte Carlo simulations indicate that for a position resolution of the order of 20 cm we need a timing resolution of 1 ns per PMT. Since the PMTs can inherently achieve this timing resolution or better, the electronics must not deteriorate it further.

Table II. Expected number of raw neutrino events per spill at the detector sites

| Site | $\nu_\mu n \rightarrow \mu^- p$ | $\nu_e n \rightarrow e^- p$ | $\nu N \rightarrow \nu N \pi^0$ | Total Rate |
|---|---|---|---|---|
| D1 | .51 | $5.1 \times 10^{-3}$ | 0.10 | 0.86 |
| D3 | $5.7 \times 10^{-2}$ | $5.7 \times 10^{-4}$ | $1.1 \times 10^{-2}$ | $9.7 \times 10^{-2}$ |
| D24 | $8.9 \times 10^{-4}$ | $8.9 \times 10^{-6}$ | $1.8 \times 10^{-4}$ | $1.5 \times 10^{-3}$ |
| D68 | $1.1 \times 10^{-4}$ | $1.1 \times 10^{-6}$ | $2.2 \times 10^{-5}$ | $1.9 \times 10^{-4}$ |

The electronics must be able to handle the event rate which in our case is from two sources: neutrino induced events and cosmic rays. The flux of cosmic rays is 80 kHz. However, since we will run synchronously with the accelerator our concern is only with the number of events

occurring in the time window when the data acquisition is operational. The *BEAM-ENABLE* window of 10 $\mu$sec implies that the contribution from the cosmic rays to the number of events within the time window will be $\sim$1 per pulse on average. The rate of real events will depend on the detector distance to the accelerator and it is summarized in Table II, assuming $2 \times 10^7$ spills over 16 months. Consequently, the effective rate that we need to handle will be 1–2 events per single AGS macro-cycle of 1.6 sec, or of the order of 1 Hz. For each hit PMT the data packet will consist of the charge and time, channel address, global trigger, and appropriate flags giving a total of approximately 10 bytes. An average event involves 400 hit PMT; therefore the total event size will be approximately 4 kilobytes. The highest event rate will be in D1 and will be less than 2 events per spill, yielding less than about 10 kilobytes per second.

With the above requirements in mind we have chosen to use the existing electronics design of the Sudbury Neutrino Observatory (SNO) [1] for each of the four independent detectors. The performance specifications of the SNO electronics are listed in table III.

Table III. SNO Electronics Performance Specifications

| | |
|---|---|
| time resolution | $<$ 1.0 ns. |
| charge resolution | $\sim$0.1 p.e. |
| maximum charge | $\sim$1000 p.e. |
| trigger deadtime | none |
| low energy throughput rate (continuous) | 1 kHz |

The SNO front end electronics are designed for a wider dynamic range than is needed for E889, and have excellent timing resolution. Furthermore it can sustain a rate of 1 kHz and bursts of up to 1 MHz, which are also more than adequate for the present experiment. Finally, it is designed, costed, and will be tested by the time E889 will need to commence construction.

### SNO Electronics Overview

The SNO system is packaged in custom VME (9U) crates with modified backplanes which hold 16 Front End cards and one Trigger Card (see Figure 5). The Front End cards handle signals from 32 PMTs each, and interface with a larger trigger system through the Trigger Card. When the Front End cards receive a Global Trigger (GT) through their Trigger Card, they digitize amplitude and time information for all PMTs above a given threshold, and store the data in a dual port memory which can be read through the backplane by a standard VME

master. The back of the crate also houses 16 High Voltage cards, each of which supplies power to 32 PMTs. The signals and high voltage are carried on a single cable to each PMT connected to the rear of the crate. Since each SNO crate can handle up to 512 PMTs, we will use 5 crates at each detector, which will be connected to a VME Master Crate with VME memory mapped repeaters.

The major signal processing elements of the Front End cards are (1) a wide dynamic range integrator, (2) a fast, sensitive, discriminator and timing circuit, and (3) an analog/digital pipeline memory, all of which are full custom, application specific, integrated circuits. These handle all of the analog signal processing except for the analog to digital conversion. The logic diagram for one PMT channel is shown in Figure 6 and the block diagram of the basic electronics setup for a detector is shown in Figure 7.

### High Voltage Distribution Cards

The high voltage part of the electronics crates consists of 16 cards, 32 channels each, with a common distribution card for each crate. The HV is provided for each crate from five commercial regulated bulk supplies that can supply 100 mA at 3.0 KV. Each HV supply can be controlled and read back from the SNO crate controller. The raw HV will be distributed to the crates from these supplies and each crate can provide power for 512 PMT's. The HV card, in addition to providing high voltage, will AC-couple the analog signal to the Front End card. These cards will sit on the rear of the electronics crates back to back with the Front End Cards, sharing PMT signals via a common P2 connector.

### The Front End Cards

The Front End card receives 32 PMT signals and will discriminate, store, digitize, and buffer the time and charge information. The card consists of two different custom bipolar front end integrated circuits (SNOINT and SNOD), a custom CMOS timing and analog pipeline integrated circuit (QUSN6), commercial ADCs, memories, standard logic and programmable logic devices.

Each bipolar chip set (SNOINT and SNOD) has four complete channels, each of which contain: two self gating integrator (HI/LO) channels, a fast discriminator and a timing sequence with three programmable intervals. Shown in Figure 8 are the chip level blocks and connections for a single PMT input. The charge gain is determined by the size of the external integration capacitor chosen for each channel and the relative attenuation ratio

between the two dual ranging channels is set by external resistors. A signal is detected by a fast discriminator on the SNOD chip that monitors the PMT activity. The SNOD chip fires the discriminator if the differentiation of the input pulse exceeds an externally applied threshold. The threshold can be set to any range and to effectively turn off a channel one only needs to set this value very high. The discriminator is optimized to give a very fast response time and low walk and jitter. The SNOINT chip controls the actual charge integration with an effective dynamic range of more than 14 bits. A charge integration is triggered by a signal over threshold in the SNOD chip discriminator. The SNOD chip provides two gating functions for the SNOINT chip, called RESET and SAMPLE. The RESET signal controls the charge integrator reset switches, and is used to initiate a time measurement cycle and to provide primitive system triggers. The SAMPLE signal controls the separate recording of charge from the instantaneous and reflected photons. The outputs of the SNOINT & SNOD are the signals from the high and low integrator sections of SNOINT and the SAMPLE and RESET from the SNOD. These signals are presented to QUSN6. The SNOINT and SNOD chipset is fabricated in AT&T's advanced, fully custom, high speed CBICU-2 process.

QUSN6 provides three charge and one time analog memory, time to amplitude conversion (TAC), and channel and trigger logic for the detector. A single channel timing sequence is shown in Figure 9. On the leading edge of a RESET signal a timing cycle and TAC is initiated. The TAC for any PMT can be stopped by a centrally generated Global Trigger (GT) signal. The charge integral measurement voltages, low and high gain, from SNOINT are sampled on the leading and trailing edges of the SAMPLE signal. If a GT trigger arrives from the central trigger system before an internal time-out is reached, the four analog voltages are stored in one of the 16 analog memory banks and a digital memory records the sequence number of the GT, the memory location, and any set condition flags. If no GT arrives before the internal time-out is reached, the channel resets itself and is ready to accept another PMT input. Therefore, the dead time will be the per PMT dead time of one GT timing sequence that can be set to allow for light reflection across the E889 detector volume. In addition to this FIFO like data path, the QUSN6 chip includes a trigger generation function, some basic utility functions, and self-test capability. To keep independent track of PMT noise rates and error conditions, separate internal counters are used for the RESET signal. All of the latches and counters are accessible for testing and programmable adjustments for fine tuning the TAC slope are built in.

The write process into the analog memory is data driven by a coincidence of a PMT signal and a GT pulse. The readout sequence from the analog memory is a separate and

asynchronous process. The channel voltages stored in QUSN6 are buffered out of the chip and are fed into commercial 12 bit 2 $\mu$sec ADC's for digitization. The output of charge and time ADC's go to a large local buffer memory on the card which acts like a FIFO. The ADC outputs, the channel address, global trigger, and appropriate flags comprise a 12 byte data packet for a particular PMT event and is loaded into the onboard memory. The memory is standard SIMM DRAM and can be read out via the modified VME backplane by a crate master. The three word data structure for each PMT is shown in Figure 10 along with the data flow diagram.

### The Trigger Card

The trigger is formed in stages by doing a local Front End Card sum of the 32 channels and then a crate sum of the 16 front end cards. The leading edge of the RESET signal from the SNOD chip in the Front End Card is used in QUSN6 to initiate a pair of digitally programmable current pulses. The longer pulse approximately 100 ns is sent to the first stage of a 2195 input analog sum. This first stage which basically sums up the individual 32 channels on a front end card is implemented using a high speed operational amplifier located on the front end card and shown in Figure 11. This output is sent via the backplane to the crate trigger card which then sums the 16 individual front end cards in its crate to form a signal whose amplitude is proportional to the number of PMT hits in the crate. This Crate Trigger Signal is then sent to the Trigger System (see below) which will decide whether or not to distribute a global trigger back to all the Crate Trigger cards, based upon the presence of *BEAM-ENABLE*, number of hits from the other SNO crates, as well as any other logic decisions we may wish to apply. Upon receipt of GT, the Crate Trigger cards initiate data read cycles.

## Trigger

The basic trigger for the experiment at each site will be based on the multiplicity of phototubes above certain threshold (Figure 12). Therefore a basic trigger will simply be some number of PMTs going off simultaneously within some timing window. This timing window will be approximately equal to the transit time of light across the detector. The tanks are approximately 15 m across and it takes light about 60 ns to travel that distance in water so a trigger resolving time of about 100 ns will allow time enough for all the photons from the Cherenkov radiation to be counted towards a trigger. Since this coincidence does not present

a sharp edge it will not be appropriate for timing measurements. We will generate a sharp edge timing signal artificially using the logical *and* of the coincidence signal and a 200 MHz clock signal (see next section). The arrival of light at the PMT is measured with respect to the clock edge.

In addition to the event trigger we will make use of other triggers such as calibration, random and cosmic trigger to monitor the performance of the detector.

## Timing System

Accurate timing of events will be achieved using Global Positioning System (GPS) receivers. Using averaging techniques and ensuring that receivers which are geographically separated track the same satellite above the horizon (Common View Mode[2]), relative timing accuracies of less than 10 ns can be achieved. The 10 ns synchronization error will most likely be the maximum possible error, rather than a Gaussian distributed error. Given the 12 hour orbit of each GPS satellite it is possible that we observe a worsening in the timing during periods when the GPS receivers are locking to a new satellite, but this should take only a few seconds.

For DAQ the time of the event will be stored in two scalers. One that will be counting the 10 MHz signal from the GPS receiver which is equipped with either a Cesium or Rubidium clock. This will provide us with a timing mark accurate to 100 ns. A second oscillator with higher frequency conditioned by the GPS 10 MHz signal will provide a fine grain timing information. A 200 MHz crystal oscillator will be used for this purpose. Upon the decision by the trigger system that a valid event happened in the tank both values will be recorded. Both scalers, with enough bits to run for one day, will be reset at 0.00 hours based on the GPS 1 pulse per second accurate signal. See also Appendix I.

## Computers

Readout of the SNO electronics will be easily handled by a VME Single Board Computer (SBC), *i.e.* a Motorolla 68040, running a real-time kernel such as OS-9. This SBC will sit in the VME Master Crate which is connected to the SNO crates via a memory mapped VME repeater chain. This repeater gives the SBC direct master control of the SNO crates. When triggered by a VME interrupt generated from trailing edge of the *BEAM-ENABLE* signal arriving from the AGS, it will read all individual PMT data packets from the onboard memory, collected by the SNO electronics during the *BEAM-ENABLE* window, and will also record the digital time from the accurate timing system described above.

In addition to PMT and timing data, housekeeping and controls information will also be recorded, as well as any additional electronics (CAMAC scalers, etc.) output. Data will be written immediately to a DAT tape (for backup) but will also be transmitted to a nearby RISC workstation for local monitoring and subsequent retransmission to a base station at BNL. At the base station, there will be a high-end RISC computer that collates and re-formats event records from the individual sites on the basis of the digital time-stamps.

While a telecommunications company can provide a T1-style data link to the remote sites, we currently favor a TCP/IP-ready microwave electronics system, since we will deliver the *BEAM-ENABLE* signal from the AGS to the remote sites via a microwave link in any case. In addition to analog channels, microwave transceivers typically provide more than one T1 channel, allowing extensive two-way traffic for remote monitoring, control, and software development without degrading performance of the primary data path.

### Housekeeping

Since the detectors will be unmanned for most of the time it is important to monitor each detector and its associated electronics from the base station. For each site we will implement a monitoring system to read quantities such as the water temperature, high voltages, water level, etc. This information will be available in the network together with the regular data stream and recorded on tape. This system will not handle the alarm system but will be only used to monitor the conditions at different sites.

## Beam History at the Neutrino Production Site

The precise micropulse time will be generated from a VME-based multihit TDC placed near the beam dump station, D0. The multihit TDC will be recording the timing difference between the AGS extraction signal and the time muons arrive at scintillator pads located near the beam dump, $t_\mu$. The TDC start time will be also be measured with respect to a GPS-synchronized timing system like those at the detectors. This information will be recorded to give us a time history of the AGS beam buckets. ¿From this record, we can produce a history of bucket arrival times at the detector sites, allowing an effective time cut to be made on background events.

## Summary of Section III C.

This section has described the detector electronics, relative timing of the several detectors and the AGS, and the distributed data collection system for E889. This system is planned to run synchronously with the AGS extraction cycle, and requires a bi-directional communication system in which the timing signal from the accelerator is propagated to the detector sites and digitized data returned to a base station at BNL.

In considering the choice of the front end electronics we have opted to use the same system as that designed for the SNO detector. In spite of the differences in the event rates between our detectors and SNO, the synchronous mode of operation should easily provide for use of the SNO electronics in E889. By choosing this particular front end we profit from an existing design. SNO is scheduled to start taking data in 1996 and therefore most of the front end electronics will be available to us by the end of 1995.

The estimated rates for the cosmic ray background should not present a problem in the synchronous running mode. Estimates indicate that with a 10 $\mu s$ gate to enable the DAQ at every site, the background rate is a few Hz. The timing signal is distributed to all sites by means of microwave links. To the far sites we would allow a timing jitter of about 1 $\mu s$ which should not be a problem. The same microwave link will be used for digital communications. Since we do not expect rates higher than 10 kbytes/sec from each site this link should be more than adequate for the transmission of digitized data from the distant sites. Data from all sites will be collated at the base station in BNL. However each site will have its own tape to backup the local data.

Finally, a comment on our estimated timing resolution. Since the current plan is to use GPS receiver systems to time each event we expect a resolution less than 10 ns. This resolution is not to be confused with the PMT resolution which will be of the order of 1 ns. While we present here our current idea of how to assign a time stamp to each event, we are pursuing other options. These are detailed in appendix I.

## APPENDIX I: Other Avenues for Accurate Timing

We expect a resolution of less than 10 ns from our baseline GPS-based timing system. However, it is our understanding that this value may be significantly reduced. We are therefore studying other approaches in the hopes of further improving the timing resolution and present three here:

- **Direct Transmission of the AGS Beam Time Signal**: The Division of Time, Frequency, and Lasers of the National Institute in Science and Technology (NIST) at Colorado presently maintains nanosecond-level synchronization between atomic clock standards in Boulder and Europe via a microwave satellite link. To achieve a sharp pulse edge, they use a spread-spectrum Ku and C band modem, and to monitor and adjust for propagation delay variations, they employ a technique of simultaneous two-way time transmission at both sites. Since we plan microwave links for the transmission of the BEAM-ENABLE signal for computer telecommunications, we are investigating these methods to see if they can be employed by us between sites.

- **Geostationary Satellite Services**: To prevent accurate positioning of commercial GPS receivers, the high precision bits of the broadcast signal are intentionally encrypted so that non-military systems only obtain the time to within ~100 ns. While the techniques of averaging and running simultaneous systems in Common View Mode can increase this, a problem remains of time loss when satellite re-acquisition occurs.

  We are investigating timing receiver services which use an alternative satellite system, called INMARSAT, which is launched and maintained by an international consortium for the purposes of accurate navigation. This system presents no intentional degradation of accuracy; timing resolutions of 5 ns are possible. Furthermore, these satellites are *geostationary*, so there is no problem of satellite loss and re-acquisition. We are currently in contact with a manufacturer who could provide us with receivers for this system in the very near future.

- **Full GPS Access.** The dithering of GPS timing information on the civilian channel is referred to as Selective Availability or SA. Another avenue that we will explore is the possibility of obtaining access to full information from the GPS satellites. We have learned that the CASA (Cosmic Air Shower Array) detector can achieve 7 ns resolution using GPS with no SA.

## APPENDIX II: Physical Layout and Power at Each Detector Site

Each site will have 5 electronics crates holding the Front End Cards, the High Voltage Cards, and a Crate Trigger card. The electronics crates will be controlled by the Master Crate at each site.

## Power Requirements

Each detector will have approximately 2550 PMTs to be readout and and supplied with high voltage. At each detector site there will be:

1. 5 electronics crates :

   16 High Voltage Cards per crate with 32 channels each

   16 Front End Cards per crate 32 channels each

   1 on-board repeater per crate

   1 Trigger Control Card per crate

2. 1 DAQ system (or Master Crate):

   1 on-board computer with tape drive and hard disk

   1 Global Trigger Card

   1 Global Timing Card

   1 GPS Timing System

3. 4 Low Voltage Power Supplies,

4. 5 High Voltage Power Supplies.

There will be six racks per detector location. Four electronics racks containing 2 electronics crates (512 PMT channels per crate) for a total of 1024 PMT channels per electronics rack, the low voltage power supplies, the Master Crate, and one NIM bin. The High Voltage Supplies will occupy one rack, as will the DAQ system.

The total power needs for each detector location is approximately 5 kilowatts, which is slightly higher than the SNO numbers because of some duplication of the control electronics. If allowance is made for growth in the system, the power needs should not exceed 7000 Watt per site.

## References

[1] D.F. Cowen, T. Ekenberg, J.R. Klein, F.M. Newcomer, R. Van Berg, R.G. Van de Water, P. Wittich, A. Biman and R.L. Stenson. *The Sudbury Neutrino Observatory Electronics Chain*, IEEE Trans. on Nucl. Science (1995), in print.

[2] C. Chen, *Common View Mode GPS Test Data*, DATUM INC., Anaheim, California 92806-5790.

## Figure Captions

Figure 1. Structure of the Fast Extracted Beam (FEB) from the AGS and the BEAM-ENABLE gate. In the FEB running mode the AGS macro cycle is 1.6 s. Each spill consists of 8 buckets 30 ns long and spaced by 335 ns. The Data Acquisition System will be enabled for a 10 $\mu s$ long gate which brackets the 2.7 $\mu s$ long AGS beam spill.

Figure 2. Overview of the Distributed E889 Data Acquisition System. The BEAM-ENABLE signal will be propagated to the detector sites over microwaves. Digital data from detector sites will be collated at the Base Station using fiber optics and microwave network links. Each site will be equipped with a precision oscillator synchronized by GPS receivers to provide a time stamp for each event.

Figure 3. The AGS Extraction Timing. During the AGS acceleration cycle $t_{AGS}$ signal is generated. An integer number of orbits after its generation the beam will be extracted.

Figure 4. Overview of the detector DAQ system.

Figure 5. SNO Electronics packaging. The Front End Cards will be housed in custom 9U VME crates. The Trigger card sits in the center of the crate and interfaces to the F.E.C via the backplane. Each Front End Card (F.E.C.) connects to 32 PMTs trhough the backplane P2 connector. P3 provides links to trigger and VME Master. P1 is the High Voltage bus.

Figure 6. The Logic Diagram for one PMT Channel. Each PMT is connected to the system via a single Coaxial Cable. The signal is decoupled from the High Voltage by a capacitor at the input of the preamplifier. The preamplifiers are followed by custom design integrated circuits to digitized and store charge and time measurements.

Figure 7. Front End Electronics setup at one detector.

Figure 8. Block Diagram of the SNO bipolar chipset, SNOD and SNOINT.

Figure 9. Single Channel timing cycle for the SNO front end electronics.

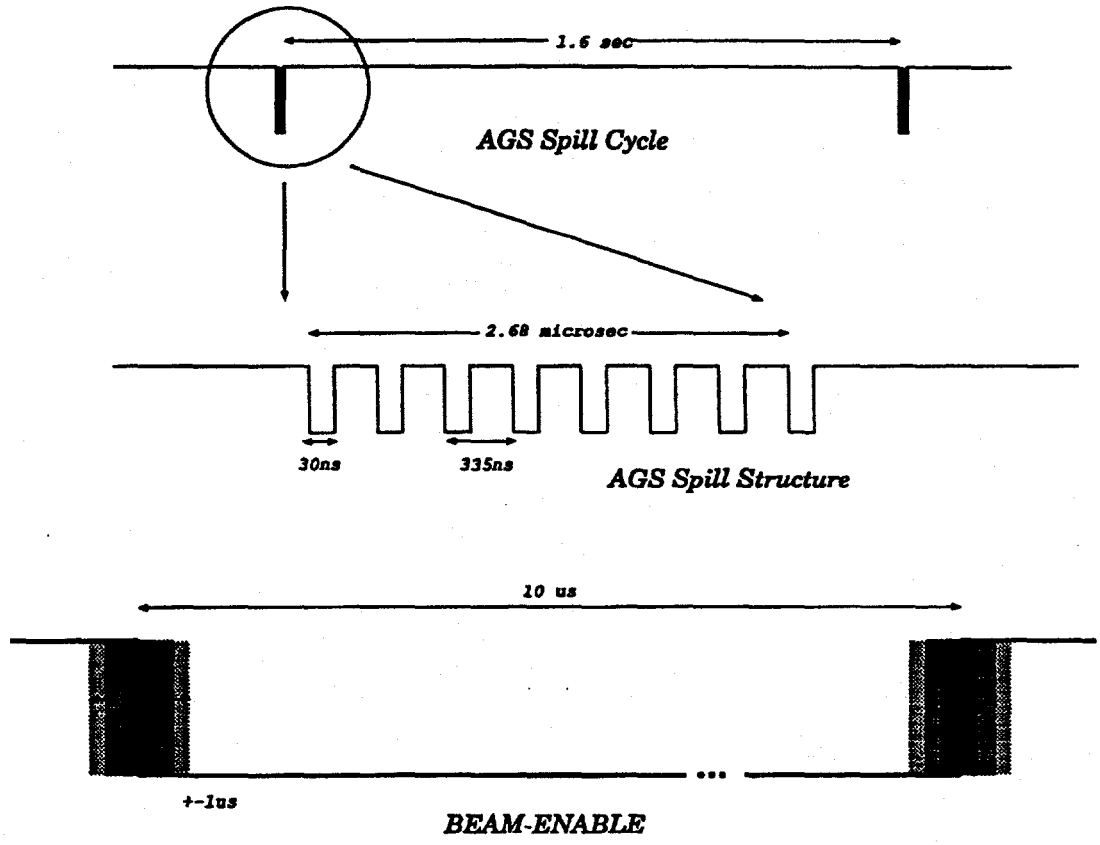
1.6 sec
AGS Spill Cycle
2.68 microsec
30ns
335ns
AGS Spill Structure
10 us
+-1us
BEAM-ENABLE

Fig. 1

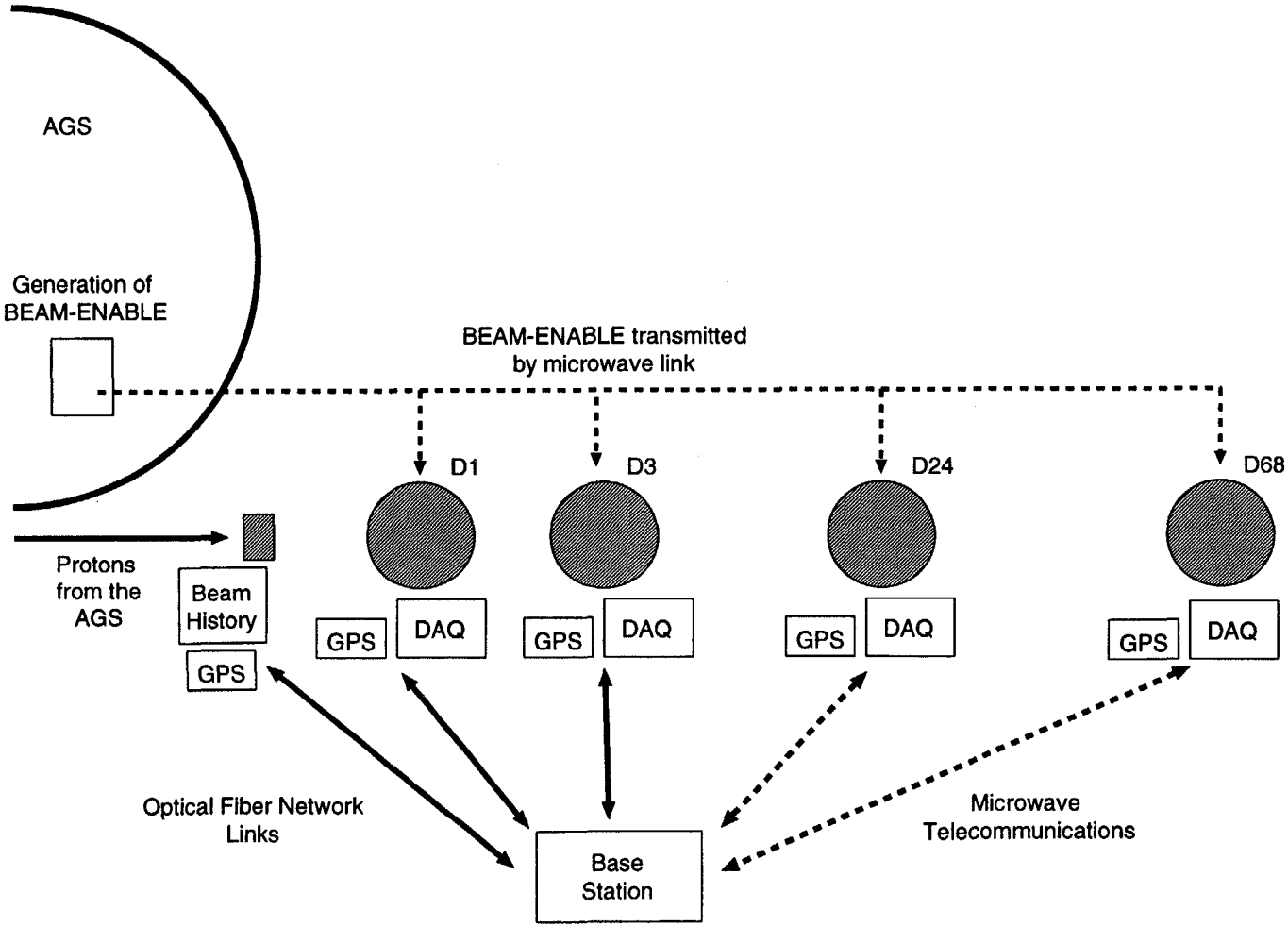
AGS
Generation of
BEAM-ENABLE
BEAM-ENABLE transmitted
by microwave link
D1
D3
D24
D68
Protons
from the
AGS
Beam
History
GPS
GPS
DAQ
GPS
DAQ
GPS
DAQ
GPS
DAQ
Optical Fiber Network
Links
Base
Station
Microwave
Telecommunications

**Fig. 2**

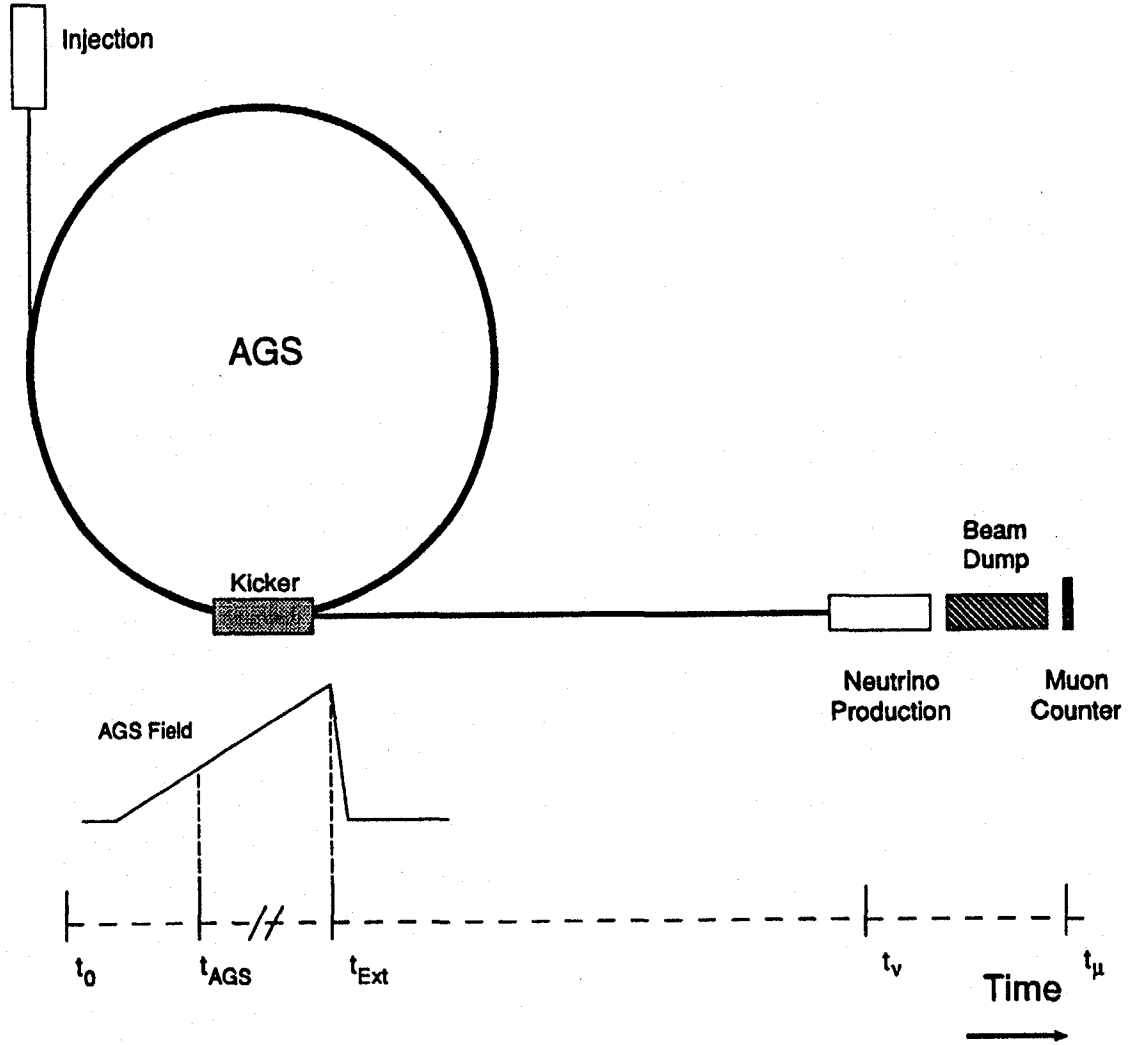
Injection
AGS
Kicker
Beam
Dump
Neutrino
Production
Muon
Counter
AGS Field
$t_0$
$t_{AGS}$
$t_{Ext}$
$t_\nu$
$t_\mu$
Time

Fig. 3

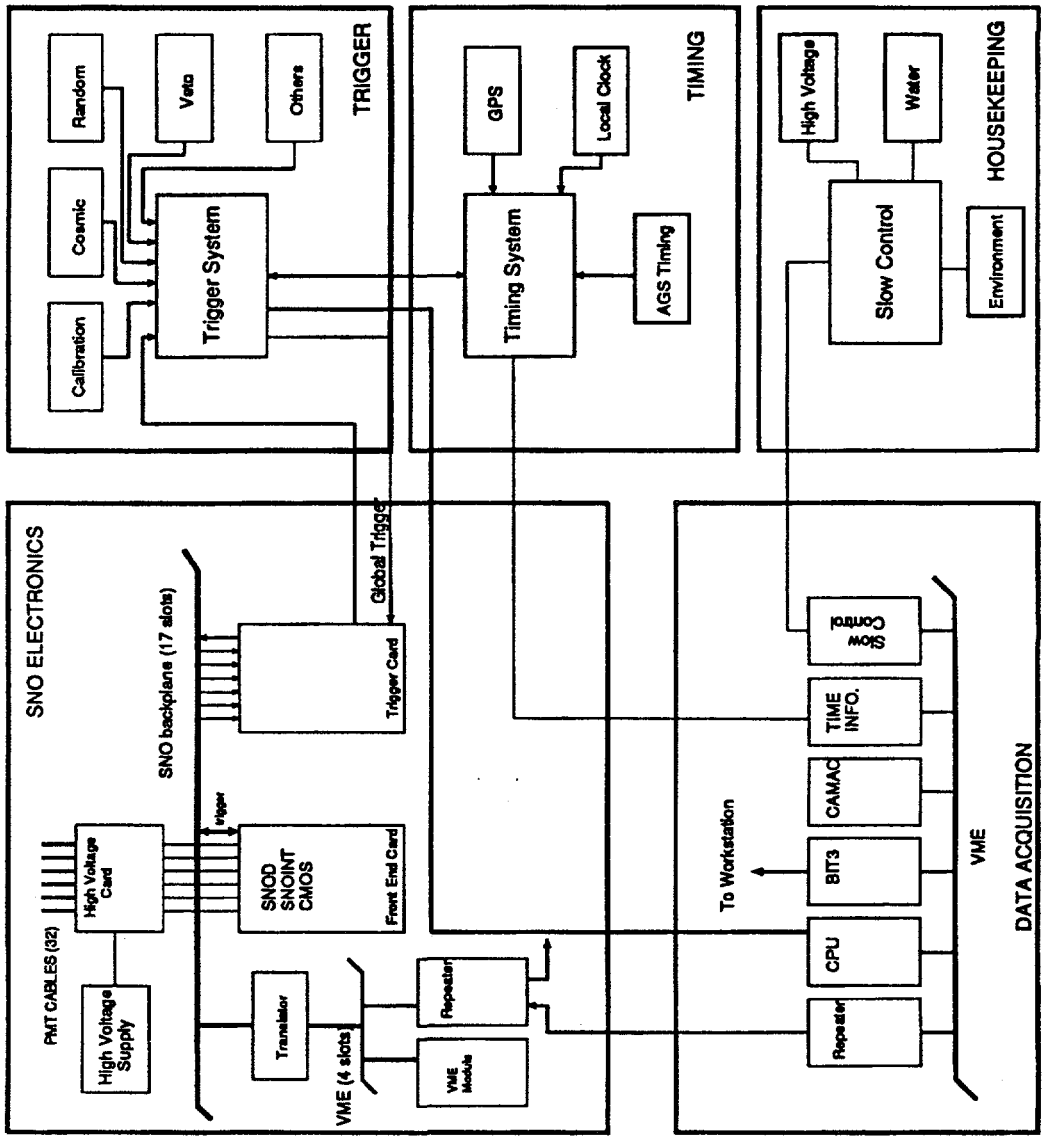
TRIGGER
Random
Veto
Others
Cosmic
Calibration
Trigger System
TIMING
GPS
Local Clock
Timing System
AGS Timing
HOUSEKEEPING
High Voltage
Water
Slow Control
Environment
SNO ELECTRONICS
Global Trigger
SNO backplane (17 slots)
Trigger Card
High Voltage Card
SNOD SNOINT CMOS
Front End Card
PMT CABLES (32)
High Voltage Supply
Translator
VME (4 slots)
Repeater
VME Module
To Workstation
TIME INFO.
CAMAC
BIT3
CPU
Repeater
VME
DATA ACQUISITION

Fig. 4

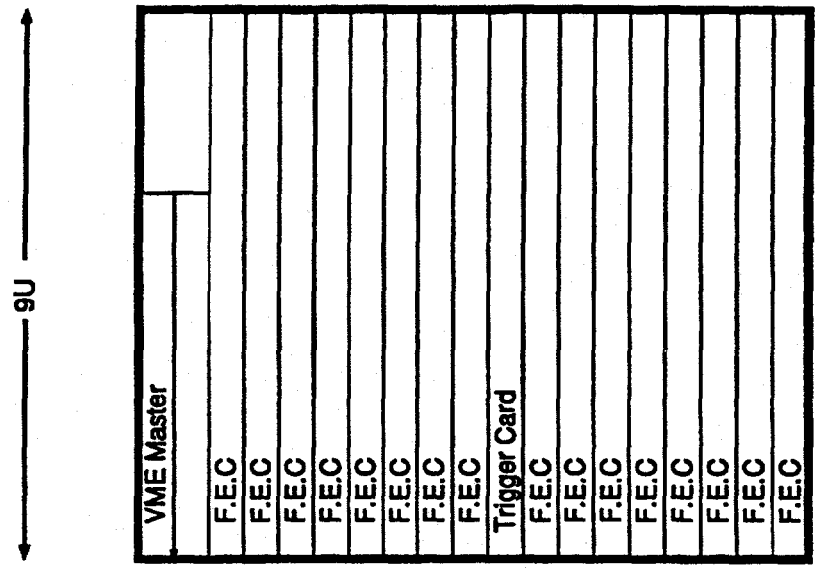


SNO Electronics Crate
Front View

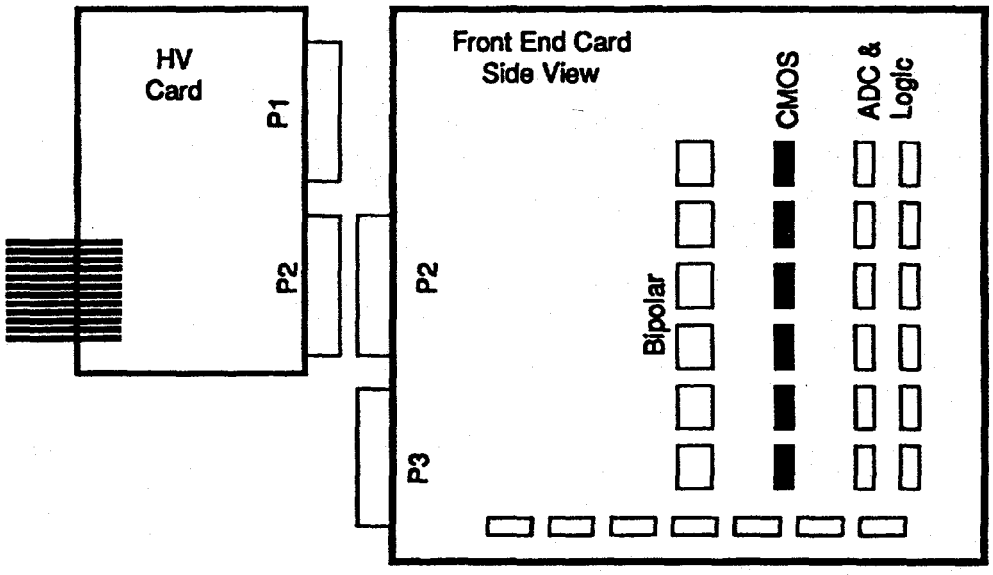


Fig. 5

Logic Diagram - PMT Electronics

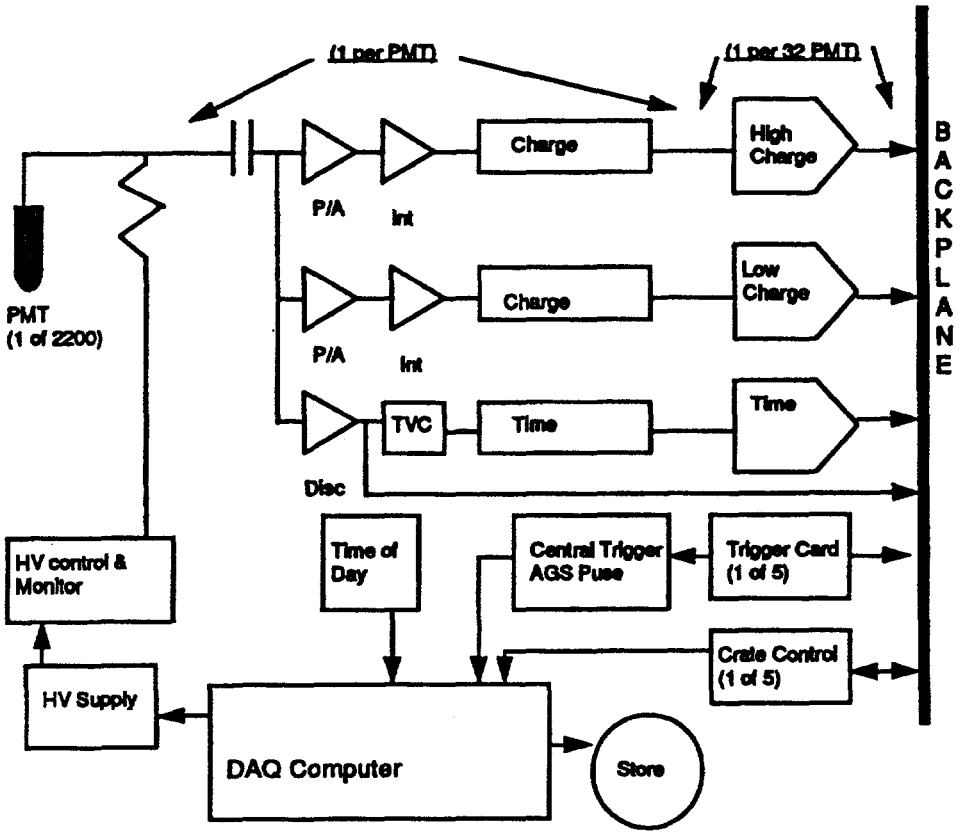


Fig. 6

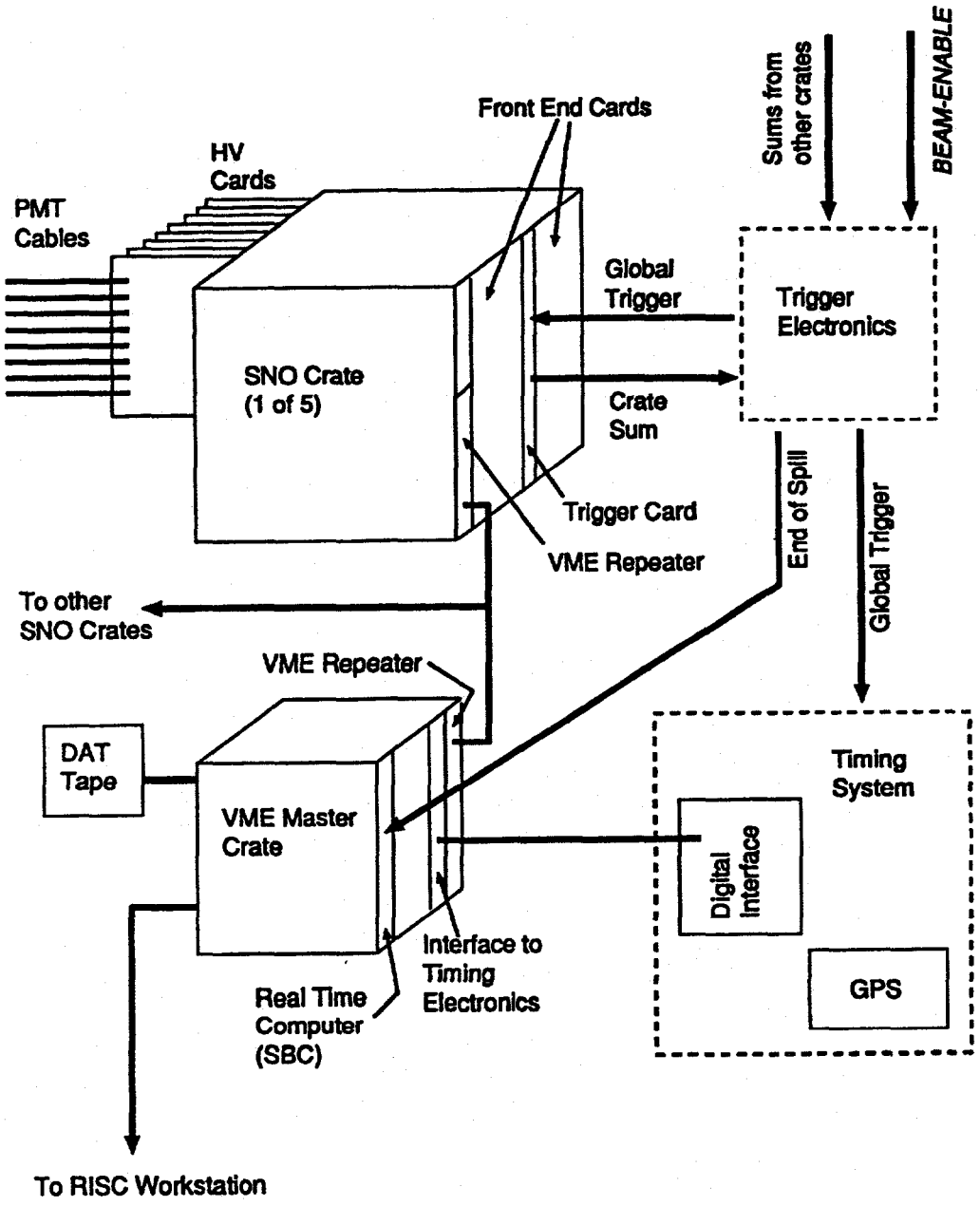
Front End Cards
HV
Cards
PMT
Cables
Sums from
other crates
BEAM-ENABLE
Global
Trigger
Trigger
Electronics
SNO Crate
(1 of 5)
Crate
Sum
Trigger Card
VME Repeater
End of Spill
Global Trigger
To other
SNO Crates
VME Repeater
DAT
Tape
VME Master
Crate
Timing
System
Digital
Interface
Interface to
Timing
Electronics
Real Time
Computer
(SBC)
GPS
To RISC Workstation

Fig. 7

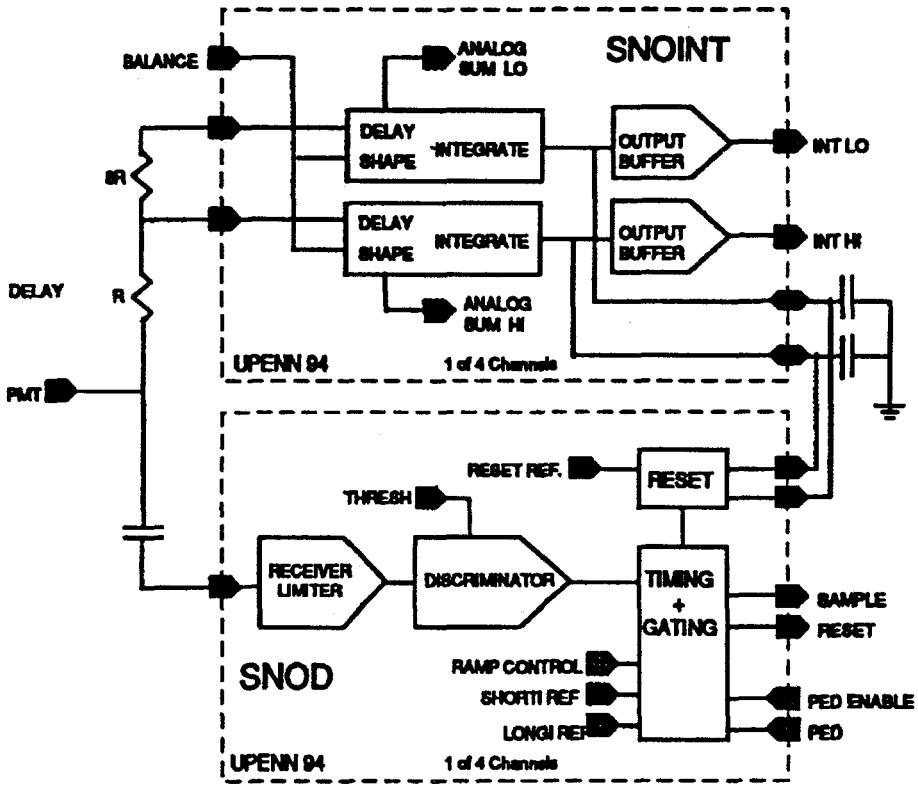
SNOINT
BALANCE
ANALOG SUM LO
DELAY
SHAPE
INTEGRATE
OUTPUT BUFFER
INT LO
8R
DELAY
SHAPE
INTEGRATE
OUTPUT BUFFER
INT HI
DELAY
R
ANALOG SUM HI
UPENN 94
1 of 4 Channels
PMT
RESET REF.
RESET
THRESH
RECEIVER LIMITER
DISCRIMINATOR
TIMING + GATING
SAMPLE
RESET
SNOD
RAMP CONTROL
SHORTI REF
LONGI REF
PED ENABLE
PED
UPENN 94
1 of 4 Channels

Fig. 8

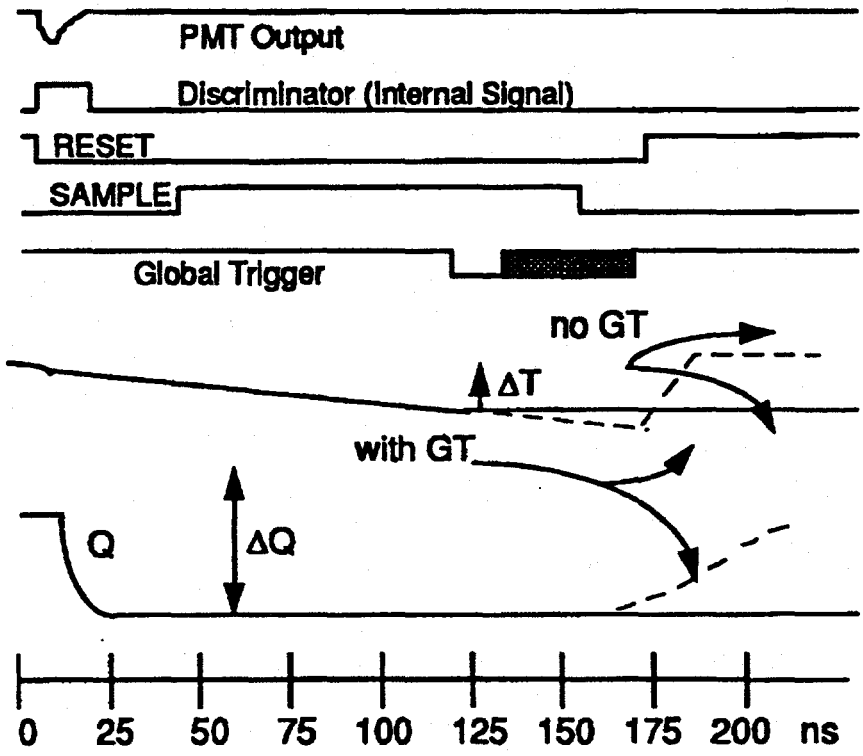
PMT Output
Discriminator (Internal Signal)
RESET
SAMPLE
Global Trigger
no GT
ΔT
with GT
Q
ΔQ
0
25
50
75
100
125
150
175
200
ns

Fig. 9

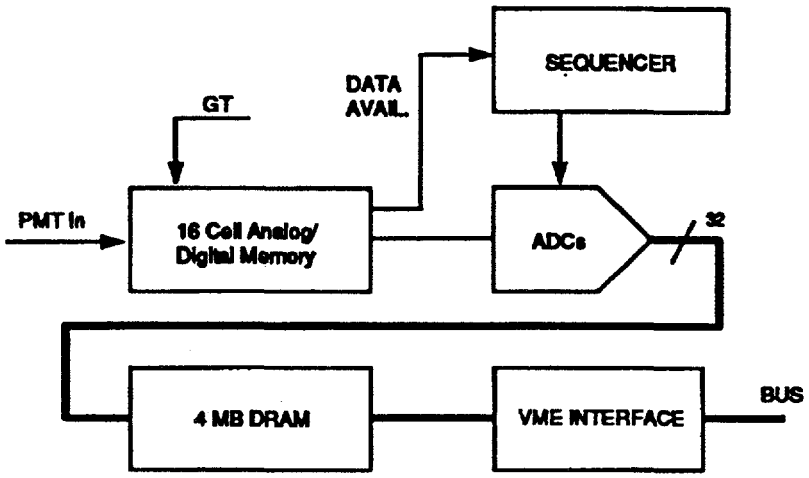


The Three Word Data Structure Table

| | | | |
|---|---|---|---|
| 1 | Flag 2 | Crate + Channel 5 \| 9 | Trigger Identifier \| 8 \| 8 |
| 2 | Err 4 | QLoLong \| 12 | Flag 4 \| QHiLong \| 12 |
| 3 | Cell 4 | TAC \| 12 | Flag 4 \| QHiShort \| 12 |

Fig. 10

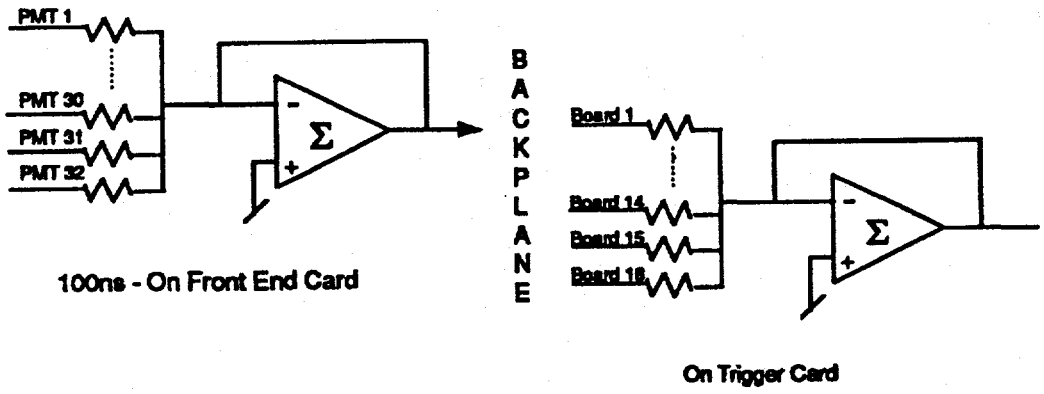
PMT 1
PMT 30
PMT 31
PMT 32
Σ
100ns - On Front End Card
BACKPLANE
Board 1
Board 14
Board 15
Board 16
Σ
On Trigger Card

Fig. 11

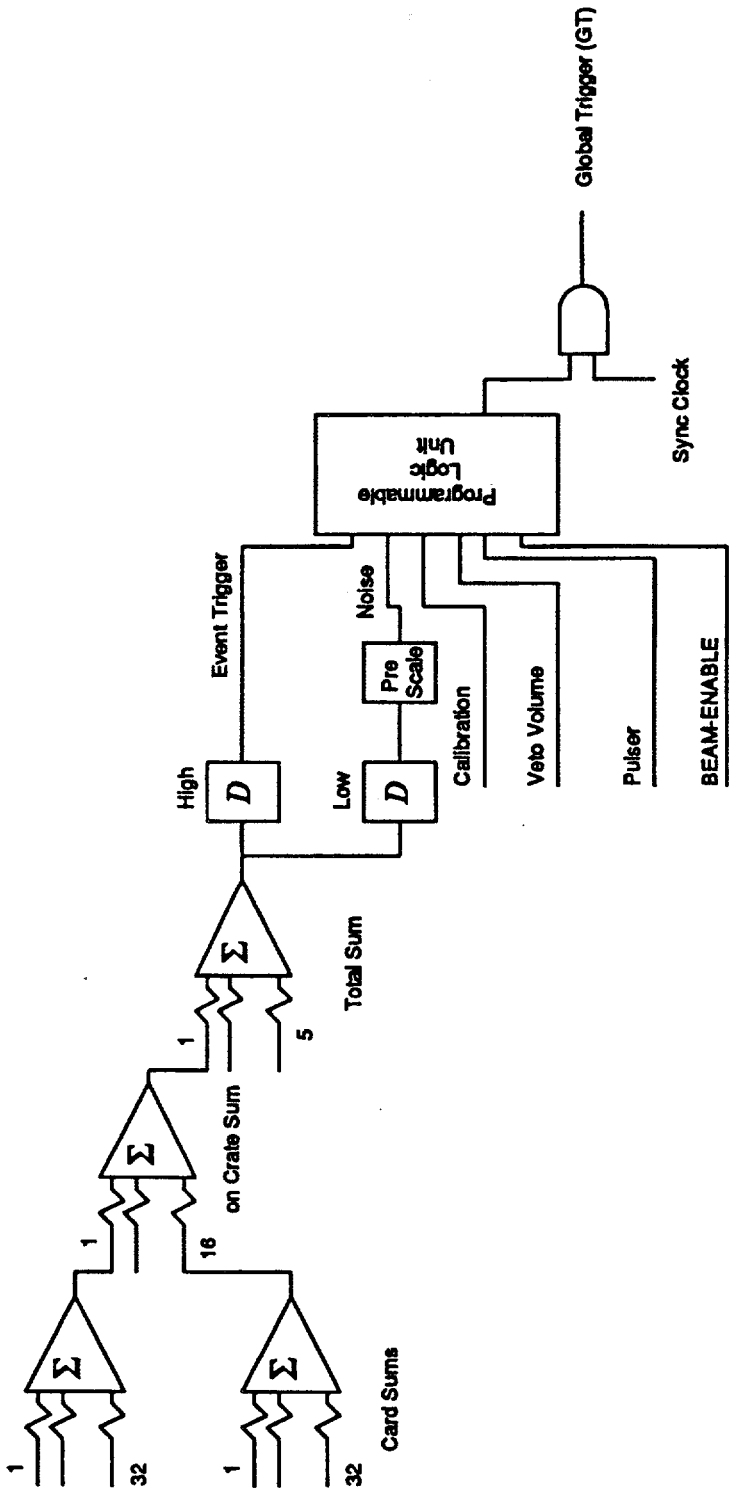
Global Trigger (GT)
Sync Clock
Programmable Logic Unit
Event Trigger
Noise
Pre Scale
Calibration
Veto Volume
Pulser
BEAM-ENABLE
High
Low
D
D
Total Sum
on Crate Sum
Card Sums
1
5
1
16
1
32
1
32

Fig. 12

# IV. Pattern Recognition and Particle Identification

## Introduction

This is not the first neutrino experiment to use imaging water Cherenkov detectors. The data reduction and analysis methods originally developed by the Kamiokande and IMB detectors serve as an invaluable basis for the techniques to be used in E889. They are described in detail in Ph.D. theses cited at the end of this chapter. Accordingly, we do not here attempt an in-depth discussion of those relatively well-known methods. Instead, we discuss their application to the needs of E889 to show that those needs can be well satisfied. Specifically, we address the important questions of muon-electron separation; of the efficiency with which WNC($\pi^0$) events can be recognized and also distinguished from WCC($\pi^0$) events; and the extent to which aberrant WNC($\pi^0$) events might constitute a background in the $\nu_\mu \leftrightarrow \nu_e$ search. With the neutrino beam for E889 described in Chapter III, the dominant neutrino reaction product is a quasielastic muon, and to a much lesser extent a quasielastic electron, both single Cherenkov ring events. Single pion production, yielding two- or three-ring events is also an important event type. In addition, we comment briefly on our progress in developing methods of automatic pattern recognition and reconstruction of multiring events.

## Previously Developed Methods of Analysis

Neutrinos interacting in a large water detector will produce charged particles, each of which may produce a Cherenkov cone of ultraviolet and visible photons. Where the cone intersects the inner surface of the detector tank a ring-like pattern of PMT will be lit. A pattern may consist of a single ring, two or more separated or overlapping rings, or in a few cases PMT hits with no clear organization. The recorded time, amplitude and known location of each hit PMT provide all the information necessary to reconstruct the event and classify it according to the number and quality of rings observed. Both the disappearance and appearance modes of E889 depend on the efficient classification of hit patterns, specifically, discrimination among the patterns produced by muon, electron, and weak neutral current (WNC($\pi^0$)) events, and weak charged current (WCC($\pi^0$)) events. Previous underground experiments performed this task by reconstructing the vertex and particle direction corresponding to each designated ring, supplemented by visual scanning of the events. Reconstruction of single ring events was done automatically, i.e., without direct human operator intervention, while multiring events were reconstructed with an interactive manual program.

The resolution in position of event vertices, $\sigma_{pos}$, and of track directions, $\sigma_\theta$, for single ring muon and electron events is well understood in both the Kamiokande and IMB detectors. $\sigma_{pos}$ as a function of the number of photoelectrons (and momentum) is shown in Fig. 1a; $\sigma_\theta$ in Fig. 1b. These results obtained with Monte Carlo generated events are from the thesis of M. Takita. Essentially the same results are presented in the theses of D.W. Casper and E.D. Frank, all cited here. For E889 we expect somewhat better position resolutions due to the better quality of time information from our 20 cm PMTs than the Kamioka PMTs. Our present simulations suggest that position resolution of $\sim$ 30 cm parallel and $\sim$ 15 cm perpendicular to the direction of a particle of 1 GeV/c is possible. This is entirely adequate for the experiment. The energy response of the detector for various particles is shown in Figure V.6.

## E889 Analysis

The same procedures will be followed in analyzing the data of E889 which, like Kamiokande and IMB, is basically an electronic detector. From the times recorded by the hit PMT, a first estimate of the vertex of a given event is made. This is iterated after correcting the raw times for the flight path of the Cherenkov light from the estimated vertex to a given PMT. For a single ring the corrected times fall within an interval of less than 20 ns FWHM, superimposed on a flat distribution due to scattered Cherenkov light and multiple scattering of delta rays. Another iteration in which much of the flat distribution is not included in the vertex calculation usually brings the FWHM value of corrected time distribution to less than 15 ns. There are several refinements to this procedure, e.g., introducing the charge amplitude of the hits independently of or in combination with the time information, limiting the analysis to events with a minimum number of hit PMT and charge, etc. Using the final iterated vertex coordinates and the known positions of the hit PMT, the direction of the axis of the Cherenkov cone, i.e., the particle direction, can be found and specified by its direction cosines. The corrected total charge observed in the ring yields the particle momentum which can be checked against its range from properties of the ring.

With the vertex specified the events within the fiducial volume can be selected. The quality of these events, signified by the errors in the vertex coordinates and track direction cosines, the width of the time distribution, the ratio of the number of tightly bunched-in-time PMT hits to the number in the flat time distribution, etc, is used to determine whether the event under consideration is a single-ring event or not. In E889 we expect roughly 20% of

events to involve more than one ring, so that this procedure separates the dominant single ring quasielastic muon sample, with each event fully reconstructed, from the multiring sample, which requires further analysis.

It should be emphasized that the method of analysis outlined here which provides first order pattern recognition is the result purely of computer processing of PMT signals. No visual scanning of events is necessary, apart from the initial checks on the validity of the programs and the parameters. It involves an analysis simpler in form and less demanding of computer time than analyses of magnetic field-chamber-counter experiments.

The roughly 20% of the data that does not satisfy the single ring criteria needs separate analysis. This can be done for the number of events of that type expected in E889 by an operator assisted interactive program which handles each ring in a multiring event, i.e., identifies the PMT hits belonging to each ring and reconstructs the parameters of each ring separately, and of the complete event in combination. Event samples consisting of $10^4$ events in D1 would contain about $2 \times 10^3$ multiring events to be analyzed in this way, not a serious burden for the collaboration since only analysis of large samples in D1 and D3 is required to set the criteria and conditions for the analyses of all the multiring events in D24 and D68.

It is, however, an interesting and challenging problem to develop programs capable of automatic pattern recognition and reconstruction of multiring events. While not required to do the experiment, these would facilitate data analysis and provide useful redundancy. We have begun work in this direction which is briefly described in the last section of this chapter.

### Muon-Electron Separation

There are available a number of algorithms with which to distinguish single-rings produced by muons (or charged pions) from those produced by electrons. These are described in detail and evaluated in the references given here. Muon-electron separation has been accomplished previously with high efficiency, as indicated by the agreement between the results from the IMB and Kamiokande collaborations on atmospheric neutrinos, and by the internal consistency of the results obtained within each collaboration when identical event samples are processed using different algorithms. Again, this aspect of the analysis is carried out at least in first order by computer processing. The small number of electron (single showering ring) events expected in E889 permits them to be studied visually as well as electronically without appreciable extra effort. Recently, a 1-kiloton test imaging water Cherenkov detector has been exposed to muon and electron beams at KEK of several momenta, differently positioned

within the detector. Some unpublished results—confirming in quantitative detail the previously claimed muon-electron separation—are shown in Fig. 2. One sees that the degree of muon-electron separation depends on particle momentum, but by 400 MeV/c the separation achieved with the algorithms employed in the analysis is complete within the statistical limits of the samples. These preliminary results will soon be supplemented by larger event samples.

The particle identification requirement in E889, where the relative intensities of electron and muon are in the approximate ratio $10^{-2}$, is moderately severe. Misidentification of muons from $\nu_\mu n \to \mu^- p$ as if they were electrons coming from $\nu_e \mu \to e^- p$ should be less than 1 part in $10^3$, if the search for oscillations in the appearance channel $\nu_\mu \leftrightarrow \nu_e$ is to be carried out below the 1% level. We are confident that this can be accomplished in part because of the data in Fig. 2. Also, by combining several algorithms each known to be of $\gtrsim$ 90% efficiency, and each based on an independent quantity, e.g., PMT hit location, PMT hit time, PMT hit charge, with visual scanning of the small number of electron candidates, there appears to be no intractable difficulty in reaching 1 part in $10^3$.

Note that exclusion of questionable events from both the muon and electron samples will not induce an apparent positive oscillation effect, but dilution of a real $\nu_\mu \leftrightarrow \nu_e$ signal must be guarded against. Note further that muon and electron event selection criteria will be set empirically by study of those event types in the upstream detectors D1 and D3, where the electron to muon number ratio to be expected in the far detectors in the absence of oscillations will also be measured. Muon-electron discrimination is discussed again briefly in the section on event recognition below.

## Multiring Events

The other ring patterns of interest are the products of exclusive channel inelastic reactions, principally those involving single pion production, i.e., the flavor preserving WNC($\pi^0$) reactions $\nu_n \to \nu n \pi^0$ and $\nu p \to \nu p \pi^0$, the single WCC($\pi^0$) reaction $\nu_\mu n \to \mu^- p \pi^0$, and the WCC($\pi^\pm$) reactions. The patterns of all these reactions are in general distinguished by the presence of two or more rings. Given the rates of these reactions with respect to the quasielastic reaction rate, discussed earlier in Chapter II and later in Chapter V, the problem of identification is focused on distinguishing the relatively few events with more than a single ring from the multitude with only a single ring. The inverse problem is relatively unimportant. With the usual automatic pattern recognition and reconstruction of single ring events described above, those events in the detector fiducial volume not satisfying an event-quality

criterion, e.g., a chi-square fit to the ring, can efficiently be set aside for visual inspection and interactive manual reconstruction. All of the data in D24 and D68 can be handled in this way, and large data samples from D1 and D3 treated the same way to fix event selection criteria and serve the purpose of normalization. The efficiency with which visual scanning permits discrimination of WNC($\pi^0$) events from WCC($\pi^0$) is treated in the next section, as is the discrimination of WNC($\pi^0$) from electrons when one of the rings from the $\pi^0$ is not evident.

## Visual Event Recognition

Simulated QE($\mu$), QE(e), WCC($\pi^0$), and WNC($\pi^0$) events have been generated and scanned visually. In all cases, the particles were generated by allowing the spectra of $\nu_\mu$ and $\nu_e$ planned for E889 to interact in a cylinder of water 15m high $\times$ 15m in diameter. The PMT lining the walls of the cylinder were simulated by sensitive disks 25.2 cm in diameter, an approximation to physical PMT 20 cm in diameter with Winston cone light collectors. The spectral response of the PMT was included in the simulation. 2195 such tubes are placed uniformly on the inner walls of the detector tank to attain 10.3% coverage. This configuration allows efficient visual identification of all WNC and WCC events for a relatively small total area of photocathode. It is possible that a non-uniform configuration of PMT would be more efficient in light collection for E889, but this has not yet been studied with sufficient care.

Quasielastic muon events have single Cherenkov rings with sharp outer edges and relatively few PMT hits outside the ring. Quasielastic electron events have single rings with fuzzy edges and many hits outside the ring due to multiple scattering and bremsstrahlung. Examples of real and simulated muon and electron events from the Kamiokande detector illustrating these properties are shown in Figs. 15 and 16 of Chapter II. Similar displays of Monte Carlo muon and electron events using E889 programs are shown in Chapter V. When quantified, the event properties in those figures form the bases of the algorithms for muon-electron identification mentioned above.

Most WNC($\pi^0$) events display two fuzzy edged rings; most WCC($\pi^0$) events exhibit a clear muon ring in addition. Examples of a WNC($\pi^0$) event and a WCC($\pi^0$) event from the E889 Monte Carlo event simulation and display programs are shown in Figs. 3 and 4, which exhibit the characteristic properties of those event types.

In our visual scanning exercise of $\pi^0$ events, positive event type recognition is considered to be achieved when the correct number and type of rings are clearly observed. However,

interaction kinematics and detector response may lead some events to have signatures which are less than ideal. For example, asymmetric ($\pi^0$) decays may produce a gamma ray whose shower has too little energy to yield a clear ring, causing only one ring to be observed. Similarly, if the vertex of the reaction is near the boundary of the fiducial volume, one of the gammas from a symmetric decay may not convert far enough within the fiducial volume to produce a clear ring, or indeed any ring. Alternatively, $\pi^0$with higher momentum will yield gamma rays with overlapping rings, which in some cases appear as a single ring. Conversely, a small fraction of WNC($\pi^0$) events may show three fuzzy edged rings if either the $\pi^0$decay is directly to $\gamma e^+e^-$ or if one of the $e^+e^-$ pair produced in the gamma conversion scatters at a large angle.

For these reasons the results of a visual scan of one thousand WNC($\pi^0$) and one thousand WCC($\pi^0$) events, shown in Table 1, are divided into the following categories: one ring; one ring plus a number of PMT hits representing a substantial part of, but not a complete, second ring; two rings; two rings plus; three rings; three rings plus; and unidentifiable events. In addition, the WCC($\pi^0$) events have been divided into those in which a muon ring is clearly identified, and those in which the muon is not evident. The fiducial volume for the two samples is a cylinder of diameter 13 m and height 13 m. Events with fewer than 50 PMT hits or fewer than 300 photoelectrons ($p$ ($\pi^0$) $\sim 10^2$ MeV/c) were not included.

Combining the results for the (1 ring +) and 2-ring samples in Table 1 yields a detection efficiency of 75% for WNC($\pi^0$) events. If, however, the criterion for $\pi^0$identification is restricted to require 2 rings which reconstruct manually to give the invariant mass of the $\pi^0$, the detection efficiency should be approximately 50%. This exercise was originally carried out on Monte Carlo generated events by Katsushi Arisaka in the first Ph.D. thesis from Kamiokande; his result is shown in Fig. 5. The results in Table 1 have been reproduced independently by three different scans.

Comparing the data in the two WCC columns indicates that at least 81% of the WCC($\pi^0$) events can be identified by the presence of a clear muon ring. Hence, efficient rejection of the WCC($\pi^0$) background at the 20% level in the WNC($\pi^0$) sample is possible simply by requiring a clear muon ring, since both WNC($\pi^0$) and WCC($\pi^0$) production occur at approximately 20% and 15%, respectively, of the quasielastic muon rate. The approximately 20% of 1-ring events in the top row of Table 1 are not a serious background for the $\nu_\mu \leftrightarrow \nu_e$ oscillation search as shown in Chapter V.4.

Again, note that in both the case of WCC($\pi^0$) contamination of the WNC($\pi^0$) signal, and the case of 1-ring $\pi^0$ contamination of the electron signal, the upstream detectors D1

and D3 are used to set empirically the criteria for event selection and to normalize the ratios of event types to be detected in the far detectors. No reliance on Monte Carlo predictions is necessary.

## PMT Diameter and Areal Coverage

Similar scans of WNC and WCC($\pi^0$) events were performed for two other PMT coverage schemes to check that the coverage adopted for E889 is adequate for those event types, which require larger coverage for efficient detection than do the single ring events.. Scheme II used 1807 PMT each 20 cm in diameter and having no light collector. The total coverage was 5.4%. Scheme III used 1002 50 cm diameter PMT also without light collectors (as in Kamiokande II) for a total coverage of 18.6%. Results for the WNC scan, along with those from scheme I (10.3% coverage), are shown in Table 2. Since the visual scans for schemes II and III did not include the categories of fractional rings, events in those categories in scheme I were evenly divided between integral ring categories for the sake of comparison.

Table 2 shows that in going from 5.4% to 10.3% coverage significantly more 2-ring events are identified. At the same time the number of WNC($\pi^0$) 1-ring events decreases correspondingly. Going to 18.6% coverage produces no appreciable increase in the number of 2-ring events observed, indicating that an approximate plateau in coverage is reached at 10.3%. Similar results are obtained in the scan of WCC events. Even the 5.4% coverage is adequate for single ring events.

## Automated Pattern Recognition and Reconstruction of Multiring Events.

There are several methods of automated pattern recognition of multiring events aimed largely at facilitating data analysis in E889, which are currently being explored. These make use of pattern properties such as the fraction of PMT hits outside the Cherenkov cone, and the circularity of the event pattern, and attempt ring recognition and reconstruction by automatic scanning and neural networks.

1. The fraction of PMT hits outside the Cherenkov cone can be found by first computing an event vertex and apparent track direction from timing information alone. The reconstructed apparent track direction is taken to be the average of all rays connecting the vertex to hit PMT locations, and the angle between each ray and the apparent track direction is computed. The fraction of hits, including random hits from light scattering,

etc., with angles in various angular regions outside the nominal Cherenkov ring may be used to discriminate between single and multiring events.

2. Circularity is a measure of the moments of the PMT hit pattern projected onto a sphere. This method utilizes the idea that momenta of the PMT charge distribution of multiring events with respect to the angular separation from the mean should be larger in one azimuthal direction than the corresponding distribution for single ring events.

3. A possible automatic ring search routine employs a faster scan to locate and identify the number of rings in a hit pattern the same way the eye does in visual scanning. This method is quite general and does not depend upon knowing the event vertex. A search for hits is made, first over the rows, then the columns of the PMT array in the detector. The first hit encountered in each row and column which is above a given photoelectron threshold is saved. The saved set of hits is thus the outline of the event pattern. When tested on single ring events, the ring size and shape is faithfully reproduced. When generalized to multiring events, this feature may allow assignment of PMT hits to the appropriate rings which might then be used to reconstruct multiple particle tracks.

4. In a more speculative direction, work is in progress on the application of neutral networks to recognition of the pattern of PMT hits in an event.

All of this work is in early stages of development. Nevertheless, sufficient progress has been made which encourages us to believe that one or more of these algorithms will be successful.

## Summary

In this chapter we have discussed the methods of data reduction and analysis inherited from previous collaborations on imaging water Cherenkov detectors, and described in some detail how they are directly applied to the data of E889 principally by computer processing. Specifically, we have confronted the questions of muon-electron recognition and separation, vital to a search in the $\nu_\mu \leftrightarrow \nu_e$ oscillation channel; and of the efficiency with which WNC($\pi^0$) events can be recognized and detected, essential to accurate measurement of the ratio WCC($QE\mu$)/WNC($\pi^0$) within each of the four E889 detectors. Aberrant WNC($\pi^0$) events may simulate quasielastic electron events and WCC($\pi^0$) may simulate WNC($\pi^0$) events if the muon is not evident. Both of these sources of background may be largely eliminated in direct ways, as described in this chapter, so that they are unlikely to introduce serious limitation

of the sensitivity of E889 oscillation searches. A more detailed analysis of the effect of these backgrounds on the E889 sensitivity is given in Chapter V. Finally, a brief progress report was given on methods of automatic pattern recognition and reconstruction of multiring events under development by the E889 collaboration.

Table 1: Result of visual identification of WCC($\pi^0$) and WNC($\pi^0$) events from Cherenkov ring patterns. Entries marked with an asterisk do not show a ring with a clear sharp outer edge.

| Classification | WNC($\pi^0$) | WCC($\mu$ not seen) | WCC($\mu$ seen) |
|---|---|---|---|
| 1 ring | 18.1% | 1.5% | 0.5% |
| 1 ring + | 20.8 | 1.5 | 2.9 |
| 2 rings | 54.2 | 6.1 | 11.2 |
| 2 rings + | 3.8 | 4.1* | 18.8 |
| 3 rings | 1.9 | 4.7* | 41.8 |
| 3 rings + | 0.4 | 1.0* | 5.6 |
| unidentifiable | 0.8 | 0.3 | 0.0 |

Table 2: Result of visual identification of WNC$\pi^0$ events for three PMT coverages.

| Classification | 5.4% coverage | 10.3% coverage | 18.6% coverage |
|---|---|---|---|
| 1 ring | 59% | 29% | 34% |
| 2 rings | 40 | 66 | 60 |
| 3 rings | 0 | 4 | 1 |
| $>$ 3 rings | 1 | 0 | 5 |
| unidentifiable | 0 | 1 | 0 |

## References

The publications in refereed journals of the Kamiokande & IMB groups, following the usual custom, tend to emphasize physical results rather than methods and techniques. The latter are, however, described in detail in the Ph.D. theses, Master's thesis and undergraduate senior theses, which are listed below.


1. K. Arisaka, "Experimental Search for Nucleon Decay", Ph.D. Thesis, University of Tokyo (1984) unpublished.

2. T. Kajita, "Search for Nucleon Decays in Antineutrino Plus Mesons", Ph.D. thesis, University of Tokyo (1985) unpublished.

3. S.C. Seidel, "A Search for Nucleon Decay Employing Particle Identification, Invariant Masses, and Complete Track Reconstruction in a Water Cherenkov Detector", Ph.D. Thesis, University of Michigan (1987) unpublished.

4. M. Nakahata, "Search for $^8B$ Solar Neutrinos at Kamiokande II", P.H.D. Thesis, University of Tokyo (1988) unpublished.

5. W. Zhang, "Experimental Search for Electron Antineutrinos from Past Supernovae", Ph.D. Thesis, University of Pennsylvania (1988) unpublished.

6. M. Takita, "An Experimental Study of the Atmospheric Neutrino Flux with the Kamiokande Detector", Ph.D. Thesis, University of Tokyo (1989) unpublished.

7. S.B. Kim, "Real time, Directional Measurement of $^8B$ Solar Neutrinos in the Kamiokande-II Detector and Search for Short-Time Variation", Ph.D. Thesis, University of Pennsylvania (1989) unpublished.

8. D.W. Casper, "Experimental Neutrino Physics and Astrophysics with the IMB-3 Detector", Ph.D. Thesis, University of Michigan (1990) unpublished.

9. E.D. Frank, "A Study of Atmospheric Neutrino Interactions in the Kamiokande-II Detector", Ph.D. Thesis, University of Pennsylvania (1992) unpublished.

10. Scott Smith, "Prospects for the Observation of Low Energy Neutrinos in a Massive Imaging Water Cherenkov Detector", M.S. Thesis, University of Pennsylvania (1985) unpublished.

11. Jared Anderson, "Computer Simulation of a Long Baseline Neutrino Oscillation Experiment", Undergraduate Thesis, University of Pennsylvania (1994) unpublished.

12. Siun-Chuon Mau, "Reconstruction Program for a Long Baseline Neutrino Oscillation Experiment", Senior Thesis, University of Pennsylvania (1994) unpublished.

## Figure Captions

Fig. 1. (a) Vertex resolution for muons (open circles) and electrons (solid circles) as a function of the total number of photoelectrons (and momentum). (b) Angular resolution for muons and electrons as a function of total number of photoelectrons. From the Ph.D. thesis of M. Takita.

Fig. 2. Preliminary results of muon-electron separation from the Kamiokande-KEK test detector. (a) Data. (b) Monte Carlo simulation.

Fig. 3. Simulated WNC($\pi^0$) event showing the two Cherenkov rings from the decay $\pi^0 \rightarrow \gamma\gamma$.

Fig. 4. Simulated WCC($\pi^0$) event showing the two fuzzy edged rings from the $\pi^0$ decay and the sharp edged ring from the muon.

Fig. 5. Reconstruction of the invariant $\pi^0$ mass from a number of simulated WNC($\pi^0$) decays as in Fig. 2 from the Ph.D. thesis of K. Arisaka.

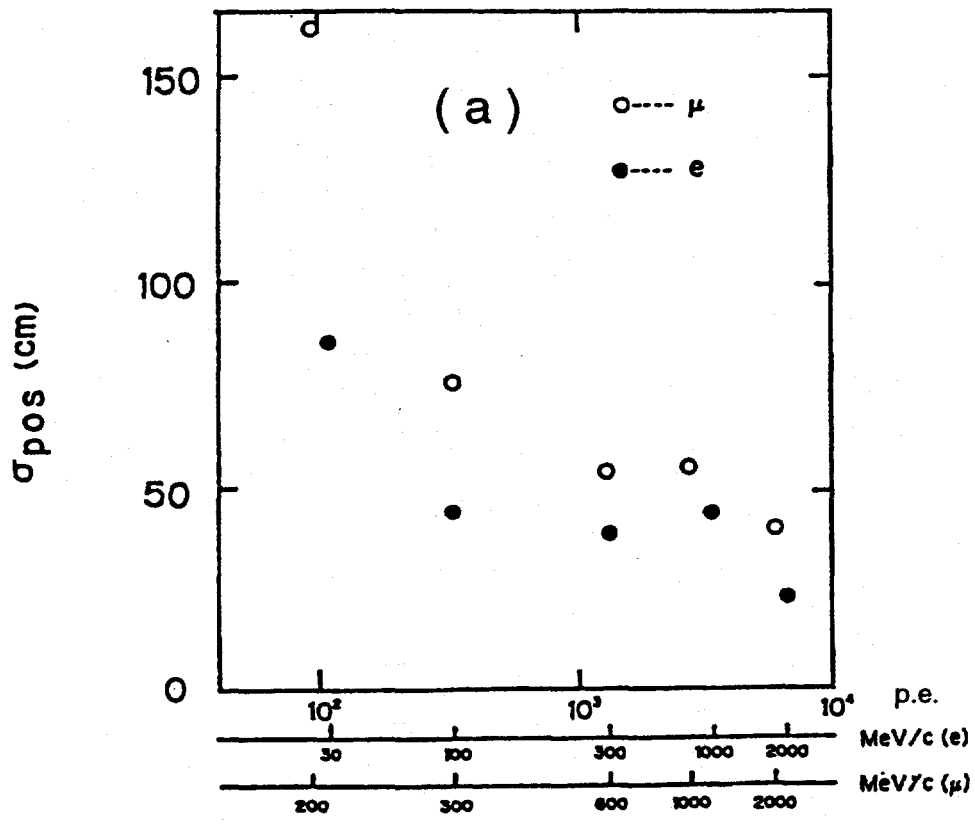


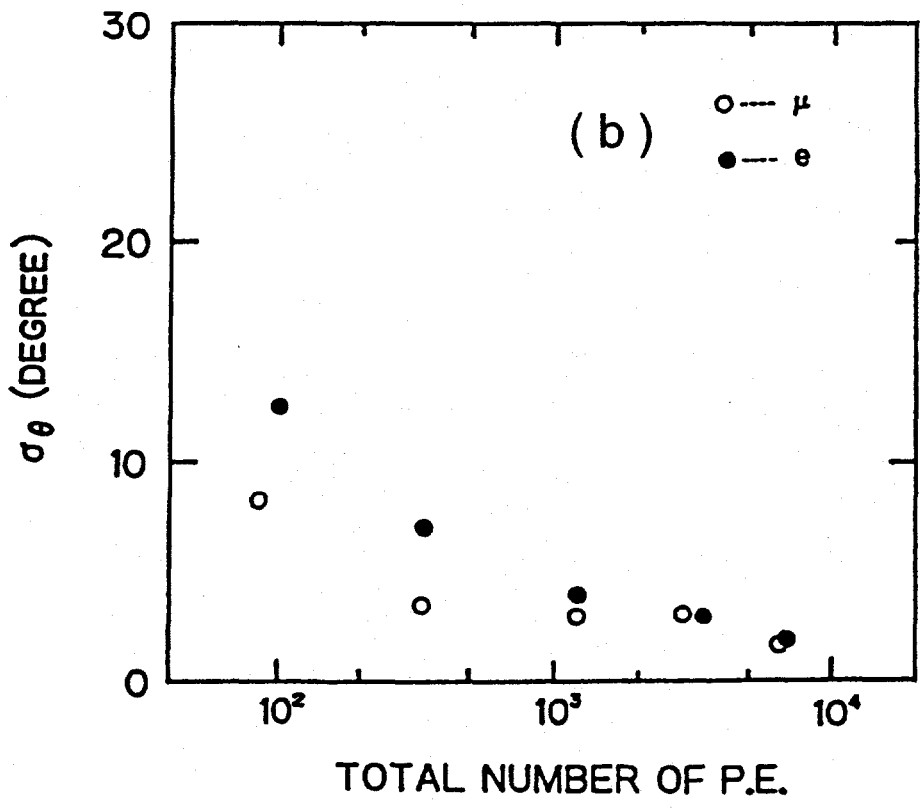


Fig. 1

95-0092y1

Number of Events

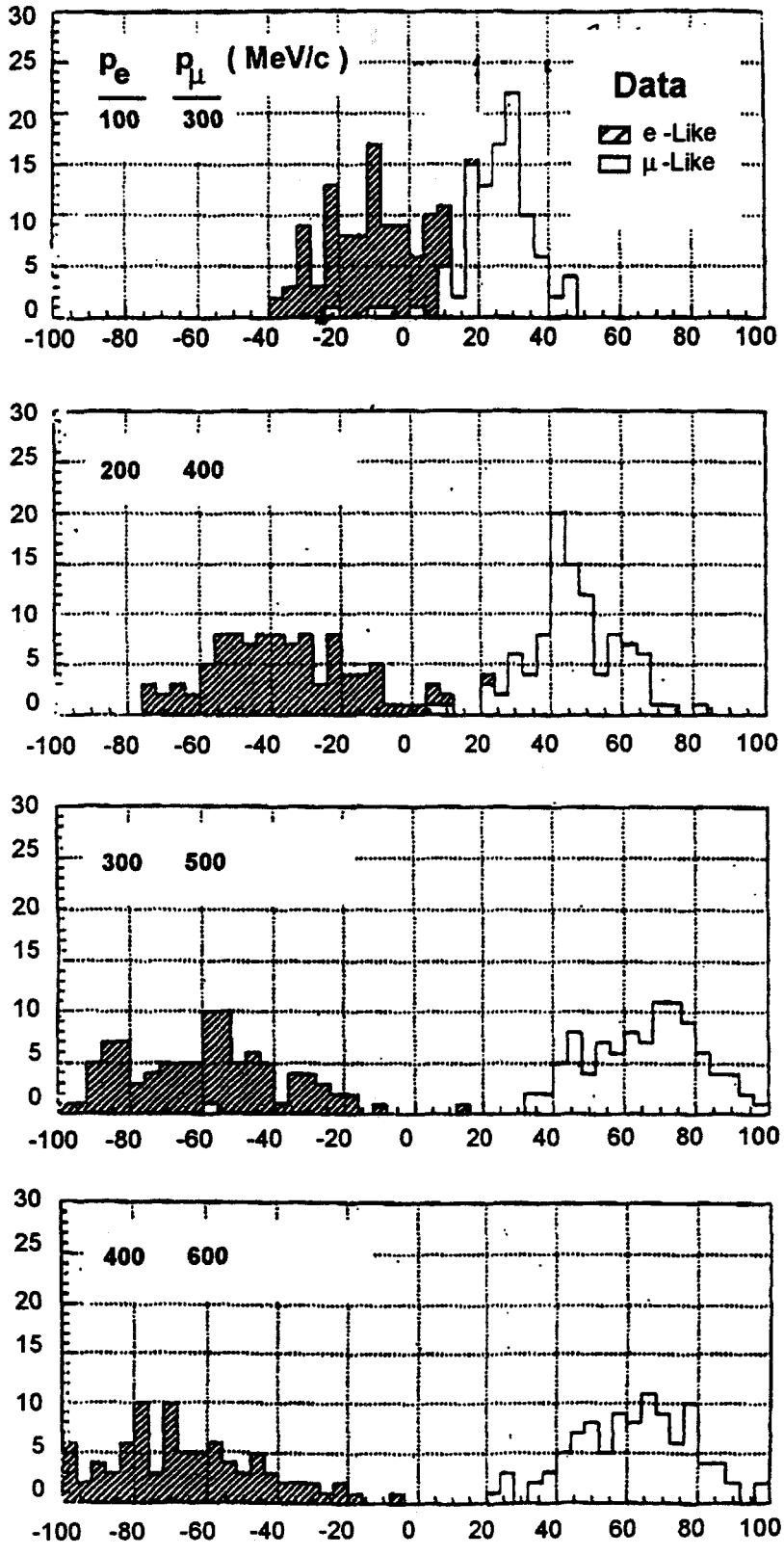


$\log_{10} L(\mu) - \log_{10} L(e)$

Fig. 2a

95-0092a2

Number of Events

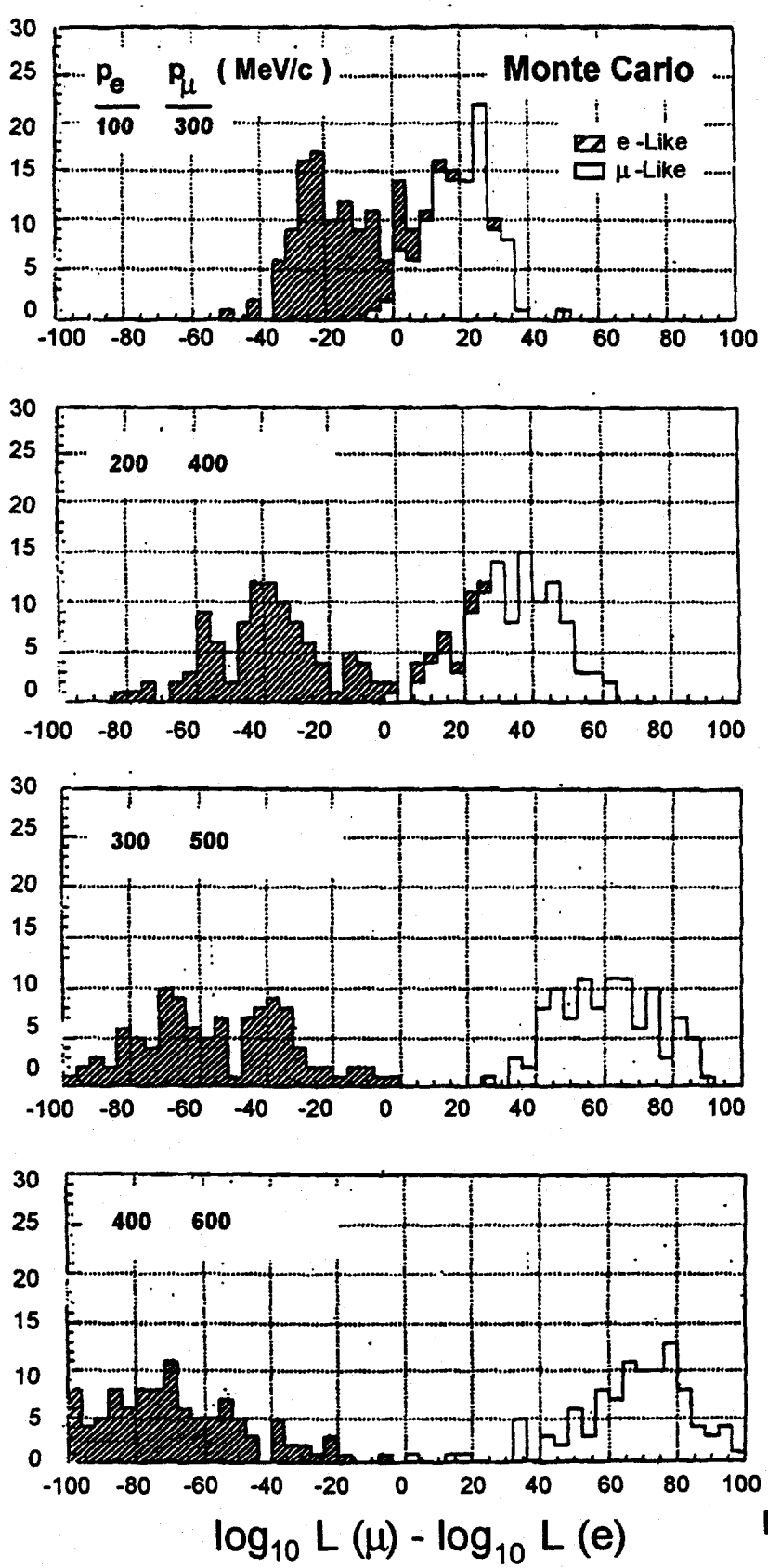


Fig. 2b

95-0092b2

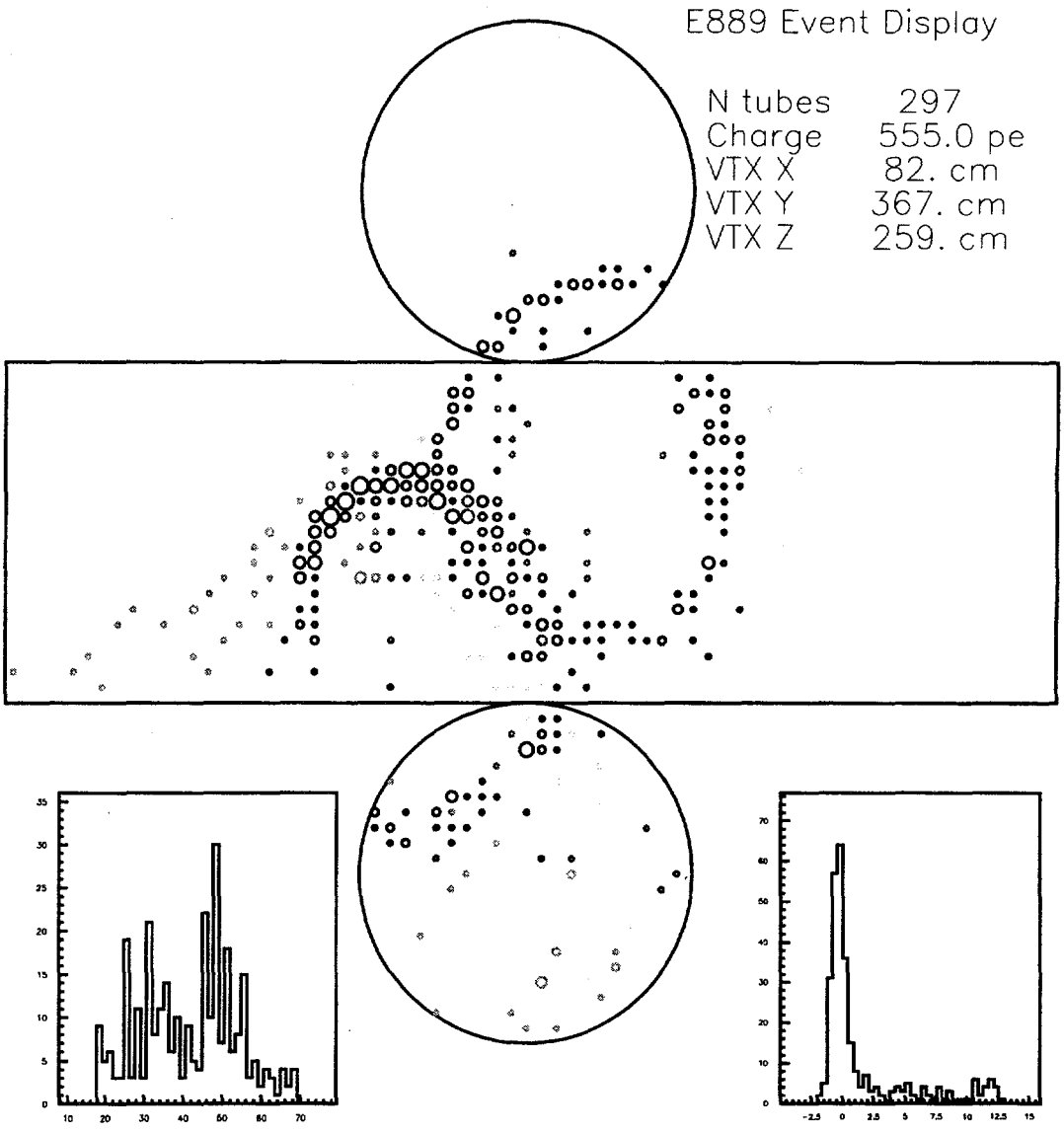
E889 Event Display
N tubes 297
Charge 555.0 pe
VTX X 82. cm
VTX Y 367. cm
VTX Z 259. cm

Fig. 3

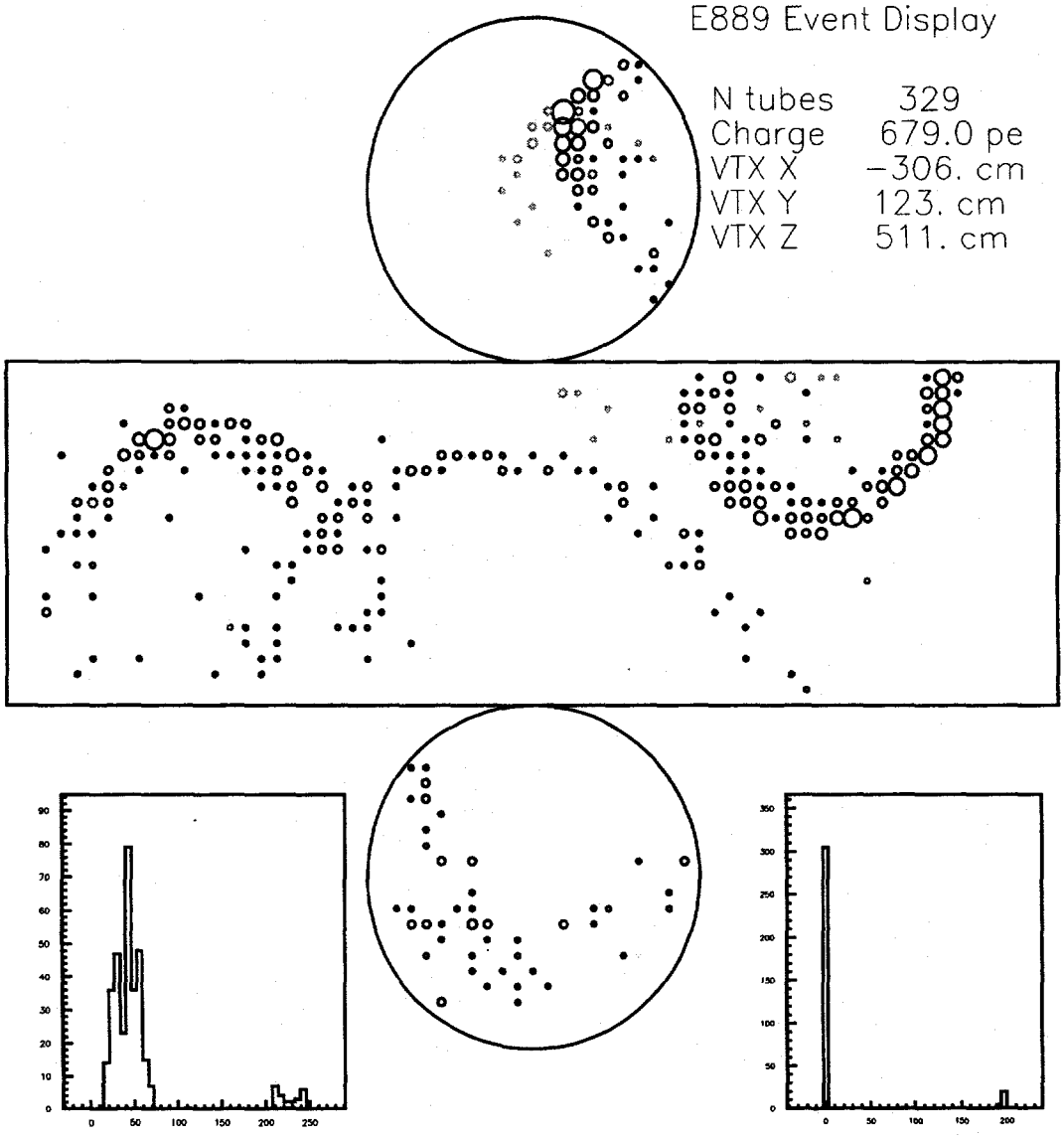
E889 Event Display
N tubes 329
Charge 679.0 pe
VTX X −306. cm
VTX Y 123. cm
VTX Z 511. cm

Fig. 4

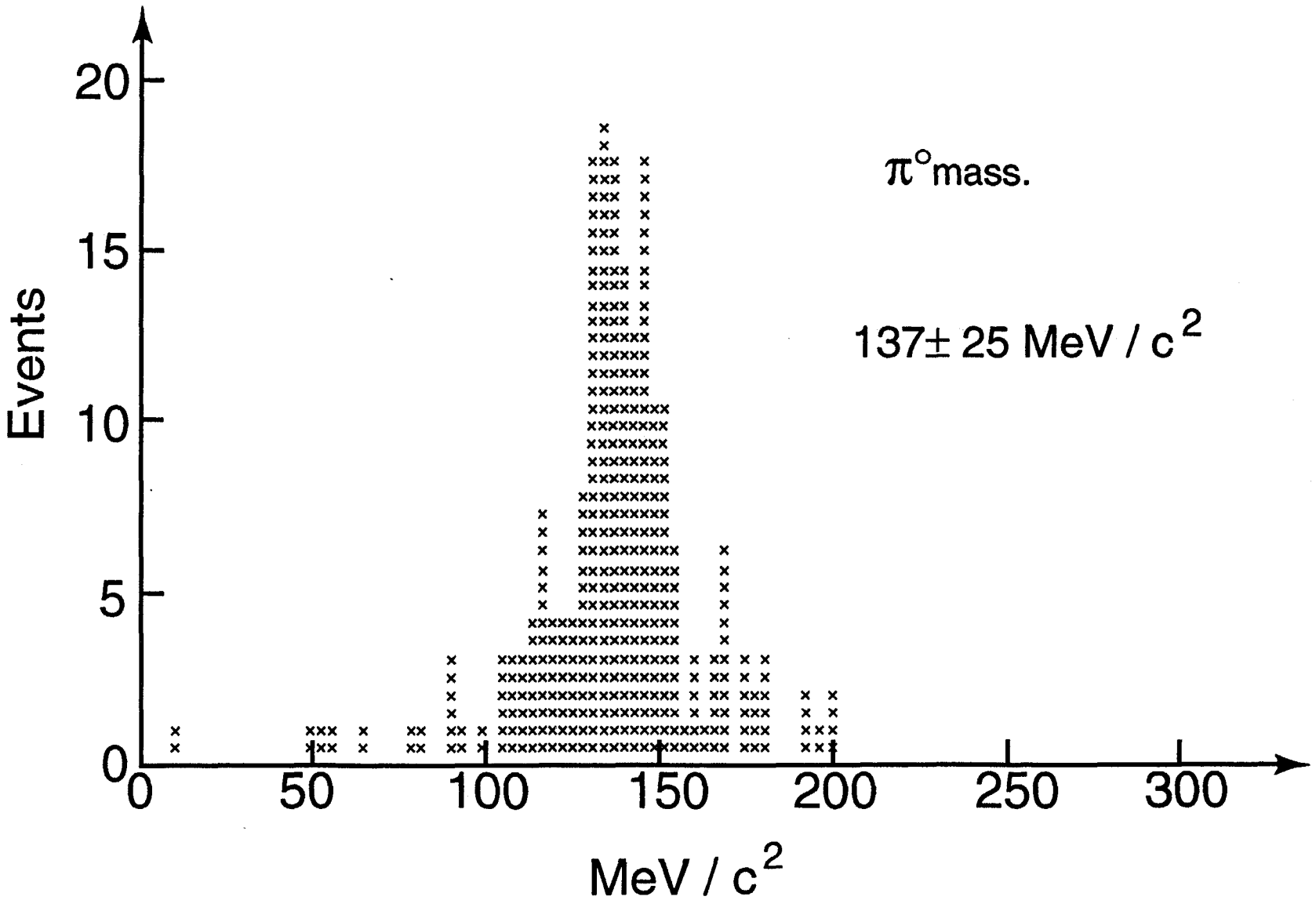
Events
20
15
10
5
0
0
50
100
150
200
250
300
MeV / c²
π°mass.
137± 25 MeV / c²

Fig. 5

# V. PHYSICS AND SIMULATIONS

## V.1 INTRODUCTION

We have performed detailed Monte Carlo simulations to determine the sensitivity of E889 with a few assumptions about the detectors and for several different channels of analysis. We have included both the beam and detector related systematic errors and the effects of backgrounds in a unified manner. These effects have been estimated by Monte Carlo calculations using the proposed geometry of E889 or by using published data from previous experiments.

We estimate our sensitivity for neutrino oscillations in the three most important *analysis* channels. They are (1) direct $\nu_\mu$ disappearance, (2) $\nu_\mu$ disappearance using the neutral current $\pi^0$ events as normalization, and (3) $\nu_e$ appearance. The actual *oscillation* channel ($\nu_\mu \rightarrow \nu_\tau$, $\nu_\mu \rightarrow \nu_e$, or $\nu_\mu \rightarrow \nu_s$, where $\nu_s$ is sterile) can be uniquely determined over most of the parameter range with the above three analysis channels. Identification of the oscillation channel is performed by counting quasi-elastic muon, quasi-elastic electron, and neutral current $\pi^0$ events. At the AGS energies quasi-elastic muon neutrino events account for about 60% of the total neutrino cross section. About 12% of all events will be from neutral current $\pi^0$ production. Only about 1% of the events will be quasi-elastic electron neutrino events from the electron neutrino contamination in the beam. Depletion of muons will be seen in the far detectors for all three oscillation channels. Oscillation into electron neutrinos will cause an increase of electrons, while in the unlikely case that oscillations are into a sterile neutrino with no weak interactions a depletion of neutral current $\pi^0$ events will be seen. In all analysis channels the observations in the near detectors are used to predict the event rates and the spectrum in the far detectors assuming no oscillations. The important issues of pattern recognition and event reconstruction for a water Cherenkov detector are addressed in Chapter IV.

Most of the studies in this chapter assume two near detector tanks on the BNL site, one at 1 km and one at 3 km, and one far detector tank at the 24 km Northville site and another far detector tank at the 68 km Plum Island site. Each tank is 18 m in diameter and 18 m high. There are 2195 photomultiplier tubes with 20 cm diameter photocathodes facing inside placed about 68 cm apart on a cylinder 15 m in diameter and 15 m high (the active or inner volume) centered inside the tank. The active veto volume, 1.5 m of water between the two cylinders, is viewed by 400 photomultiplier tubes facing outside. The PMTs facing inside are equipped with light collectors that increase the coverage by a factor of 1.6; the veto PMTs do not have the light collectors. The nominal fiducial volume is 13 m diameter $\times$ 13 m high,

but, of course, in the actual experiment we will vary the fiducial cuts for different samples of events and studies. We have assumed actual running time of 16 months with 20 hrs of fast extracted beam every day at an intensity of $4 \times 10^{13}$ protons on target per 1.6 s. This corresponds to $8.8 \times 10^{20}$ protons on target (POT); we will also comment on the first two runs of 4 months duration or $2.2 \times 10^{20}$ protons on target each. It should be noted that the AGS has already exceeded this assumed intensity and more improvement is planned.

## V.2 DIRECT MEASUREMENT of $\nu_\mu$ DISAPPEARANCE

### V.2.1 FORMALISM

The disappearance of muon neutrinos is signaled by a reduction of the weak charged current quasi-elastic muon neutrino reactions ($\nu_\mu + n \rightarrow \mu^- + p$) at a detector located far from the source of the neutrinos. The following expression approximates the number of events classified as quasi-elastic muon neutrino interactions, $f$, induced by neutrinos within a single energy bin.

$$f = \frac{A}{(r - r_0)^2}[1 - \sin^2(2\theta)\sin^2(\frac{1.27\Delta m^2(r - r_0)}{E}) + B] + C_B \qquad (1)$$

Here $r$ is the distance of the detector in km from the production target, while $r_0$ is an effective distance of the mean origin of neutrinos. $A$, the number of events without oscillations at 1 km, is a normalization constant. $\Delta m^2$, mass difference squared in units of $\mathrm{eV}^2$ and $\theta$, the mixing angle, are the usual oscillation parameters. $E$ is the neutrino energy in GeV. $B$ quantifies the fraction of events that are background from two sources: neutral current events that are misidentified as quasi-elastics and misidentified multiparticle background due to neutrinos in the high energy tail of the neutrino spectrum (without appreciable oscillation probability). $C_B$ is the number of cosmic ray events that cause background to the quasi-elastic sample. Two main approximations in this formula are as follows: Although the neutrinos are generated over the entire tunnel length with a distribution based on the momentum distributions of both pions and kaons, we have approximated the effect of the tunnel as an average position ($r_0$) within the tunnel. Secondly, we have ignored the effects of placing detectors at a small angle with respect to the tunnel axis. For large angles, one must replace $(r - r_0)$ by the vector equivalent $|\vec{r} - \vec{r}_0|$, but in our case $(r - r_0)$ and $|\vec{r} - \vec{r}_0|$ are close enough to be considered indistinguishable.

We denote the counts measured at three different sites as $f_a$, $f_b$, and $f_c$ where $a$, $b$, and

$c$ are the designations of the near and the middle sites (both on the BNL site), and the far site (at 24 or 68 km), respectively. The sites are also sometimes referred to as D1, D3, D24, and D68. We will denote the flux predicted at the far sites using the observations at $a$ and $b$ under the assumption of no oscillations as $f_p$. An oscillation signal results when $f_c$ (at 24 or 68 km) is observed to be significantly different from $f_p$. The significance of the oscillation result will clearly depend on the systematic errors in calculating $f_p$ from $f_a$ and $f_b$, the effects of oscillations on the near site counting rate, the background and cosmic ray level, and most importantly the statistics at the far site.

There are several important features of Equation 1: For small oscillations ($\frac{\Delta m^2(r-r_0)}{E} << 1$) the number of events missing is independent of distance. Then using the inverse square law (a good approximation when $r >> r_0$) for the number of expected events one calculates that the significance of oscillations increases linearly with distance if one considers only the statistical error at the far site, while $\sin^2(2\theta)$ reduces the significance linearly. Not subtracting the neutrino induced background fraction, $B$, from the rates observed in both the near and the far detectors then reduces the significance by an amount $\frac{1}{(1+B)}$. Lastly, the cosmic ray background, $C_B$, is independent of the distance and therefore increases in importance relative to signals with distance of the far detectors. Since the loss of events due to small oscillations is independent of distance a small cosmic ray background could limit the sensitivity. Therefore we have placed much emphasis on understanding and eliminating any cosmic ray backgrounds.

### V.2.2 QUASI-ELASTIC MUON NEUTRINO EVENTS

Before deriving the expected size of the disappearance signal, we will describe the nature of the quasi-elastic events in the detectors. At the neutrino energies at the AGS ($E_\nu > 300$ MeV) the cross sections for the quasi-elastic reactions on light nuclei may be calculated to good approximation using a relativistic Fermi gas nuclear model with a semiempirical nucleon binding energy value [1]. Above 300 MeV, in this model the bound and free neutron cross sections differ by less than 20%, and the $\nu_e$ and $\nu_\mu$ quasi-elastic cross sections are approximately equal despite the muon-electron mass difference. Both the total cross section as a function of energy and the differential cross section have been measured in previous experiments [2,3] (Figure 1 and 2).

We have performed detailed simulations of the quasi-elastic events and backgrounds in our water Cherenkov detectors. For these simulations, rays of neutrinos were generated from the decay tunnel according to our GEANT based beam simulation program. If a neutrino ray was found to intercept one of the four detector tanks located at the correct distance and

| | 1 km | 3 km | 24 km | 68 km |
|---|---|---|---|---|
| Events in Detector | $10.3 \times 10^6$ | $11.5 \times 10^5$ | 17916 | 2232 |
| Events in Fiducial | $6.80 \times 10^6$ | $7.54 \times 10^5$ | 11820 | 1473 |
| Contained | $5.21 \times 10^6$ | $5.80 \times 10^5$ | 9102 | 1136 |

Table 1: *The number of quasi-elastic muon events after 16 months of running at the four detector sites with one detector tank each. The uncertainty on the absolute normalization is about 15%.*

offset from the beam axis, then a neutrino event was generated after appropriate weighting for the cross section as a function of energy and the path-length through the detector. Using the 1.5 degree offset spectrum (Figure 3) computed in Chapter III.A we compute the integral $\int dE\phi(E)\sigma(E)$ over the interval $0 < E_\nu < 5$ GeV to be $1.78 \times 10^{-47}$ per proton on target at 1 km. There is an additional correction that suppresses the total cross section by 0.93 due to Pauli exclusion effects in the nucleus. Thus the number of events in water at 1 km is given by $4.43 \times 10^{-15}$/kTon/POT. In Table 1 the event counts in each of the detectors is shown as a function of several cuts after $8.8 \times 10^{20}$ POT. The first row is the number of events in the entire inner volume viewed by the PMTs (15 m diameter and 15 m height), and the last row is with both fiducial ( vertex within 13 m diameter and 13 m height) and containment (muon stop within 15 m diameter and 15 m height) cuts. There is an uncertainty of about 15% on the absolute neutrino flux, most of which is due to the uncertainties in the simulation of the hadronic showers in the horn-target system. The spectrum of neutrinos, however, has much less uncertainty because we have checked our simulation against the results from a previous AGS experiment in a similar neutrino beam, E734 (Figures 2 and 4).

Most of the contained events with the vertex in the fiducial volume will have a single clear ring with a sharp edge characteristic of a muon. We can decide if the muon is contained by two separate methods. We can look at the pattern and the pulse height of the photomultiplier hits at the center of the ring. For an exiting muon the ring does not have a hole and the photomultipliers in the center have very large pulse heights. For the second method we can make cuts on the pulse height in the veto volume that corresponds to the center of the ring in the inner detector. The first method causes a small loss of events because some events will be rejected because their tracks end close to the edge of the detector. In any case, we intend to use both methods to check our results. Assuming that a cut on the veto

volume is used, 0.77 of the events in the fiducial volume are contained. Figure 5a shows the muon momentum spectrum of these contained events. Figure 5b shows the spectrum of the neutrinos that produce these muons. Also interesting is the number of photoelectrons (Figure 5c) and the number of hit photomultipliers (Figure 5d) in the detector configuration described at the beginning of this chapter. Two further cuts on the contained events that will be needed to obtain a clean sample of muons with little background are cuts on the number of photoelectrons and on the muon angle. These cuts will be tuned to eliminate low momentum particles that are difficult to classify as muons or electrons and wide angle backgrounds. Figure 6 shows the response of the detector for muons, electrons, and charged pions as a function of momentum. The vertex and angular resolutions are discussed in Chapter IV.

In the next few sections we will show how the effect of oscillations and background modifies the total number of events and the spectrum at the far sites at 24 and 68 km. It can be seen immediately, however, that the statistics at the near detectors will be sufficiently large that we will be able to predict the spectrum and the number of events at the far sites with minimal statistical error and a small systematic error. The systematic error will be due to the beam and detector effects discussed in detail below. The statistical error at D24 will be about 1%, and therefore the oscillation sensitivity at D24 will depend on whether we can control the systematic errors to be less than or equal to that value. The statistical error at D68 will about 3%, and therefore the oscillation sensitivity will likely not depend on the systematic error. Thus we will be able to pursue two approaches to this oscillation experiment: high statistics with low systematic error, and statistics-limited with a larger oscillation signal.

### V.2.3 BACKGROUNDS

#### V.2.3.1 NEUTRINO INDUCED BACKGROUNDS

#### WEAK CHARGED CURRENT BACKGROUNDS

The WCC background event information, listed in Table 2, contains data obtained in the ANL 12 foot $H_2/D_2$ bubble chamber with the neutrino beam shown in Figure 7 and compares them with the results of a calculation based on the Monte Carlo simulation for the Kamiokande detector [4]. Normalization of the calculation is done by adjusting the calculated quasi-elastic total to the measured. We utilize these results because the 1.5 degree neutrino spectrum is similar to the spectrum with which the 12 foot chamber results were obtained. The results show the agreement of the simulation with the data and with earlier theoretical estimates in Ref. 5.

| Interaction | Argonne | $\nu$ Monte Carlo |
|---|---|---|
| $\nu p \rightarrow \mu^- p\pi^+$ | $308 \pm 24$ | 301 |
| $\nu p \rightarrow \mu^- p\pi^+ (m\pi^0) m \geq 1$ | $20 \pm 5$ | 22.3 |
| $\nu p \rightarrow \mu^- n\pi^+\pi^+ (m\pi^0) m \geq 0$ | $15 \pm 5$ | 12.2 |
| $\nu p \rightarrow \mu^- p\pi^+\pi^+\pi^-$ | $10 \pm 3$ | 2.5 |
| $\nu p \rightarrow \mu^- p\pi^+\pi^+\pi^-\pi^0$ | - | 1.3 |
| $\nu p \rightarrow \mu^- n\pi^+\pi^+\pi^+\pi^-$ | $1 \pm 1$ | 0.5 |
| $\nu p \rightarrow \mu^-$ strange particle | $1 \pm 1$ | - |
| $\nu n \rightarrow \mu^- p$ | $833 \pm 41$ | 833 |
| $\nu n \rightarrow \mu^- p\pi^0$ | $124 \pm 14$ | 129 |
| $\nu n \rightarrow \mu^- n\pi^+$ | $90 \pm 11$ | 89.0 |
| $\nu n \rightarrow \mu^- p (m\pi^0) m \geq 2$ | $31 \pm 13$ | 13.1 |
| $\nu n \rightarrow \mu^- n\pi^+ (m\pi^0) m \geq 1$ | $29 \pm 12$ | 24.6 |
| $\nu n \rightarrow \mu^- p\pi^+\pi^-$ | $20 \pm 5$ | 21.1 |
| $\nu n \rightarrow \mu^- p\pi^+\pi^- (m\pi^0) m \geq 1$ | $8 \pm 4$ | 9.1 |
| $\nu n \rightarrow \mu^- n\pi^+\pi^+\pi^- (m\pi^0) m \geq 0$ | $3 \pm 2$ | 6.1 |
| $\nu n \rightarrow \mu^- p\pi^+\pi^+\pi - \pi -$ | 0 | 1.5 |
| $\nu n \rightarrow \mu^-$ strange particle | $12 \pm 4$ | - |

Table 2: *The event rate of each exclusive interaction in the Argonne data compared with the results of the Kamioka Monte Carlo calculation. The calculation is normalized to the* $\nu_\mu n \rightarrow \mu^- p$ *event rate. Taken from Ref. 4.*

Even if there is no discrimination whatsoever against weak charged current backgrounds to the direct $\nu_\mu$ disappearance measurement, this experiment will detect neutrino oscillations because these backgrounds come from neutrinos that also oscillate. Since their energy distribution will not be as well known as that of the quasi-elastic signal, weak charged current backgrounds could lead to errors in measuring the oscillation parameters using the spectrum shape, but they will not fake a statistically significant oscillation signal. Furthermore, from Table 2 we see that because of the low beam energy, all such backgrounds combined are only about 2/3 of the quasi-elastic signal. To improve the accuracy of the measurement, we shall use several methods to exclude backgrounds. Some characteristics that permit exclusion are: (1) Backgrounds tend to have extra Cherenkov rings. (2) Single ring background events usually have low visible energy. (3) As is discussed in the Pattern Recognition section, electromagnetic showers produce Cherenkov rings that are quite different from rings produced by fast muons. Any $\pi^0 \rightarrow \gamma\gamma$ in a background will in general produce two electromagnetic showers that will mimic a single muon less than 0.2% of the times. (4) Muons and $\pi^+$ both lead to Michel electron production, typically a few microseconds after the initial event. If two Michel decays are detected near the origin of a quasi-elastic candidate event in both space and time, that candidate is likely to be a background. Because of the cosmic muon rate, this last method requires some care to avoid losing real quasi-elastic events; in what follows we discuss how well we can do without its use.

*(a) MULTIPIONS*

The multipion event total in Table 2 is 17% of the quasi-elastic event total. In general, WCC multipion events are contained and will exhibit two, three, or sometimes four Cherenkov rings and two or more muon decays. Most events have a final state $\pi^0$. Where rings overlap, the complex PMT hit pattern serves as convincing evidence of a multiring event. Figures 8, 9, and 10 show typical quasi-elastic muon, quasi-elastic electron, and multiring pion events, respectively.

As an illustration of the discrimination against multipion backgrounds in the $QE(\mu^-)$ sample, we consider in detail the reaction $\nu_\mu n \rightarrow \mu^- p \pi^+ \pi^-$ with a rate 0.024 of the quasi-elastic rate. Neglecting the proton, there are 3 charged particles in the final state and 2 muon decays. From the calculated momentum distributions of the $\mu^-, \pi^+$ and $\pi^-$ [4] which give the fractions above detection threshold, one has the normalized probabilities: 45% of all events exhibit 3 rings, 42% exhibit 2 and only 2 rings, 12% show 1 and only 1 ring, and 1% show no rings. Thus such events could contribute a background that is only 0.3% as large as the expected quasi-elastic signal. If we apply the same reduction factor of 12% to

all the multipion events we calculate that the maximum possible background is about 2%. One must keep in mind that additional cuts to reduce this small background are possible. In particular, most of the multipion events will have very low visible energy, wide angles, and several muon decay electrons. In our case with cosmic ray muons within the detector the detection of muon decays may not be as effective a rejection tool as in the case of Kamioka. Nevertheless, with these additional cuts the contamination in the quasi-elastic signal events from charged current multipion events should be reduced to less than 1%.

*(b) SINGLE CHARGED PION*

The two single charged pion reactions $\nu_\mu p \rightarrow \mu^- p\pi^+$ and $\nu_\mu n \rightarrow \mu^- n\pi^+$ produce a signal which is 48% of the quasi-elastic total in Table 2. The momentum distributions of the $\pi^+$ and $\mu^-$ are shown in Figure 11. We have visually scanned these events and found that if both the muon and the pion produce more than 50 photoelectrons each the event can be easily identified as a two ring event. 50 photoelectrons corresponds to about 170 MeV/c (250 MeV/c) for muons (pions). With such a cut we find that 40% of the events will show one ring (principally the $\mu^-$). Figure 12 shows the photoelectron spectrum of these events. We see that 0.65 of these single ring events are above 300 photoelectrons while 93% of the quasi-elastic muons will be above 300 photoelectrons (Figure 5). Therefore about 0.12 ($0.48 \times 0.40 \times 0.65$) of the events identified as quasi-elastic muons could be from charged current single pion channels. The detection of two muon decays could be used to further suppress this background. However, as we stated earlier these background events do not affect the sensitivity very much because the spectrum of neutrinos that produce these events (Figure 12) is very similar to the spectrum that produces the quasi-elastic muons events.

Only 0.20 of the single ring charged current pion events with more than 300 photoelectrons will come from neutrinos above 1.5 GeV where the oscillation probability is small in the parameter range of interest. This low level of background from high energy neutrinos is one of the advantages of the narrow off-axis (1.5 degree) neutrino spectrum (Figure 3). This background would be higher by a factor of about 2.5 in the 0 degree beam. Other multiparticle backgrounds would also increase and the event patterns would not remain simple.

*(c) SINGLE NEUTRAL PION*

The reaction $\nu_\mu n \rightarrow \mu^- p\pi^0$ (the only allowed WCC-$\pi^0$ reaction) is 15% of the total quasi-elastic rate. The momentum distribution of $\mu^-$ and $\pi^0$ are essentially the same as those in Figure 11. We have visually scanned Monte Carlo events of this type (see Chapter IV for complete details) for single rings with clear muon like patterns. Only 0.5% of the WCC-

$\pi^0$ events will look like quasi-elastic muon events because at least one of the gamma rays from the $\pi^0$ decay is usually visible. Thus this background is negligible in the quasi-elastic sample. If, however, both the $\mu^-$ track and the $\mu$ decay are missed, the event might be misidentified as WNC-$\pi^0$. This is addressed in the section on the oscillation analysis using the ratio $QE(\mu)/NC(\pi^0)$.

In summary, the WCC backgrounds in the $QE(\mu^-)$ sample are expected to be less than 13% of the $QE(\mu^-)$ sample in any of the four detectors. We expect to eliminate half of these by looking for events that show more than one muon decays close in both space and time to the event vertex. Since these backgrounds are $\nu_\mu$–induced they will respond to a $\nu_\mu$–disappearance resulting from neutrino oscillations in the same way as the $QE(\mu^-)$ events. Less than 3% of the $QE(\mu^-)$ sample will consist of WCC-multiparticle events from high energy neutrinos ($> 1.5$ GeV) with small oscillation probability. Furthermore, the treatment of systematic errors will show that these background will be the same in all the detectors to first order. Therefore the distortion of the measured muon spectrum and the $E_\nu$ distribution produced by the WCC backgrounds can be simulated and subtracted with a small systematic error.

## WEAK NEUTRAL CURRENT BACKGROUNDS

*(a) MULTIPIONS*

The WNC multipion reactions total 5% of the $QE(\mu^-)$ rate at low $\nu_\mu$ energies, and produce final states with 2, 3, or 4 Cherenkov rings, counting only events with three or fewer pions. Of the eight such final states, four have a $\pi^0$, and all final states except one (which has a $\pi^0$) have at least one $\pi^+$. Detailed reasoning similar to that for the WCC multipion background reactions indicates that the principal background sources are the final states $\nu n\pi^+\pi^-$ and $\nu p\pi^+\pi^-$. For these, the probability of showing 1 and only 1 track is 0.32 which yields a background in the $QE(\mu^-)$ sample less than 1.6%.

*(b) SINGLE CHARGED PION*

The WNC single charged pion reactions, $\nu p \rightarrow \nu n\pi^+$ and $\nu n \rightarrow \nu p\pi^-$, each have a rate 7.3% of the $QE(\mu^-)$ rate. These reactions will produce single ring events that are not distinguishable from quasi-elastic events from the pattern alone. The momentum distribution of the final state pion is shown in Figure 13. The shape of the pion momentum distribution and the spectrum of photoelectrons are very different from those of the $QE(\mu^-)$. A cut at 300 photoelectrons eliminates 94.5% of these events while keeping more than 93% of the quasi-elastic signal. Therefore the amount of background from this source in the quasi-elastic

sample will be about 0.8% ($2 \times 0.073 \times 0.055$).

In summary, WNC events will cause less than 2.4% background in the $QE(\mu^-)$ sample. If left unsubtracted this background will dilute any oscillation effect by a small amount since the background will be the same fraction in all four detectors.

### V.2.3.2 COSMIC RAY BACKGROUNDS

#### COSMIC RAY MUONS

The cosmic ray muon flux at the surface of earth at sea level is given by the following equation [6].

$$j(\theta,\phi) = \frac{360}{\pi}\cos^2(\theta) m^{-2} s^{-1} str^{-1} \tag{2}$$

Here $\theta$ is the angle with respect to the zenith or the vertical axis and $\phi$ is the azimuthal angle, and the flux is the number of particles incident on a sphere of unit cross sectional area per unit time per unit solid angle. To convert this quantity into the number of particles crossing a horizontal surface area we evaluate the following integral.

$$\int_A \int_{\theta<\pi/2} j(\theta,\phi)\cos(\theta) d\Omega dA \tag{3}$$

where the first integral is over the surface area and the second integral is over the upper hemisphere. Similarly for the vertical surface of the tank we have the following integral.

$$\frac{1}{2}\int_A \int_{\theta<\pi/2} j(\theta,\phi)\sin(\theta) d\Omega dA \tag{4}$$

where the extra factor of 1/2 takes into account that only the muons crossing from outside the tank wall are relevant. We use Equations 3 and 4 to calculate the muon rates in both the veto counter and the inner detector entering from the top and the side (Table 3). The surface area for the veto counter is calculated by assuming a diameter of 18 m and height of 18 m whereas the inner detector has a diameter of 15 m and a height of 15 m. The total muon rate in the inner detector of some 80 kHz might be considered high, especially for the far detectors where the neutrino event rates are low. However, the rejection obtained with the use of an active veto counter, the time structure of the beam, and the characteristics of the events themselves is quite adequate. The high cosmic rate is not a problem, but a source to test and calibrate the detectors in an identical fashion before and during the neutrino data runs.

| | Into the Veto | Into the Inner |
|---|---|---|
| Muons from the Top | 45780 Hz | 31790 Hz |
| Muons from the Sides | 71860 Hz | 49900 Hz |
| Total Muons | 117640 Hz | 81690 Hz |
| Stopping Muons | - | 43132 Hz |

Table 3: *Cosmic ray muons entering the veto volume of the detector and then the inner volume per second. The spectrum of muons from Ref. 10 is used to calculate the number that stop in the inner detector.*

## NEUTRAL COSMIC RADIATION

The rates in the inner volume due to muons should be somewhat lower than our calculation because of the passive shielding effect of the veto volume. This passive shielding effect will be more effective for neutral cosmic radiation of neutrons and photons. The high energy neutron intensity at sea level is approximately 1/30 the intensity of muons [7–10]. The minimum 1.5 m thickness of water in the veto volume corresponds to 1.74 absorption lengths (the Fe tank structures and the insulation are not considered but should also help); therefore the rate of neutron induced interactions in the inner detector should be less than $6 \times 10^{-3}$ times the rate of muon interactions. We do not expect much background from photon induced interactions because high energy photons from the atmosphere are normally associated with electromagnetic showers that contain charged particles, electrons and positrons. These will produce hits in the active veto, and in the extremely rare case that a single high energy photon enters the detector it must pass through 4.17 radiation lengths in the active veto without interacting to enter the inner detector.

## ACTIVE VETO

We plan on rejecting the muons at an early stage using the active veto. The exact geometry of the photo-multiplier tubes in the active veto volume has not yet been finalized. We are looking at two different options: 1) Photomultipliers on the inner cylinder facing outwards with enough density to have at least one hit for any high energy charged particle no matter what the entry angle. Reflective coating on the walls will increase the light yield, but also cause many more PMTs to be hit over a longer period of time. 2) Photomultipliers isolated from each other by enclosed cells with reflective coating on the inside.

In the past veto inefficiency of similar veto shields has been found to be much less than

$10^{-3}$ (See References in Chapter IV). The number of photoelectrons collected from the veto will depend on the efficiency of the reflective coating as described in Ref. 12. Assuming 400 PMTs in the veto volume and a reflection efficiency of 60%, we calculate that we will collect more than 150 photoelectrons for a cosmic ray muon entering the tank at right angles. The main reason for any veto inefficiency will then be dead PMTs or electronics deadtime. We estimate that $10^{-3}$ is a very conservative number.

## THE TIME STRUCTURE

The most important tool in eliminating cosmic events from the neutrino data is the use of the accelerator time structure. The AGS fast extracted beam will be delivered every 1.6 s to the neutrino production target in 8 buckets with a width of 20-30 ns each. The buckets will be 335 ns apart. We intend to measure the absolute time of both the AGS beam buckets at the beam stop and the neutrino events at the detectors with synchronized clocks. As explained in Chapter III.C, we will be able to synchronize the clocks to within 10 ns of each other. The 10 ns error in the synchronization will most likely be the maximum possible error, rather than a Gaussian distributed error. The error in the reconstructed time of the event (about 1.5 ns) from the PMT hits will be negligible on this scale. Thus the effective duty factor associated with the timing cuts will be less than $2.5 \times 10^{-7} = \frac{8\times(10+30+10)\text{ ns}}{1.6\text{ s}}$. Figure 14 shows the reconstructed time of neutrino events in experiment E734 which was in a similar AGS neutrino beam. We see no difficulty in finding the neutrino events in E889 by using this type of timing.

## RECONSTRUCTION

To gain additional discrimination with respect to cosmic rays we have performed GEANT Monte Carlo simulations of both muons and neutrons in the detectors using the experimentally measured and parameterized spectra in Figures 15 and 16 [7,10]. The muon spectrum has considerable dependence on zenith angle; we have parameterized this dependence as an angle dependent inflexion point at which the momentum spectrum changes from a flat to a power law spectrum. The neutron spectrum is somewhat softer than the muon spectrum. The neutron zenith angle dependence is not well known; we assumed it to be the same as for muons. The spectrum of photo-electrons and the total number of photomultipliers is shown in Figure 17. The character of the cosmic events can be seen to be quite different from the quasi-elastic neutrino events in Figure 5. If we require that the number of photo-electrons be greater than 300 ($P_\mu > 300$ MeV) and less than 3500 ($P_\mu < 4.0$ GeV) then we reduce the signal quasi-elastic events by about 7%, but the same cut retains only 47% of the muon and

| | Muons | Neutrons |
|---|---|---|
| Raw rate kHz | 81.7 | 2.7 |
| Reduction factors | | |
| Beam time structure | $2.5 \times 10^{-7}$ | $2.5 \times 10^{-7}$ |
| Passive/active shielding | $10^{-3}$ | 0.18 |
| Energy cuts | 0.47 | 0.26 |
| Vertex and Direction | $3.3 \times 10^{-3}$ | $6.2 \times 10^{-2}$ |
| Total reduction | $3.9 \times 10^{-13}$ | $7.2 \times 10^{-10}$ |
| Background in 16 months | 1.1 events | 68 events |

Table 4: *Cosmic ray background to quasi-elastic muon neutrino events in each detector tank after 16 months of running. Over 1100 quasi-elastic muon events are expected in D68 over the same period.*

26% of the neutron cosmic events.

We have applied our reconstruction algorithm to a sample of the remaining muon cosmic events. Figure 18 shows the reconstructed vertex position for a sample of muon cosmics entering the inner detector within the above energy cuts. A fiducial cut to restrict the reconstructed vertex to be within a cylinder of 13 m diameter and 13 m height leaves a background of only 4 events out of 306 events. Requiring that the muon be within 90 degrees of the neutrino beam direction keeps only 1/4 of these remaining events.

An eye-scan of the neutron induced events simulated by GEANT that passed the energy cuts was performed. Since typical high energy neutron interactions produce several particles, we found that only 1/8 of the remaining neutron events looked like single ring muon-like events that could be a background to the quasi-elastic signal. The number of single ring showering events that could be background for the electron neutrino appearance search was found to be negligible. These single tracks are approximately isotropically distributed, and therefore a requirement that the track point within 90 degrees of the neutrino beam direction reduces this background further by a factor of 2.

In Table 4 we have collected all of these reduction factors to compute an estimate of the cosmic ray contamination to neutrino events after 16 months of running. We see that the background is small even at the far distance of 68 km where over 1100 quasi-elastics are expected over the same running period. We also note that most of the reduction depends on

the time structure and the active/passive veto shield, which are relatively simple systems. We need not perform complete analysis and reconstruction of the data to have confidence in the detector at an early stage of the experiment.

### COSMIC BACKGROUND SUBTRACTION

The data acquisition electronics and the trigger of the experiment will be quite flexible so that events can be collected continuously for 10-15 $\mu$s after the AGS beam gate (to search for muon decay electrons, for instance). The trigger can also be enabled outside the beam gate. In this manner we intend to collect large amounts of cosmic ray data for background studies and calibration. We will use these data to subtract the cosmic ray background from each detector before comparing the event rate. The procedure will introduce a small systematic error which will depend on knowing the time windows over which the subtraction must occur at each of the detectors. Since the correction is of the order of 6% at the 68 km site, an error of 5% (from possible jitter in the *BEAM-ENABLE* signal) in subtraction will cause a systematic error of 0.3% at that farthest site. In the present analysis, however, we prefer to show our sensitivity without this subtraction.

## V.2.4 SYSTEMATIC ERRORS

The systematic errors for the experiment fall in two broad somewhat overlapping categories: 1) beam related and 2) detector related. In the following we describe our experimental design which will minimize effects that cause spurious oscillation signals to arise. In the past most neutrino oscillation experiments have reported oscillation type effects at an early stage of the experiments, always at the edge of their sensitivity. We want to avoid these difficulties by having redundant measurements and very little reliance on Monte Carlo simulations to detect oscillations over most of our sensitivity range.

In the following we will discuss the systematic errors in the context of the direct muon disappearance experiment. The same results with small modifications will also be true for the systematic error on the background for the $\nu_e$ appearance analysis. The systematic error on the indirect $\nu_\mu$ disappearance search using the ratio of quasi-elastic muons to neutral current $\pi^0$s ($QE(\mu^-)/NC(\pi^0)$) will not have many of the contributions discussed below. In any case, the systematic error will not be important to either the $\nu_e$ appearance or the $QE(\mu)/NC(\pi^0)$ technique at small values of $\Delta m^2$ because the statistical errors will dominate. Similarly, the systematic error will not be important at D68 compared to the expected statistical error of 3% for the direct $\nu_\mu$ disappearance analysis.

### V.2.4.1 BEAM SYSTEMATIC ERROR

### BEAM PARAMETERS

Before a complete discussion of the systematic errors due to the neutrino beam we will demonstrate the assumption that the neutrino origin can be approximated as some average position within the tunnel. Let $\rho(r')$ be the distribution of neutrino origins in the decay tunnel; $r'$ is the position where a meson decayed and produced a neutrino that caused an interaction in the detector. We normalize $\rho(r')$ so that $\int_0^L dr'\rho(r') = 1$ where $L$ is the length of the decay tunnel. If $F(r)$ is the true count rate due to these neutrinos in a detector located at $r$ then

$$\begin{aligned} F(r) &= \int_0^L dr'\rho(r')\frac{A}{(r-r')^2} \\ &= \int_0^L dr'\rho(r')\frac{A}{r^2}(1+2\frac{r'}{r}+3\frac{r'^2}{r^2}+...) \\ &= \frac{A}{r^2}(1+2\frac{<r'>}{r}+3\frac{<r'^2>}{r^2}+...) \end{aligned} \tag{5}$$

If we make the approximation that the neutrino origin is some average position inside the decay tunnel, $r_0 =< r' >$, then from Section V.2.1

$$\begin{aligned} f(r) &= \frac{A}{(r-<r'>)^2} \\ &= \frac{A}{r^2}(1+2\frac{<r'>}{r}+3\frac{<r'>^2}{r^2}+...) \end{aligned} \tag{6}$$

Therefore the error we make with this approximation to lowest order is given by

$$F(r) - f(r) \approx 3\frac{A}{r^2}(\frac{<r'^2> - <r'>^2}{r^2}) \tag{7}$$

An exponentially decaying distribution of origins inside the tunnel (mostly from decaying pions) has a smaller value of $< r'^2 > -< r' >^2$ than does a flat distribution, for which the fractional error on $f(r)$ is approximately $L^2/4r^2$. For $r$ as small as 1 km, with a 180 m long tunnel, the approximation of all neutrinos from $r_0 =< r' >$ results in a fractional error on the detector rate of less than $L^2/4r^2 = 0.8\%$. Even this error will be mostly eliminated because the actual data analysis will not assume that all neutrinos come from the same point. In effect it will correct for the error described by Equation 7; so the systematic error from the

fact that the neutrino origin has a spread in positions will come from the Monte Carlo error in a correction whose full size is less than 0.8%. The systematic error from this effect will therefore be negligible. What will not necessarily be negligible is the error in our Monte Carlo estimate of $< r' >$. Thus almost all of the beam systematic error will be contained in our determination of $r_0 =< r' >$.

The beam in each energy bin is well defined by two parameters: the overall normalization, $A$, and the average origin, $r_0$. These two parameters can either be measured by placing detectors close to the beam origin or they can be calculated. If only one detector (at 3 km) is near the beam origin then we will have to rely on a calculation of $r_0$ to predict the flux or the number of muons at the far detector. Due to resolution and acceptance effects these muons will come from a range of neutrino energies, and therefore $r_0$ will be a complicated function of the beam and detector geometry, as well as the analysis cuts and the background contamination. An error in this complex calculation of $r_0$ will produce a systematic error in $f_p$ given by:

$$\frac{\delta f_p}{f_p} \approx 2\frac{\delta r_0}{(r_a - r_0)} \tag{8}$$

where $r_a$ is the distance to the first detector, $f_p$ is the predicted count rate at the far detectors, and the factor of 2 arises because of the $\frac{1}{(r-r_0)^2}$ dependence.

This systematic error caused by having only one detector near the beam origin could lead to a spurious oscillation signal when the statistical error in the far detectors becomes small after several months of running. Therefore it is desirable to eliminate this source of systematic error. Placing two detectors separated by 1-2 km near the beam origin eliminates the reliance on a Monte Carlo calculation of $r_0$. The two near detectors allow us to extrapolate the number of events at site $a$ and $b$ to the far sites to obtain $f_p$ and to the origin to obtain $r_0$. In such a situation the detector at site $b$ serves to monitor the normalization and the detector at site $a$ serves to define the source of the neutrinos.

## ERROR IN DETERMINATION OF BEAM PARAMETERS

The above formulation of the beam parameters is based on the assumption that either the beam is isotropic or the detectors are infinitesimal in size; neither of these is true. The neutrino beam is quite strongly focused in the forward direction. In the presence of such anisotropy, $r_0$ cannot be interpreted as the actual average origin of the neutrinos; nevertheless, it remains a useful parameter to understand the beam properties and the systematic error.

At 0 degrees the flux has a maximum and falls approximately as the square of the angle (or horizontal distance). Therefore event counts in detectors of equal size placed at various

distances at 0 degrees will not follow the $1/(r-r_0)^2$ law. On the other hand, at 1.5 degrees the quadratic term across the detector is small, and a linear fall in intensity dominates the flux shape (Figure 19). This linear fall does not cause a deviation from the $1/(r-r_0)^2$ behavior, since it is an odd function with respect to the center of the detector. Figure 19 also shows the change in spectrum across D1. The mean $E_\nu$ changes by about 10% across the fiducial volume. Figure III.10 shows that the average spectrum at D1 is however very close to the spectra at D3 and the far detectors. Below we will show that when combined with the effects of path-length and cross section this change in the spectrum across the detector at D1 does not cause significant deviation from $1/(r-r_0)^2$ law.

| Angle | % deviation from linearity |
|---|---|
| $0^0$ | 1.47 |
| $0.25^0$ | 1.04 |
| $0.5^0$ | 0.27 |
| $1.0^0$ | -0.31 |
| $1.5^0$ | -0.17 |
| $2.0^0$ | -0.12 |

Table 5: *The deviation from linearity (extrapolated minus calculated divided by the calculated flux at the far site) for* $q = 1/\sqrt{f}$.

In Figure 20 we have plotted $q = \frac{1}{\sqrt{f}}$, where $f$ is the total neutrino flux in a 15 meter diameter circular aperture located at r =1, 3, and 24 km from the target at various angles with respect to the tunnel axis. The calculations of these fluxes were performed using the GEANT based program originated at TRIUMF (see Figure 3). Since $q$ should be linear in $r$ we have drawn a line through the first two points and extrapolated it to the 24 km point. The vertical size of the box at the 24 km point corresponds to the statistical error expected after 16 months of running E889. The deviation of the central value at the 24 km point from the line is an indication of the departure from the $1/(r-r_0)^2$ behavior. This deviation is tabulated in Table 5. We see that the deviation from the $1/(r-r_0)^2$ behavior is strongest at 0 degrees and diminishes rapidly with angle. Although we don't display the results for the 68 km site, the same arguments hold. In the actual analysis we will use a complete simulation involving the observations in D1 and D3 to predict the event counts in D24 and D68. Nevertheless, we want to design a system that obeys simple geometric laws as fully as

possible. This is achieved in our experiment with detectors at 1.5 degrees.

The calculations shown in Figure 20 did not include the actual cylindrical shape of the detector and the neutrino cross section. The cylindrical shape of the detectors causes the path-length of the neutrinos at the centers of the detectors to be largest, and thus reduces the effect of the change in intensity across the detector. The effect of the change in spectrum across the detector (Figure 19) is small because the quasi-elastic cross section is slowly varying around 1 GeV neutrino energies. We have performed detailed Monte Carlo simulations of the neutrino beam and the resulting interactions in the detectors placed at 1, 3, 24 and 68 km locations with the 1.5 degree offset.

Table 6 shows the number of neutrino quasi-elastic events without cuts at the 1, 3, 24 km detector sites calculated by tracing neutrino rays from the decay tunnel to the detectors and properly accounting for path-lengths and cross section on an event by event basis. The apparent origin, $r_0$, can be calculated with the formula

$$r_0 = \frac{r_a - r_b\sqrt{(f_b/f_a)}}{1 - \sqrt{(f_b/f_a)}}. \tag{9}$$

We have varied the hadron production models (FLUKA [13] and GHEISHA[14]) used for the beam simulations as well as the neutrino cross section model (Kamiokande versus E734). Variations in the Monte Carlo clearly alter both the overall normalization and the parameter $r_0$ by significant amounts, but the extrapolation to 24 km using results at 1 and 3 km and the $1/(r - r_0)^2$ law remains robust as shown in Figure 21. The results for the 68 km detector are similar. This figure immediately shows the need for the two near detectors; with only one detector the normalization can be fixed, but $r_0$ will still need to be calculated by simulations, and systematic errors could result because of the uncertainties on the calculations. With two near detectors the experiment becomes a simple counting experiment to first order.

We plan to have two near detectors for the complete experiment, but we intend to evolve the experiment over time to explore the oscillation parameter space with increasing sensitivity. The first run of the experiment will be with only two detectors, one at 3 km and one at 24 km. Therefore we have to consider the systematic error on $r_0$ from Monte Carlo calculations for this very first run. Table 6 shows that variations in the hadronic shower physics and the neutrino cross sections can vary $r_0$ by about 9 m. A few additional geometrical systematic errors must also be considered for a two detector experiment; they are the knowledge of the target-horn materials, geometry, the current, and the proton beam steering (angle and position) on the target during the run. Including these effects, we estimate the total systematic error on the calculation of parameter $r_0$ to be about 20 m. If the near detector is the one at 3 km the

| r (km) | MC-1 | MC-2 | MC-3 |
|---|---|---|---|
| 1 km | $2749 \pm 5 \times 10^3$ | $2490 \pm 5 \times 10^3$ | $2575 \pm 9 \times 10^3$ |
| 3 km | $293 \pm 1 \times 10^3$ | $267 \pm 1 \times 10^3$ | $278 \pm 1 \times 10^3$ |
| 24 km | $4.52 \pm 0.05 \times 10^3$ | $4.05 \pm 0.05 \times 10^3$ | $4.33 \pm 0.03 \times 10^3$ |
| 24 km pred. | $4.50 \times 10^3$ | $4.11 \times 10^3$ | $4.29 \times 10^3$ |
| $r_0$ | $30.6 \pm 2.8$ m | $26.2 \pm 2.8$ m | $21.3 \pm 4.0$ m |

Table 6: *Quasi-elastic events in the cylindrical detectors placed at 1.5 degrees from the beam axis. Also shown is the prediction at 24 km using a the* $1/(r - r_0)^2$ *law. Figure 21 also shows this extrapolation. MC-1 is FLUKA beam with Kamioka cross sections. MC-2 is GHEISHA beam with Kamioka cross sections. MC-3 is FLUKA beam with E734 cross sections. The 1 and 3 km results were extrapolated to 24 km and to the horizontal axis to obtain* $r_0$. *The normalization is for* $2.2 \times 10^{20}$ *POT. The errors are from Monte Carlo statistics.*

beam related systematic error (Equation 8) in predicting the event counts at the 24 km site will be about 1.3%.

In summary, in the direct measurement of muon disappearance it is essential to have two near detectors to reduce beam related systematic errors that result from the extrapolation of event counts to the far detectors by Monte Carlo calculations. If the acceptances and efficiencies of all the detectors are well understood then an experiment with two near detectors can be considered a simple counting experiment that follows the $1/(r - r_0)^2$ law. The error due to beam calculations in predicting the flux at the 24 or the 68 km sites using two near detectors will be negligible compared to the statistical error at those sites after 16 months of running (about 1% and 3% for the D24 and D68, respectively). Moreover, since the two near detectors, which are identical to the far detectors, decouple the beam from the detector response the experiment will not be to a spurious oscillation signal.

Since we envision that the first run of the experiment will have only one near detector the systematic error in the determination of the parameter $r_0$ by Monte Carlo calculation must be considered. We estimate it to be $\delta r_0 \approx 20$ m. The beam related systematic error on the prediction at the far site for a two detector experiment given by Equation 8 will be 1.3% if the near detector is at 3 km.

Finally, the beam related systematic error is of importance mainly for the result using D24 where the statistical error will be about 1% after 16 months (2% after 4 months); the

statistical error at D68 will be about 3% after 16 months and therefore the results from D68 will not be limited by systematic errors.

### V.2.4.2 DETECTOR SYSTEMATIC ERRORS

We may combine the effects of all detector related systematic errors into a single systematic error on the number of events in one of the near detectors, $\delta f_a$. Then it can be shown that the error on the predicted number of events at the far site, $\delta f_p$, is, in the case of a two detector experiment:

$$\frac{\delta f_p}{f_p} \approx \frac{\delta f_a}{f_a}. \tag{10}$$

In the case of a three detector experiment we use the known distances to the near two detectors to extrapolate the counts to the far site (Figure 21) and if the near two detectors are sufficiently far apart so that $f_a >> f_b$ then

$$\frac{\delta f_p}{f_p} \approx \frac{r_a - r_o}{r_b - r_a} \frac{\delta f_a}{f_a}. \tag{11}$$

Here $f_a$ and $f_b$ are the counts in the near two detectors, and $r_a$ and $r_b$ are the distances to the near detectors. $f_p$ is the prediction for the far detector, and $r_0$ is the parameter that describes the beam. We have assumed that most of the systematic error is in the nearest detector in either the two or the three detector situation. Now we will estimate the size of the systematic error in the near detectors due to various contributions.

### DETECTOR LOCATIONS

We have located the detectors so that they are all close to each other in both polar and azimuthal angles about the beam axis. Table 7 shows the locations in latitude and longitude of the selected sites which are chosen to lie on a great circle. The local elevations of the ground with respect to sea level are also indicated. There are no severe constraints at any of the sites including the Northville and the Plum Island sites on the exact locations of the detectors. There is also freedom to place the tanks below the existing ground elevation by about 4-5 m by excavation. We will place the bottom of the detector tank, D1, 4 m below the ground level. Figure 22 shows the four detectors as viewed from the neutrino production target in polar and azimuthal angular co-ordinates with respect to the beam axis. We have ignored the small angular tilt ($0.25^o$ at D68) in the detector axis due to the earth's curvature at different sites for the purposes of this analysis. The figure shows that all detectors are aligned with respect to their axes and that D1 covers all detectors in solid angle. The beam can be pointed so that both D24 and D68 are at the same polar angle of $1.5^o$, but about $10.2^o$

| Site | Latitude | Longitude | Elevation m |
|---|---|---|---|
| Production Target | 40°52′34.167″ N | 72°52′43.940″ W | 22.9 |
| D1 at 1 km | 40°52′50.682″ N | 72°52′07.189″ W | 18.0 |
| D3 at 3 km | 40°53′23.704″ N | 72°50′53.672″ W | 17.0 |
| D24 at Northville | 40°58′49.996″ N | 72°38′44.573″ W | 35.0 |
| D68 at Plum Isld. | 41°10′59.184″ N | 72°11′17.350″ W | 10.7 |

Table 7: *Locations of the sites in latitude and longitude. The local ground elevation with respect to sea level is shown in the last column.*

apart in azimuth. Since the detectors are located with their axes precisely at the same polar angle with respect to the beam, we do not need to make corrections to the numbers of events in each of the detectors to compare them to each other. In particular, the linear component in the flux variation across the detectors in Figure 19 is unimportant because the detectors are aligned to within a fraction of a milliradian. With the alignment shown in Figure 22 any corrections will be quite small. The small difference in the azimuth between D24 and D68 is mainly due to the earth's curvature; we have performed Monte Carlo studies of the beam to see if the neutrino flux can vary over this small angular interval. We have found that such effects, mainly due to proton beam misalignments, will be quite small, and in any case, the neutrinos that go to both D68 and D24 will be monitored by D1.

## FIDUCIAL VOLUME AND SOLID ANGLE

The far detectors, which are identical in size and photomultiplier coverage to the near ones, subtend smaller solid angles with respect to the beam. The neutrino flux varies with the angle, and the near detectors see neutrinos at both smaller and larger angles than the far ones. We have chosen to separate the systematic errors due to the effects of flux variation across the detectors into two parts: We have already discussed the systematic error on the apparent origin of the neutrinos which must be computed if we have only one near detector. The second source of potential systematic error results after the analysis cuts from each of the detectors are applied to the events. Because the geometry causes the progenitor distribution of the neutrino events to be somewhat different in each detector tank, the acceptances computed in each detector for the analysis cuts – fiducial, containment, and angle or energy – will be somewhat different. Figures 23 and 24 show the distribution of event vertices across the detector tanks in the horizontal coordinate (perpendicular to the neutrino beam axis). The

| Cuts | 1 km | 3 km | 24 or 68 km |
|---|---|---|---|
| Fiducial Contained | $0.492 \pm 0.005$ | $0.494 \pm 0.005$ | $0.496 \pm 0.005$ |
| Muon angle $< 60^o$ | $0.323 \pm 0.005$ | $0.337 \pm 0.005$ | $0.329 \pm 0.005$ |

Table 8: *Acceptance for quasi-elastic events for fiducial, containment, and angular cuts for detectors at the various locations. The error is from Monte Carlo statistics.*

figures show that the fiducial (1 m in from the PMT surface) and containment cuts combined with the cylindrical geometry of the detectors tend to force the vertex distributions to be similar at all locations. The nearest detector will have a small excess of events on one side of the detector compensated by a small deficit on the other side. The systematic error on the differences in acceptance will affect both types experiments, i.e. that with only one near detector and that with two near detectors. Table 8 shows the acceptance for quasi-elastic events at the different detector sites. There is a small increase (about 0.8%) in acceptance between the detector at 1 km and the far detectors at 24 km or 68 km. We will have to correct for this change in acceptance to get back to raw event counts displayed in Figure 21. At the moment we will consider this entire change as a systematic error.

**SPECTRUM**

We have examined the spectrum of muons and the neutrinos that generate the muons for each of the four detector sites. Figure 25 shows that the spectrum of photoelectrons observed in the 3 km and the far detectors should be very close to each other in the absence of oscillations. The spectrum at 24 km and 68 km are identical to each other, and so the 68 km spectrum is implicit when we discuss the 24 km spectrum. The spectrum at 1 km is softer by a small amount. The fraction of the spectrum below 750 photoelectrons ($P_\mu \approx 550 MeV/c$) is about 8% higher in the case of the 1 km detector compared to the 24 km detector. We can correct for this by Monte Carlo or by making tighter fiducial cuts in the 1 km detector and then correcting for the different acceptance. For the purposes of an oscillation analysis the spectrum from the 3 km detector can be used with no corrections for comparison with the spectra from the far detectors.

Figure 26 shows the spectrum of neutrinos that produce the events in Figure 25. Both the detector response and the event characteristics could depend on this spectrum which is slightly different for the 1 km, the 3 km , 24 km, and 68 km detectors. The mean energy of the neutrinos is 0.922 GeV in the 1 km detector and 0.956 GeV in the 3, 24, and 68 km

detectors. Most of the systematic error from the change in the spectrum has already been accounted for in the acceptance cuts (Table 8). Any corrections to the detector efficiencies because of the combination of spectrum change and detector resolutions will be smaller than the acceptance change.

## CALIBRATION

Small differences in the detectors could be caused by dead photomultiplier tubes, differences in the light attenuation length in water, differences in the calibration constants or the timing signals, etc. These differences will translate into small differences in the efficiencies for detecting signal events and rejection of backgrounds between detectors. As explained in the section on detector construction we intend to test the photomultiplier tubes and associated hardware for reliability and increase the number of photomultipliers by a small factor to compensate for the probability that some of the tubes will not work after several years of running. From previous experiences in the Kamioka and IMB detectors the probability of dead tubes is less than 5% over the course of the running time. One advantage of having the detector tanks on the surface is the ability to continuously monitor the detector calibration with cosmic rays. With careful control of the hardware and calibrations the systematic errors due to differences in the detectors should be small.

## DEAD TIME

There are two main causes of deadtime in the experiment: 1) overlapping cosmic ray events, and 2) overlap of two events from the neutrino beam.

As shown in Chapter III the total spill length for the AGS beam is $2.68\mu s$. Within this time there could be 0.2 cosmic ray events. The readout electronics is such that each PMT will remain dead for 60 to 200 ns after a hit. If we assume that no spatial separation between real cosmic rays and neutrino induced events is possible, then for a neutrino event to be deadtimed a cosmic ray event must occur 200 ns before the time of one of the 8 buckets. This corresponds to 1.5% of the neutrino events lost in each of the detectors. We intend to make this loss smaller by adjusting the PMT deadtime to be less than 200 ns. Some spatial separation of the event vertices is also possible but has not been studied in detail yet. In any case, the deadtime due to cosmic rays will be the same in all detectors and monitored closely by having a separate trigger for cosmics with a fixed gate outside the AGS beam gate.

The second type of deadtime could pose a systematic problem since the event rate in the near detectors is much higher than the event rate in the far detectors. In the case of neutrino events we only need to consider the rate of overlapping events in the same time

bucket because the time between buckets (335 ns) is long enough for the PMTs to recover. The total neutrino event rate in the entire inner volume of the nearest detector at 1 km will be about 0.86 events per AGS spill (with 8 buckets). Using Poisson probability function, 0.37 of the events will be accompanied by at least one other event in one of the 8 buckets; therefore 5% of the events will actually have two separate events in the same bucket. We will most likely reject events as multiring events if the event vertices are closer than $\pm 2$ m in all dimensions. Given that the detector volume is 7.5 m in radius and 15 m in height, a correction of about 0.12% will have to be applied to the event rate in the closest detector. The vertex resolution will be much better than 2 m, but light from two widely separated vertices could still fall on the same PMTs depending on the direction of the particles.

Another way to correct for the loss due to deadtime is by taking a few different runs of data at different intensities. The 1 km detector has an approximate rate of about $10^5$ $QE(\mu^-)$ events per week at the nominal intensity of $4 \times 10^{13}$ POT. In two different running periods (2 weeks each) with 1/3, and 2/3 of the full intensity one can gather data to study the deadtime correction with an error of about 10% of the value of the full correction of 5%.

To further illustrate the trade-offs, if we place the nearest detector at 2 km instead of 1 km the deadtime will reduce by a factor of 4 and the change in the spectrum between the nearest and the farthest detector will also be smaller. On the other hand one could argue that we want a near detector that covers a much larger solid angle than the far detectors to study the beam. At the moment we have optimized with a detector at 1 km, but are studying other possibilities. We will assume a systematic error of 0.5% due to the deadtime corrections.

## BACKGROUND SUBTRACTION

As shown in Section V.2.3 we expect a contamination of 5.4% from neutral current events and charged current events of high energy (above 1.5 GeV) neutrinos in the quasi-elastic muon sample. The total contamination above 300 photoelectrons including WCC and WNC events from neutrinos below 1.5 GeV will be about 15%. Also we expect a 6% contamination due to cosmic ray events in the 68 km detector after the full running time.

We are confident that the neutrino induced background can be calculated and subtracted; any error in such a subtraction will dilute an existing signal rather than introduce a new one. The main systematic error in the background procedure will be due to the differences in the neutrino spectrum. The change in the mean energy of the neutrinos between D1 and D24 (or D68) is about 3.6%. Since the cross sections for the backgrounds are approximately linear with energy in this region the maximum systematic error due to neutrino background

subtraction will be about 0.5%. The sensitivity of the experiment does not depend on this background subtraction since 2/3 of the background are WCC events from $\nu_\mu$ of the same energy spectrum as the $QE(\mu^-)$ signal. If left unsubtracted the significance of an oscillation signal will simply reduce by 5.4% which is the background fraction that does not oscillate.

The cosmic ray background will be measured extremely well. But we will assume no background subtraction for the cosmic ray events when calculating the sensitivity. If we were to subtract the cosmic ray background we are confident that it can be done without introducing a systematic error greater than 0.3% as pointed out in the previous discussion on cosmic ray backgrounds.

### V.2.5 SUMMARY OF DIRECT $\nu_\mu$ DISAPPEARANCE ANALYSIS

In summary, consider the size of the total systematic error compared to the statistical error on the event counts at the far sites. The statistical error at D24 and D68 will be about 1.0% and 3.0%, respectively after 16 months of running, using the contained event count in Table 1. In the case of an experiment with only two detectors, one near at 3 km and one at 24 or 68 km, the total systematic error will come from both the beam calculations (1.3%) and the detector corrections (1.1%). (Equations 8 to 10). Therefore the total systematic error in the case of a two detector experiment will be 1.7%.

In the case of an experiment with three detectors, two near at 1 and 3 km and one far at 24 or 68 km, the contribution from the beam calculations will be small. The main systematic error will be from the detector corrections of 1.1% in the nearest detector. Using Equation 11 which accounts for the use of the second near detector for extrapolation, the systematic error on the prediction at the far detector will be 0.6%.

To get maximum sensitivity with a far detector at 24 km one must perform a three detector experiment which reduces the systematic error below the expected statistical error. On the other hand with a far detector at 68 km the maximum possible sensitivity will be determined by the statistics at that far site. Nevertheless, two near detectors will be essential to eliminate the dependence to first order on a Monte Carlo calculation of the beam and to irrefutably establish a signal. With four detectors as shown in Figure 22 we will satisfy all requirements of statistical and systematic precision and perform an experiment with many independent controls. Moreover, in the case of a positive oscillation signal we will measure the oscillation parameters precisely using the count rates in detectors at different oscillation lengths from the neutrino origin. The discussion of the sensitivity of the direct $\nu_\mu$ disappearance result is

in Section V.5.

## V.3 NEUTRAL CURRENT $\pi^0$ EVENTS

### V.3.1 INTRODUCTION

If a signal for $\nu_\mu$ disappearance is observed, it will be important to establish it in as many different ways as possible. An independent way to perform the $\nu_\mu$ oscillation experiment is to compare the ratio of charged current muon neutrino events to neutral current $\pi^0$ production interactions ($QE(\mu^-)/NC(\pi^0)$) in the near and far detectors. The analysis for such a measurement is very different from the muon disappearance analysis. In particular, since the number of reconstructed neutral current pion events will always be smaller than the number of muons the sensitivity will be dominated by the pion statistics and will be lower than the direct muon disappearance analysis. The systematic errors will not be as important because first they will be smaller than the statistical error on the pion counts at the far detectors and second most of the beam or detector related systematic errors will cancel out in the ratio. This method of analysis will also be important in the unlikely case that the oscillations are occurring into a sterile neutrino ($\nu_\mu \rightarrow \nu_s$) that does not interact through charged or neutral current interactions. In such a case a deficit of muon events will be accompanied by the same fractional deficit of pion events, and the ratio of muons to neutral current pions will remain the same at all distances from the beam. In the following we show that the measurement of the ratio ($QE(\mu^-)/NC(\pi^0)$) could be performed with sufficient precision in our apparatus to be sensitive to most of the oscillation parameter space as the direct muon disappearance search. The measurement of this ratio will independently establish or rule out the Kamioka signal.

### V.3.2 SIGNAL AND BACKGROUND

The two main neutral current single $\pi^0$ channels are

$$\nu n \rightarrow \nu n \pi^0 \tag{12}$$

$$\nu p \rightarrow \nu p \pi^0 \tag{13}$$

The ratio of the neutral current single $\pi^0$ cross section to the charged current quasi-elastic cross section has been calculated over the energy region of the AGS beam (Figure 27) [5]. When averaged over the flux the ratio of cross sections is 0.10 for each of the above two channels. About 6% additional $\pi^0$ are expected from coherent production off oxygen nuclei

| | 1 km | 3 km | 24 km | 68 km |
|---|---|---|---|---|
| Events in Detector | $20.7 \times 10^5$ | $23.2 \times 10^4$ | 3632 | 453 |
| Events in Fiducial | $13.6 \times 10^5$ | $15.1 \times 10^4$ | 2364 | 295 |
| 2 Ring Events | $7.37 \times 10^5$ | $8.17 \times 10^4$ | 1281 | 160 |
| 1 Ring and Extra Energy | $2.83 \times 10^5$ | $3.13 \times 10^4$ | 492 | 61 |
| Total Reconstructed | $10.2 \times 10^5$ | $11.3 \times 10^4$ | 1773 | 221 |

Table 9: *The number of neutral current $\pi^0$ events for $8.8 \times 10^{20}$ POT or 16 months of running at the four detector sites with one detector tank each. The events are in the fiducial volume and have at least 50 PMTs hit. There will be about 15% background from charged current $\pi^0$ production.*

[11]. The cleanest signature of a $\pi^0$ is two electromagnetic Cherenkov rings. A sample of Monte Carlo WNC $\pi^0$ events were scanned visually to identify event topologies. These events were tagged as to the number of rings and whether extra energy was present indicating the presence of another photon. Further details of the pattern recognition can be found in Chapter IV. The scanning results indicate that 54% of the events inside the fiducial volume produced two rings without extra energy. An additional 21% of the $\pi^0$ events have a single ring with extra energy indicating the existence of the other photon. The extra energy can be either an incomplete ring or an accumulation of energy at the edge of the ring. These events could be recovered with a more sophisticated analysis that reconstructs the mass of the $\pi^0$ using the energy measurement of the complete and the incomplete photon rings (see Chapter IV). Combining the numbers, the total number of $\pi^0$ events with two clean rings will be about 11% ($0.2 \times 0.54$) of the quasi-elastic muon rate. A 40% gain in the $\pi^0$ statistics would result if we also use events with one incomplete ring. Table 9 gives the total number of neutral current $\pi^0$ events in the fiducial volume expected in each detector for a 16 month run with $8.8 \times 10^{20}$ POT.

The principal background comes from the charged current channel $\nu_\mu n \rightarrow \mu^- \pi^0 p$ which normally produces three rings. We have visually scanned these events to find the fraction that appears as two showering rings to be 6% (Chapter IV). In most of these remaining events the muon will be below detection threshold. The fraction of events with one complete showering ring and some extra energy is 1.5%. Since the ratio of the $\mu^- \pi^0 p$ cross section to the quasi-elastic cross section is 0.3, the expected background from the charged current

single $\pi^0$ in the neutral current single $\pi^0$ channels is 16% ($\frac{0.3\times0.06}{0.11}$) using only the two ring sample. The background for the two ring plus one ring with extra energy sample is 15%. However this sample might have some additional contribution from misidentified particles since the incomplete ring may not be recognized as a clean showering particle. We have not yet examined this background and the obvious method of eliminating it by reconstructing the $\pi^0$ mass. The charged current background could be subtracted with the introduction of a small systematic error. If it is left unsubtracted it will dilute the oscillation sensitivity. In neither case will it cause a statistically significant spurious oscillation signal.

The methods we intend to employ in reconstructing the events are discussed further in Chapter IV on pattern recognition. The important point that should be repeated here is that the event samples in the far detectors are small enough that a manual scan of the data can be performed. A random sample of events in the near detectors can be manually scanned to obtain the expected ratio of muons to $\pi^0$s. If the random sample is chosen to be sufficiently larger than the number of events in the far detectors, the $\nu_\mu$ disappearance analysis normalized to the neutral current $\pi^0$s can be performed without the use of computer pattern recognition.

### V.3.3 SYSTEMATIC ERROR ON $(QE(\mu^-)/NC(\pi^0))$

As shown in Table 9 the statistical error after 16 months of running on the $\pi^0$ counts will be about 2.4% at D24 and 6.7% at D68. Most of the systematic errors discussed for the direct muon disappearance analysis are either small compared to the $\pi^0$ statistics or cancel out in the ratio $QE(\mu^-)/NC(\pi^0)$. The systematic error that may not cancel will be due to the spectrum change between the near and the far detectors. The change in the mean energy of the spectrum does not affect the muon counts since the quasi-elastic cross section is approximately flat in the 1 GeV energy region. The cross section for $\pi^0$s, however, is linear with energy in the 1 GeV energy region; therefore a correction that accounts for the different cross section dependencies on the energy will have to be made when comparing the ratios measured in the near and far detectors.

We showed in Figure 26 that the neutrino spectra in D3, D24, and D68 are nearly identical, therefore the correction to the ratio when comparing the ratio in D3 and the far detectors will be much smaller than the statistical errors on the $\pi^0$ counts. The mean energy of the spectrum does change by 3.6% between D1 (0.922 GeV) and D3 (0.956 GeV), and therefore if we use the near detectors, D1 and D3, to look for oscillations at $\Delta m^2 > 0.1$ eV$^2$ they will most likely be limited by systematic error on the calculation of the correction to the ratio.

We use the cross sections in Figure 27 to estimate this correction to be 2%. For the current analysis we will assume the entire correction to be the worst case systematic error of 2%. The discussion of sensitivity to neutrino oscillations with the ratio method is in Section V.5.

## V.4 $\nu_e$ APPEARANCE

### V.4.1 INTRODUCTION

If a signal of $\nu_\mu$ disappearance is observed, it will be important to understand its origin, and in particular check whether the deficit of $\nu_\mu$ flux is accompanied by an excess of $\nu_e$. Any deviation between the expected number of $\nu_e$ events at a far detector and the observed number will constitute an electron neutrino appearance signal. We have discussed in detail how backgrounds, systematic and statistical errors affect the muon neutrino disappearance experiment. The concerns for a $\nu_e$ appearance experiment are quite different. As explained in Chapter III.A the contamination of electron neutrinos in the beam is quite small; therefore even a small increase of electron neutrino type events will be detectable if the backgrounds from other processes (mainly misidentification of $\pi^0$s) can be kept low. Even if some background is present we will show that very good sensitivity to $\nu_\mu \rightarrow \nu_e$ is obtained by using the near detectors as monitors of the background. Unlike the direct muon neutrino disappearance analysis, the beam or detector systematic errors play a minor role.

### V.4.2 BACKGROUNDS TO THE $\nu_e$ SIGNAL

The principal background contributions to the $\nu_e$ appearance signal come from (1) the small contamination of $\nu_e$'s in the AGS beam, (2) the misidentification of neutral current $\pi^0$s as electrons, and (3) the misidentification of a small number of $\mu$'s as electrons, troublesome since the dominant component of the beam is $\nu_\mu$.

#### V.4.2.1 $\nu_e$ CONTAMINATION IN THE BEAM

The $\nu_e$ contamination in the AGS neutrino beam is well understood. The experimentally measured ratio of flux, $\frac{\nu_e}{\nu_\mu}$, from experiment 734 is shown in Figure 28. The total $\nu_e$ contamination in E734 was measured to be $7.3 \pm 1.4 \times 10^{-3}$. The curve in this figure is from the neutrino beam simulation program indicating the reliability of the calculation. Unlike E734, the detectors in E889 are positioned at $1.5^o$ off the neutrino beam axis. The off-axis geometry causes an increase in the $\nu_e$ contamination in the beam because a majority of it comes from kaon decays which tend to emit $\nu_e$'s at wider angles than the decays of pions which are the main source of $\nu_\mu$. Figure 29 shows the expected ratio of $\nu_e$'s to $\nu_\mu$'s in the $1.5^o$ beam; the

calculation includes contributions from both charged and neutral kaons, muon decays, and also a tiny contribution from pion decays. The total fraction of $\nu_e$, $\frac{\int \Phi(\nu_e) dE}{\int \Phi(\nu_\mu) dE}$, for this beam is 1.04%. The contamination from $\bar{\nu}_e$ in the beam is much smaller (0.11%), and therefore will be ignored in the rest of the analysis. The contamination $\nu_e$ spectrum tends to be somewhat higher energy than the $\nu_\mu$ spectrum (Figure 3). We should be able to use this difference to statistically separate out the signal $\nu_e$ which come from the oscillation of lower energy $\nu_\mu$.

### V.4.2.2 $\pi^0$ MISIDENTIFICATION AS ELECTRONS

Events containing $\pi^0$s can appear like $\nu_e$ quasi-elastic events if the $\pi^0$ is misidentified as an electron and any other charged particles in the event are below detection threshold. A $\pi^0$ will generally appear as two Cherenkov rings, but some times only a single ring will appear because either the $\pi^0$ distributes its energy between the photons asymmetrically so that only one ring has enough Cherenkov light to be visible or the two photon showers overlap. To establish the fraction of $\pi^0$ events that would be identified as electrons, we have visually scanned both neutral and charged current $\pi^0$ events (the $\nu n \pi^0$, $\nu p \pi^0$, and $\mu^- p \pi^0$ channels). The generated momentum distribution of these pions is the same as in Figures 11 and 13 with a mean momentum of about 300 MeV/c. The events were classified as to the number of rings that were present and if there was extra energy outside the ring that might indicate the presence of another low energy particle. A more thorough description of the visual scanning results is presented in the pattern recognition section.

We have found that 23% of the neutral current $\pi^0$ events in the entire inner volume appear as single ring events. Only 5% of the charged current $\pi^0$ events appear as single ring; furthermore when we require that the single ring should not look like a muon only 1% of the charged current $\pi^0$ events remain. Therefore charged current $\pi^0$ events do not constitute a significant background. We have examined the vertex and energy distribution of the single ring neutral current $\pi^0$ events and found that they tend to be preferentially at the edge of detector; this is understandable because both the probability of losing one of the two photons and of overlapping photons is higher if the $\pi^0$ is at the edge of the detector. With a fiducial volume cut of 6.5 m in radius and 13.0 m in height the scanning results indicate that 20% of the NC-$\pi^0$'s within the fiducial volume look like single ring events; with a tighter fiducial cut of 6.0 m in radius and 12.0 m height 17% look like single ring events. Since a fiducial cut also lowers the statistics on the signal there will be some optimum fiducial cut for the highest statistical measure of sensitivity, but for the purposes of this analysis we will assume our standard fiducial volume of 6.5 m in radius and 13.0 m height. A cut on the angle of the showering particle with respect to the neutrino direction of 90 degrees gets rid of another

25% of the pion background since it is at wider angles, but retains more than 94% of the quasielastic electron signal from oscillated $\nu_\mu$. When combined with the cross section for neutral current pion production of 10% of the quasi-elastic muon rate for each of the two neutral current channels, we obtain that the single ring showering particle background from $\pi^0$s will be about 3.0% ($2 \times 0.10 \times 0.2 \times 0.75$) of the quasi-elastic muon rate.

This low background level from $\pi^0$ contamination is one more advantage of the off-axis 1.5 degree low energy beam. If we were to use the on-axis 0 degree beam, the background could be a factor of 2-3 higher because the higher energy neutrinos have a higher cross section for pion production, and the higher energy pions also have a higher probability for producing events with overlapping showering rings.

### V.4.2.3 MUON MISIDENTIFICATION

The misidentification of muons as electrons could be a background since $\nu_\mu$ is the dominant component of the neutrino beam. We have visually scanned many muon quasi-elastic events and found that the muon-electron separation rapidly improves with energy. Above a cut of 500 photoelectrons (corresponding to about 350 MeV in energy for electromagnetic showers and 400 MeV/c for muon momentum) the fraction of muon events misidentified as electrons will be less than 1% while the particle identification efficiency for electrons will remain more than 95%. Previous water Cherenkov experiments, Kamioka and IMB, have developed sophisticated statistical tests for electron-muon separation. Relying on their experience and the recent beam test conducted at KEK in a smaller water Cherenkov tank, the background from $\mu$/e misidentification is expected to be quite small. The results from the beam test and the appropriate references are discussed in Chapter IV on pattern recognition and reconstruction. We continue to improve our methods for shower recognition, but since this particular background will be small, particularly above the 500 photoelectron cut, we do not include it in the analysis for $\nu_e$ appearance.

Other sources of background to electron-like events could be neutral current coherent production of $\pi^0$ off the oxygen nuclei, $\pi^0$ production due to charge exchange interactions of charged pions produced in other interactions, and $\pi^0$ production due to cosmic ray neutrons. We have considered all these sources of background and found them to be small either because the cross sections are small or because they are accompanied by other charged particles above detection threshold.

Figure 30 shows the photoelectron spectrum of the single ring electron like event background. Table 10 shows the expected rate of background single ring showering events. As expected the pion contamination, which dominates the distribution, peaks at about 500 pho-

| | 1 km | 3 km | 24 km | 68 km |
|---|---|---|---|---|
| Events in Detector | $5.77 \times 10^5$ | $6.44 \times 10^4$ | 1003 | 125 |
| Events in Fiducial | $3.40 \times 10^5$ | $3.77 \times 10^4$ | 591 | 74 |
| Events Angle $< 90^0$ | $2.72 \times 10^5$ | $3.02 \times 10^4$ | 473 | 59 |

Table 10: *The number of single ring showering events expected from electron neutrino contamination and misidentified $\pi^0$ in the absence of neutrino oscillations after $8.8 \times 10^{20}$ POT or 16 months of running.*

toelectrons. Both the $\nu_e$ contamination and the signal events from oscillated $\nu_\mu$ will be more widely distributed in energy. Therefore a cut at 500 photoelectrons should be quite effective in getting rid of half of the pion contamination and selecting events that can be unambiguously identified as electrons.

### V.4.3 BACKGROUND SUBTRACTION AND SYSTEMATICS

The contributions to $\nu_e$ background from the $\nu_e$ contamination and from NC–$\pi^0$ misidentification can be well determined from data in the near detectors. The $1/(r-r_0)^2$ law will allow a reliable determination of the expected rate of showering single rings at the far detectors. Because the total rates for these events are quite low (Table 10) at the far detectors the systematic errors on the extrapolation will not be important. However, we also wish to use the near detectors, D1 and D3, to search for oscillations at higher values of $\Delta m^2$. The background statistics in the D3 detector will be large enough so that the sensitivity in $\sin^2(2\theta)$ at these values of $\Delta m^2$ will be limited by systematic errors after the full running period. The treatment of systematic errors in this case will be very similar to what was discussed for the direct $\nu_\mu$ disappearance analysis, except that the systematic errors will be on the background which will be 4.0% of the quasi-elastic muon rate; the signal is expected to be much larger than the background at full mixing. If we use a total systematic error of 1.7% including both beam and detector related effects on the background prediction at D3 using observations in D1, then we should be able to reach sensitivity in $\sin^2(2\theta)$ below 0.001 at $\Delta m^2 \approx 0.5$ eV$^2$. The discussion of the sensitivity of the $(\nu_\mu \rightarrow \nu_e)$ experiment is in Section V.5.

## V.5 SENSITIVITY TO NEUTRINO OSCILLATIONS

In this section we will use the results obtained in Sections V.2, V.3, and V.4 on the backgrounds and the systematic errors to estimate the sensitivity to neutrino oscillations in each analysis channel.

### V.5.1 DIRECT $\nu_\mu$ DISAPPEARANCE

The main channel of analysis is the disappearance of muon neutrino quasi-elastic events. The quasi-elastic event counts in the near detectors will be used to predict the counts in the far detectors. The spectrum of the events in the near and far detectors can also be compared. If the number of events in the far detectors is found to be less than the predictions then the significance (the number of sigmas) of the result will depend on the statistical error on the event counts in the far detector and the systematic error on the prediction. We have used Equation 1 and the systematic errors described in the previous sections to perform this calculation with a number of rather conservative and simplifying assumptions. Our main thrust in this analysis is the identification and elimination of effects that could cause spurious oscillation signals.

- We have integrated all the events up to 3.0 GeV. If we use the energy spectrum of the events then the significance of the result will certainly be higher. The neutrino spectrum at $1.5^o$ is essentially a narrow band spectrum around 1 GeV. This is of great benefit because one can extract an oscillation signal with minimal analysis of the spectrum.

- We have assumed subtraction of the neutrino beam related backgrounds and included a systematic error associated with it. As explained earlier the neutral current backgrounds mainly dilute the effect of the oscillations. If we under-subtract this background then the remaining background events will dilute the signal; if we over-subtract then the statistical power of the event sample will be lessened. The total significance of the oscillation signal will increase with a proper background subtraction with no chance of a spurious signal.

- We have assumed no subtraction of the cosmic ray background events. This background contributes a constant number of events at each of the detector sites, and thus if left unsubtracted works in the opposite direction to the diminution of quasi-elastic events expected from neutrino oscillations. We have shown that cosmic background will contribute about 6% of the quasi-elastic signal events at the 68 km site. The fraction at the

nearer sites is much smaller. We will be able to measure this background very well by using cosmic ray data from outside the AGS beam gate. By subtracting the measured rate of background from the neutrino events we will be able to increase the sensitivity to neutrino oscillations. However, if we over-subtract the cosmic background there is a danger of causing a spurious oscillation signal. Therefore we prefer not to subtract the cosmic ray background.

- We use a simple formula to predict the number of events at the far site assuming a $1/(r - r_0)^2$ behavior:

$$f_p = f_a \frac{(r_a - r_0)^2}{(r_c - r_0)^2} \tag{14}$$

$$r_0 = \frac{r_a - r_b\sqrt{(f_b/f_a)}}{1 - \sqrt{(f_b/f_a)}} \tag{15}$$

Here $a$ and $b$ denote the near sites. $f_p$ is the predicted number of events at the far site $c$ located at $r_c$, at 24 or 68 km. And $r_0$ is obtained from the measurements at the near sites. We apply this formula using the number of events at each of the sites including the effects of oscillations, background and efficiencies. We define the significance of the oscillation signal as:

$$\sigma = \frac{f_p - f_c}{\sqrt{({\sigma_p}^2 + {\sigma_c}^2)}} \tag{16}$$

where $f_c$ is the actual number of events at the far site including the effects of oscillations, backgrounds, and efficiencies which have been discussed in the previous sections. $\sigma_p$ and $\sigma_c$ are the systematic error on the prediction and the statistical error on the number of events at the far site, respectively. We do not correct for the small oscillation effects between the near sites in Equation 14. A small oscillation effect at 3 km will cause us to predict a smaller number of events at the far site and reduce the significance of the oscillation signal by a small amount with no chance of a spurious signal. In the actual analysis of data, we will, of course, fit the detected number of events at the various locations with the oscillation parameters to get the best sensitivity. But here we wish to show the strength of the experiment by displaying the large unmistakable oscillation signal that will result after a simple analysis.

The most exciting possibility is the discovery that the atmospheric neutrino oscillation signal seen in the Kamioka and IMB data is correct (Figure 31). We have calculated the

| | D24 | D68 |
|---|---|---|
| Single ring muon-like expected | 12150 | 1478 |
| Deficit $\Delta m^2 = 0.01$ eV$^2$ | 1490 | 875 |
| Deficit $\Delta m^2 = 0.005$ eV$^2$ | 400 | 329 |

Table 11: *Event deficit and the expected signal after* $8.8 \times 10^{20}$ *POT or 16 months of running at both of the far sites. The muon-like event counts include background from neutral current and charged current single pion production and cosmics.* $\sin^2(2\theta) = 1.0$ *for the result in this table.*

spectrum of single ring muon-like events that will be observed in the far detectors. Figure 32 shows the muon spectrum after the full running time of the experiment with and without oscillations using the best fit oscillation parameters from Kamioka ($\Delta m^2 = 0.01$ eV$^2$ and $sin^2(2\theta) = 1.0$). We have included the spectrum of the background events and the appropriate amount of systematic error. The oscillation signal will be large and unmistakable, and will not be caused by spurious effects. In Table 11 we show the numbers of muon like events that should disappear at the far sites compared to the predicted numbers of events for two values of $\Delta m^2$ at full mixing.

Figure 33 shows the 90% confidence level sensitivity of the full experiment after 16 months of running, and for intermediate steps. As we have stated above, an analysis of the spectrum will clearly push the sensitivity below that shown in Figure 33. We have designed the experiment, so that we need not wait until all the detectors are built and operated to perform much of the physics. We envision that we will be able to do the physics as soon as the beam and two detectors, one near and one far, are ready to take data. The first run (about 4 months long or $2.2 \times 10^{20}$ POT) of the experiment will have a detector at 3 km and one at 24 km. At both of these sites we will have large event rates to study and perfect our technique, and the oscillation sensitivity will be sufficient to study most of the Kamioka allowed region. We expect to have the 68 km detector ready for the second run of the experiment; the limit obtained with running the 68 km detector for 4 months is also shown in Figure 33. If large effects are detected in the first run then the 68 km detector will confirm them. For the first two runs there will be only one detector on site and so the systematic errors associated with the beam will be larger. We have included these systematic errors in the calculation of Figure 33. In the final stage of the experiment another detector will be added on site at 1 km to

eliminate the beam related systematic errors and the dependence on a beam calculation. This is reflected in the improved final sensitivity with D24 in the region $0.005 < \Delta m^2 < 0.1$ eV$^2$. We have also included the limit obtained with the use of 1 and 3 km detectors at high values of $\Delta m^2$ in the final sensitivity of the experiment. We assume at the moment that the limit at high $\Delta m^2$ will be limited by systematic errors in about 4 months of running. We note that after the full running the statistics accumulated in the 24 km detector will be so large that the result from it will most likely be limited by systematic errors. On the other hand the results from the 68 km detector will continue to improve with statistics.

Clearly, observation of a deficit of events at two different locations with the respective statistical and systematic errors can be used to measure the oscillation parameters. In Figure 34 we show the 1 $\sigma$ confidence level contour that will result if the oscillation parameters are $\Delta m^2 = 0.01$ eV$^2$ and $\sin^2(2\theta) = 0.5$. A measurement of $\Delta m^2$ with about 20% error will result. For higher $\Delta m^2$ or mixing the error will be smaller.

### V.5.3 NEUTRAL CURRENT $\pi^0$ NORMALIZATION

As we have described above, comparison of the ratio ($R = QE(\mu^-)/NC(\pi^0)$) measured in the near and the far detectors is an independent way to establish $\nu_\mu$ oscillations. Since the number of reconstructed neutral current pion events will always be smaller than the number of muons the statistical sensitivity will be dominated by the pion statistics and will be lower than the muon disappearance analysis. The systematic errors will not be as important because first they will be smaller than the statistical error on the pion counts at the far detectors and second most of the beam or detector related systematics will cancel out in the ratio. This method of analysis is also important in the unlikely case that the oscillations are occurring into a sterile neutrino ($\nu_\mu \rightarrow \nu_s$) which does not interact through charged or neutral current interactions. In such a case a deficit of muon events will be accompanied by the same fractional deficit of pion events, and the ratio of muons to neutral current pions will remain the same at all distances from the beam.

We have assumed that we will be able to use both the clean double ring events and the events with one clean ring and extra energy (Table 9). The limits obtained with the somewhat lower statistics sample of double ring events with two complete rings are not very different. We have assumed that we will subtract the WCC$\pi^0$ background of about 15% from the $\pi^0$ sample without introducing a systematic error that is larger than the statistical error. Since the rate of this background will be measured using the WCC$\pi^0$ events with visible muons, this background subtraction will most likely be semi-empirical. If we leave

the background unsubtracted the sensitivity will be diluted by 15%, but in neither case will there be a spurious oscillation signal because the background procedure will be identical in all detectors.

The significance of an oscillation result is defined by:

$$\sigma = \frac{R_{near} - R_{far}}{\sqrt{(\sigma^2_{stat} + \sigma^2_{syst})}} \tag{17}$$

where $R_{near}$ and $R_{far}$ are the ratios measured in the near and the far detectors and the difference is divided by the total error. The error when comparing the ratio between D3 and the far sites D24 and D68 is dominated by the statistical error on $\pi^0$ counts at D24 (2.4%) or D68 (6.7%). When comparing the ratio in D1 and D3 to explore the $\Delta m^2$ region above 0.1 eV$^2$ the systematic error will dominate; we presently take this systematic error between D1 and D3 to be 2%. The 90% confidence level limit is obtained when the significance is set equal to 1.6 (Figure 35). Once again we have assumed three different running scenarios: an initial $2.2 \times 10^{20}$ POT run with D3 and D24, a second $2.2 \times 10^{20}$ POT run with D68 added, and the complete running, $8.8 \times 10^{20}$ POT, with all detectors. The sensitivity using the the ratio, $QE(\mu^-)/NC(\pi^0)$, will certainly be less than the sensitivity in the direct muon disappearance method. But this method will be free of the kind of systematic errors that were discussed for the direct muon disappearance method. The sensitivity in the ratio will be limited by the $\pi^0$ statistics only. If a signal is found in the direct muon disappearance method, every effort will be made to run for a long time with high proton intensity to get sufficient $\pi^0$ statistics to establish the signal beyond any doubt.

### V.5.2 $\nu_e$ APPEARANCE

In the case of $\nu_\mu \rightarrow \nu_e$ oscillations relevant limits exist from reactor experiments that look for $\bar{\nu}_e$ disappearance. Figure 36 shows the limits from several different reactor experiments in the interesting region of mass and mixing parameters. The allowed region of parameters if the Kamioka result is interpreted as $\nu_\mu \rightarrow \nu_e$ oscillations is also shown. We see that most of the Kamioka parameter space is already eliminated by the reactor experiments [16]. The Kamioka parameters are, however, at the edge of the sensitivity of all the reactor experiments so far. New reactor experiments at Chooz and San-Onofre intend to extend the reach in $\delta m^2$ to lower values [17]. None of the reactor experiments, new or old can have sensitivity to small mixing, however. We will show below that with E889 we will be able to definitively eliminate the Kamioka parameter space, and also be sensitive to mixing as small as $\sin^2(2\theta) = 0.001$ in a short period of time.

| $\Delta m^2$ ($eV^2$) | energy cut | D24 4 Mo | D68 4 Mo | D68 16 Mo |
|---|---|---|---|---|
| 0.01 | no cut | 297 | 188 | 754 |
| | > 500 pe | 252 | 176 | 706 |
| | > 800 pe | 155 | 120 | 480 |
| 0.005 | no cut | 79 | 69 | 276 |
| | > 500 pe | 66 | 60 | 240 |
| | > 800 pe | 40 | 37 | 150 |
| 0.003 | no cut | 29 | 27 | 110 |
| | > 500 pe | 23 | 23 | 92 |
| | > 800 pe | 15 | 14 | 57 |
| background | no cut | 114 | 15 | 58 |
| | > 500 pe | 70 | 9 | 36 |
| | > 800 pe | 36 | 5 | 18 |

Table 12: *The number of $\nu_e$ oscillation signal events for $\Delta m^2 = 0.01$, 0.005 and 0.003 $eV^2$ are shown along with the expected background under three run scenarios.* $\sin^2(2\theta) = 1.0$ *for this table.*

As an illustration of the sensitivity of E889 to $\nu_e$ appearance we have calculated the numbers of signal and background events in the far detectors for the same evolutionary scenario that was discussed for the muon disappearance type of analysis (Table 12). An initial run of four months with $2.2 \times 10^{20}$ POT with the D3 and D24 detectors will be followed by another four month run with $2.2 \times 10^{20}$ POT and D68. The complete experiment will have $8.8 \times 10^{20}$ POT or 16 months of running with all four detectors. At 68 km the $\nu_e$ oscillation signal will stay approximately the same as at 24 km while the backgrounds will fall by a factor of 8. The events are shown with no energy cut, and a cut requiring 500 photoelectrons (350 MeV for electrons) and 800 photoelectrons (560 MeV for electrons), respectively. Such a cut preferentially eliminates background from misidentified $\pi^0$s and also increases the confidence of the electron identification. We have also required that the showering particle be within an angle of 90 degrees of the neutrino beam and be within the standard fiducial volume. The initial four month run with D3 and D24 would have a signal to background of one for $\Delta m^2 = 0.005$ $eV^2$ at maximum mixing and enough statistics for more than a 5 standard

deviation effect.

We define the significance of the oscillation result by the equation

$$\sigma = \frac{f_c - f_p}{\sqrt{({\sigma_c}^2 + {\sigma_p}^2)}} \tag{18}$$

where $f_c$ is the actual number of events at the far site including the effects of oscillations, backgrounds, and the cuts which have been discussed in the previous sections. $f_p$ are the predicted number of background events extrapolated from observations in D1 and D3. $\sigma_p$ and $\sigma_c$ are the systematic error on the background prediction and the statistical error on the number of events at the far site, respectively. The numerator is simply proportional to $\sin^2(2\theta)$. We show the spectrum of the single ring showering events in Figure 37 at D24 and D68 after 16 months of running with oscillation parameters of $\Delta m^2 = 0.01$ eV$^2$ and 0.005 eV$^2$ at full mixing along with the expected background. The oscillation signal will be very large and unmistakable.

The 90% confidence limit is obtained by placing $\sigma = 1.64$ and calculating the value of $\Delta m^2$ and $\sin^2(2\theta)$ that produce such an effect at each of the far sites including D3. Figure 38 shows the $\Delta m^2$ versus $\sin^2 2\theta$ 90% confidence level plot for the three run scenarios. An initial four month run with detectors at D3 and D24 would produce a $\Delta m^2$ limit of 0.0025 eV$^2$ at maximal mixing. The limit in mixing angle from this initial run would be $\sin^2 2\theta > 0.01$ for $\Delta m^2 > 0.05$ eV$^2$. The 16 month run with the full detector should set a limit in $\Delta m^2$ of 0.001 eV$^2$ with maximal mixing. The limit in $\sin^2 2\theta$ will be less than 0.001 for large $\Delta m^2$ which can be obtained by using D3 as the far detector and D1 as the near detector.

## V.6 CONCLUSION

In this chapter we calculated the sensitivity of the experiment with a complete Monte Carlo simulation of the neutrino beam and the detector. The calculation was performed for three analysis channels (1) direct $\nu_\mu$ disappearance, (2) $QE(\mu)/NC(\pi^0)$ ratio, and (3) $\nu_e$ appearance. For each analysis channel we have included the statistical and systematic errors expected at both D24 and D68. The event counts in D24 will be large enough that the ultimate sensitivity will be obtained by careful control of the systematic errors using the two near detectors. On the other hand, the oscillation signal at D68 will be large so that even with smaller statistics we will extend the sensitivity to small values of $\Delta m^2$. If a signal is found in the direct muon disappearance mode then it will be confirmed by the comparison of the ratio $QE(\mu)/NC(\pi^0)$ in the near and far detectors.

The direct muon disappearance method will be sensitive down to $\Delta m^2 = 0.003$ eV$^2$ at full mixing and to $\sin^2(2\theta) = 0.015$ at high $\Delta m^2$ at 90% confidence level (Figure 33). The $QE(\mu)/NC(\pi^0)$ ratio method will be sensitive down to $\Delta m^2 = 0.004$ eV$^2$ at full mixing and $\sin^2(2\theta) = 0.03$ at high $\Delta m^2$ (Figure 35). This method will be an independent check on the direct muon disappearance method. The electron appearance method will have an extraordinary reach down to $\Delta m^2 = 0.001$ eV$^2$ at full mixing and $\sin^2(2\theta) = 0.001$ at high $\Delta m^2$ (Figure 38). If an oscillation signal is observed the combination of all three methods will unambiguously determine the actual oscillation channel between $\nu_\mu \rightarrow \nu_\tau$, $\nu_\mu \rightarrow \nu_e$, or $\nu_\mu \rightarrow \nu_s$ where $\nu_s$ is a sterile neutrino.

We have designed the experiment to develop over time and explore the oscillation parameter space with increasing sensitivity. Figures 33, 35, and 38 show the complete sensitivity of the experiment and also the sensitivity in the initial runs of the experiment. The experiment will establish or rule out the Kamioka atmospheric anomaly in the very first run of 4 months duration with only half the number of detector tanks. The complete experiment will not only irrefutably establish the signal, but will measure $\Delta m^2$ with an error of 10-20% (Figure 34).

The analysis in this chapter was based on various conservative assumptions. The most conservative assumptions are the fiducial volume and the AGS intensity. There will be almost twice as many events in the entire detector as the nominal fiducial volume of 6.5 m radius and 13 m height. We will certainly use all of these events for analysis, although some of them might be poorly measured. In particular the non-contained events will be from higher energy neutrinos; therefore comparison of the ratio of contained to non-contained events in the near and far detectors could be another independent method of analysis. The AGS has now started to deliver $6 \times 10^{13}$ protons per pulse, much more than our assumption of $4 \times 10^{13}$ protons per pulse. We have shown the sensitivity using a simple counting and extrapolation scheme. Further analysis of the energy spectrum and vertex distributions in each of the tanks will no doubt increase the sensitivity of the experiment.

REFERENCES


1. C. H. Llewellyn Smith, Phy. Rep. **3**, no. 5 (1972) 261.
2. S. J. Barish, et al., Phys. Rev. **D16** (1977) 3103.
3. L. A. Ahrens, et al., Phys. Rev. **D34** (1986) 75; ibid **35** (1987) 785.
4. M. Nakahata, et al., J. Phys. Soc. Japan **55** (1986) 3786.
5. Dieter Rein and Lalit Sehgal, Annals of Physics **133** (1981) 79.
6. Review of Particle Properties, Physical Review D **50** (1994) 1173.
7. Private communication, Howard Nicholson, Mount Holyoke college.
8. W.N. Hess, et al., Physical Review **116** (1959) 445.
9. W.N. Hess, E.H. Canfield, R.E. Lingenfelter, J. Geophys. Res. **66** (1961) 665.
10. S. Hayakawa, 'Cosmic Ray Physics; nuclear and astrophysical aspects,' Wiley-Interscience, New York (1969).
11. D. Rein and Lalit M. Sehgal, Nuclear Physics B**223** (1983) 29.
12. 'Proposal to Participate in the Super-Kamiokande Project,' C.B. Bratton, et al., The US Kamikande collaboration, December 23, 1992.
13. FLUKA92, A.Fassò, A.Ferrari, J.Ranft, P.R.Sala, G.R.Stevenson and J.M.Zazula, Proceedings of the Workshop on Simulating Accelerator Radiation Environments, Santa Fe, USA. 11-15 January, 1993.
14. H.C. Fesefeldt, Simulation of hadronic showers, physics and applications. Technical Report PITHA 85-02, III Physikalisches Institut, RWTH Aachen Physikzentrum, 5100 Aachen, Germany, September 1985.
15. Y. Fukuda, et al., Physics Letters **B** (1994) 237.
16. B. Achkar, et al., Nuclear Physics B **434** (1995) 503. G. Zacek, et al., Phys. Rev. D **34** (1986) 2621. G. S. Vidyakin, et al., JETP Lett. **59** (1994) 364.
17. R.I.Steinberg, DUHEP-9306001, Jun 1993. Presented at Int. Workshop on Neutrino Telescopes, Venice, Italy, Mar. 1993.

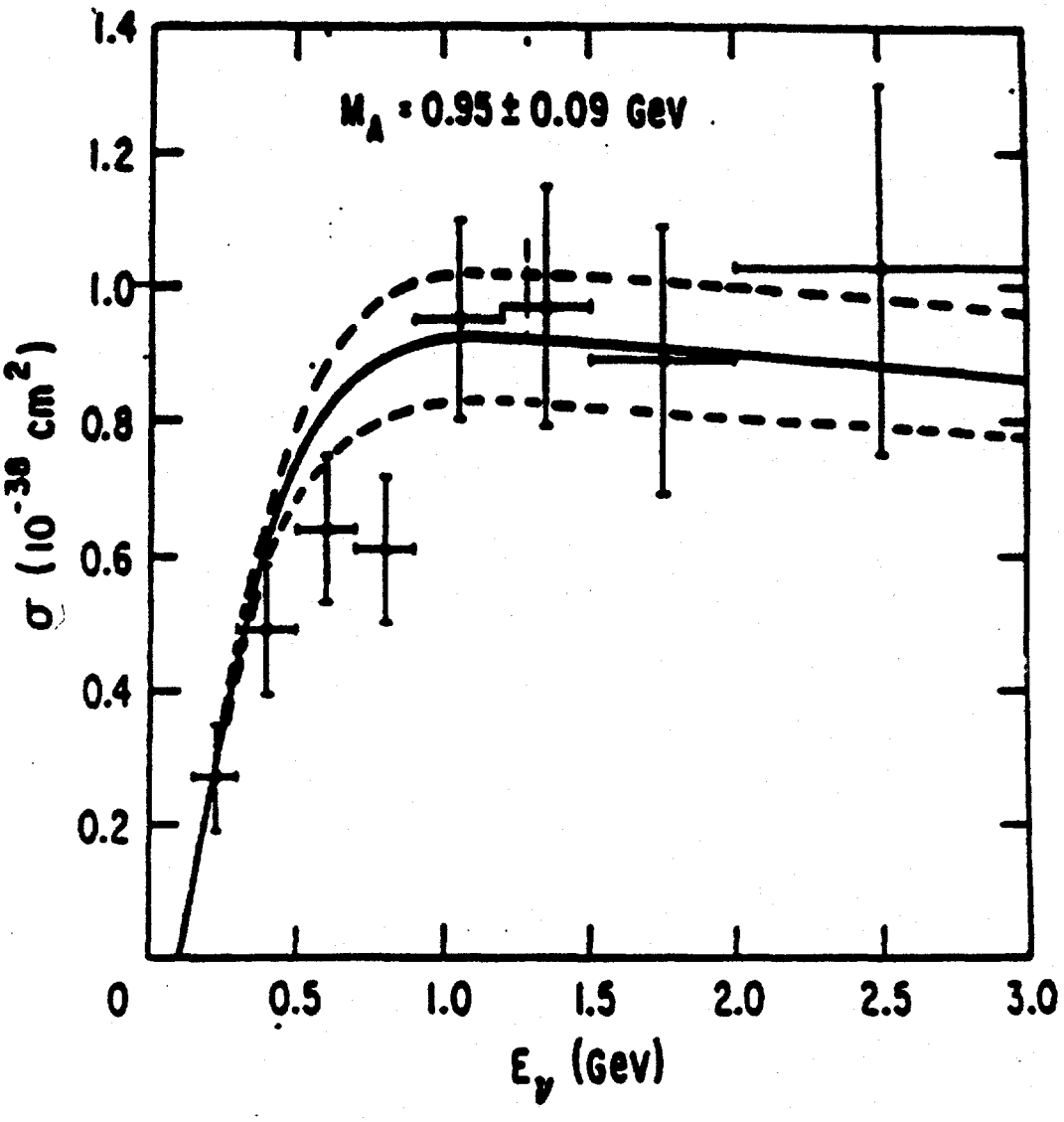


Figure 1: *Total cross section for $\nu_\mu n \rightarrow \mu^- p$ as a function of neutrino energy. The dashed curve shows the theoretical error.*

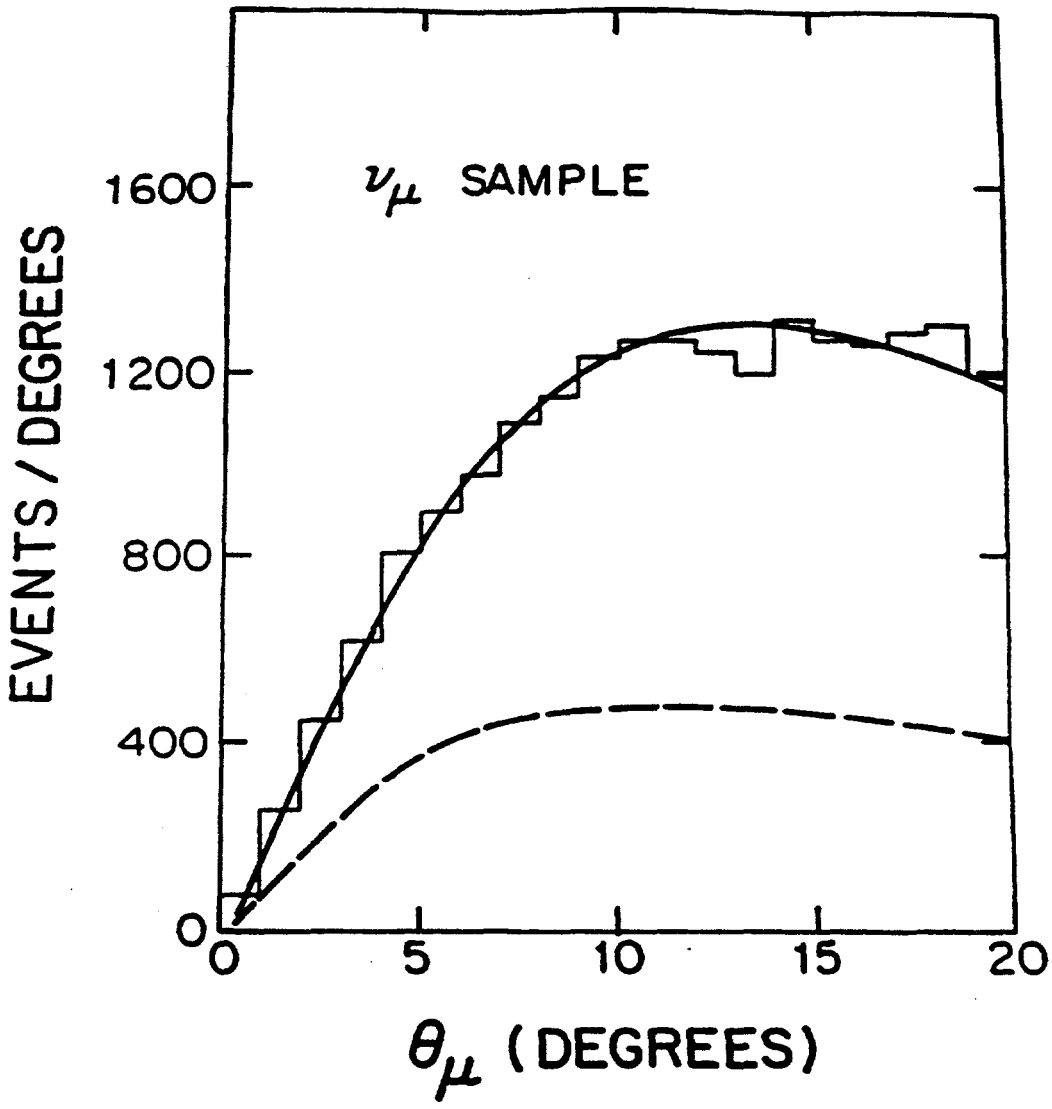


Figure 2: *Quasi-elastic muon events versus the angle of the muon as measured in E734 at the BNL-AGS. The histogram is the data, the solid curve is a Monte Carlo calculation of the spectrum of all muon-like events, and the dashed curve is a calculation of the background from charged and neutral current pion production events.*

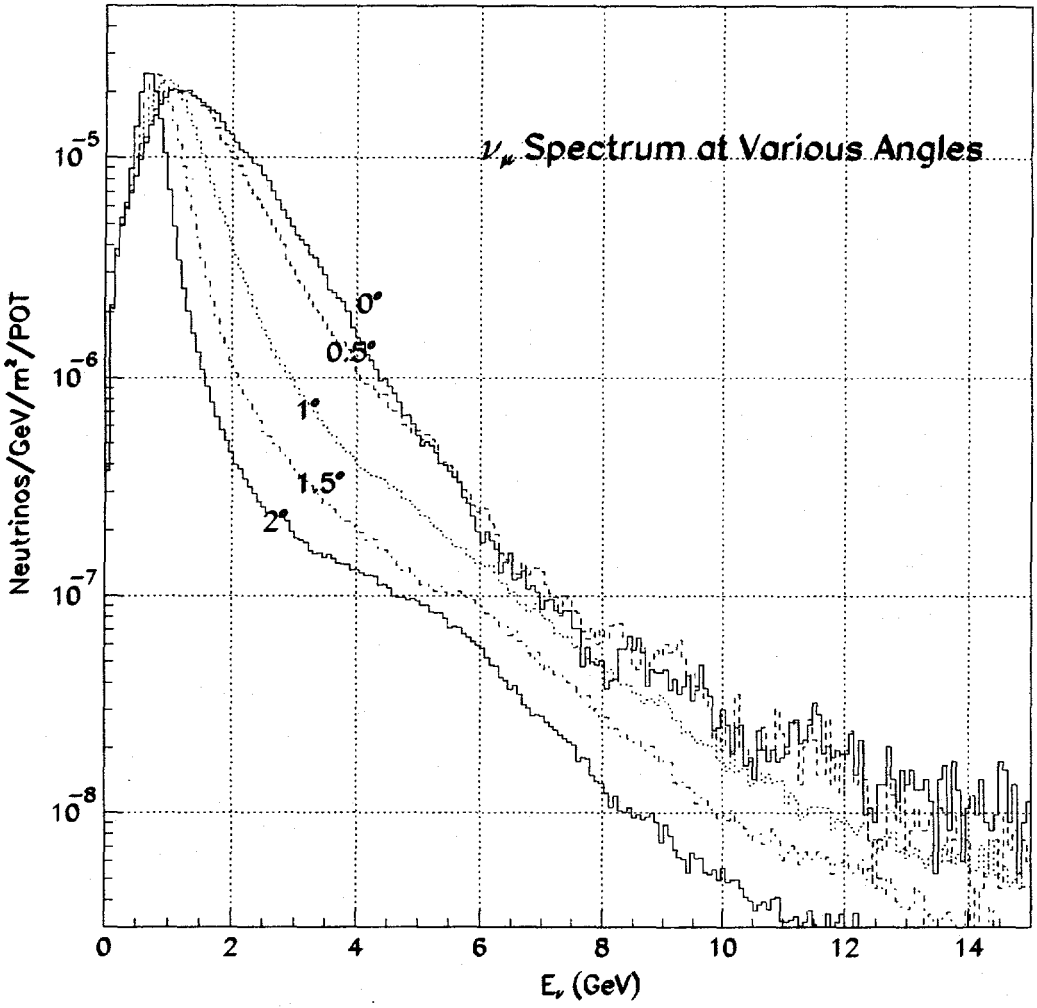


Figure 3: *Spectrum of neutrinos at 1 km at various angles with respect to the decay tunnel axis. The 1.5 degree spectrum was used for calculating the total event rates, however the event simulations in the detectors were performed using the full energy-angle correlation on an event by event basis.*

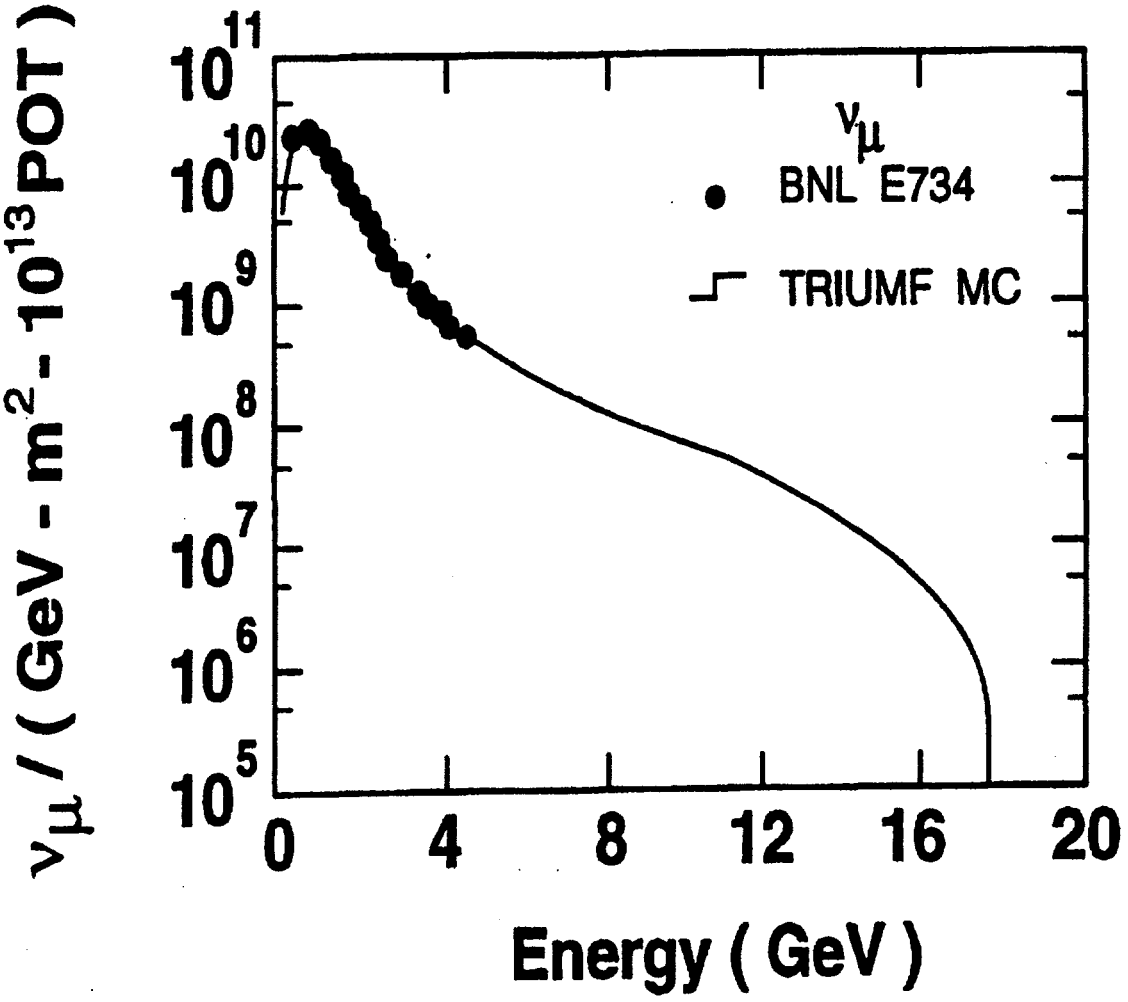


Figure 4: *Neutrino spectrum measured in E734 compared to the Monte Carlo calculation used for this proposal.*

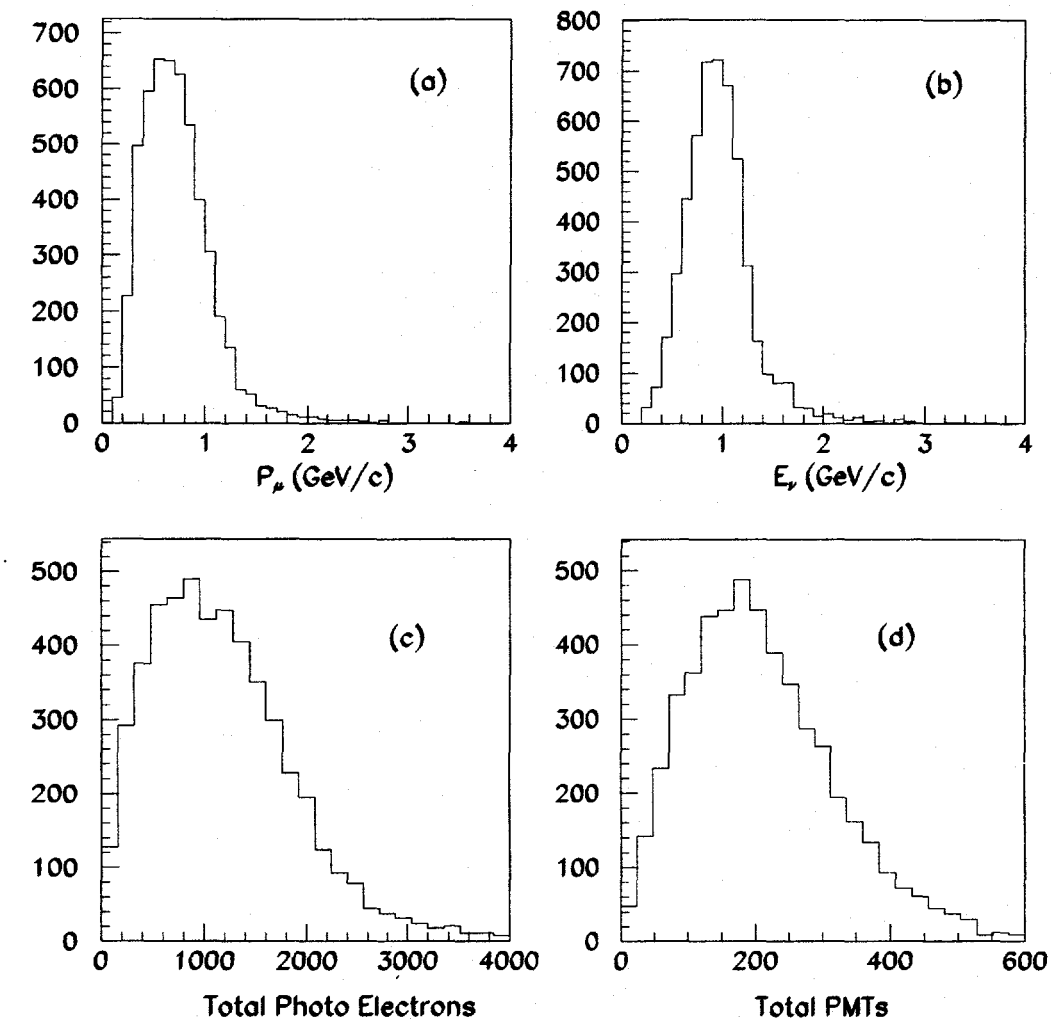


Figure 5: *Spectrum of contained muons (a) from quasielatic interactions of neutrinos with spectrum (b). The number of photoelectrons and the number of photomultipliers are also shown in (c) and (d), respectively. The simulation was for 5000 events with vertices in the fiducial volume and contained muons.*

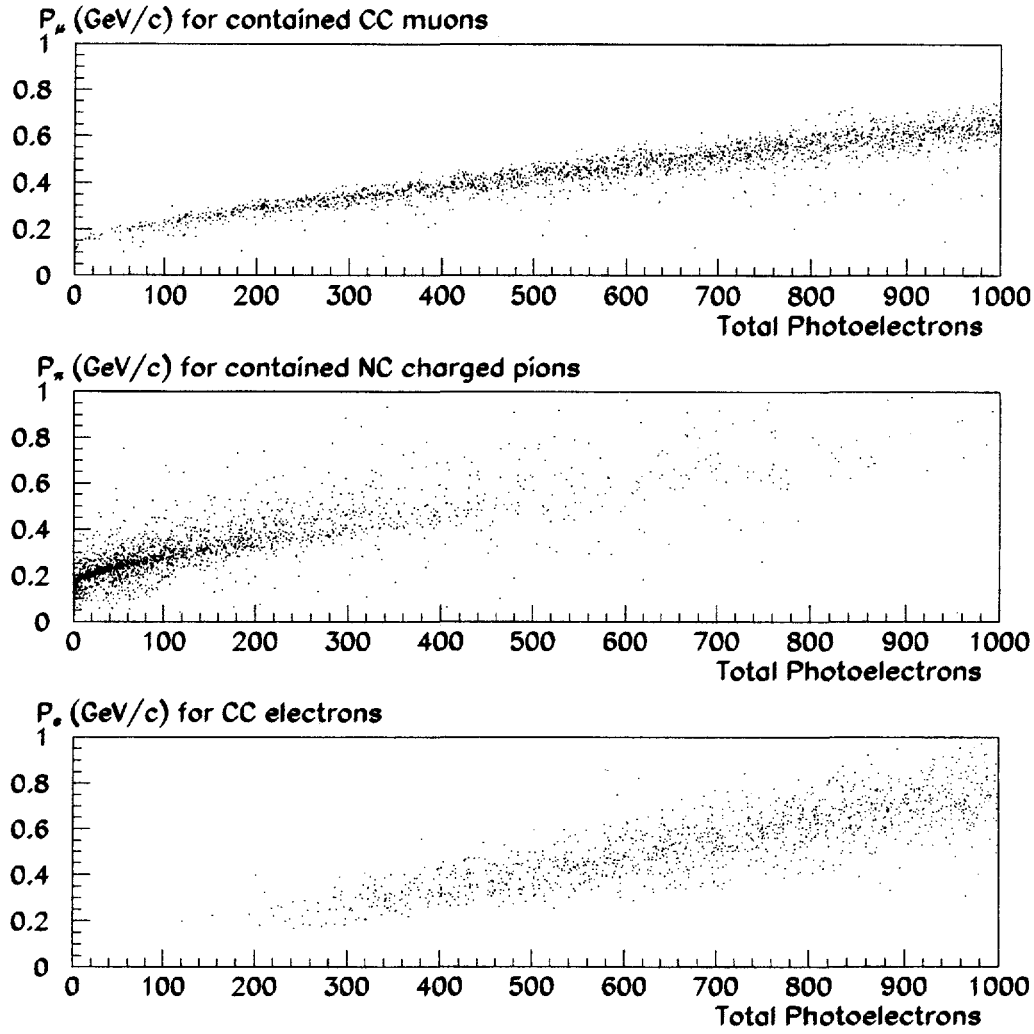


Figure 6: *The response in total number of photoelectrons of the water Cherenkov detector for muons, charged pions, and electrons as a function of momentum.*

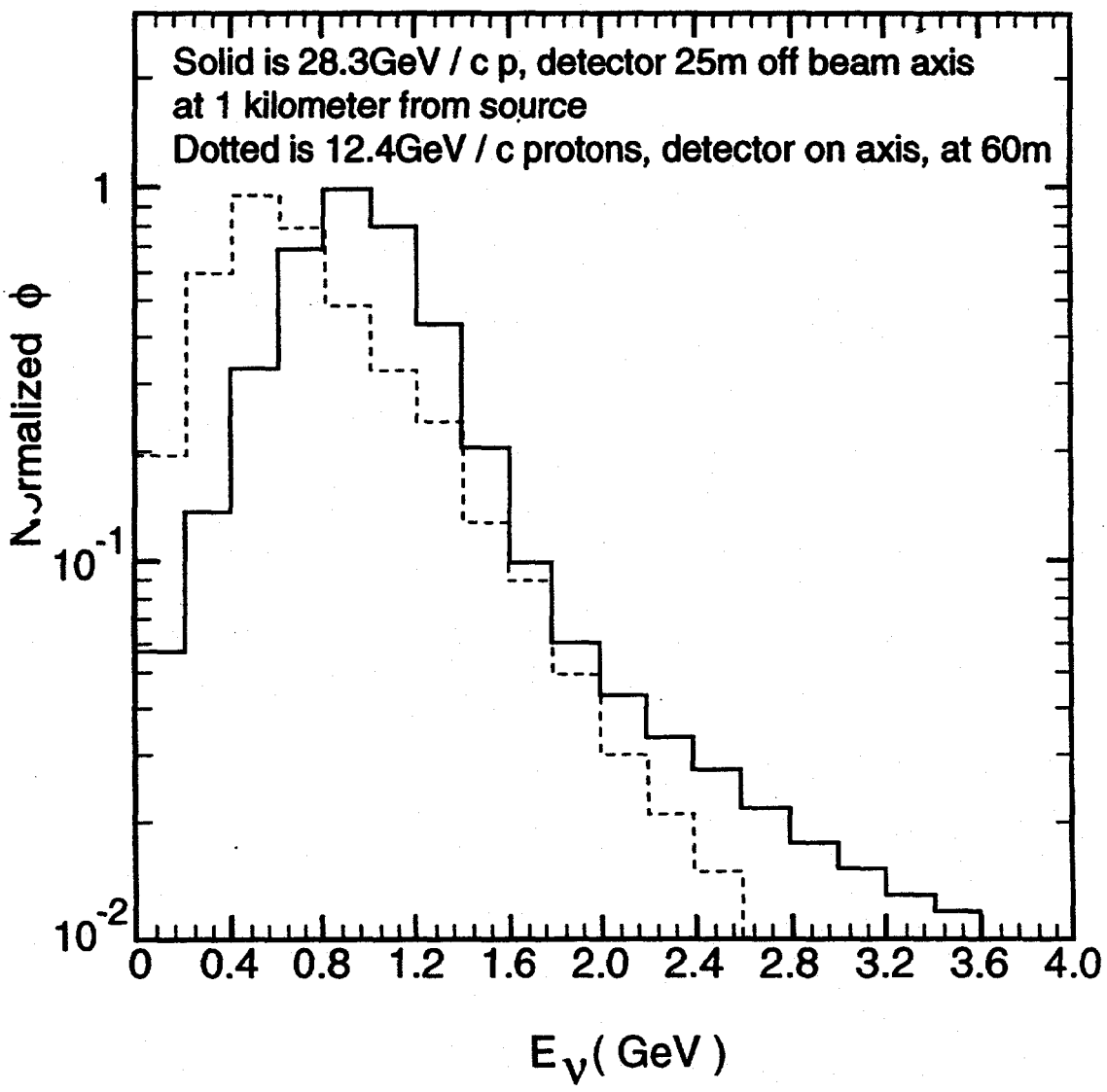


Figure 7: *Spectrum of neutrinos at the Argonne National Laboratory ZGS accelerator (dotted, 12.4 GeV) compared to the BNL-AGS neutrino spectrum (solid) at 1.5 degrees or 25 m off beam axis at 1 km.*

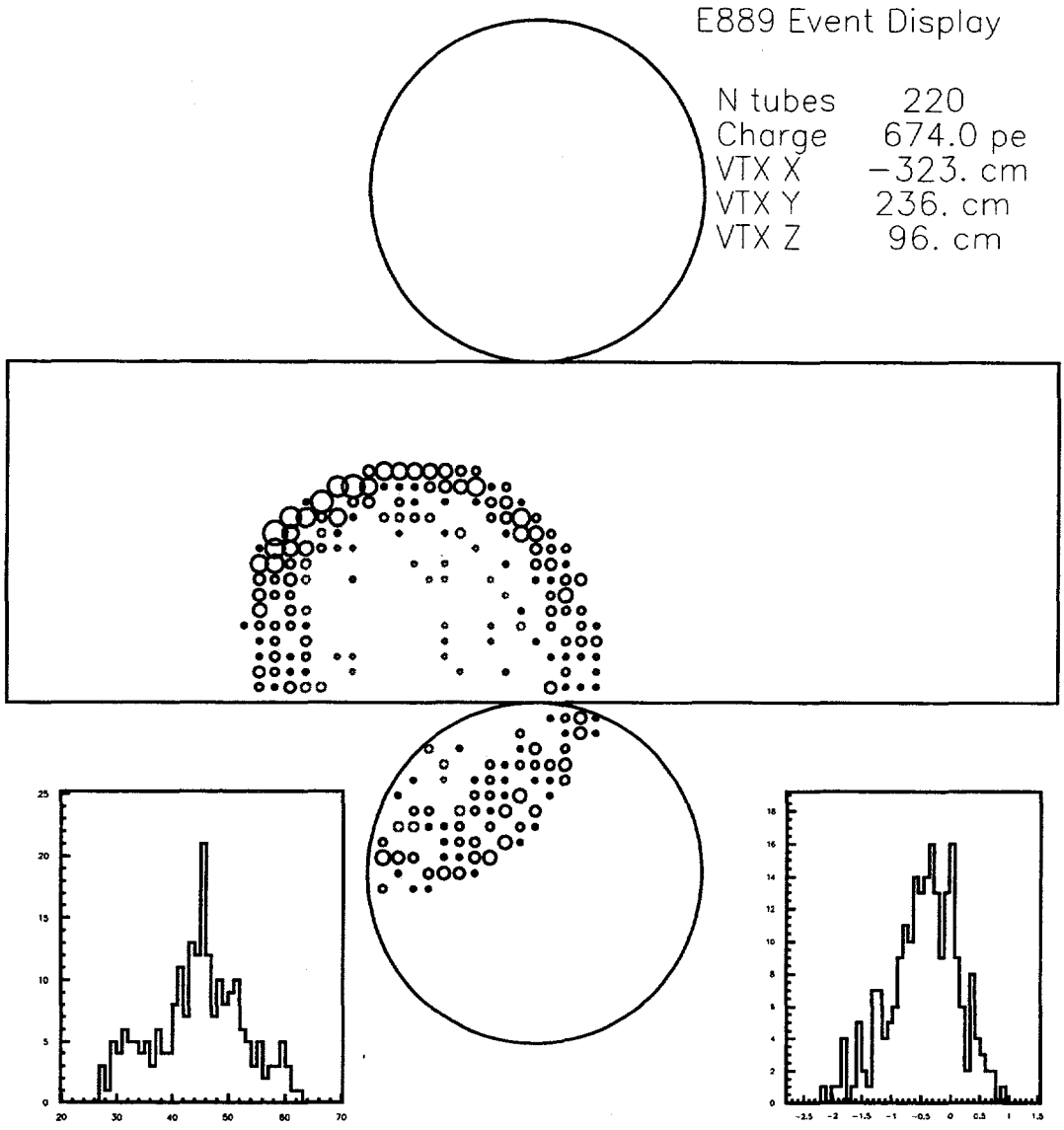


Figure 8: *Typical $QE(\mu^-)$ event in the fiducial volume. The size of the circles indicates the pulse-height in each PMT. The histogram on the left is of the raw time (ns) of the PMT hits with the event time set to 0. The histogram on the right is of the corrected time (ns) which is the raw time minus the flight time to the vertex.*

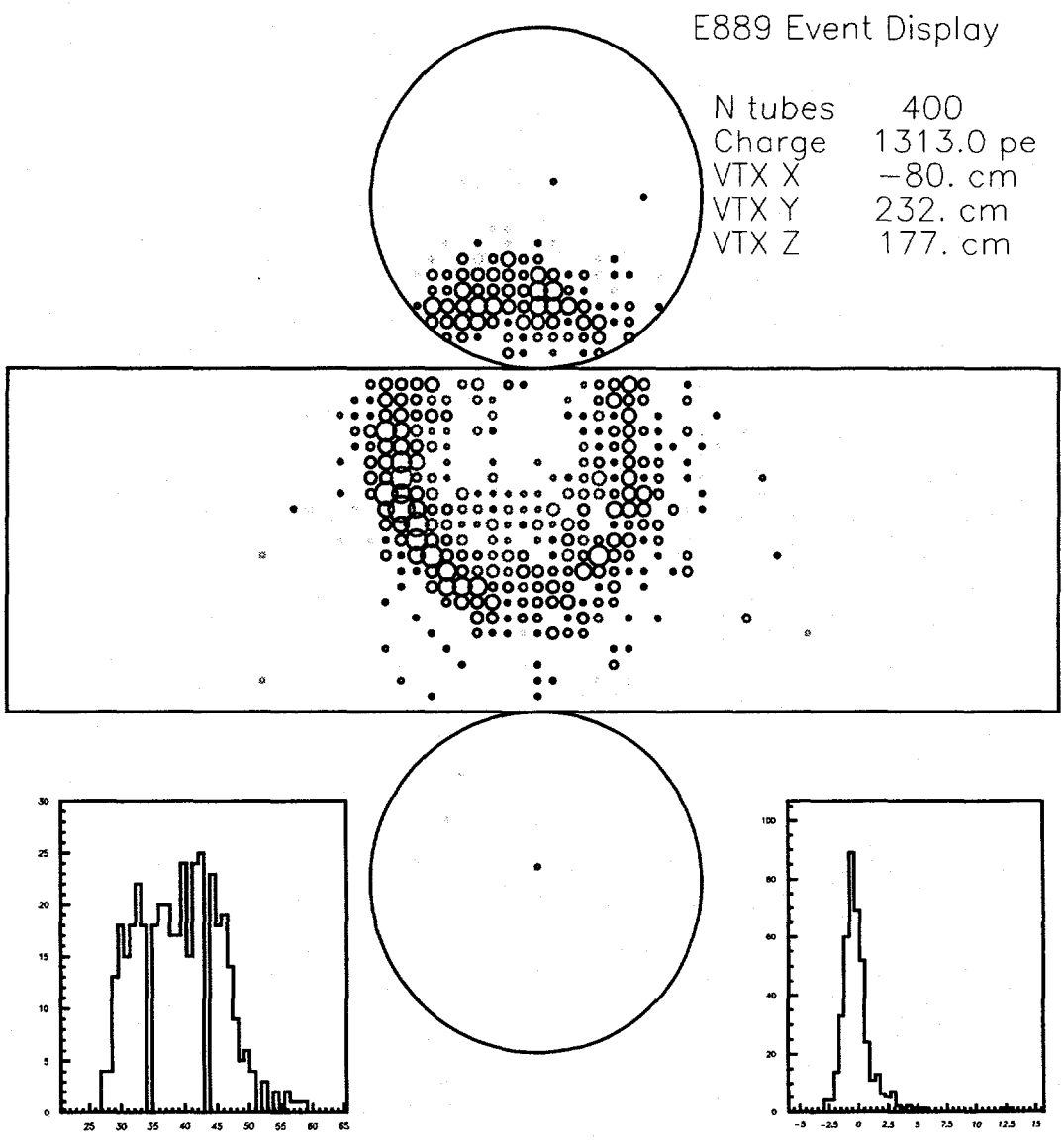


Figure 9: *Typical $QE(e)$ event in the fiducial volume. See the caption of Figure 8 for the description.*

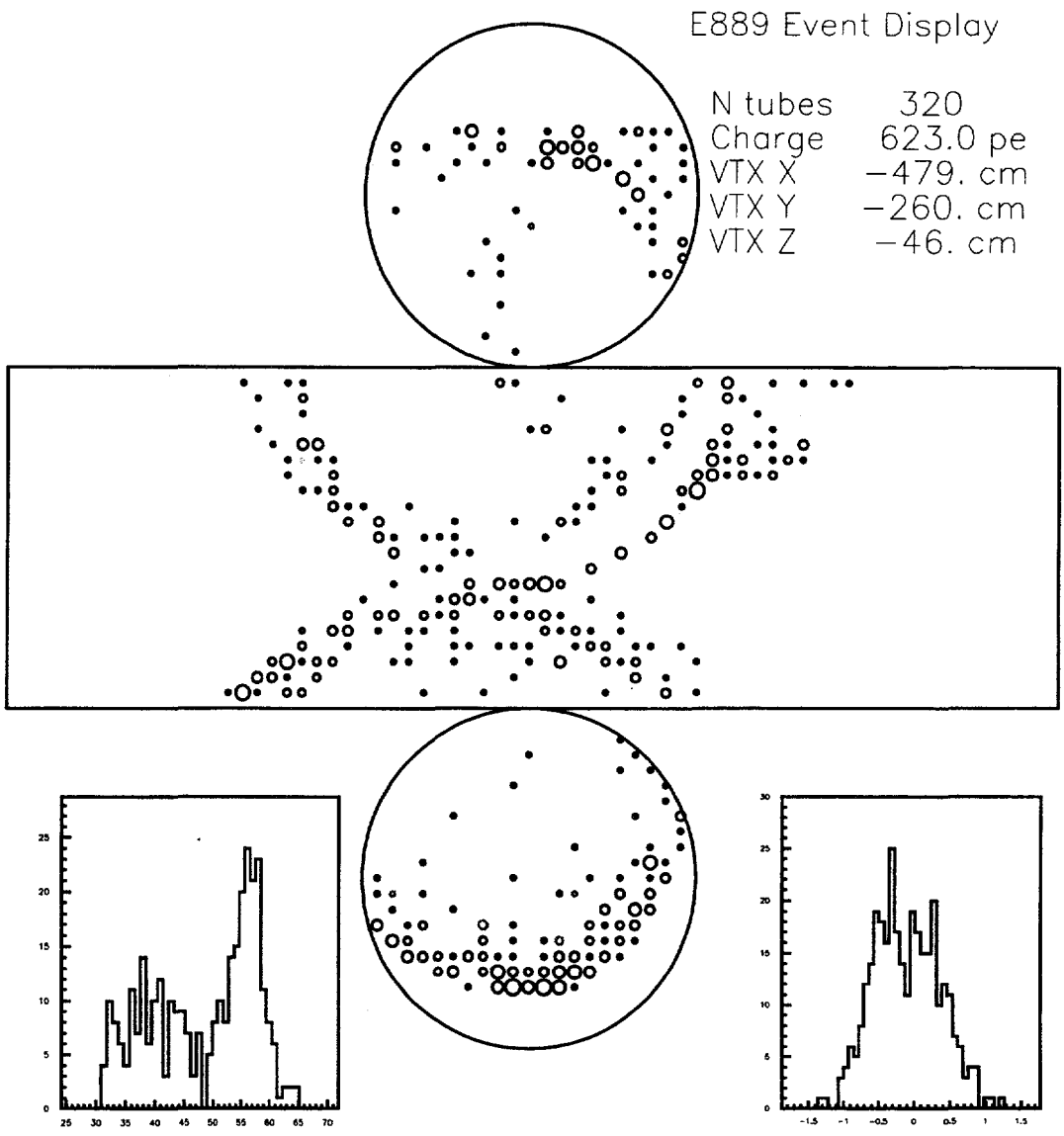


Figure 10: *Typical multi-ring pion event in the fiducial volume. See the caption of Figure 8 for the description.*

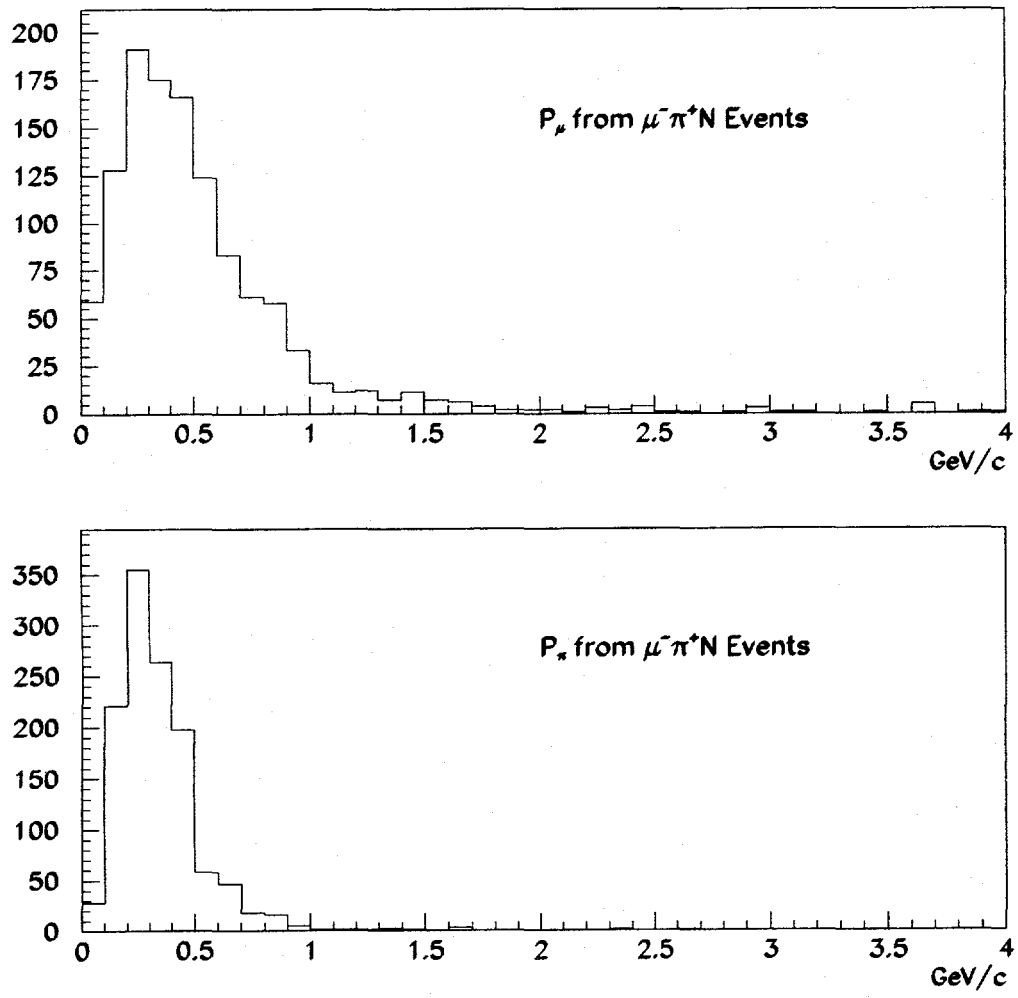


Figure 11: *Momentum distribution of muons (top) and pions (bottom) in charged current single pion production events.*

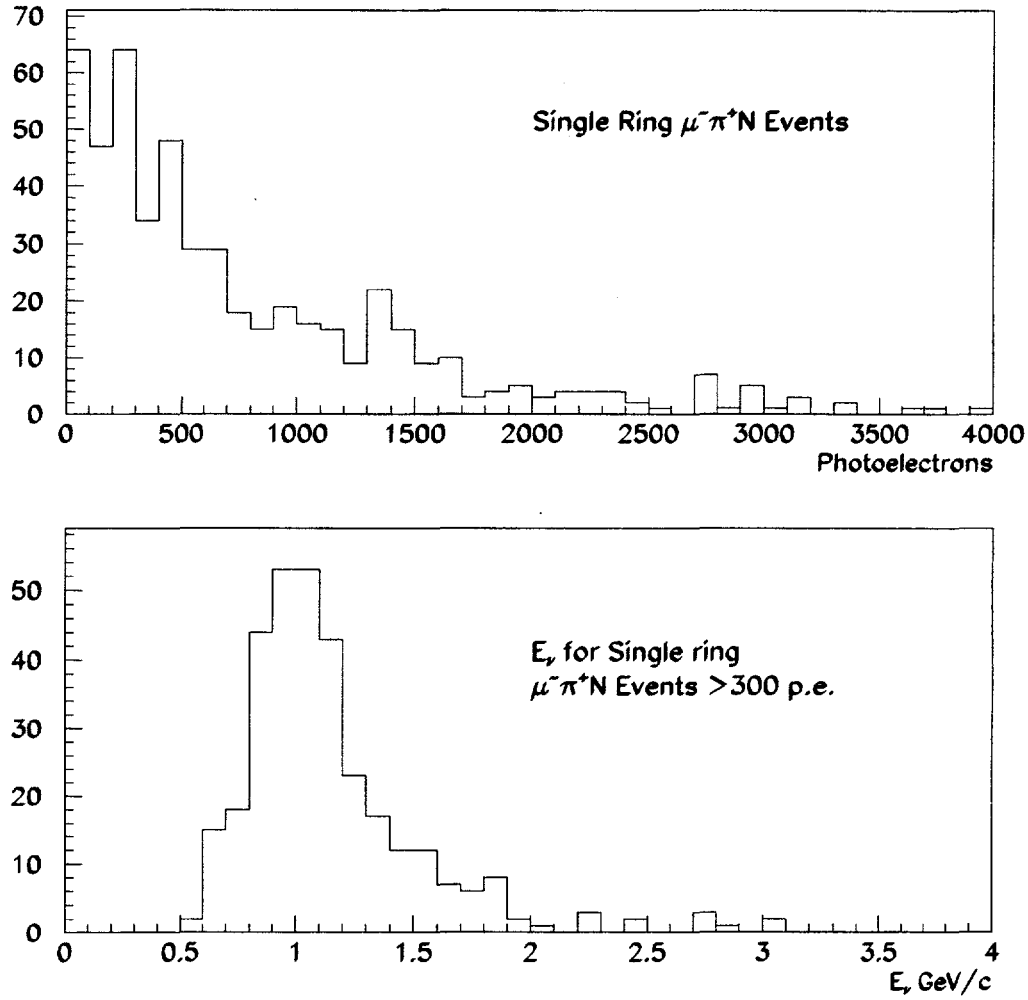


Figure 12: *Photoelectron distribution of single ring charged current single pion production events (top) and the spectrum of the neutrinos (bottom) that produce the events above 300 photoelectrons.*

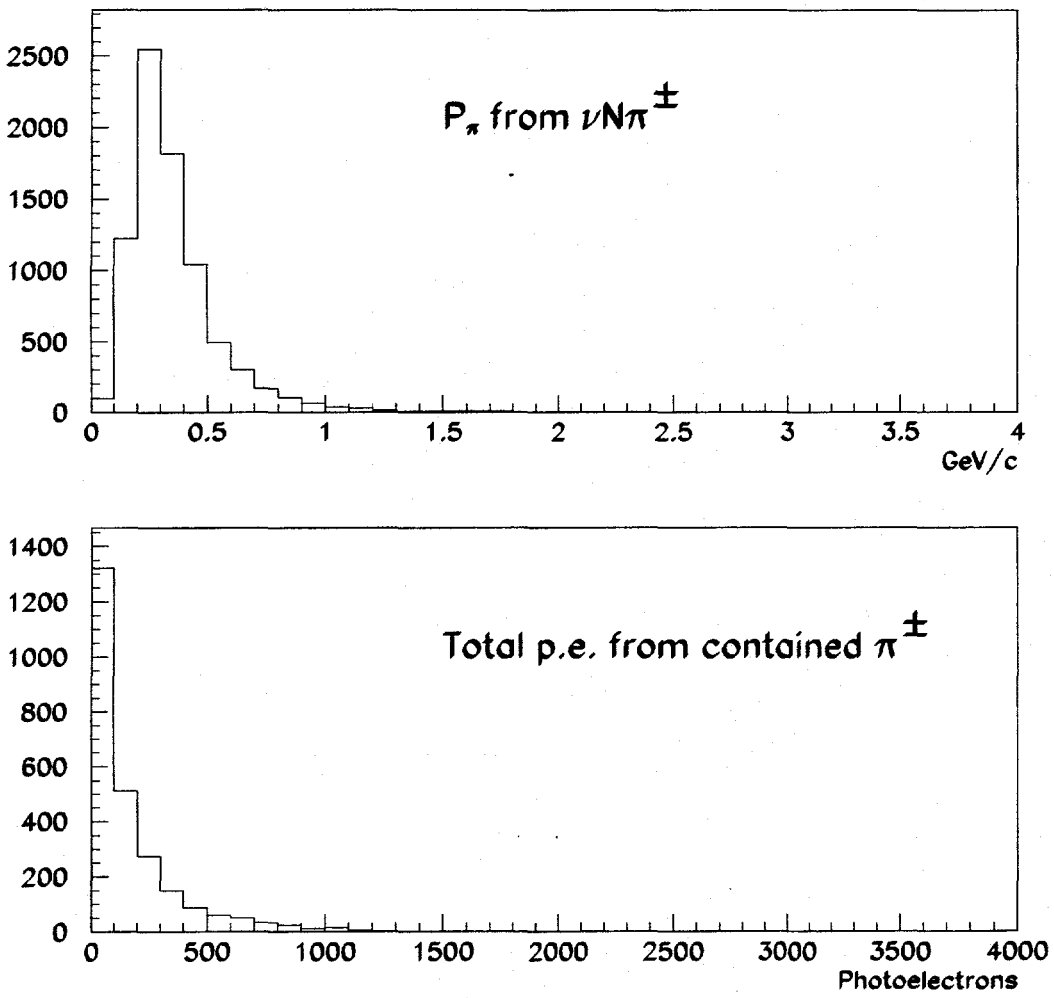


Figure 13: *Momentum and photoelectron spectrum of charged pions from neutral current single charged pion events.*

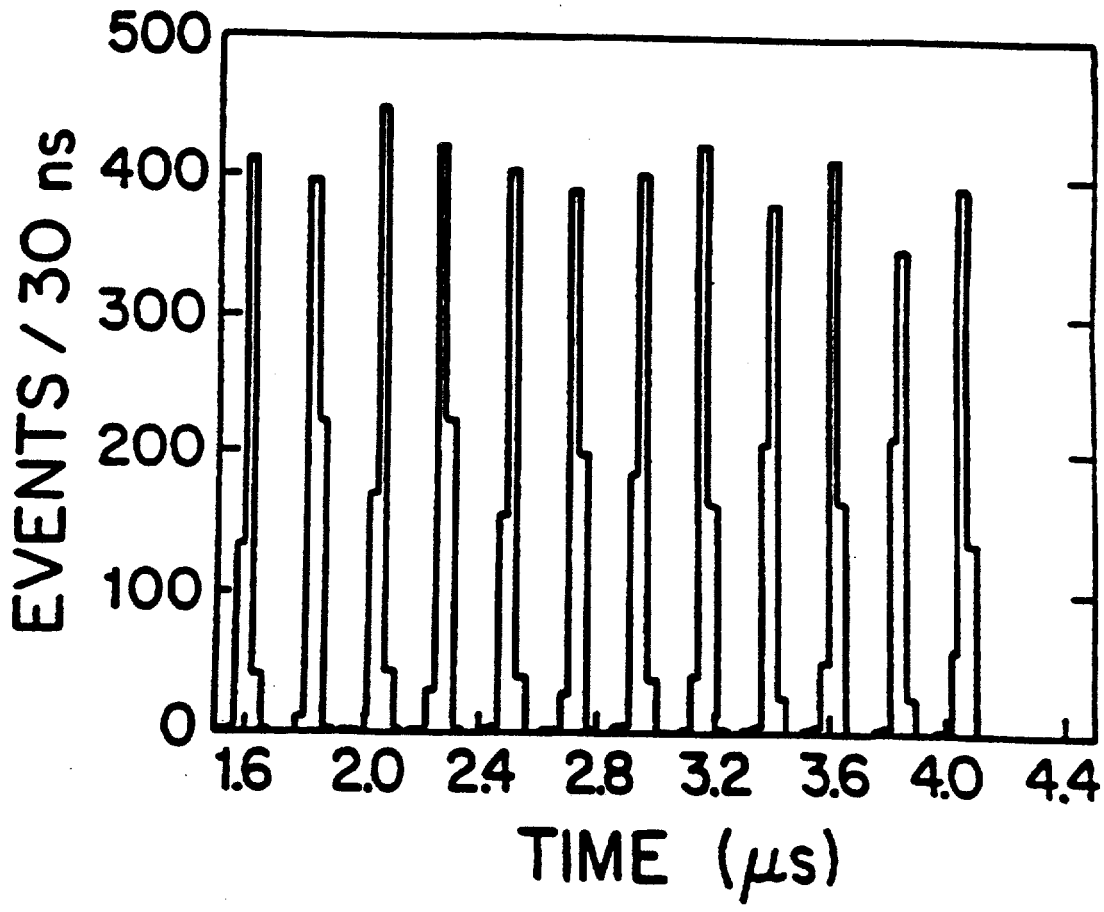


Figure 14: *The bucket structure of the AGS neutrino beam reconstructed in the E734 detector from neutrino events. The AGS beam for E734 had 12 buckets of 22 ns width and 220 ns apart.*

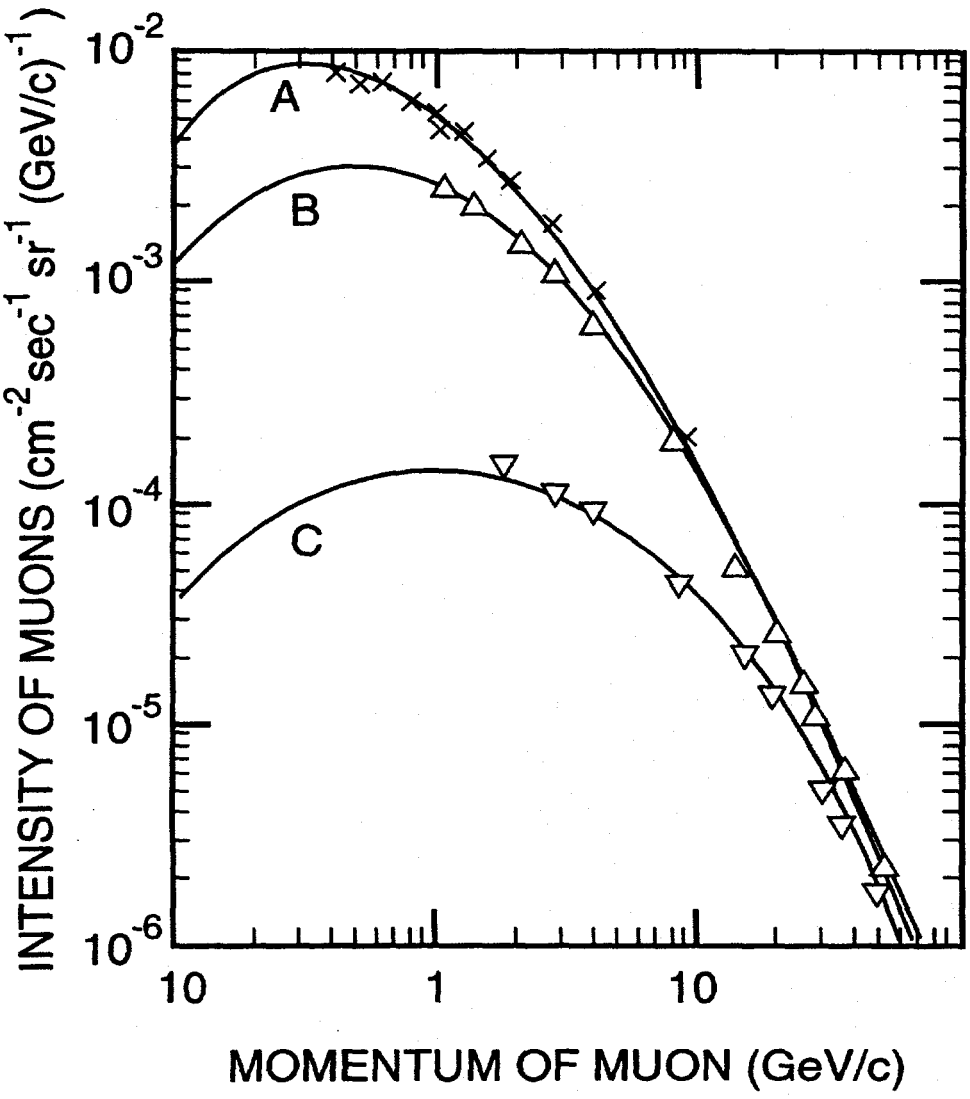


Figure 15: *The cosmic ray muon spectrum at sea level and at a mountain top from Ref. 10. (A) vertical flux at 3200 m, (B) vertical at sea level, (C) 68° at sea level.*

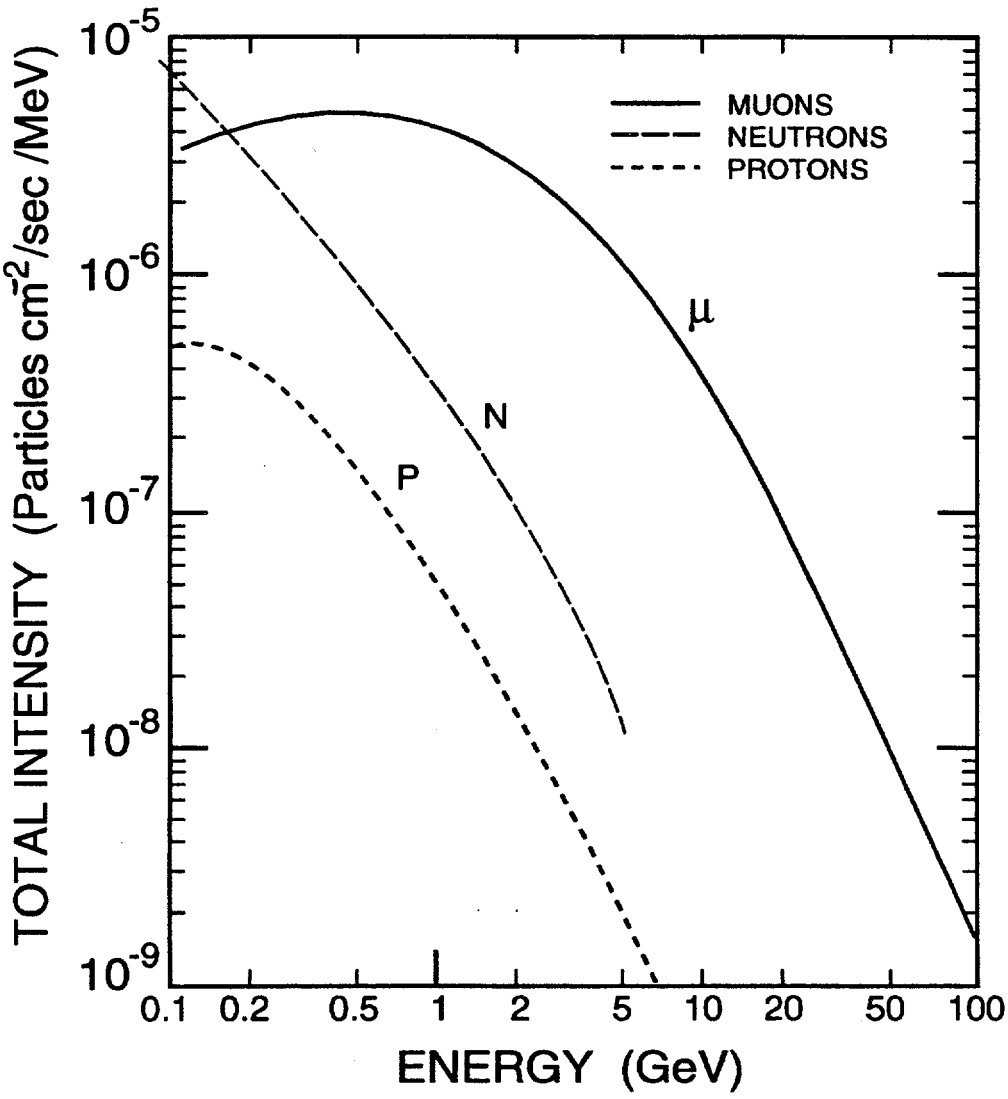


Figure 16: *The cosmic ray spectra for muons, neutrons, and protons from Ref. 7. Also see Ref. 8 and 9.*

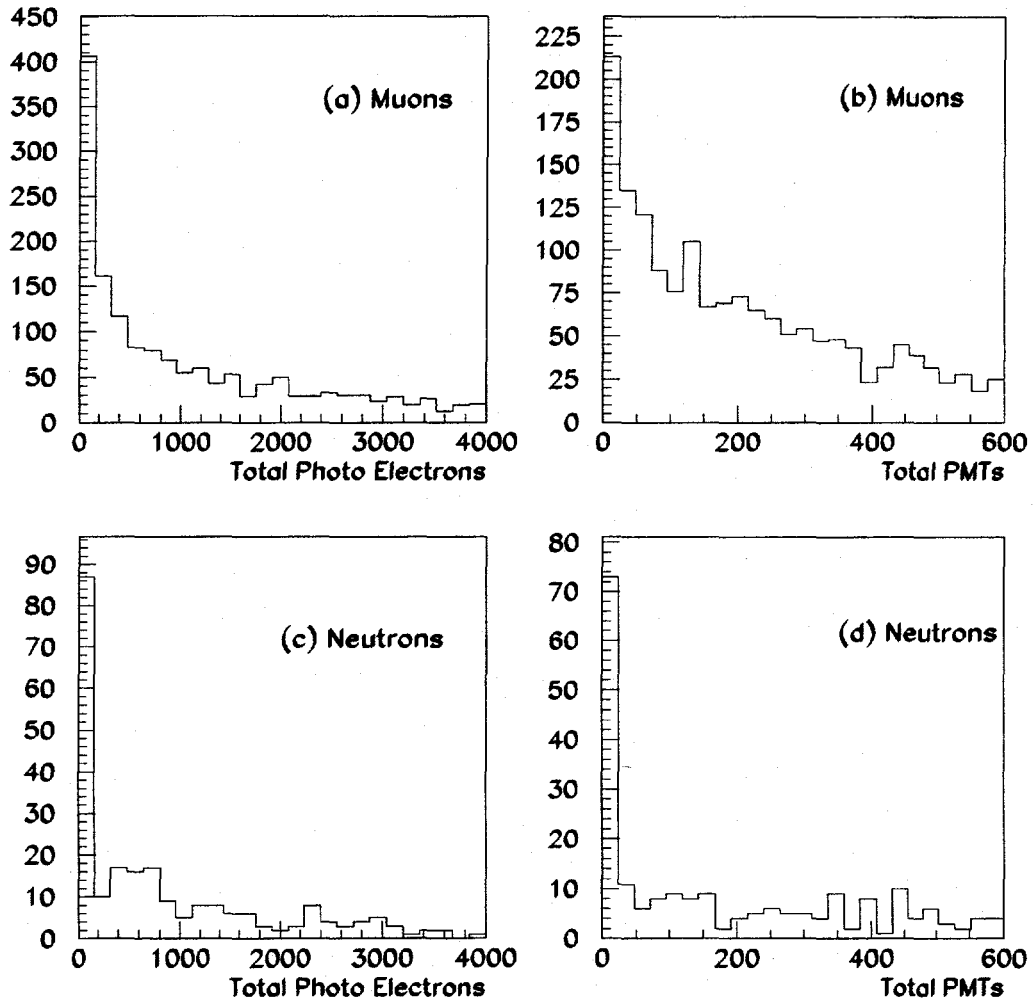


Figure 17: *The spectra of photoelectrons and the number of PMTs from cosmic ray muon and neutron events. Comparing to Figure 5, simple cuts on the pulse height should be very effective in removing large part of the background.*

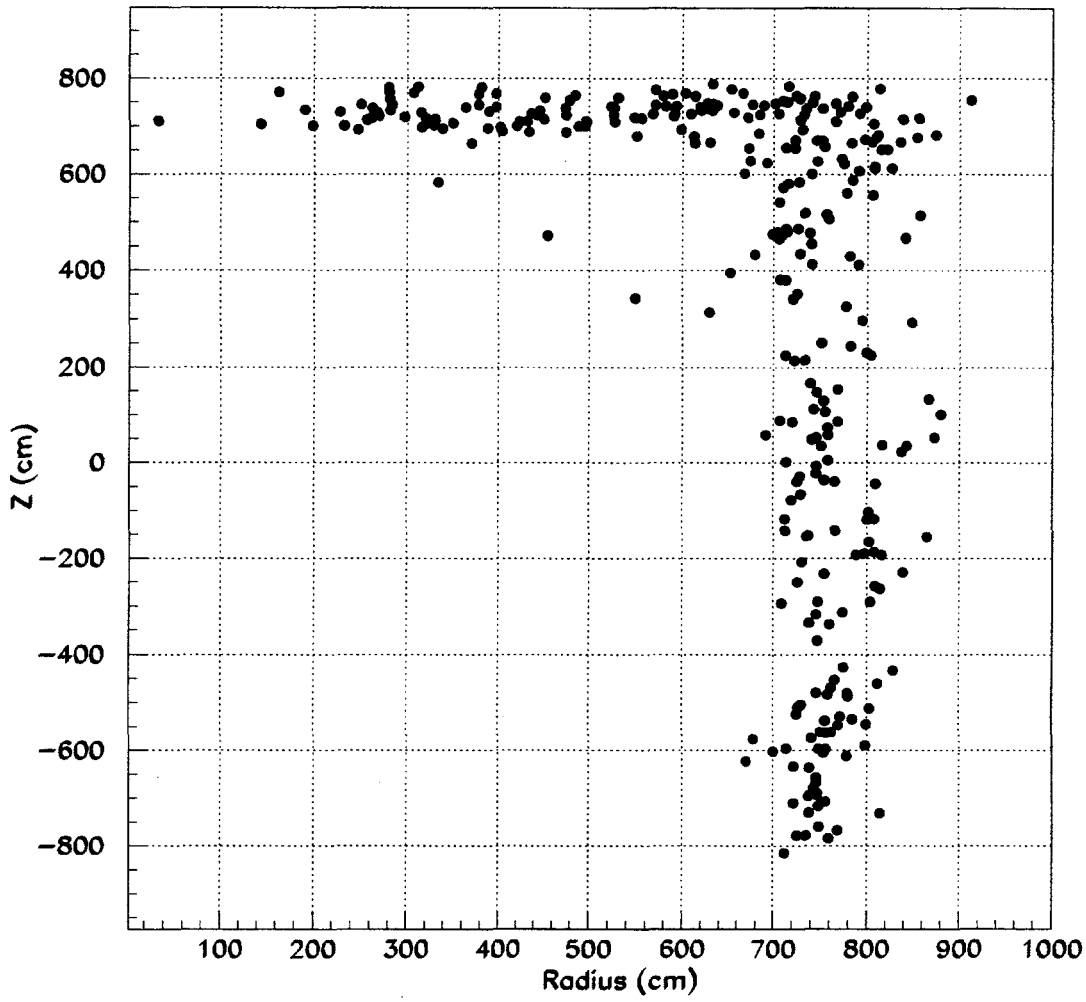


Figure 18: *The reconstructed vertex positions (radius versus Z, co-ordinate along the tank cylinder axis) of a cosmic ray muon entering the inner detector. The vertex resolution is different for the two orthogonal coordinates, in the direction of the muon and perpendicular to it.*

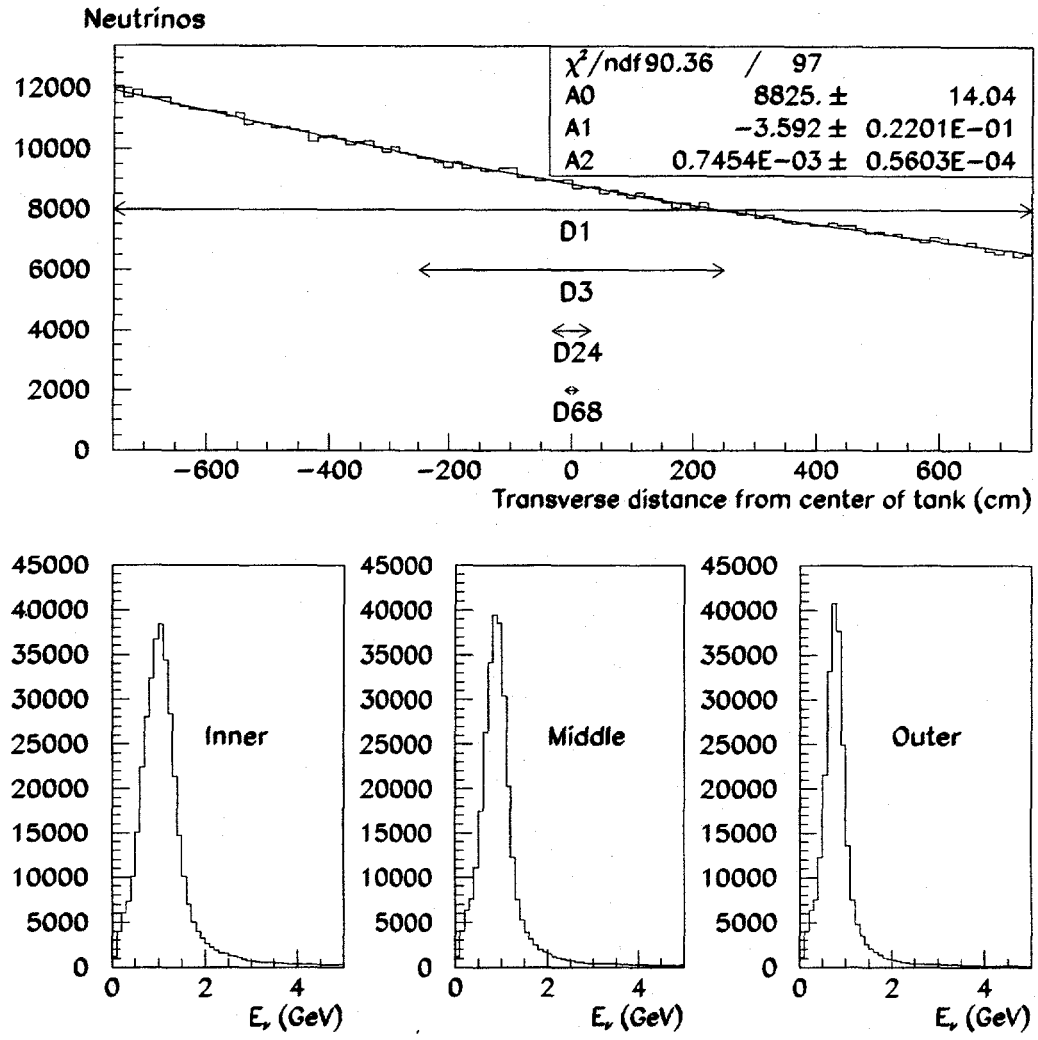


Figure 19: *Distribution of neutrinos incident on a flat square offset by 1.5° from the beam axis. The fall of neutrino intensity is well fit by a function* $A_0 + A_1 x + A_2 x^2$ *where x is the distance transverse to the beam axis from the center of the tank. The neutrino spectra for the inner 1/3 (-7.5 m to -2.5 m), the middle 1/3 (±2.5 m), and the outer 1/3 (2.5 m to 7.5 m) are shown at the bottom.*

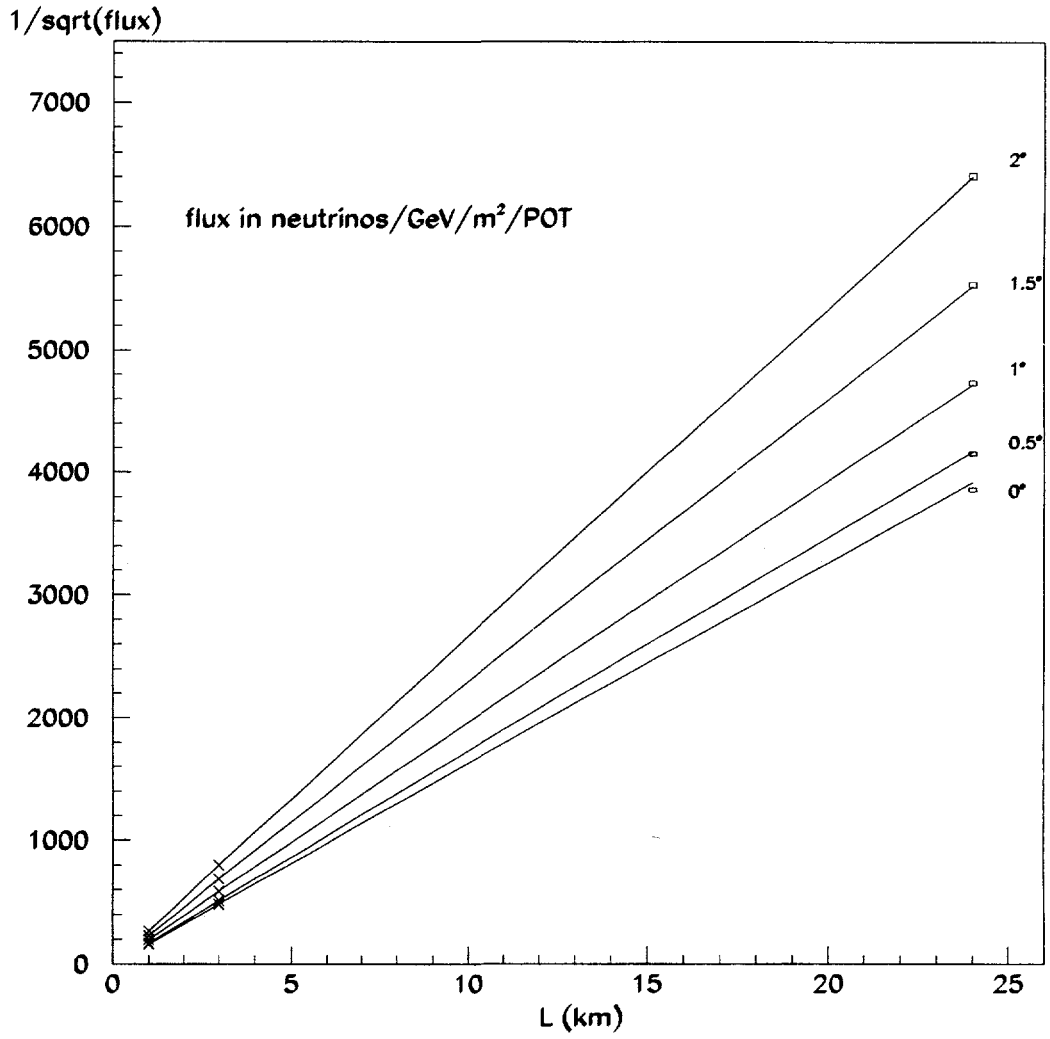


Figure 20: $1/\sqrt{flux}$ *versus distance from a GEANT Monte Carlo simulation. A line drawn through the points at 1 and 3 km predicts the flux at the 24 km site. The* $1/(r-r_0)^2$ *behavior does not depend on the angle, and it is better at 1.5 degrees than at 0 degrees. The Monte Carlo calculated flux at the 24 km is indicated by a box, the vertical size is the statistical error achieved after 16 months of running E889. The results are similar for the 68 km site.*

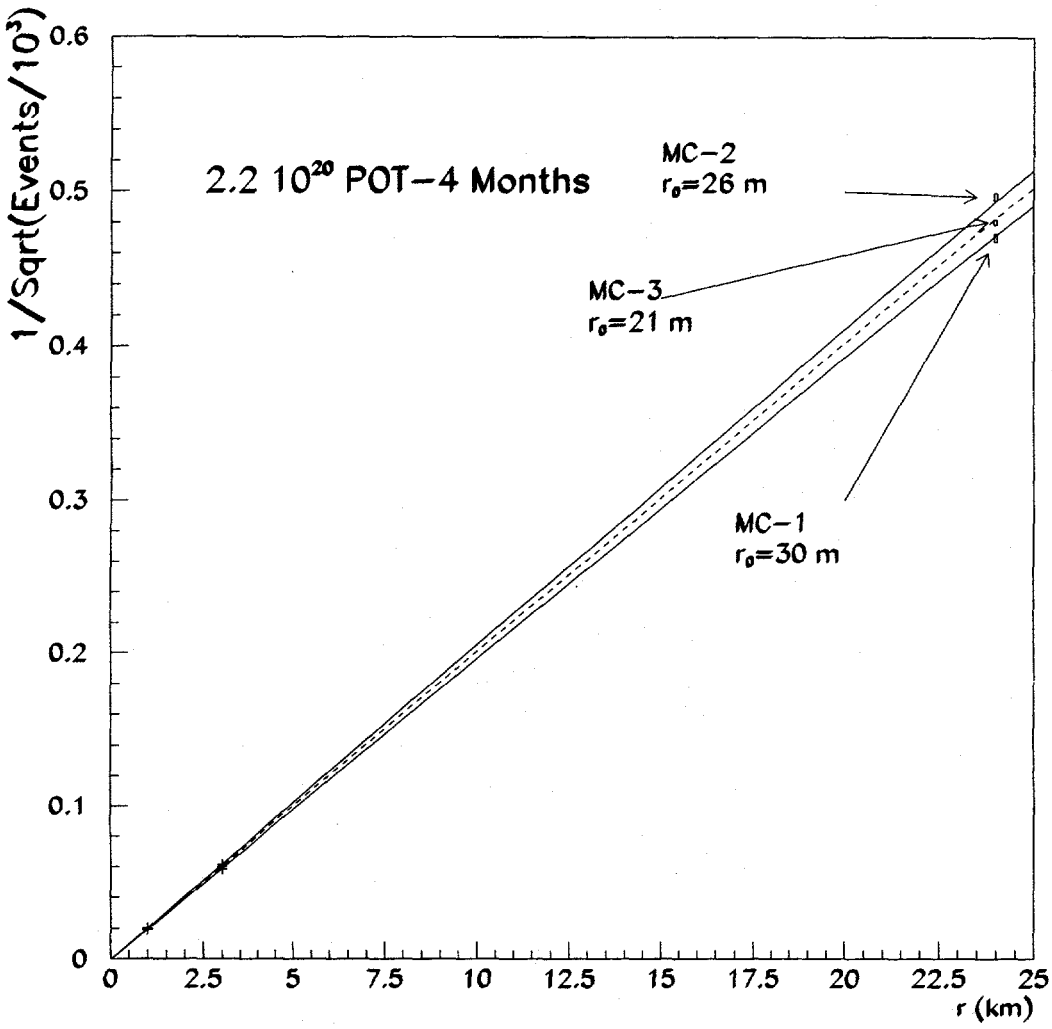


Figure 21: *The count rates of quasi-elastic muon events in 4 months, displaying the* $1/(r - r_0)^2$ *law. Though Monte Carlo variations alter both the overall normalization and* $r_0$*, the* $1/(r - r_0)^2$ *behavior does not change. The effects of path-length and cross section in the detectors are included using three different Monte Carlo calculations (Table 6). The Monte Carlo statistical error is shown as a box at 24 km. The 68 km results are similar.*

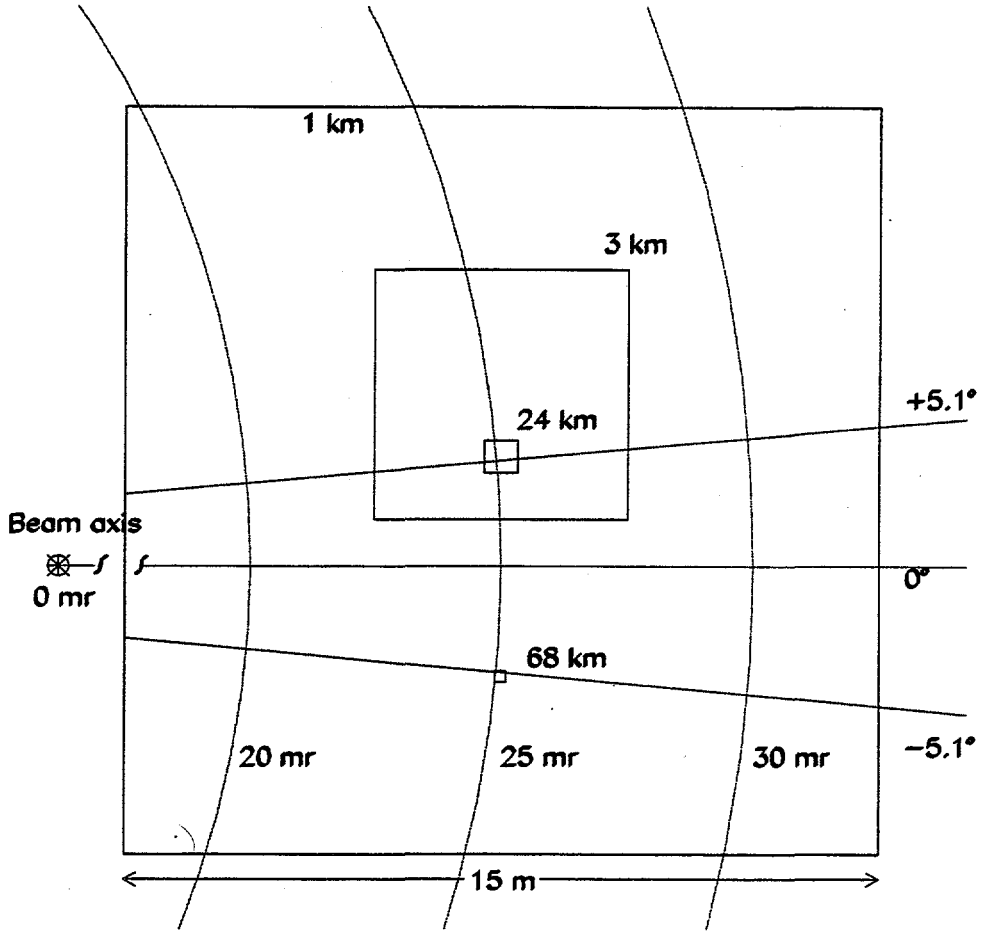


Figure 22: *The detectors as viewed from the production target in polar (in mr) and azimuthal (in degrees) angle with respect to the beam axis. The largest square is the area of D1, the smaller square is the area and location of D3, etc. The beam axis is oriented so that both Northville and Plum Island locations are at the same polar angle, but separated only by* $10.2^{o}$ *in azimuth. All detectors and the beam are assumed to be on the ground except for the 1 km detector, D1, which is below current ground level by 4 m.*

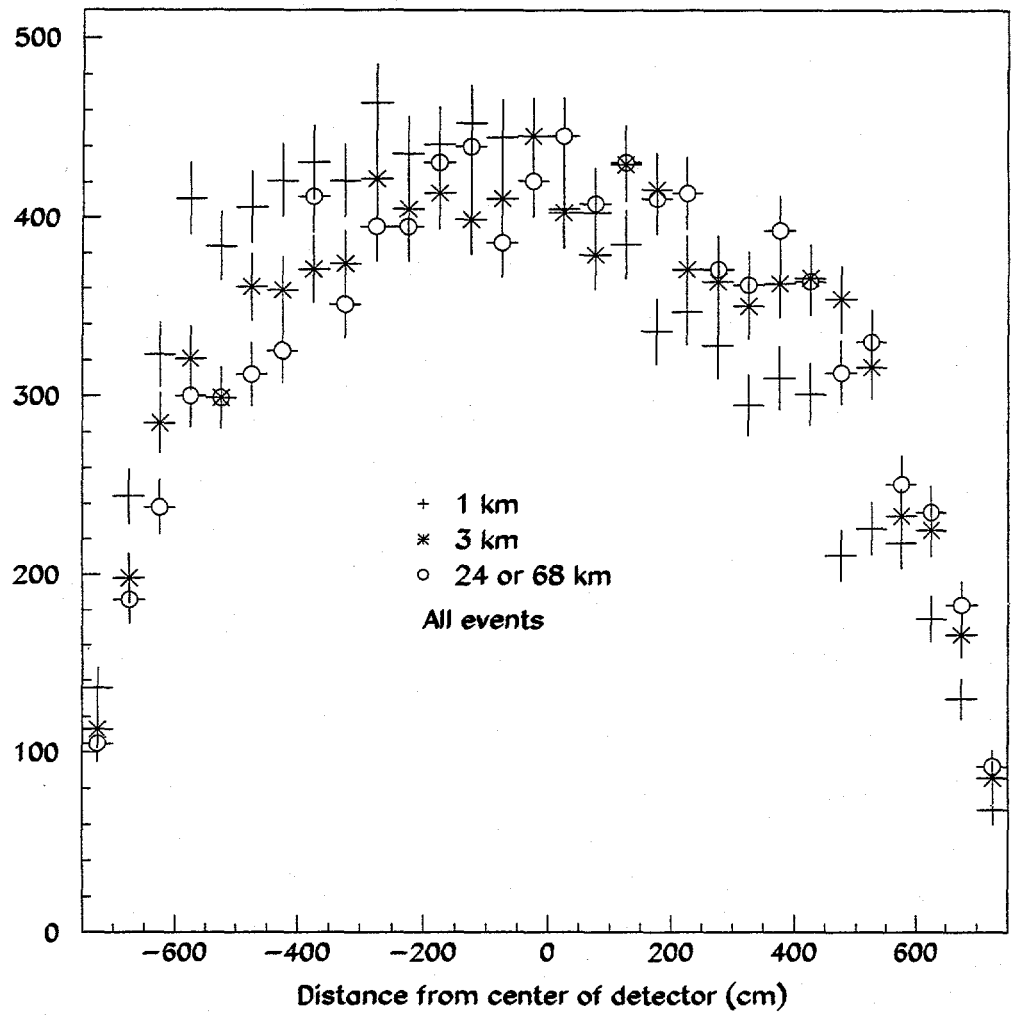


Figure 23: *Distribution of the quasi-elastic event vertices inside the entire inner volume of cylindrical tanks located at 1, 3, 24, and 68 km. The same number of events were generated for all detectors. The statistical errors on the simulation are also shown.*

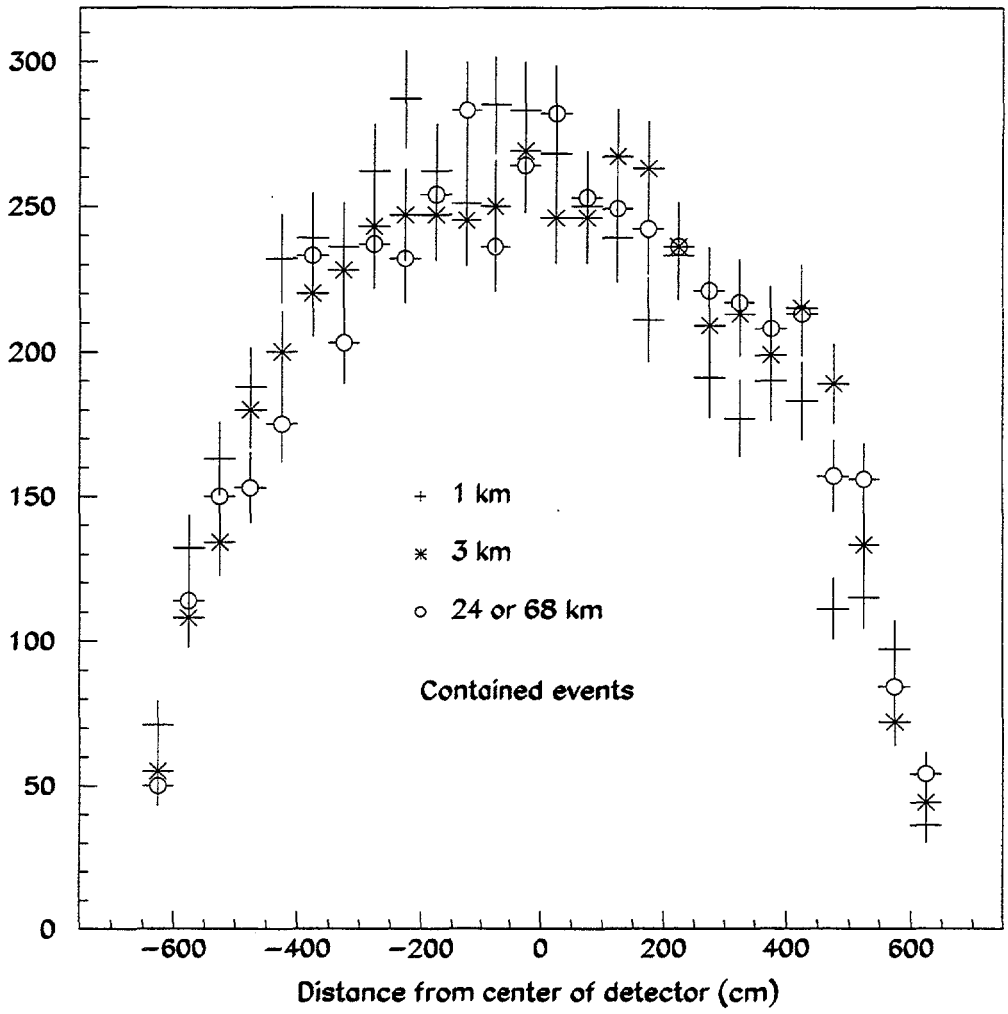


Figure 24: *Distribution of the contained quasi-elastic event vertices inside the fiducial volume of cylindrical tanks located at 1, 3, 24, and 68 km. The fiducial and containment cuts were applied to the events shown in Figure 23.*

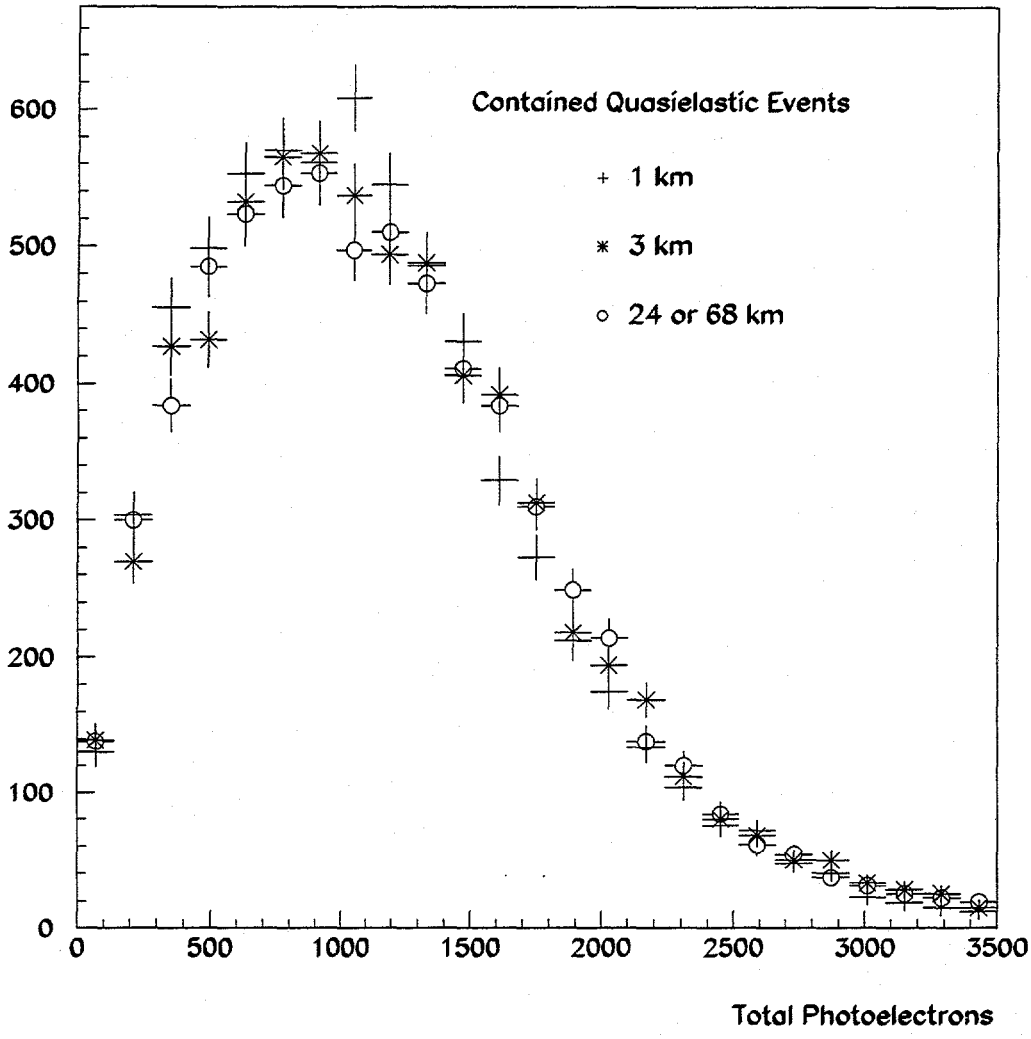


Figure 25: *Photoelectron spectrum of quasi-elastic events with the fiducial and containment cuts. The same number of events were generated for each detector location. The error bars are from Monte Carlo statistics. 750 photoelectrons corresponds to about 550 MeV/c muon momentum.*

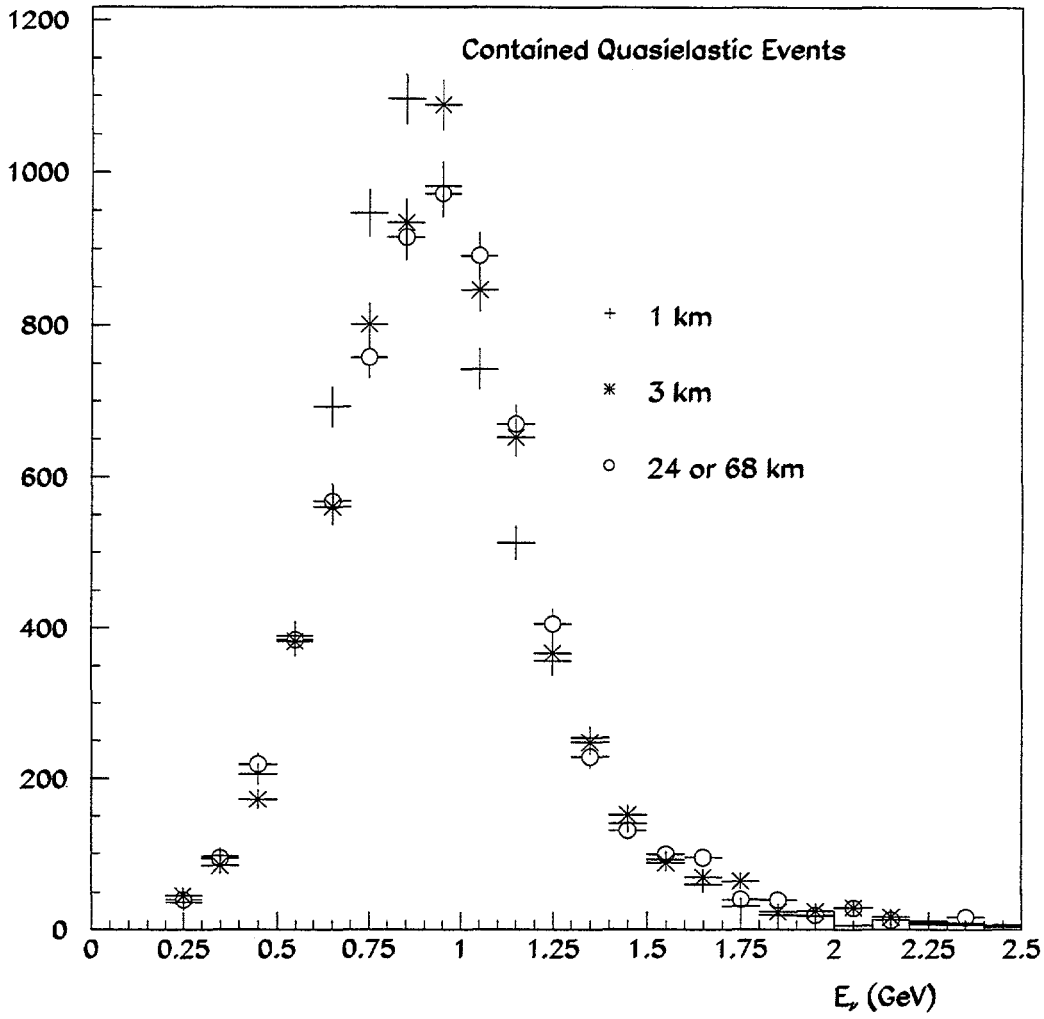


Figure 26: *Spectrum of neutrinos that produce quasi-elastic events in Figure 25. The same number of events were generated for each detector location. The error bars are from Monte Carlo statistics.*

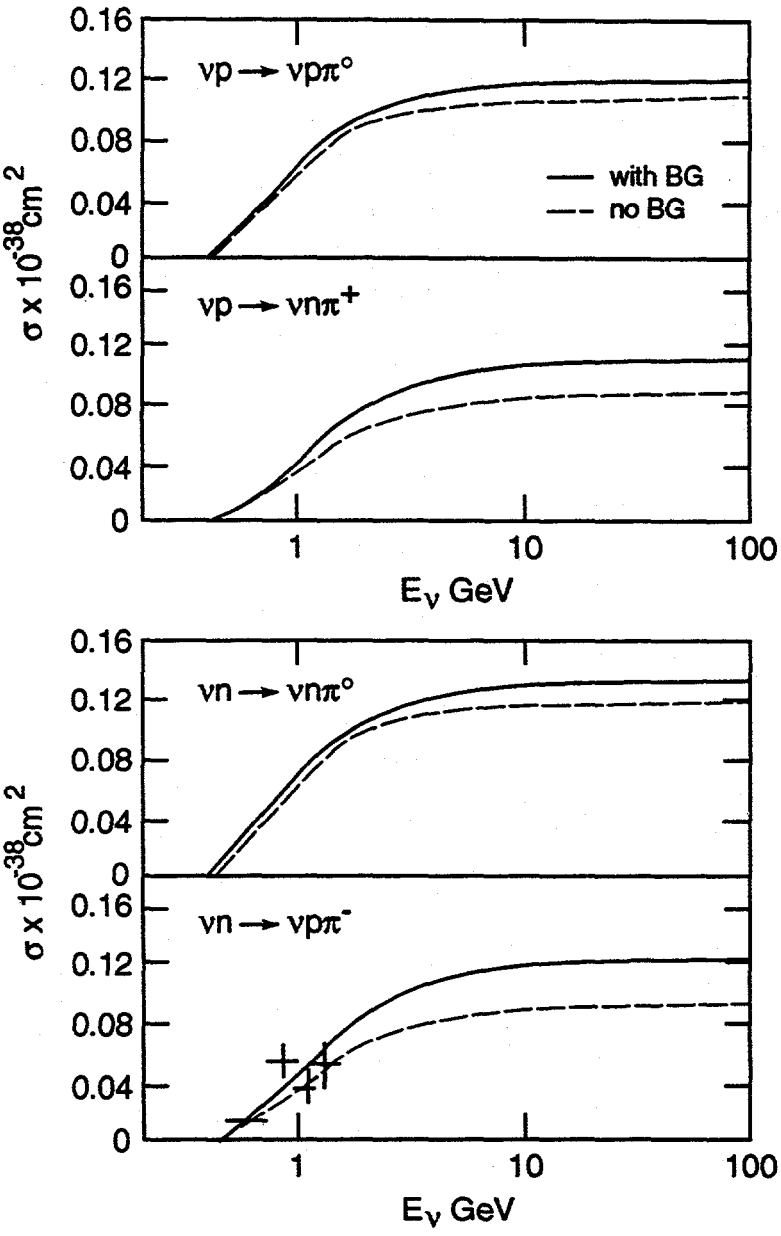


Figure 27: *Cross sections for various neutral current pion production channels from Ref. 5. Calculations are for a pure resonant model (dashed) and a model with both resonant and incoherent nonresonant production (solid).* $m_A = 0.95\ GeV/c^2$ *and* $\sin^2\theta_W = 0.22$ *for these calculations.*

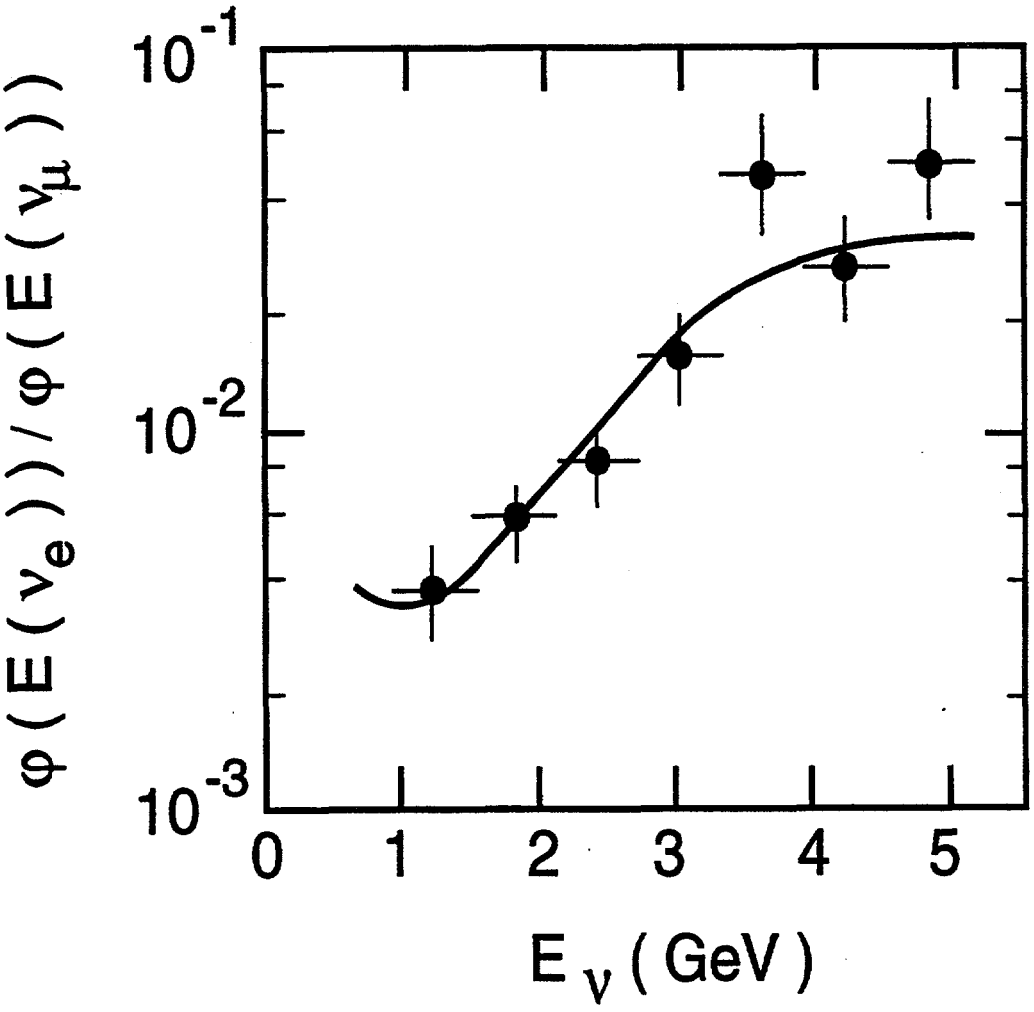


Figure 28: *Measurement of the ratio* $\frac{\Phi(\nu_e)}{\Phi(\nu_\mu)}$ *as a function of energy in experiment BNL-E734.*

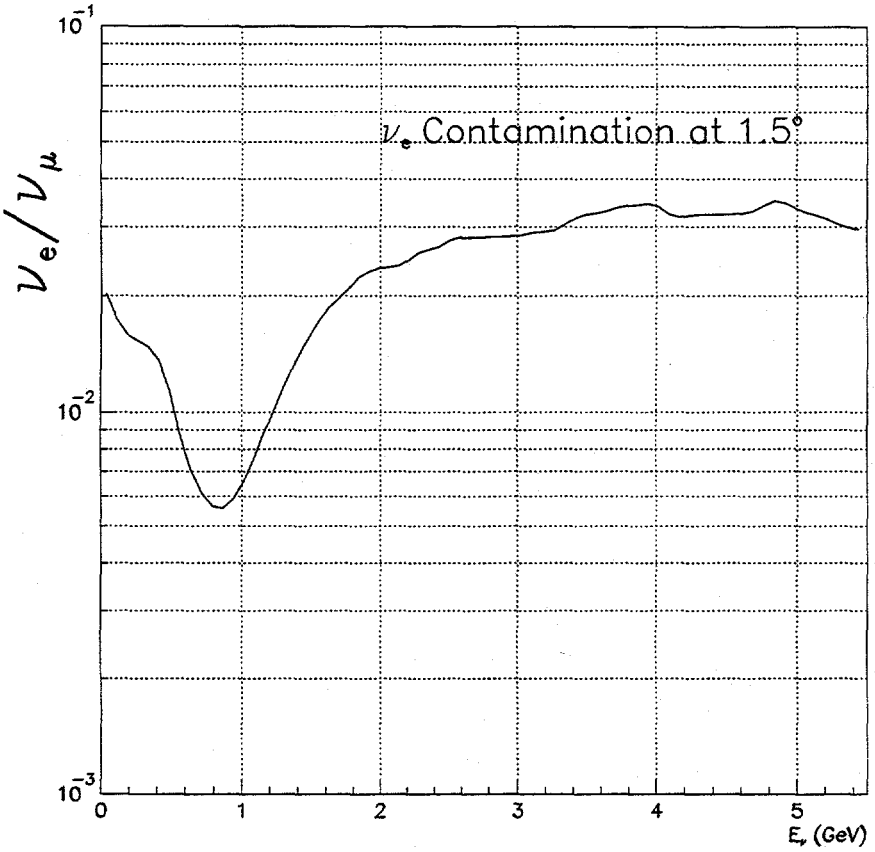


Figure 29: *Calculation of the ratio* $\frac{\Phi(\nu_e)}{\Phi(\nu_\mu)}$ *as a function of energy at* $1.5^o$ *from the beam axis.*

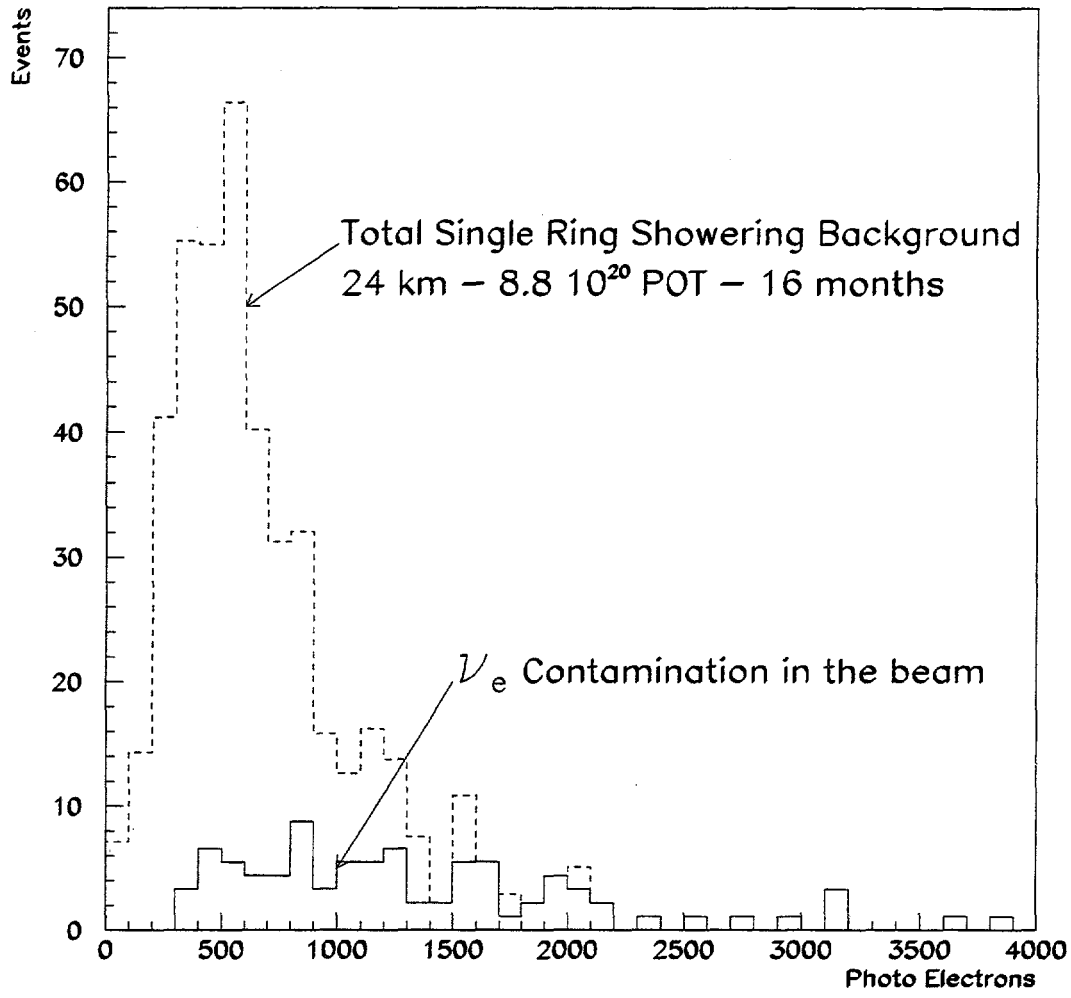


Figure 30: *The expected photoelectron spectrum from background single ring showering events at detector D24 after* $8.8 \times 10^{20}$ *POT or 16 months of running. The spectrum will be the same at D68, but the number of events will be about 1/8. The solid distribution is from the* $\nu_e$ *component in the beam and total (dashed) includes misidentified* $\pi^0$*s from neutral current events. The fraction of events due to* $\nu_e$*'s is 1/4, but about 20% are above 4000 photoelectrons.*

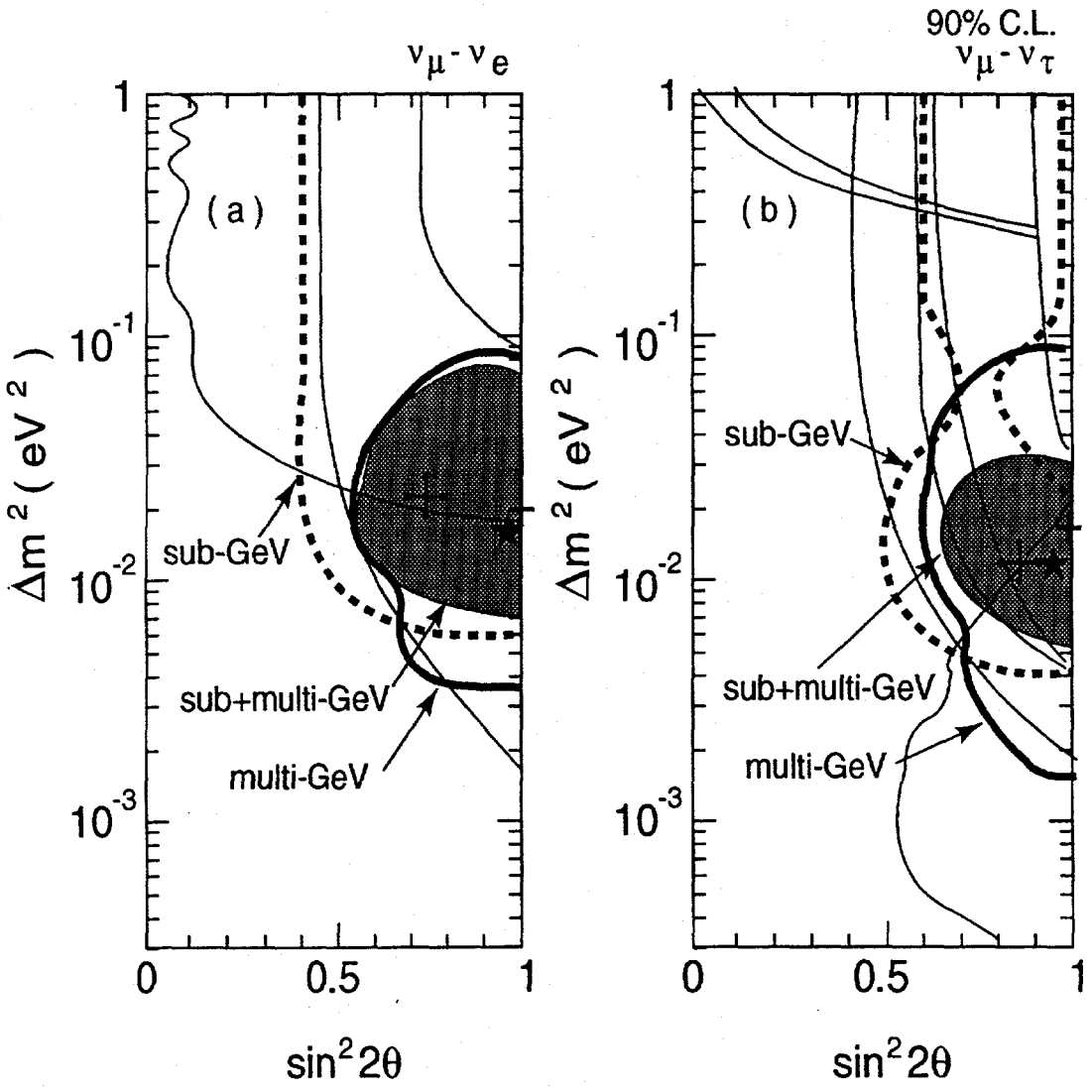


Figure 31: *Allowed region in* $\Delta m^2$ *and* $\sin^2(2\theta)$ *from the atmospheric neutrino results in Kamioka from Ref. 15.*

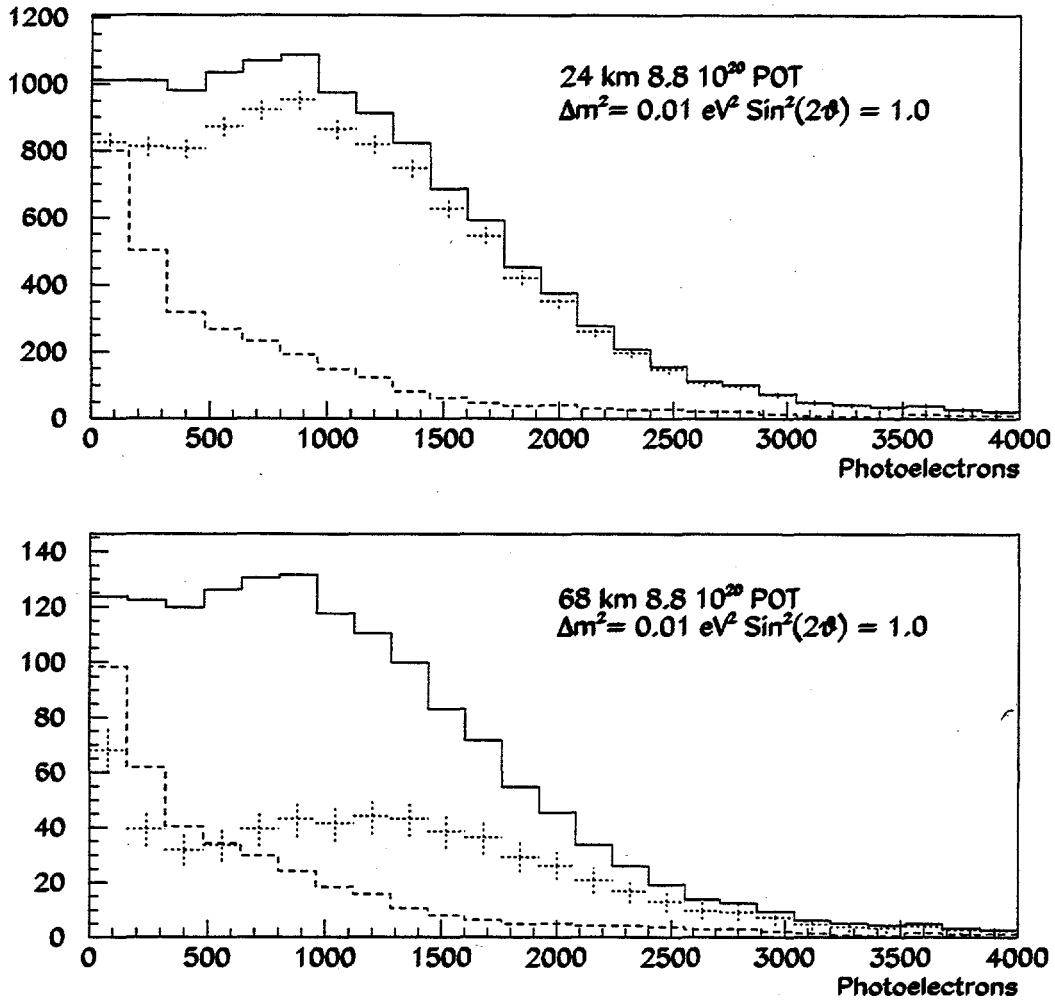


Figure 32: *Top: Spectrum of single ring muon like events in units of the number of total photoelectrons without (the solid histogram) and with (error bars) oscillations* ($\Delta m^2 = 0.01\ eV^2$, $\sin^2(2\theta) = 1.0$) *at the 24 km site. Bottom: Same at the 68 km site. The shape and normalization of the spectrum without oscillations will be predicted from measurements in D1 and D3. The systematic errors on this prediction is included in the error bars. The background from all sources for no oscillations is shown as the dashed histogram. The running time is for* $8.8 \times 10^{20}$ *POT or 16 months.*

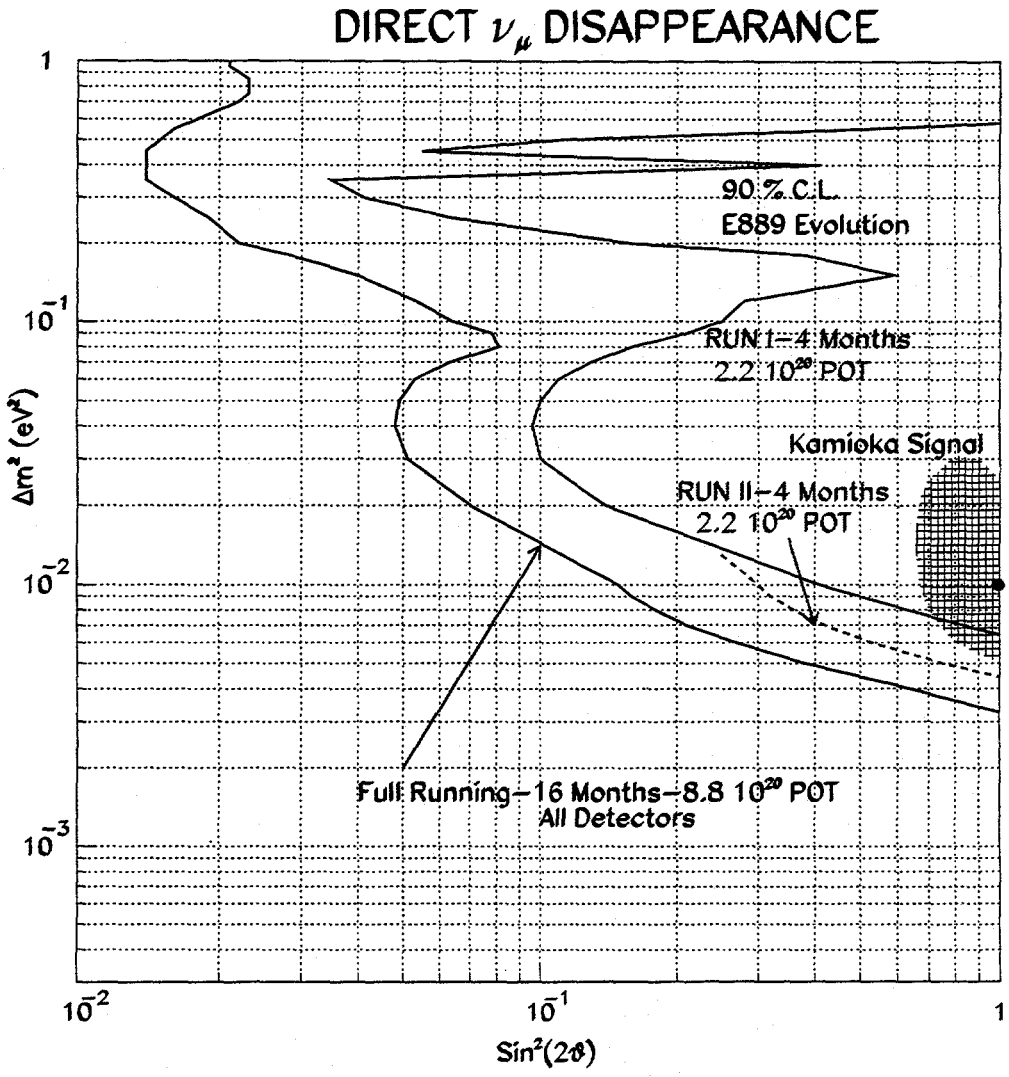


Figure 33: *The 90% confidence limit obtained with the quasi-elastic muon disappearance analysis as the experiment evolves. The first run will be with detectors at 3 and 24 km. The second run will occur after adding a third detector at 68 km, and the complete running will include a fourth detector at 1 km and* $8.8 \times 10^{20}$ *POT.*

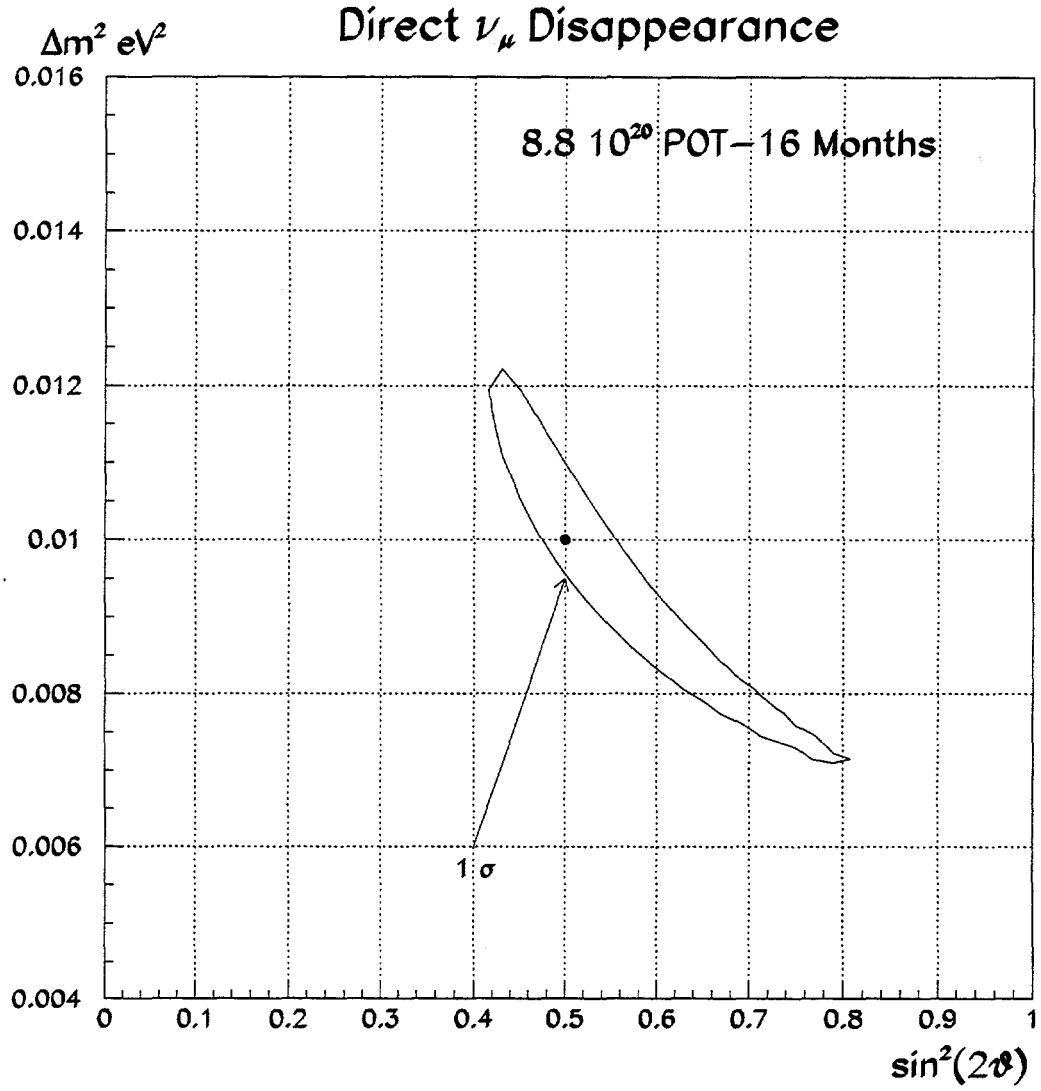


Figure 34: *1 $\sigma$ confidence level coutour from measurements at D24 and D68 assuming oscillations with* $\Delta m^2 = 0.01\ eV^2$ *and* $\sin^2(2\theta) = 0.5$.

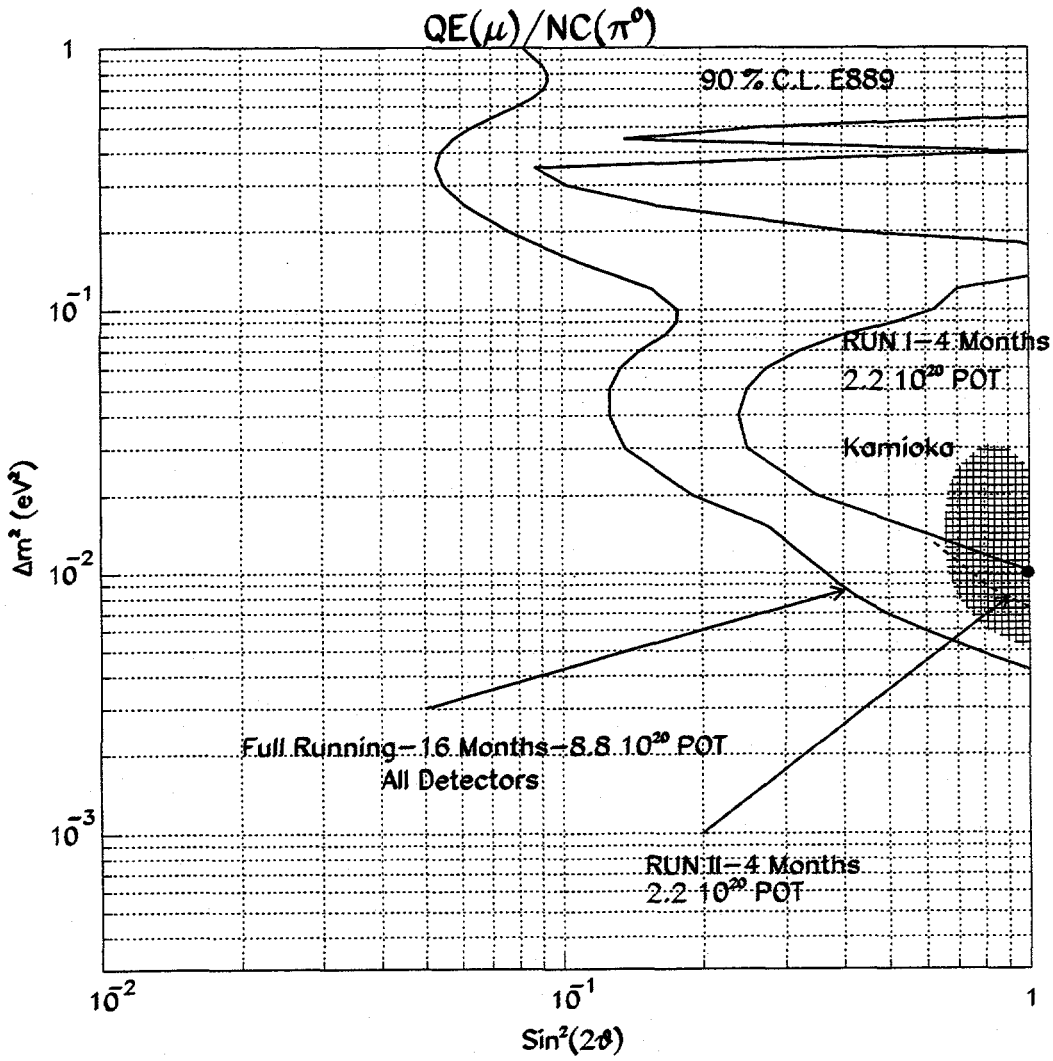


Figure 35: *90% confidence level exclusion contours for* $\Delta m^2$ *and* $\sin^2 2\theta$ *for a* $\nu_\mu$ *disappearance signature when the muon counts in each detector are normalized to the number of reconstructed neutral current* $\pi^0$ *events. The sensitivity for the complete experiment and the initial runs is shown.*

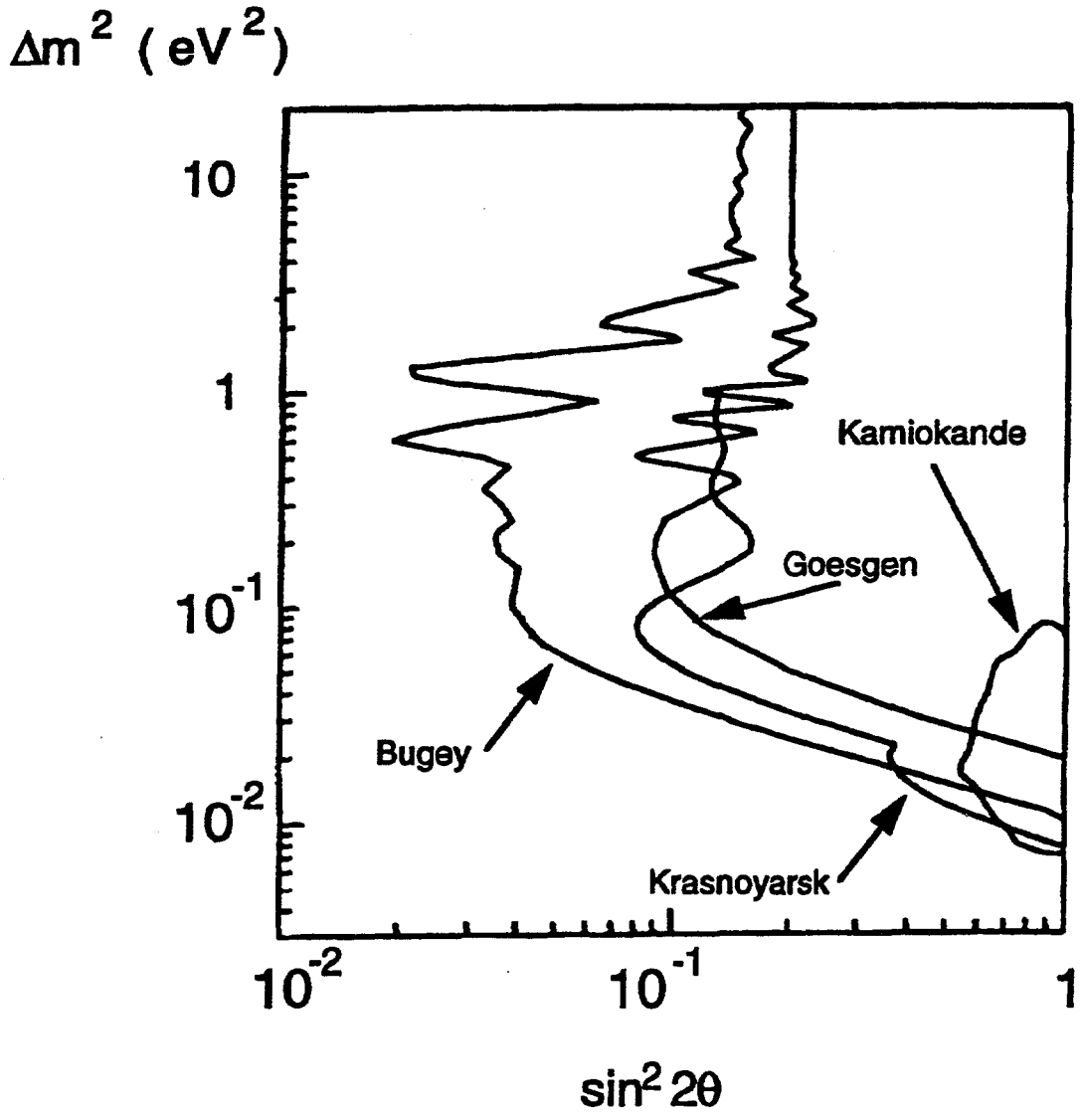


Figure 36: *Limits on anti-electron neutrino disppearance from reactor experiments and the allowed region if the Kamioka result is interpreted as* $\nu_\mu \rightarrow \nu_e$ *oscillations.*

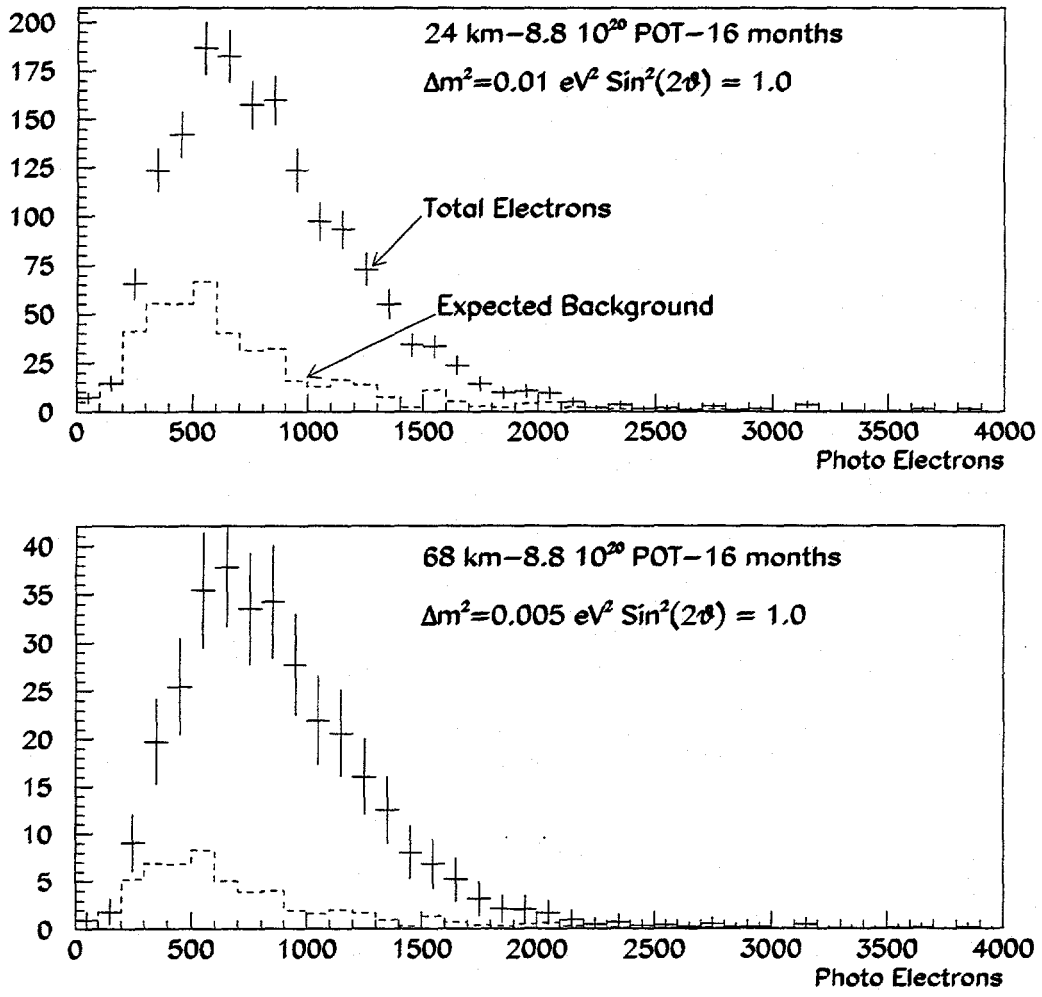


Figure 37: *The photoelectron spectrum of single ring showering electron-like events in the presence of* $\nu_\mu \rightarrow \nu_e$ *oscillations.*

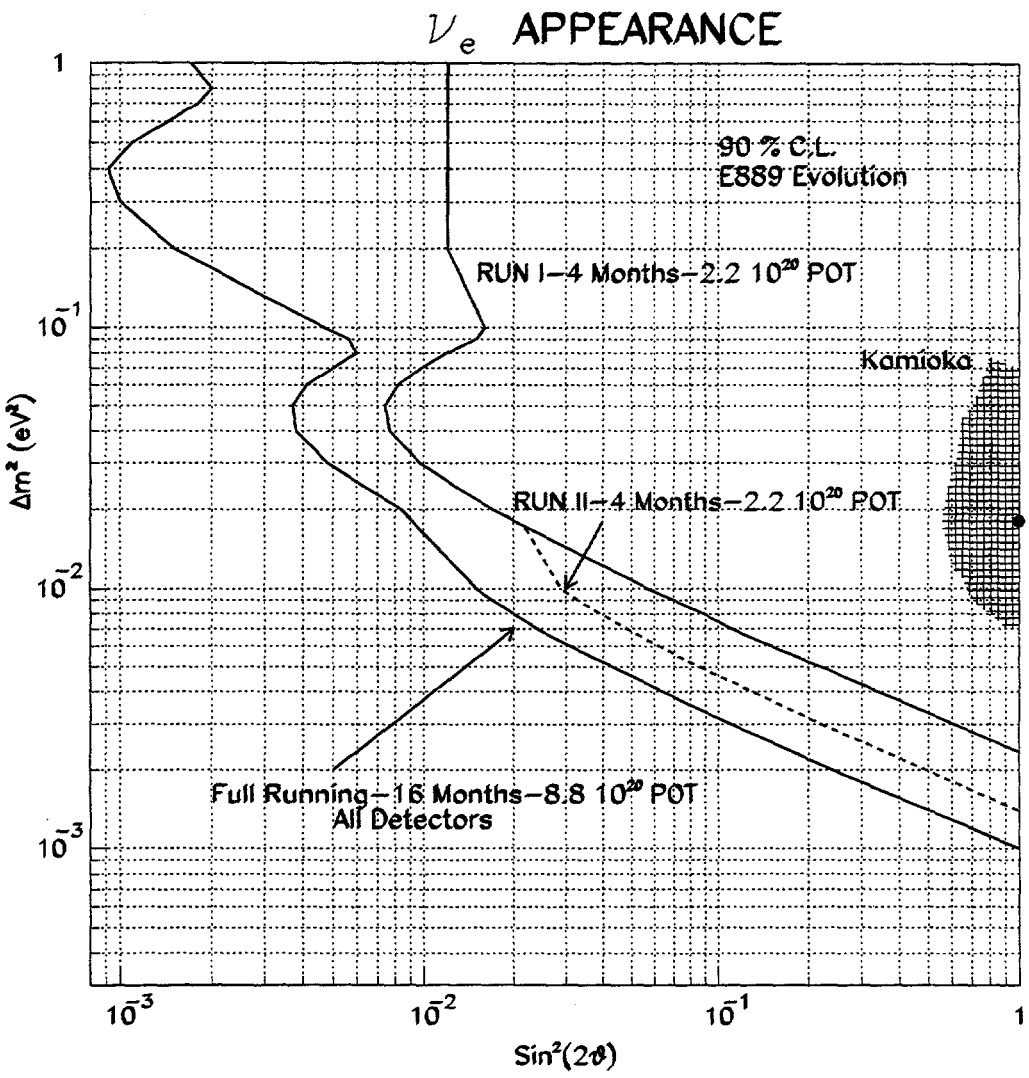


Figure 38: *90% confidence level exclusion contours for* $\Delta m^2$ *and* $\sin^2 2\theta$ *for a* $\nu_e$ *appearance signature for the complete experiment and for the initial runs.*

# VI. Other Physics

The primary intent of this proposal as emphasized above is to carry out a definitive long baseline neutrino oscillation search in the region of the oscillation parameters suggested by the anomaly in the atmospheric neutrino data. If successful in reaching a positive result, the experiment would answer long standing questions concerning neutrino mass and mixing and open a new avenue to physics beyond the standard model. It is therefore desirable to perform the experiment as well as possible, and this has been the guiding principle in its design.

Nevertheless, it should be recognized that the new neutrino beam facility discussed in Section II B would also make possible other unique neutrino scattering experiments of fundamental importance. We briefly discuss here one such experiment primarily to provide the physics motivation for it. Detailed design would require more elaboration than is appropriate here.

## A. Neutrino Magnetic Moment, Anomalous and Charge Radius-Anapole Moment, and Extra $Z'$-bosons.

An experiment to measure the precisely normalized absolute cross section of the reaction $\nu_\mu e^- \rightarrow \nu_\mu e^-$ with small statistical error and high angular resolution, when compared with the accepted Electroweak Theory (Standard Model) prediction, would lead to valuable searches for intrinsic properties of neutrinos other than mass and mixing, and for physics beyond the Standard Model.

We show in Table 1 the current limits on possible magnetic moments of neutrinos. One sees that laboratory based limits lag significantly behind those derived from astrophysics measurements which, while probably roughly correct, are indirect and require substantial inductive reasoning to extract them. There is a large theoretical literature relating to the possible existence of a neutrino magnetic moment, much of it attempting without appreciable success to dissociate neutrino mass from neutrino magnetic moment. Accordingly, significant improvement in laboratory searches for a neutrino magnetic moment, even without a positive result, would complement the neutrino oscillation searches, and aid in the formation of a complete picture of the intrinsic properties of neutrinos. Neutrino mass and a directly measurable neutrino magnetic moment are properties beyond those attributed to neutrinos in the Standard Model.

The charge radius-anapole moment of neutrinos is related to the magnetic moment in that all may be considered as the source of neutrino coupling to the electromagnetic field and the

| | |
|---|---|
| Laboratory | $\mu_{\bar{\nu}_e} < 4 \times 10^{-10}\mu_B$<br>$\mu_{\nu_\mu} < 9.5 \times 10^{-10}\mu_B$ |
| Stellar cooling<br>$(\gamma \to \nu\bar{\nu})$ | $\mu_\nu < 1.1 \times 10^{-11}\mu_B$ |
| Red giants | $\mu_\nu < (2-3) \times 10^{-12}\mu_B$ |
| Nucleosynthesis<br>$(\nu_L e \to \nu_R e)$ | $\mu_\nu < 0.5 \times 10^{-10}\mu_B$ |
| SN1987A | $\mu_\nu < (10^{-13} - 10^{-12})\mu_B$ |
| Standard model<br>(Dirac mass) | $\mu_\nu < 3 \times 10^{-19}(\frac{m_\nu}{1eV})\mu_B$ |

Table 1: Limits on neutrino magnetic moments. From P. Langacker, " Testing the Standard Model," Proc. 1990 Theoretical Advanced Study Institute in Elementary Particle Physics, Ed. M. Cvetic and P. Langacker, World Scientific, 1990 (p. 892).

Feynman diagrams describing their influence on neutrino-electron scattering are similar. The charge radius-anapole moment occur to a good approximation as a gauge invariant quantity—indeed, as a radiative correction in the Standard Model— and is expected to contribute to $\nu - e$ scattering at a level just below that set by present experimental limits, approximately $10^{-32}cm^2$ [1]. To the extent that confirmation of the precise magnitude of calculated radiative corrections by experiment is a desirable test of the validity of gauge theories—witness the attempts to go to higher loop corrections, i.e., higher orders of $\alpha_{QED}$, through more and more refined measurements of $g-2$ for the charged leptons—so determination of the charge radius of the neutrino would directly test our understanding of radiative corrections in the Electroweak Theory. A deviation could point to an anomalous charge radius induced by new physics.

Still other issues of importance which may be addressed in $\nu_\mu e^- \to \nu_\mu e^-$ scattering are those of extra $Z'$-bosons beyond the known $Z^0$ at $m(Z^0) = 91.18$ GeV, and extra fermions [2]. We use as illustration here extra neutral $Z$ bosons because, in general, extra intermediate vector bosons (IVB)—beyond the Standard Model (SM) $W$ and $Z$—are universal in grand unification theories (GUTs) beyond SU(5). They arise naturally because the extension from

the SM to GUTs introduces larger gauge groups with more group generators and more IVBs. Relatively low mass IVBs might, however, develop masses in the TeV range by other than usual Higgs fields.

There are effectively two extra free parameters in the SM with an extra $Z$ boson, provided the relative fermion couplings are constrained by the underlying non-Abelian gauge group. This allows for many possibilities which are discussed in detail in Ref. [2], some of which are best searched for by other experimental means, e.g., $e^+e^-$ collisions or parity violating atomic physics measurements. There are also a number of extra $Z$-boson types for which measurement of $\sigma(\nu_\mu e^-)$ would be either the sole means of access or one strongly competitive with other means.

As remarked above, improved searches for anomalous electromagnetic properties of the $\nu_\mu$ or extra $Z$-bosons will require precise measurement of $\sigma(\nu_\mu e^-)$. This would be possible in the imaging Cherenkov counter D1 in which the momentum and angle of the recoiling electron would be directly measured with good accuracy and the event rate would be high. For example, D1 would have angular resolution (limited by multiple scattering) similar to that of the E-734 detector [3] and a substantially higher rate. Normalization would be provided by quasielastic events in D1 and D3. Many of the uncertainties involved in the E-734 normalization would not occur in D1 and D3 because of the larger mass of the detectors, the larger distance of the detectors from the beam origin, and the almost monochromatic beam with little high energy tail at 1.5 degrees.

## REFERENCES


1. G. Degrassi, A. Sirlin, and W.J. Marciano, Phys. Rev. D39, 287 (1989).

2. P. Langacker, M. Luo, A.K. Mann, Rev. Mod. Phys. 64, 87 (1992).

3. L.A. Ahrens, et al. (E734 Collaboration), Phys. Rev. D 34, 75 (1986); ibid 35, 785 (1987).

## VII. Cost and Schedule

The detailed cost and schedule for E889 is contained in a formal Conceptual Design Report (CDR) being submitted by Brookhaven National Laboratory to DOE as a line-item request for a new construction start in FY97. The schedule is based on this construction start but assumes a reasonable amount of R&D funds (~$4M) in FY96 to do detailed studies of critical items necessary for the construction start in FY97. The present schedule (Fig. 1) shows that, with the requested funding profile, the new neutrino beam and the detector tanks at 3km and 24km would be operational in FY99, and the full contingent of 4 detectors operational about 1 year later.

If the experiment were not constrained by the FY97 construction start, the schedule could be advanced by approximately 6 months. Similarly, if R&D funding is not available in FY96, then the schedule will slip by about 6 months.

The cost estimate summarized here was developed using the Work Breakdown Schedule (WBS) structure shown in Fig. 2. The project was divided into 4 distinct and logically separate pieces. WBS 1.1 contains all civil construction associated with the construction of the new neutrino beamline and the preparation of all the detector sites together with the installation of the detector tanks and the ancillary support buildings. These estimates were developed by the BNL Plant Engineering Division which routinely handles such projects at the laboratory. WBS 1.2 contains all technical work related to extracting the proton beam from the AGS, transporting it to the neutrino target, focussing the produced mesons with a magnetic horn system and the electronics for monitoring the beam system. These estimates were developed by the AGS department which has built many external beam lines and constructed and operated a similar neutrino line in the past. WBS 1.3 contains the active elements (photomultiplier tubes) in the detector system, the associated electronics and DAQ systems necessary for the experiment. These estimates were developed by the physicists in the collaboration based on previous experience in other large water Cherenkov systems such as Kamiokande, LSND and SNO. WBS 1.4 contains all the EDIA for each of the aforementioned subsystems and the overall project management and QA functions. Full documentation is available for all estimates in the CDR.

The base cost for all conventional construction, detector systems, particle beam systems, and project support necessary for the complete experiment is $46.5M in FY 95 dollars. The project period covers the U.S. fiscal years FY 1997-99. The estimated average overhead is $14M (26.6%) due to recent changes in DOE orders relating to construction projects, and

the estimated summed contingency is \$8.7M (14.8%), relative to the base cost. With these costs included, the total comes to \$67.7M. Finally, distributing the costs by fiscal year and allowing for escalation, the total project cost becomes \$76.6M. The summary cost details are found in Vol.1, Section 5 of the Conceptual Design Report (CDR) for the Long Baseline Neutrino Oscillation Experiment (BNL project No. 97-CH-114, March 1995). Further cost estimate details are found in Vol. 2 of the same report.

In connection with costs, it should be emphasized that the experiment will be run in a mode new to BNL. It will receive the fast extracted proton beam on the neutrino target approximately 20 hours per day when the AGS is not filling RHIC. The method and speed of accomplishing the transition from heavy ion RHIC injection to proton injection for E889 has been studied and no serious obstacles encountered. The method will be explored in practice in the near future. The incremental cost of this mode of operation relative to the cost of the current AGS-HEP operation is principally for electrical power to the components of the neutrino beam line and the AGS magnets operated without a flat-top for fast extraction. This incremental cost will be a small fraction of the present AGS-HEP operating budget.

# LONG BASELINE NEUTRINO OSCILLATION
## Project Schedule

Date:2-22-95
Rev: 1

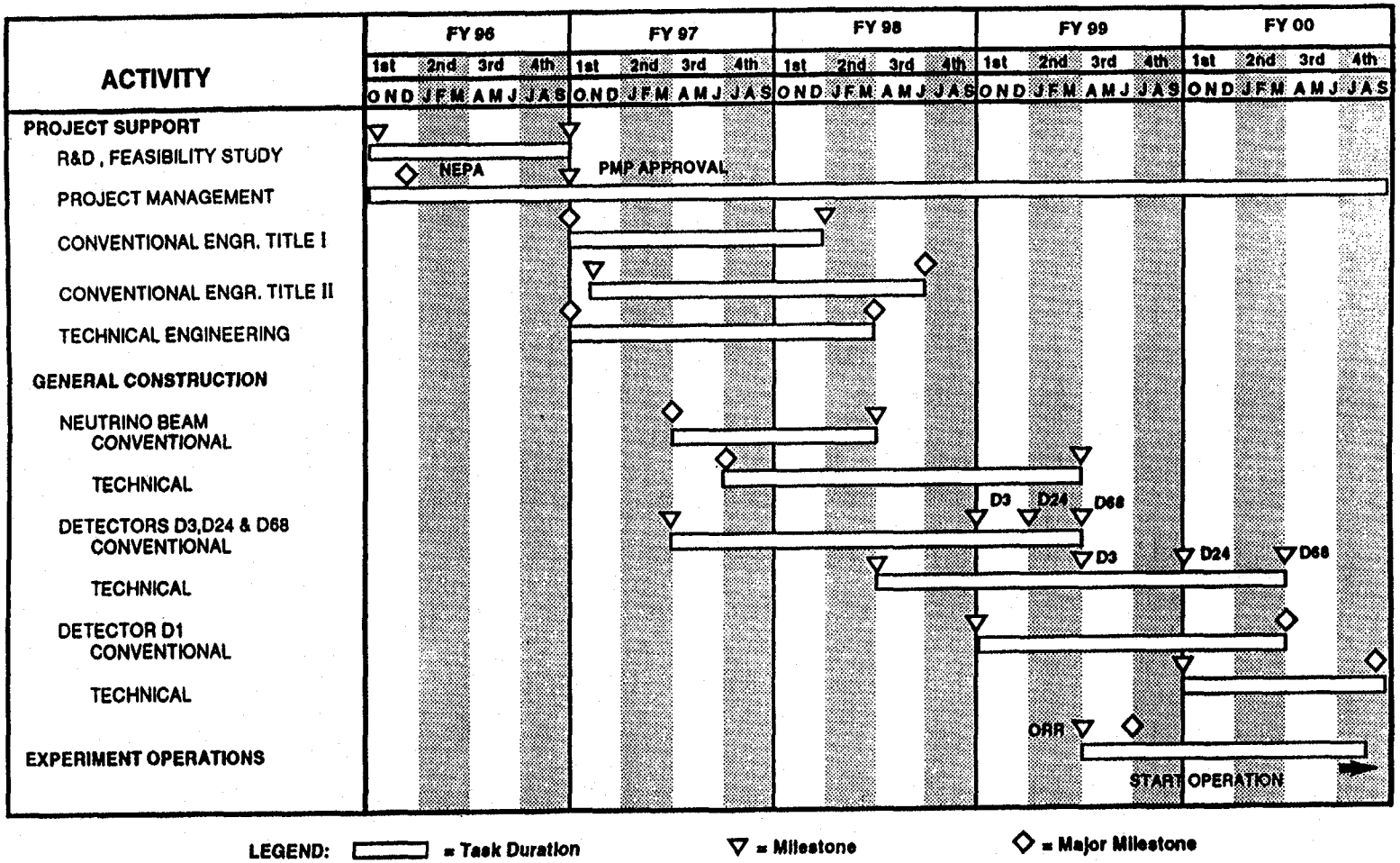


Fig. 1

# LONG BASELINE NEUTRINO OSCILLATION EXPERIMENT

## Work Breakdown Structure (WBS)

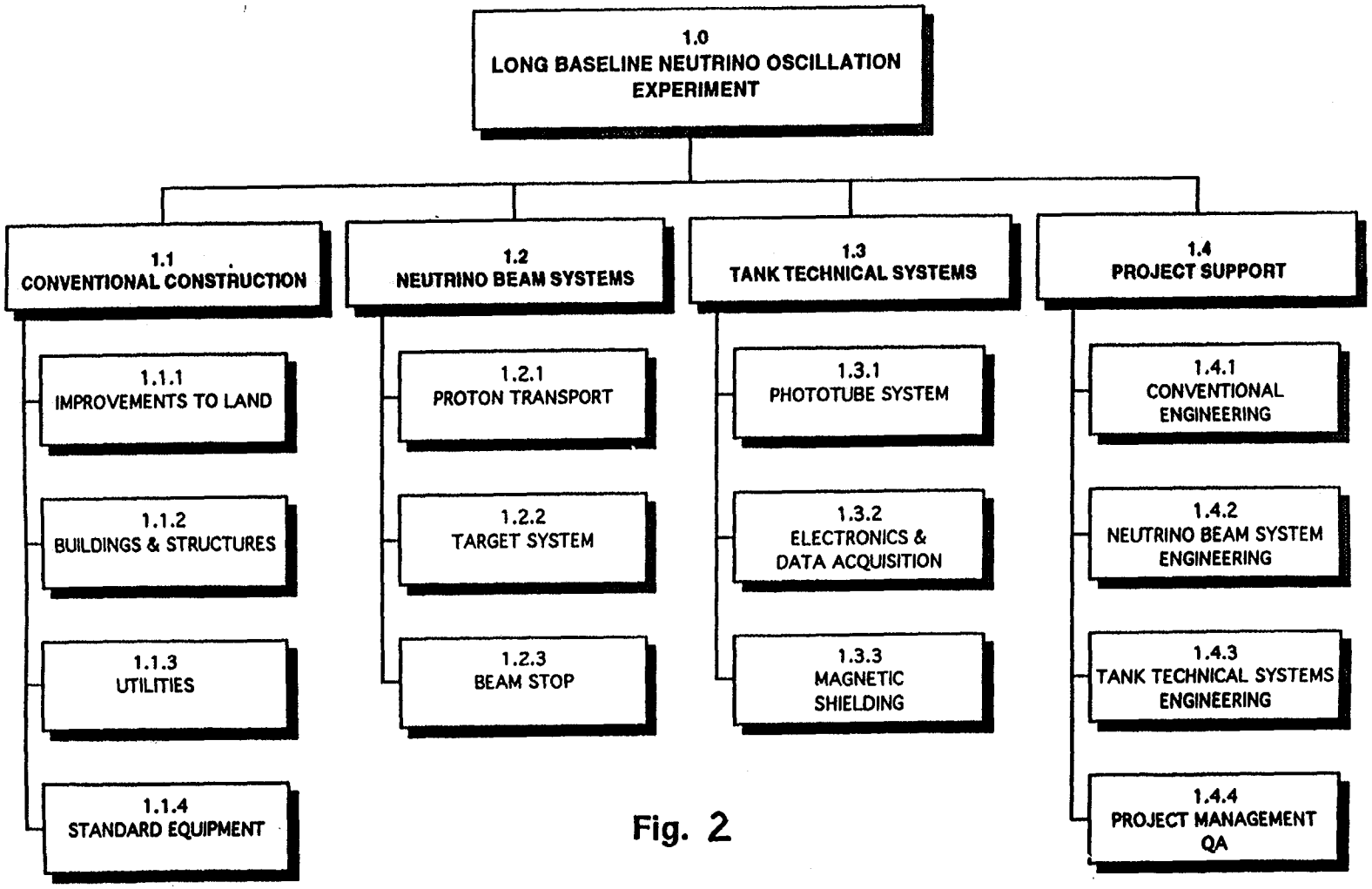


Fig. 2

# VIII. Summary

We have presented a proposal for a multi-detector long baseline neutrino oscillation experiment at the BNL AGS. The experiment will search for oscillations in the $\nu_\mu$ disappearance channel and the $\nu_\mu \leftrightarrow \nu_e$ appearance channel by means of four identical neutrino detectors located 1, 3, 24, and 68km from the AGS neutrino source. Observed depletion of the $\nu_\mu$ flux in the far detectors not attended by an observed proportional increase of the $\nu_e$ flux in those detectors will be *prima facie* evidence for the oscillation channel $\nu_\mu \leftrightarrow \nu_\tau$. The experiment is directed toward exploration of the region of the neutrino oscillation parameters $\Delta m^2$ and $\sin^2 2\theta$, suggested by the Kamiokande and IMB deep underground detectors but it will also explore a region more than two orders of magnitude larger than that of previous accelerator experiments.

The experiment is designed to capitalize on the advantages of the AGS: high proton beam intensity (currently the AGS can provide $6 \times 10^{13}$ per pulse every 1.6 sec) yielding a correspondingly high intensity, low energy, pure ( $\nu_e/\nu_\mu$ flux ratio of $10^{-2}$) muon neutrino beam, and the narrow time-structure (20-30 ns wide 8 bunches per pulse) of the fast extracted proton beam to permit the detectors to be located on the earth's surface.

A key aspect of the experimental design involves placing the detectors 1.5 degrees off the center line of the neutrino beam, which has the important advantage that the central value of the neutrino energy ($\approx$ 1 GeV) and the beam spectral shape are, to a good approximation, the same in all four detectors. Another significant advantage of the 1.5 degree beam is that the low energy ($\approx$ 1 GeV) flux is increased while the higher energy flux is decreased relative to the flux in the zero degree beam. This appreciably diminishes the rate of inelastic neutrino interactions with respect to the dominant quasielastic interactions that constitute the signals of the experiment.

The proposed detectors are massive, imaging, water Cherenkov detectors similar in large part to the Kamiokande and IMB detectors. Our design has profited from their decade-long experience, and from the detector designs of the forthcoming SNO and SuperKamiokande detectors.

An important principle in the design of the experiment has been to provide detailed, precise, and redundant control of possible systematic errors. This accounts for the requirement of four identical detectors, and their relative spacing, which yields data of high statistical quality in the upstream detectors with which to study the neutrino beam properties and the response of the massive, large volume detectors. This ensures proper understanding of the

response of the far detectors and correct high precision predictions of the fluxes reaching the far detectors in the absence of oscillations. To this end, the ratio $QE(\mu)/NC(\pi^0)$ is also measured in each of the four detectors to provide an essentially independent search for oscillations in the $\nu_\mu$ disappearance channel, as well as in the channel $\nu_\mu \leftrightarrow \nu_{(sterile)}$.

The experiment will run in a mode new to BNL. It will receive the fast extracted proton beam on the neutrino target approximately 20 hours per day when the AGS is not filling RHIC.

The experiment will evolve in a continuous fashion, dictated by the rates at which construction and funding are likely to proceed. The detectors will be built in the sequence D3, D24, D68, and the fourth detector at D1. this permits operation as soon as each detector is completed, and makes possible the extraction of significant oscillation results from D3 and D24 early in calendar 1999. All four tanks would be in operation one year later.

A cost and schedule document (CDR) has been submitted to the DOE which provides the basis for the total project cost and schedule. This schedule is funding driven and might be advanced by a half year with an improved funding profile.

The new neutrino beam facility necessary for the oscillation search would make possible other unique neutrino scattering experiments of fundamental importance. The motivation for one such experiment is briefly discussed.